UNIVERSITAT
ROVIRA i VIRGILI

New Horizons in Computational Modeling of Polyoxometalates: Biological Activity, Energy Storage and Sustainable Catalysis

Albert Solé Daura

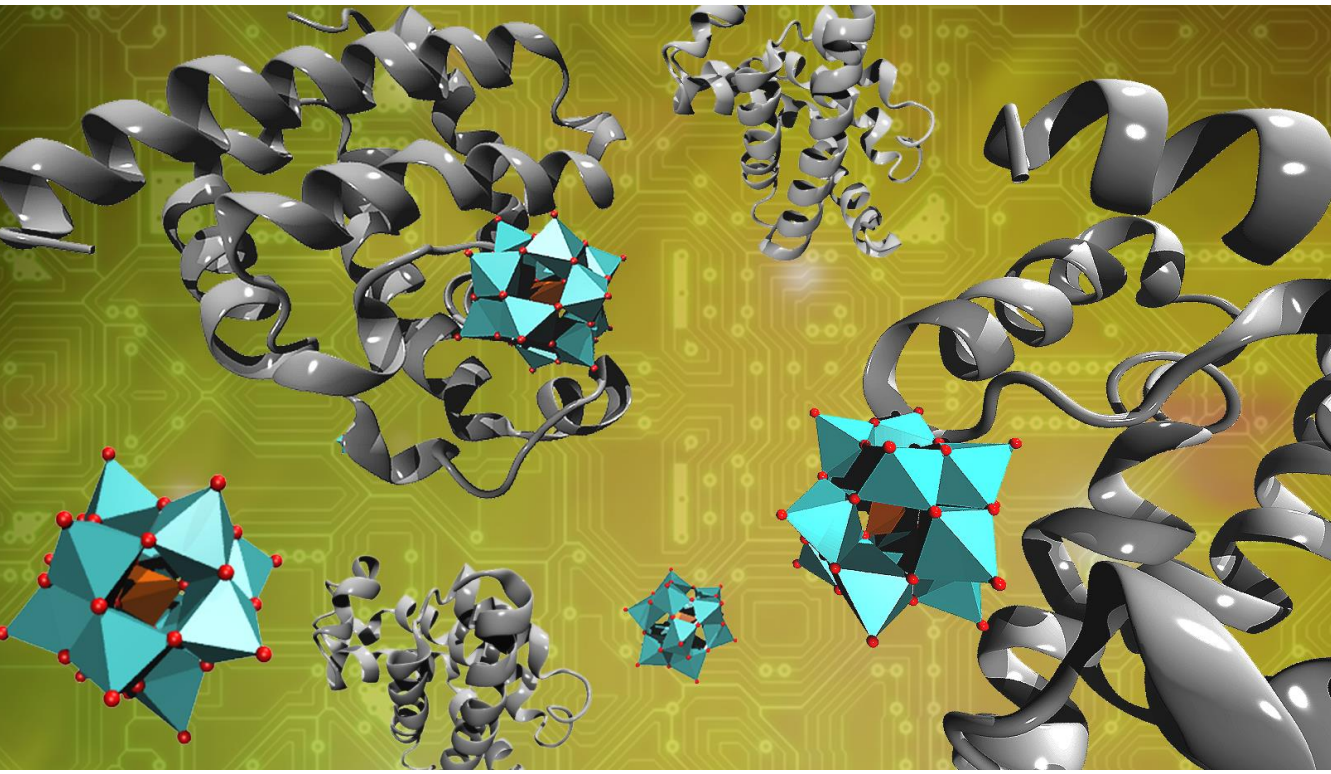

DOCTORAL THESIS
2020

UNIVERSITAT ROVIRA I VIRGILI
NEW HORIZONS IN COMPUTATIONAL MODELING OF POLYOXOMETALATES:
BIOLOGICAL ACTIVITY, ENERGY STORAGE AND SUSTAINABLE CATALYSIS.
Albert Solé Daura

Albert Solé Daura

New Horizons in Computational Modeling of Polyoxometalates: Biological Activity, Energy Storage and Sustainable Catalysis

DOCTORAL THESIS

Supervised by

Dr. Jorge Juan Carbó Martín and Prof. Josep Maria Poblet Rius

UNIVERSITAT ROVIRA i VIRGILI

Departament de Química Física i Inorgànica

Tarragona, 2020

UNIVERSITAT ROVIRA I VIRGILI
NEW HORIZONS IN COMPUTATIONAL MODELING OF POLYOXOMETALATES:
BIOLOGICAL ACTIVITY, ENERGY STORAGE AND SUSTAINABLE CATALYSIS.
Albert Solé Daura

UNIVERSITAT ROVIRA i VIRGILI

Jorge Juan Carbó Martín, Professor Agregat del Departament de Química Física i Inorgànica de la Universitat Rovira i Virgili i Josep Maria Poblet Rius, Catedràtic del Departament de Química Física i Inorgànica de la Universitat Rovira i Virgili

FEM CONSTAR que aquest treball, titulat

"**New Horizons in Computational Modeling of Polyoxometalates: Biological Activity, Energy Storage and Sustainable Catalysis**"

que presenta Albert Solé Daura per a l'obtenció del títol de Doctor, ha estat realitzat sota la nostra direcció al Departament de Química Física i Inorgànica d'aquesta universitat.

Tarragona, 27 de Setembre de 2019

Els directors de la tesi doctoral

Jorge Juan Carbó Martín

Josep Maria Poblet Rius

UNIVERSITAT ROVIRA I VIRGILI
NEW HORIZONS IN COMPUTATIONAL MODELING OF POLYOXOMETALATES:
BIOLOGICAL ACTIVITY, ENERGY STORAGE AND SUSTAINABLE CATALYSIS.
Albert Solé Daura

Contents

UNIVERSITAT ROVIRA I VIRGILI
NEW HORIZONS IN COMPUTATIONAL MODELING OF POLYOXOMETALATES:
BIOLOGICAL ACTIVITY, ENERGY STORAGE AND SUSTAINABLE CATALYSIS.
Albert Solé Daura

List of Publications

The following scientific publications have been achieved during the Ph. D.

Related to this thesis:

- Solé–Daura, A.; Goovaerts, V.; Stroobants, K.; Absillis, G.; Jiménez–Lozano, P.; Poblet, J. M.; Hirst, J. D.; Parac–Vogt, T. N.; Carbó, J. J. "**Probing Polyoxometalate–Protein Interactions Using Molecular Dynamics Simulations**" *Chem. Eur. J.* **2016**, *22*, 15280–15289 (selected for front cover).

- Maksimchuk, N.V.; Maksimov, G. M.; Evtushok, V. Y.; Ivanchikova, I. D.; Chesalov, Y. A.; Maksimovskaya, R. I.; Kholdeeva, O. A.; Solé–Daura, A.; Poblet, J. M.; Carbó, J. J. "**Relevance of Protons in Heterolytic Activation of H_2O_2 over Nb(V): Insights from Model Studies on Nb–Substituted Polyoxometalates**" *ACS Catal.* **2018**, *10*, 9722–9737.

- Zhang, T.; Solé–Daura A.; Hostachy, S.; Blanchard, S.; Paris, C.; Li, Y.; Carbó, J. J.; Poblet, J. M.; Proust, A.; Guillemot, G. "**Modeling the Oxygen Vacancy at a Molecular Vanadium(III) Silica–Supported Catalyst**" *J. Am. Chem. Soc.* **2018**, *44*, 14903–14914.

- Solé–Daura, A.; Notario–Estévez, A.; Carbó, J. J.; Poblet, J. M.; De Graaf, C.; Monakhov, K. Y.; López, X. "**How Does the Redox State of Polyoxovanadates Influence the Collective Behavior in Solution? A Case Study with $[I@V_{18}O_{42}]^{q-}$ (q = 3, 5, 7, 11, and 13)**" *Inorg. Chem.* **2019**, *58*, 3881–3894.

- Maksimchuk, N. V; Ivanchikova, I. D.; Maksimov, G. M.; Eltsov, I. V.; Evtushok, V. Y.; Kholdeeva, O. A.; Lebbie, D.; Errington, R. J.; Solé–Daura, A.; Poblet, J. M.; Carbó, J. J. "**Why Does Nb(V) Show Higher Heterolytic Pathway Selectivity Than Ti(IV) in Epoxidation with H_2O_2? Answers from Model Studies on Nb–and Ti–Substituted Lindqvist Tungstates**" *ACS Catal.* **2019**, *9*, 6262–6275.

- Solé–Daura, A.; Poblet, J. M.; Carbó, J. J. "**Structure–Activity Relationships for the Affinity of Chaotropic Polyoxometalate Anions towards Proteins**" *(submitted for publication)*

- Solé–Daura, A.; Zhang, T.; Fouilloux, H.; Robert, C.; Thomas, C. M.; Chamoreau, L.-M.; Carbó, J. J. Proust, A.; Guillemot, G.; Poblet, J. M. "**Catalyst Design for Alkene Epoxidation by Molecular Analogues of Heterogeneous Titanium-Silicalite Catalysts**"
  (submitted for publication)

Non–related to this thesis:

- Jiménez–Lozano, P.; Solé–Daura, A.; Wipff, G.; Poblet, J. M.; Chaumont, A.; Carbó, J. J. "**Assembly Mechanism of Zr–Containing and Other TM–Containing Polyoxometalates**"
  Inorg. Chem. **2017**, *56*, 4148–4156.

- Hernández, S.; Ottone, C.; Proto, S.; Tolod, K.; Díaz de los Bernardos, M.; Solé–Daura, A.; Carbó, J. J.; Godard, C.; Castillón, S.; Russo, N.; Saracco, G.; Claver, C. "**Core–substituted naphthalenediimides anchored on $BiVO_4$ for visible light–driven water splitting**"
  Green Chem. **2017***, 19, 2448–2462.*

- Linnenberg, O.; Moors, M.; Solé–Daura, A.; López, X.; Bäumer, C.; Kentzinger, E.; Pyckhout–Hintzen, W.; Monakhov, K. Y. "**Molecular Characteristics of a Mixed–Valence Polyoxovanadate $\{V^{IV/V}_{18}O_{42}\}$ in Solution and at the Liquid–Surface Interface**"
  J. Phys. Chem. C **2017**, *121*, 10419–10429.

- Nikoloudakis, E.; Karikis, K.; Laurans, M.; Kokotidou, C.; Solé–Daura, A.; Carbó, J. J.; Charisiadis, A.; Charalambidis, G.; Izzet, G.; Mitraki, A.; Douvas, A. M.; Poblet, J. M.; Proust, A.; Coutsolelos, A. G. "**Self–assembly study of nanometric spheres from polyoxometalate–phenylalanine hybrids, an experimental and theoretical approach**"
  Dalton Trans. **2018**, *47*, 6304–6313 (selected for inside cover).

- Qasim, H. M.; Ayass, W. W.; Donfack, P.; Mougharbel, A. S.; Bhattacharya, S.; Nisar, T.; Balster, T.; Solé–Daura, A.; Römer, I.; Goura, J.; Materny, A.; Wagner, V.; Poblet, J. M.; Bassil, B. S.; Kortz, U. "**Peroxo–Cerium(IV)–Containing Polyoxometalates: $[Ce^{IV}_6(O_2)_9(GeW_{10}O_{37})_3]^{24-}$, a Recyclable Homogeneous Oxidation Catalyst**" *Inorg. Chem.* **2019**, *58*, 11300–11307.

- Julian, I.; Hueso, J. L.; Lara, N.; Solé–Daura, A.; Poblet, J. M.; Mitchell, S. G.; Mallada, R.; Santamaria, J. "**Polyoxometalates as alternative Mo precursors for methane dehydroaromatization on Mo/ZSM–5 and Mo/MCM–22 catalysts**" *Catal. Sci. Technol.* **2019**, DOI: 10.1039/C9CY01490J.

- Hu, Y.; Solé–Daura, A.; Yao, Y.-R.; Liu, X.; Liu, S.; Yu, A.; Peng, P.; Poblet, J. M.; Rodríguez–Fortea, A.; Echegoyen, L.; Li, F.–F. "**Chemical Reactions of Cationic Metallofullerenes: An Alternative Route for Exohedral Functionalization**" *Chem. Eur. J.* **2019** DOI: 10.1002/chem.201904854.

UNIVERSITAT ROVIRA I VIRGILI
NEW HORIZONS IN COMPUTATIONAL MODELING OF POLYOXOMETALATES:
BIOLOGICAL ACTIVITY, ENERGY STORAGE AND SUSTAINABLE CATALYSIS.
Albert Solé Daura

List of Abbreviations

#	2D	two–dimensional
	3D	three–dimensional
A	AA	Amino acid
	abPPO4	Mushroom Tyrosinase 4 from Agaricus Bisporus
	ACE	Angiotensin Converting Enzyme
	AD	Alzheimer's Disease
	ADF	Amsterdam Density Functional
	AGT	Angiotensinogen
	AIMD	*Ab initio* Molecular Dynamics
	Ala	Alanine
	Arg	Arginine
	Asn	Asparagine
	Asp	Aspartic acid
	ATP	Adenosine Triphosphate
	Aβ	Amyloid Beta
B	BDE	Bond–Dissociation Energy
	bFGF	Basic Fibroblast Growth Factor
	BNPP	Bis(p–nitrophenyl)phosphate
	BOMD	Born–Oppenheimer Molecular Dynamics
	BSC	Barcelona Super–Computing Center
C	ca.	*circa* (approximately)
	CASPT2	Complete active space 2nd order perturbation theory
	CASSCF	Complete active space self–consistent field
	cat.	Catalyst
	CD	Circular Dichroism
	CFP	Cyan Fluorescent Protein
	cgAUS1	Aurone Synthase from Coreopsis Grandiflora
	ChelPG	CHarges from ELectrostatic Potentials using a Grid–based method
	CK2	Casein Kinase 2
	COM	Center of Mass
	CPMD	Car–Parrinello Molecular Dynamics
	CPUs	Central Processing Unit
	CV	Cyclic Voltammogram
	CyH	Cyclohexene

	CyOct	Cyclooctene
	Cys	Cysteine
	Cyt C	Cytochrome C
D	DDCI	Difference Dedicated Configuration Interaction
	DFT	Density Functional Theory
	DNA	Deoxyribonucleic acid
	DTNB	5,5'–Dithiobis–(2–nitrobenzoic acid)
	DTPA	Diethylenetriaminepentaacetic Acid
E	e.g.	*exempli gratia* (for example)
	E_a	Activation Energy
	et al.	*et alii* (and others)
	EXAFS	Extended X–Ray Absorption Fine Structure
F	FES	Free–Energy surface
	FF	Force Field
	FI	Fluorescence Imaging
G	GGA	Generalized Gradient Approximation
	Gln	Glutamine
	Glu	Glutamic Acid
	Gly	Glycine
H	Hb	Hemoglobin
	HER	Hydrogen–Evolution Reaction
	HEWL	Hen Egg–White Lysozyme
	HF	Hartree–Fock
	HHM	Horse Heart Myoglobin
	His	Histidine
	HIV	Human Immunodeficiency Virus
	HOMO	Highest Occupied Molecular Orbital
	HPA	Heteropolyanion
	HPC	High Performance Computer
	HPNP	2–hydroxypropyl–4–nitrophenyl phosphate
	HSA	Human Serum Albumin
	HSV	Herpes Simplex Virus
I	i.e.	*id est* (that is)
	IEF–PCM	Integral Equation Formalism – Polarizable Continuum Model
	ITC	Isothermal Titration Calorimetry
L	LCAO–MO	Molecular Orbitals as Linear Combination of Atomic Orbitals

	Leu	Leucine
	LOO	Leave–One–Out
	LUMO	Lowest Unoccupied Molecular Orbital
	Lys	Lysine
M	MD	Molecular Dynamics
	MECP	Minimum Energy Crossing Point
	MEP	Molecular Electrostatic Potential
	MIR	Multiple Isomorphus Replacement
	MM	Molecular Mechanics
	MO	Molecular Orbital
	MoSto	Molybdenum Storage Protein
	MRI	Magnetic Resonance Imaging
	mRNA	Messenger Ribonucleic Acid
N	NHE	Normal Hydrogen Electrode
	NMR	Nuclear Magnetic Resonance
	NPA	Natural Population Analysis
	NPP	(p–nitrophenyl)phosphate
	NPT	Isothermal–Isobaric ensemble (constant number of particles, pressure and temperature)
	NTB	2–nitro–5–thiobenzoate
	NTP	Nucleoside Triphosphate
	NVT	Canonical Ensemble (constant number of particles, volume and temperature)
O	OVA	Ovoalbumin
P	PBC	Periodic Boundary Conditions
	PCET	Proton–Coupled Electron Transfer
	PDB	Protein Data Bank
	PES	Potential–Energy Surface
	PLS	Partial Least Squares
	PME	Particle–Particle Mesh Ewald
	POM	Polyoxometalate
	POSS	Polyhedral Oligomeric Silsesquioxanes
	POT	Polyoxotungstate
	PP	Pseudopotential
	pUC19	Plasmid University of California 19
Q	QM	Quantum Mechanics
	QM/MM	Quantum Mechanics/Molecular Mechanics
	QR	Quick Response

	QSAR	Quantitative Structure–Activity Relationship
R	RAM	Random Access Memory
	RDF	Radial Distribution Function
	RMSD	Root Mean Square Deviation
	RMSPE	Root Mean Square Prediction Error
	RNA	Ribonucleic acid
	rRNA	Ribosomal Ribonucleic Acid
	RSV	Respiratory Syncytial Virus
S	SAXS	Small–Angle X–ray Scattering
	SCF	Self–Consistent Field
	Ser	Serine
	SET	Single Electron Transfer
	SOC	Spin–Orbit Coupling
	SOMO	Singly–Occupied Molecular Orbital
	SWNT	Single–Wall Carbon Nanotube
T	TBA	Tetrabutylammonium
	TBHP	Tert–butyl hydroperoxide
	Thr	Threonine
	ThT	Thioflavin T
	TM	Transition metal
	Trp	Triptophan
	TS	Transition State
	TS–1	Titanium Silicalite 1
	Tyr	Tyrosine
	TZP	Triple–Zeta plus Polarization
U	UFF	Universal Force Field
	URL	Uniform Resource Locator
	UV	Ultraviolet
	UV–Vis	Ultraviolet–visible
V	Val	Valine
	vs.	*versus* (against)
W	WOC	Water Oxidation Catalyst
Z	ZPE	Zero-Point Energy

Overview of the Thesis

This Ph. D. thesis covers computational investigations on polyoxometalates (POMs), which are polynuclear metal oxide clusters formed by early transition metal ions, such as W, Mo or V in their highest oxidation state. Specifically, the research works discussed in this thesis are related to the application of POMs in three different fields of current interest that are biochemistry, energy storage and sustainable catalysis. These areas of POM chemistry along with the computational techniques used in POM modeling are reviewed in *Chapter 1*. Then, *Chapter 2* describes the general and the specific aims of the Ph. D. thesis.

During the last decades, POMs have shown potential application in the fields of biochemistry and medicine, including *in vitro* and *in vivo* anticancer, antiviral and antibacterial activity. Also, within the framework of protein crystallography, POMs have been widely used for phasing or as crystallization additives. Directly related to this thesis, the group of Prof. Parac–Vogt demonstrated the hydrolytic activity of POM structures incorporating a Lewis acid ion such as Zr^{IV}, Ce^{IV} or Hf^{IV} towards dipeptides and oligopeptides, and more importantly, towards peptide bonds in a wide range of proteins in a highly selective manner. Despite the fact that the biological activity of POMs has been experimentally studied for decades, an atomistic description of the interactions between POMs and proteins and the physicochemical foundations governing them is still lacking.

Initially in *Chapter 3*, we performed atomistic Molecular Dynamics (MD) simulations with explicit solvent molecules to characterize the interactions between POMs and proteins at atomistic label. We used the experimentally tested case of hen egg–white lysozyme (HEWL), which is selectively hydrolyzed in the presence of Zr–substituted POMs at two peptide bonds located between Trp28 and Val29 and between Asn44 and Arg45, labeled as *site I* and *site II*, respectively. Simulations revealed that anionic POMs interact in solution with positively charged patches on the protein surface. These interactions mainly involve electrostatic interactions and hydrogen bonds with positively charged and polar amino acids such as arginine, lysine, threonine, tyrosine and so forth, although water–mediated contacts with these amino acids were also observed. In addition, we identified two positively charged regions were POMs interact persistently that could be related with the observed selectivity in the peptide bond hydrolysis, as they are located close to the cleavage sites or involve amino acids belonging to the cleavage sites themselves.

The comparison between different POM structures suggested that the affinity of POMs to proteins is highly sensitive to the structure of the polyoxoanion, as previously noted by several authors on the basis of experimental results. Nevertheless, clear structure–activity relationships are still missing, likely due to the difficulty of modifying a single parameter of the POM structure experimentally without affecting others. Aiming to understand how different structural parameters of POMs influence their affinity to biological systems, we carried out in *Chapter 4* a systematic MD study with series of POMs whereby the charge density and the size and shape of the POM are modified systematically, keeping constant the other ones. This study revealed that the affinity to proteins follows a quadratic dependence on the POM charge due to the shift from *chaotropic* (water–structure–breaking) to *kosmotropic* (water–structure–forming) behavior of POMs in solution as increasing the charge density at their surface. Thus, anions bearing low charges do not provide strong enough POM···protein interactions to allow persistent contacts, while those bearing too high charges present sub–optimal interactions due to their high affinity to the solvent. This intricate interplay of forces indicates that optimal binding requires a moderate charge density of the POM to balance the strength of the interactions with the protein and with the solvent. In addition, cationic pockets of HEWL were found to be size–specific for Keggin–type anions, which exhibited the highest affinity to the protein. Smaller structures cannot take benefit from cooperative effects with several interacting amino acids, whereas bigger clusters leave a too large POM surface exposed to the solvent during their interactions with the protein, both features being detrimental for the persistence of POM···protein interactions. Furthermore, we built a quantitative multivariate mathematical model for protein affinity with predictive ability ($r^2 = 0.97$; $q^2 = 0.88$) using two molecular descriptors that account for the charge density (charge per metal ratio; q/M) and the size and shape (novel shape weighted–volume descriptor; V_S). As a response variable we used the *% time binding* obtained from MD simulations with 13 POM structures. The use of normalized descriptors allowed us to conclude that the charge density influences the interactions of POMs with biological systems in a larger extent than their size or shape.

Chapter 5 is divided in two main sections that are devoted to study two different reactions of POMs towards biological systems: the selective hydrolysis of peptide bonds in proteins catalyzed by Zr–substituted POMs and the disulfide bridge reduction promoted by reduced POM clusters. Part of these projects was carried out during a nearly 4–months stay at the University of Nottingham (U.K.) under the supervision of Prof. J. D. Hirst. Initially, we studied the mechanism responsible for the hydrolysis of the Asn44—Arg45

peptide bond in HEWL protein (*site II*, introduced in *Chapter 3*) promoted by a Zr–monosubstituted Lindqvist anion and using a cluster model. This consists of four main steps: i) the coordination of the Zr center to the amide oxygen to polarize the peptide bond; ii) the nucleophilic attack to the amide carbon of either the Zr—OH ligand or an external water molecule assisted by the Zr–hydroxo group acting as a Brönsted base; iii) the protonation of the amide nitrogen and iv) the cleavage of the C—N bond. According to the uphill nature of the computed free–energy profile, the reaction rate is given by the energy cost of reaching the transition state for the C—N cleavage from the reactants. Importantly, the height of the overall barrier is highly sensitive to the protein conformation and for this reason; we averaged the barrier over the protein conformation. The average barrier lies within the range of values obtained from experimental rate constants, supporting the mechanistic proposal. However, the overall barrier does not show significant differences between the experimentally hydrolyzed *site II* and other non–reactive peptide bonds of the same nature, thus, being unable to explain the experimental selectivity. Conversely, constrained MD simulations to analyze the coordination process of the POM to several sites of the protein revealed that unlike other sites, *site II* is surrounded by an array of positively charged and polar amino acids that can interact strongly with the anionic POM during its approach to the peptide bond. These specific interactions can trap the POM through an *enzyme–like* recognition that might shift the energy profile down and compensate to some extent the energy penalty associated to the reorganization of the POM to coordinate the amide oxygen and thus, explaining the faster reaction kinetics compared to other sites.

Also in *Chapter 5*, we analyzed the reduction of the disulfide bridge in angiotensinogen protein (AGT) promoted by reduced POMs, which finds application as a new method for the clinical diagnosis of preeclampsia. The experimental groups of Dr. Newton and Dr. Mitchel based in the University of Nottingham (U.K.) found that the one–electron reduced $[PW_{12}O_{40}]^{4-}$ can promote the reductive cleavage of the S—S bond in 5,5'–dithiobis–(2–nitrobenzoic acid), DTNB, used as a model substrate of a disulfide bond. Using DFT methods and the Marcus theory of the electron transfer, we characterized the reaction mechanism, which involves an initial single electron transfer (SET) process from a reduced POM to the organic substrate as a key step that provokes the S—S cleavage. Then, the reaction is accomplished after another SET from a second POM. For dicysteine–based oligopeptides with higher kinetic stability, the reduction requires the use of POMs with stronger reductant power than $[PW_{12}O_{40}]^{4-}$. Finally, we

evaluated by means of DFT and MD simulations the reduction of AGT, which is predicted to be feasible with the one electron–reduced metatungstate anion, $[H_2W_{12}O_{40}]^{7-}$.

Moving apart from biological systems, *Chapter 6* concerns the ability of the archetypal Wells–Dawson anion, $[P_2W_{18}O_{62}]^{6-}$, to be electrochemically reduced in aqueous solution with up to 18 electrons under certain conditions: low pH, lithium counter cations and high POM concentration (100 mM). These findings were reported by the group of Cronin and importantly, they differ from the classical redox behavior of this anion that only allows to charge this cluster with up to four or six electrons, depending on the pH. DFT calculations and classical and *ab initio* MD simulations indicate that upon reduction, POMs become charged enough to associate protons from the medium and to remove the solvation shell out of Li^+ counter cations. This permits the formation of cation–mediated agglomerates that stabilize the virtual molecular orbitals of POM clusters in about 400 mV, allowing thus, the super–reduction of POMs beyond their previously known limits. Furthermore, our calculations suggest that the super–reduced structures with 18 electrons have a number of associated protons close to 17 distributed over the bridging and terminal oxygen centers and a complex electronic structure that consists in an open–shell singlet in which the 18 electrons are unpaired but antiferromagnetically coupled. Nevertheless, other electronic structures with triplet and quintet character were located very close in energy, suggesting a strong multi–configurational character for this system. Notably, super–reduced anions also form agglomerates in solution that confers them metastable character and causes their energy levels to be in fairly good agreement with the experimental range of potential in which the whole super–reduction process occurs.

Finally, *Chapter 7* includes computational studies on a series of Nb^V–, Ti^{IV}– and Zr^{IV}–containing POMs to make a step forward towards understanding their role as selective oxidation catalysts. Transition metal–substituted POMs represent tractable molecular models of single–site heterogeneous catalysts, which have been extensively used in the last decades for the epoxidation of alkenes with hydrogen peroxide as environmentally–friendly oxidant that gives water as sole byproduct. In collaboration with the experimental groups of Kholdeeva and Errington, we studied the mechanism governing the alkene epoxidation catalyzed by Nb^V–substituted Lindqvist anions, and compared their reactivity with that of their Ti^{IV}–containing counterparts. As previously reported for other Ti^{IV}–substituted POMs, the overall process proceeds in two main steps: the heterolytic activation of H_2O_2 by the Nb–hydroxo (NbOH) species to generate a protonated Nb–peroxo (NbOO) complex and a water molecule; and the electrophilic O–transfer from the

Nb–hydroperoxo (NbOOH) complex, which is in equilibrium with the more stable peroxo, to the double bond of the alkene. The oxygen–transfer was identified as the rate–determining step of the process, which accounts for a moderate free–energy barrier of ca. 26 kcal mol^{-1}. The presence of protons was found to be crucial for reactivity, since it favors the activation of H_2O_2, increases the electrophilicity of the catalyst and permits the O–transfer step to occur from the Nb–OOH through a smoother free–energy barrier than from the peroxo complex. With the gained knowledge, we compared the performance of Nb^{V}–Lindqvist catalysts with Ti^{IV}–containing ones. Upon replacing Ti by Nb, the overall charge of the catalyst decreases from 3– to 2– due to the higher oxidation state of Nb. This fact has a positive influence on reactivity because it makes the hydroperoxo fragment more electrophilic, what favors the O–transfer step, in line with the higher conversions obtained experimentally for Nb complexes. Also, although the nonprotonated O_α of the hydroperoxide moiety is the most electrophilic one, the transfer of the O_β is favored in the Ti catalyst since Ti^{IV}, with a smaller radius than Nb^{V}, is more reluctant to increase its coordination sphere. It is also worth noting that despite the fact that the rate of the O–transfer step increases with the electrophilicity of the catalyst, if the catalyst is not basic enough to have associated protons, it can become less active towards alkene epoxidation. Thus, an *optimal* catalyst might need to balance its charge density in order to be basic enough to allow protonation but not too much in order to be able to transfer an electrophilic oxygen to the double bond of the substrate.

We also conducted a theoretical analysis of another Ti–based catalyst consisting in a hybrid tris–silanol–decorated trilacunary polyoxotungstate that accommodates the Ti center in a tetrahedral environment provided by the silanol groups. Interestingly, this system was experimentally found to catalyze the selective epoxidation of allylic alcohols at room temperature. DFT calculations showed that the lability of the Ti—OSi bonds allow the coordination of both the substrate and the oxidant to the metal center causing a partial detachment of the Ti center from the catalyst structure. This allows the O–transfer to proceed through an *inner–sphere* mechanism, which is less energy demanding than the outer–sphere pathway proposed for non–functionalized alkenes due to the enhanced flexibility around the Ti center, explaining the observed selectivity and further validating the mechanistic proposal.

Finally, we describe part of an ongoing project related to the computational characterization of the mechanism for the main side–reaction of alkene epoxidation, that is, the unproductive decomposition of hydrogen peroxide. Preliminary results suggest that

the metal–peroxo complex can promote the heterolytic cleavage of another molecule of of H_2O_2 to form H_2O and a TM–trioxidane (TM–OOOH) complex, which can evolve towards the formation of singlet oxygen, explaining the formation of the main side products. Interestingly, since the TM–OO group is acting as a nucleophile in this mechanism, the increased electrophilicity of the catalyst upon replacing Ti^{IV} by Nb^{V} would favor the electrophilic O–transfer to the alkene, but also hamper the H_2O_2 decomposition, explaining the higher selectivity towards the epoxide product observed experimentally for Nb. The main conclusions of this Ph. D. thesis are summarized in *Chapter 8*.

UNIVERSITAT ROVIRA I VIRGILI
NEW HORIZONS IN COMPUTATIONAL MODELING OF POLYOXOMETALATES:
BIOLOGICAL ACTIVITY, ENERGY STORAGE AND SUSTAINABLE CATALYSIS.
Albert Solé Daura

UNIVERSITAT ROVIRA I VIRGILI
NEW HORIZONS IN COMPUTATIONAL MODELING OF POLYOXOMETALATES:
BIOLOGICAL ACTIVITY, ENERGY STORAGE AND SUSTAINABLE CATALYSIS.
Albert Solé Daura

Chapter 1

Polyoxometalates: Structure, Applications and Computational Modeling

UNIVERSITAT ROVIRA I VIRGILI
NEW HORIZONS IN COMPUTATIONAL MODELING OF POLYOXOMETALATES:
BIOLOGICAL ACTIVITY, ENERGY STORAGE AND SUSTAINABLE CATALYSIS.
Albert Solé Daura

CHAPTER 1

Polyoxometalates: Structure, Applications and Computational Modeling

This introductory chapter is aimed to discover the polyoxometalate chemistry to a non–specialized reader, who will find in the following pages some basic concepts about the molecular and electronic structure of polyoxometalates, as well as their main applications within the fields discussed in this doctoral thesis. Furthermore, a brief overview of the computational modeling of polyoxometalates is found at the end of this chapter, meant to look back into the achievements reached in the past to move on towards more ambitious goals.

1.1 What are Polyoxometalates?

Polyoxometalates (POMs for short) constitute a wide family of well–defined polynuclear metal oxide clusters of nanometric size that are usually built up from early transition–metal atoms such as W, Mo, V or Nb in their highest oxidation state.[1,2] Within POM structures, metals ions are found in a distorted octahedral environment and linked to each other through bridging oxo ligands forming *edge–sharing* $(\mu\text{–O})_2$ and *corner–sharing* $(\mu\text{–O})$ patterns (see **Figure 1.1**). Nevertheless, other metal environments such as square or pentagonal pyramid have been also reported for V and Mo, respectively; especially in mixed–valent compounds where the metals are not found in their highest oxidation state.[3,4] Some POM species also incorporate other *p*– and less commonly *d*–block atoms, namely heteroatoms, as shown below. This feature divides the variety of POM structures into two main sub–groups: isopolyanions that do not encapsulate heteroatoms; and heteropolyanions, which include a heteroatom in their structure.

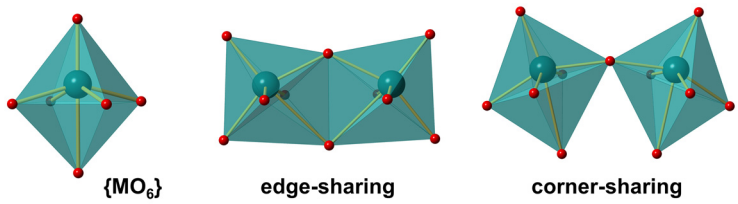

Figure 1.1 | Main POM building blocks and coordination patterns.

Some of the most representative structures are shown in **Figure 1.2** and include from the smallest to the bulkiest, the $[W_6O_{19}]^{2-}$ Lindqvist–, the $[PW_{12}O_{40}]^{3-}$ Keggin–, the $[P_2W_{18}O_{62}]^{6-}$ Wells–Dawson– and the $[NaP_5W_{30}O_{110}]^{14-}$ Preyssler–type anions. In these examples, the encapsulated heteroatom consists on a P^V, although other structures containing Si^{IV}, Ge^{IV}, Al^{III} among others are also common. Besides these examples, other structures such as the Anderson–Evans $[XM_6O_{24}]^{n-}$ (X = heteroatom), the decavanadate $[V_{10}O_{28}]^{6-}$ anion or giant Mo clusters known as Keplerates have been largely employed in molecular nanoscience.

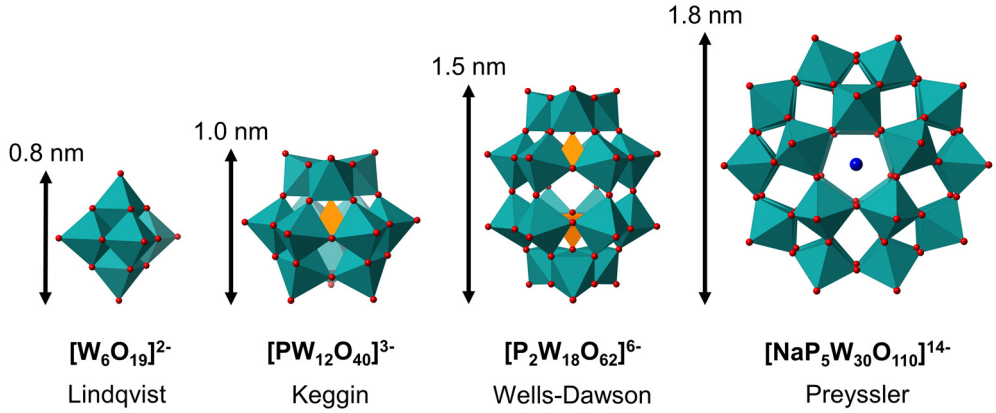

Figure 1.2 | Polyhedral representation of the most popular POM structures.

In POM synthesis, the formation of one structure or another strongly depends on experimental conditions such as the pH, the nature of the counter cation, the presence of additional salts, etc. Therefore, they represent highly tunable scaffolds, which properties can be readily tailored during the synthetic procedure. In general, POMs exhibit high solubility in water, although they can also be soluble in polar organic solvents such as acetonitrile upon replacing their alkali metal counter cations by organic ones, usually of alkyl–ammonium nature. Besides, they are highly stable in harsh conditions, including high temperatures or oxidative and hydrolytic conditions. Furthermore, POMs display an interesting redox behavior that allows them to accept a large number of electrons in a reversible manner within a usually narrow range of potential. Owing all these properties, POMs have been extensively used in material science for the construction of novel devices and nano–composites.[5,6] Moreover, the removal of one addenda ion from their plenary structure results in a highly charged monolacunary species that can be seen as a

polydentate anionic ligand that can accommodate another transition metal. This feature confers POMs a wide applicability in catalysis.[7]

More recently, the preparation of more sophisticated hybrid organic–inorganic structures as those shown in **Figure 1.3** has been reported. In particular, the group of Prof. Proust has authored many contributions concerning the preparation and application of this kind of hybrid structures. Hybrid organic–inorganic POMs are usually synthesized from lacunary POMs that miss one or more addenda ions. This feature allows them to react with organic fragments via condensation reactions.[8] Hybrid structures can be also obtained from monolacunary structures acting as a chelating ligand of an organometallic complex (see **Figure 1.3**B).[9] The POM functionalization can be used either to immobilize POMs on surfaces as represented in **Figure 1.3**C or to modulate their supramolecular properties with the aim of controlling their behavior in solution.[10] Also, functionalization with chromophore groups can serve to improve the quantum yield and the catalytic activity of POMs participating in photochemical processes.[11] Moreover, hybrid POMs also find application in biochemistry, since the functionalization with organic moieties enhances the cell penetrability and reduces their cytotoxicity (*vide infra*).[12]

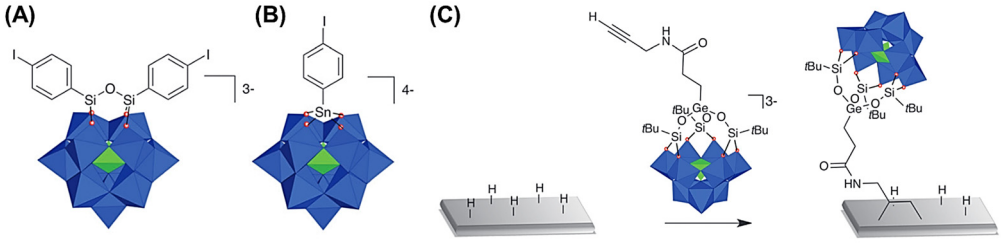

Figure 1.3 | (A) and (B) Different types of hybrid POM structures. (C) Schematic immobilization of a hybrid POM onto *n*–silicon wafers. All figures were taken from ref. 8.

A detailed historical overview of POMs has been reported elsewhere.[13–15] Nonetheless, the following lines attempt to collect the main historical highlights in a brief summary. The first scientific paper concerning POMs was published in 1778 by the Swedish Pomeranian chemist Carl Wilhelm Scheele.[16] He performed the pioneer studies of the *molybdenum blue* (also called *blue water*) found in several springs in The United States of America. Notably, he attributed the blue coloration of the solution obtained from oxidation of MoS_2 to the formation of reduced molybdenum oxides. Three decades later, Berzelius reported the synthesis of the phosphorus–containing dodecamolybdate $[PMo_{12}O_{40}]^{3-}$ upon mixing $(NH_4)_2[MoO_4]$ with an excess of H_2PO_4,[17] and forty years later, Galissard de Marignac

confirmed the 12:1 stoichiometry of the metal:heteroatom composition in the heteropoly compound.[18] Despite the fact that POMs were extensively used with analytical purposes in the following years, it was not until 1908 when Miolati and Pizzighelli and then, Pauling in 1929, reported the first insights into the molecular composition of these structures.[19,20] They identified the metals to be in a hexacoordinated environment and hypothesized that the MO_6 octahedral units were connected via corner–sharing oxygens (see **Figure 1.4**). However, the presence of edge–sharing patterns was not revealed until 1933, when James Farger Keggin elucidated the X–ray structure of the silicotungstate anion $H_4[SiW_{12}O_{40}]\cdot 6H_2O$, which received his name.[21] These findings prompted the proposal and elucidation of several other POM structures by Wells, Anderson, Evans and Dawson in the following years.[22]

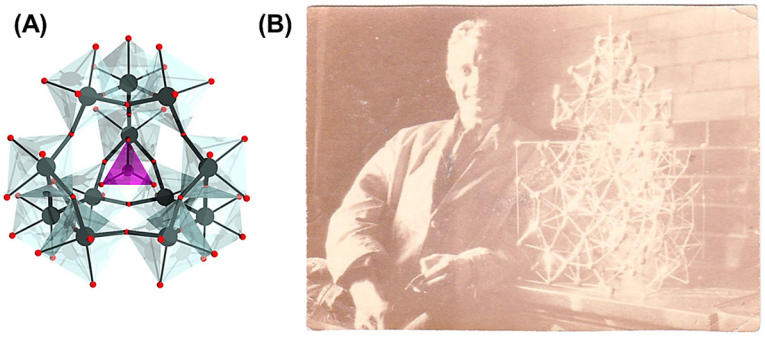

Figure 1.4 | (A) Polyhedral representation of the model for the Keggin anion proposed by Pauling; (B) Photograph of Dr. J. F. Keggin. Both figures were taken from ref. 15.

During the 20th century, many more structures were characterized with the help of modern and more accurate spectroscopic and analytical techniques and in 1983, Pope compiled all the knowledge gained in this field in a book entitled "Heteropoly and isopoly oxometalates".[1] Later on, in 1991, Pope and Müller published the most recent achievements in a review paper[23] that was followed by an exponential growth of the number of scientific publications related to POMs.[24] This rapid increase of popularity is reflected in a special issue[14] devoted to POM chemistry edited by Craig L. Hill in 1998 and in the vast number of reviews that came out in the following twenty years.[5–8,24–35] In the next sections, we review the most relevant applications of POMs within the context of this thesis.

1.2 The use of POMs in Biochemistry and Biomedicine.

One of the most emerging fields regarding the chemistry of POMs is their application for biochemical and biomedical purposes. Specifically, Chapters 3–5 of this thesis deal with the application of POMs within these fields. The first bio–related properties that POMs were found to possess are antiviral and antitumoral activity, which were identified in the early 1970s along with antibiotic activity, proven some years later. More recently, the application of POMs extended to protein crystallography, protein inhibition, enzymatic catalysis mimetic, bio–imaging and so forth. These studies have given raise to hundreds of publications collected in several reviews and book chapters.[5,28,29,31,36–40] In this section, we summarized the most significant findings, paying special attention to those directly related to this thesis.

1.2.1. Enzyme inhibition and disease treatment.

POMs have shown ability to inhibit a vast variety of enzymes with different functionalities, including kinases, phosphatases, proteases, etc.[40] For this reason, they have been attributed potential applicability in the treatment of several diseases in which these kinds of enzymes participate. As a remarkable example, the inhibition of DNA and RNA–related enzymes such as protein kinases could be used for cancer treatment.[41] Reviewing this literature, one may note that there are some structures that are described as the most potent inhibitors in several contributions. For instance, the decavanadate anion $[V_{10}O_{28}]^{6-}$ (shown in **Figure 1.5**) represents a potent inhibitor of hexokinase and phosphofructokinase at micromolar concentrations,[42] but it also provides high inhibition of several phosphatases and nucleases.[43] Thus, although $[V_{10}O_{28}]^{6-}$ is indeed a powerful inhibitor, it has the disadvantage of being poorly selective. Another potential inhibitor of several enzymes is the metatungstate anion $[H_2W_{12}O_{40}]^{6-}$, which is especially effective against nucleotidases and cholinesterases.[43b] Besides these structures, the classical Wells–Dawson, Preyssler and Anderson structures as well as more complex Nb– and Ti–substituted heteropolyanions also led to significant enzyme inhibition.[40]

Before targeting all the aforementioned enzymes, biological studies with POMs were already performed to investigate their performance as antiviral, antibacterial and antitumoral agents. However, it is worth mentioning that they can bind to many different enzymes before moving to larger systems such as viruses or bacteria, since their mode of action against them usually involves enzyme–inhibition processes. **Figure 1.5** collects

some selected POM structures with important biological activity. Regarding their antiviral activity, POMs have efficiently performed against human immunodeficiency virus (HIV–1), herpes type 1 and 2 viruses (HSV–1 and HSV–2), respiratory syncytial virus (RSV), among others.[31,39,40] Most of the POM structures displaying antiviral activity consist in polyoxotungstate frameworks substituted with Ti and Nb, similarly to those used for enzyme inhibition (**Figure 1.5**). Related to this fact, Yamase et al. stated that the antiviral activity of POMs is influenced by their ability to penetrate cell membranes and their localization inside the cell.[44] Thus, one may think that their mechanism of action involves binding to enzymes or proteins that are related to the virus–cell interaction, and specifically, Fisher et al. proposed that POMs bind to DNA polymerase interrupting the virus replication.[45] Notably, the antiviral activity against HIV–1 of the B–β–$[NaSb_9W_{21}O_{86}]^{18-}$ tungsto–antimoniate, namely HPA–23, was clinically tested, although the study was suspended due to high cytotoxicity produced by this complex.[39] Later on, the di–titanium–containing phosphotungstate $[Ti_2PW_{10}O_{40}]^{7-}$ anion showed higher inhibition activity towards HIV–1 than HPA–23 in addition to lower cytotoxicity.[46]

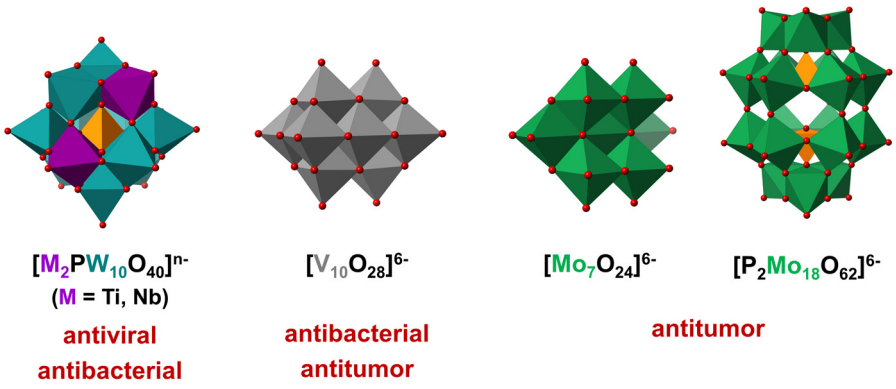

Figure 1.5 | Selected examples of POM structures exhibiting biological activity against bacteria, viruses or tumors.

Promising results concerning the use of POMs as antibacterial agents has been achieved against both gram–positive and gram–negative bacteria in two different strategies that are the direct application of POMs and the application in cooperation with other antibiotics such as β–lactam.[36,39,40] The highest synergistic effects with β–lactam were achieved with several polyoxotungstates, while in the direct application, polyoxovanadates exhibited higher activity than tungstates or molybdates towards gram–positive bacteria whereas tungstate anions containing Sb^{III}, As^{III} or V^{V} ions were the most active towards

gram–negative ones.[36] Besides, hybrid POMs,[47] as well as POM–based nanocomposites, including POM–decorated metal nanoparticles have also shown efficient antibacterial activity.[48] Some efforts to understand the origin of POM antibacterial activity were done by Sakamoto et al. They studied the interaction of $[SiW_{12}O_{40}]^{4-}$ with a model microbial membrane, and observed that deposition of POMs over the surface induces the formation of POM–lipid nano–assemblies that leave pores in the bacterial membrane.[49] These pores are supposed to be detrimental for the membrane functionality, what may be related with the death of bacteria upon interaction with POMs. Nevertheless, other studies point towards the penetration of POMs into the cell to inhibit RNA–related enzymes to suppress the transcription process from genes to messenger RNA (mRNA);[50] and organoantimony–containing POMs were found to block the peptidoglycan production to cause the death of the bacteria.[47] Thus, as recognized by Rompel and co–workers in a recent review,[36] there are several putative modes of action, which strongly depend on the nature of the employed POM.

Another interesting feature of POMs is their anti–tumor activity. For example, several Keggin–, Wells–Dawson– and Anderson–type polyoxotungstates, as well as decavanadate and octamolybdate anions can bind the fibroblast growth factor (bFGF) to inhibit tumor growth via angiogenesis suppression.[51] Other POM structures including the $[Mo_7O_{24}]^{6-}$ and $[P_2Mo_{18}O_{62}]^{6-}$ polyoxomolybdates or the Co^{II}– and Sb^{III}–containing trimeric Keggin structure $\{CoSb_6O_4(H_2O)_3[Co(hmta)SbW_8O_{31}]_3\}^{15-}$ (htma = hexamethylenetetramine) also showed anticancer activity against murine mammary, Meth A sarcoma, adenocarcinoma or ovarian cancer cells.[12a] Furthermore, polyoxovanadates such as $[V_{10}O_{28}]^{6-}$ or $[V_{18}O_{42}(H_2O)]^{12-}$ also showed excellent anticancer activity against a variety of cancer cell lines.[52] The mechanisms of action chiefly include the induction of cell apoptosis, weak interactions with DNA or the blocking of angiogenesis or ATP generation through interactions with proteins involved in these processes, such as bFGF, protein kinase CK2, NTPDase1 and so forth.[44,53] As done for boosting the biological activity of POMs as antiviral and antibacterial agents, the preparation of hybrid structures and POM–grafted nanoparticles was also exploited as a strategy to improve their anticancer activity.[54] **Figure 1.6** shows a representative example reported by She et al.[12c] of glioblastoma inhibition via apoptosis induced by a hybrid POM structure.

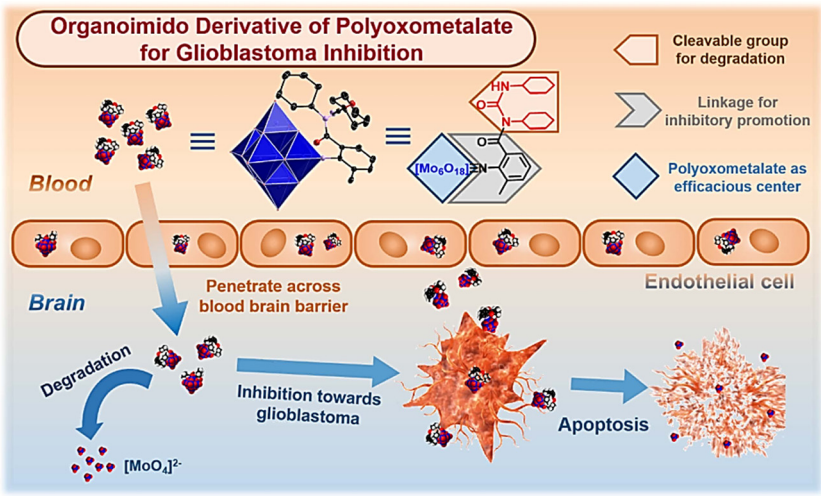

Figure 1.6 | Schematic mechanism of action for glioblastoma inhibition by hybrid organic–inorganic POM. Reproduced from ref. 12c.

There are also some studies that evince the ability of POMs to act as anti–amyloid agents for Alzheimer's disease (AD) treatment. AD is presumably caused by the aggregation of amyloid β–oligomers (Aβ) to form fibrils that can accumulate as plaques in the neural tissue.[55] Qu and co–workers reported that a series of polyoxotungstates of Keggin and Wells–Dawson structure can bind Aβ oligomers to inhibit their aggregation.[56] Among the tested structures, the most effective anti–amyloid agent was the Ni–substituted Wells–Dawson $[NiP_2W_{17}O_{61}]^{8-}$ anion, while both plenary and lacunary Keggin structures were less active and the tested polyoxomolybdates resulted inactive. The $[NiP_2W_{17}O_{61}]^{8-}$ cluster was found to bind the positively charged region in Aβ comprised between His13 and Lys16, which contains two histidine residues that can act as chelating ligands for a metal–substituted POM. Other polyoxotungstates such as the metatungstate and the Preyssler–type anion and several Keplerate–type molybdate clusters also showed the ability to interact with Aβ oligomers to disallow their aggregation.[57] More recent works have made use of POM conjugates with amino acids to form nanospheres or POM–decorated gold nanoparticles and nanorods to improve the performance of POMs as anti–amyloid agents.[58] Very recently, the efficient inhibition of Aβ has been achieved using hybrid POMs functionalized with enantiomerically pure amino acids such as D–phenylalanine.[59]

Although POMs constitute a family of potential inorganic drugs, there are two main drawbacks for their practical application *in vivo* that are their high cytotoxicity and poor selectivity. To overcome these issues, current efforts are focused on the development of less cytotoxic and more selective hybrid organic–inorganic POM–based drugs.[12]

1.2.2. Protein crystallography.

Gaining knowledge on the molecular 3D structure of proteins is crucial for understanding the biochemical processes in which proteins participate, but also for the rational design of selective drugs to inhibit their biological activity leading to any kind of pathology. One of the main limitations of X–ray protein crystallography is the so–called phase problem. This problem arises from the fact that the light detectors used in this technique can only measure the intensity of the light that reaches them and therefore, the structural information provided by the phase of the light waves is systematically lost.[60] One of the most common strategies to overcome this problem is the Multiple Isomorphous Replacement (MIR) method, which is based on incorporating heavy metal atoms into the protein structure to be crystallized to act as anomalous X–ray scatterers. Due to the large number of metals atoms in their structures, POMs are suitable candidates to be used for phasing.[29,37,39,40] In fact, Yonath and co–workers were able to determine the crystal structure of the ribosome subunits soaking the crystal with $[P_2W_{18}O_{62}]^{6-}$ anions as "super–heavy atoms" that were found to improve the diffraction power.[61] Notably, this work was awarded with the Nobel Prize for Chemistry in 2009. In addition, X–ray structures revealed that POMs were tightly attached to the ribosome surface as shown **Figure 1.7**, suggesting that besides their role as a phasing tool, POMs could be used as crystallization additives to facilitate the crystallization of proteins. Related to this, POMs were found to rigidify flexible regions of protein bodies to enable their structural determination via X–ray diffraction.[29,61]

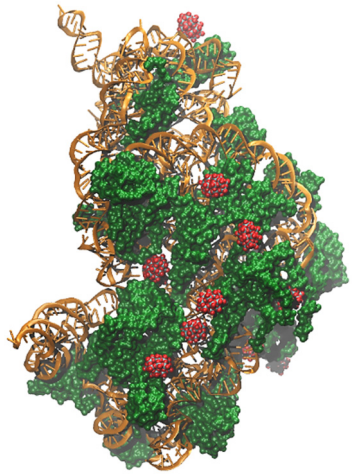

Figure 1.7 | Crystal structure of the 30S small ribosome subunit. Ribosome fragment is represented as a green surface while the brownish helix represents rRNA. The Wells–Dawson anions found in the X–ray structure are represented in spheres (PDB ID: 1I94).[61c]

Later on, other authors reported the use of POMs as crystallization additives. Parac–Vogt and co–workers were able to crystallize hen egg–white lysozyme (HEWL) with several TM–substituted POMs,[62] aiming to gain knowledge on their role as selective artificial proteases (*vide infra*). Regardless the POM structure or the nature of the embedded metal ion, the different POMs were located at the same regions in the X–ray structure, as shown in **Figure 1.8**, which correspond to positively charged patches on the protein surface. Aside from non–bonding interactions, a co–crystal of HEWL with a Zr–substituted Keggin anion showed a direct bond between the Zr center and the amide oxygen atom of the Asn65 side chain.[63] In recent years, Rompel et al. compiled the available data on the use of POMs in protein crystallography in several reviews, highlighting the superior performance of the Anderson–Evans tungstotellurate $[TeW_6O_{24}]^{6-}$ as crystallization additive compared to other POMs.[29,64] This anion was found to suffer internal rearrangements to fit positively charged clefts in protein crystals, even forming covalent bonds with carboxylate–containing amino acids. In addition, its disc–like shape allows intermolecular interactions within the crystal that favors the formation of POM–mediated protein dimers and consequently, enhances the crystal packing and stability (**Figure 1.9**). Using $[TeW_6O_{24}]^{6-}$, Rompel and colleagues reported for the first time the molecular structure of the mushroom tyrosinase from Agaricus bisporus (abPPO4) and aurone synthase from Coreopsis grandiflora (cgAUS1).[65] Also, HEWL was co–crystalized with this anion in a previously unknown crystal form.[66] Very

recently and during the preparation of this thesis, a new contribution came out describing the crystallization of proteinase K with different TM–substituted Keggin anions (TM = Co^{II}, Ni^{II}, Cu^{II} and Zn^{II}) as crystallization additives.[67] Interestingly, Co^{II}– and Ni^{II}–containing complexes became involved in covalent contacts with the carboxylate group in the side chain of Asp207. Besides, $[\alpha\text{–}PW_{11}O_{39}TM]^{5-}$ anions exhibit one single TM—OOC covalent bond, whereas two bonds were detected for the $[\beta\text{–}SiW_{11}O_{39}TM]^{6-}$ scaffold, involving both the TM and a neighboring W atom.

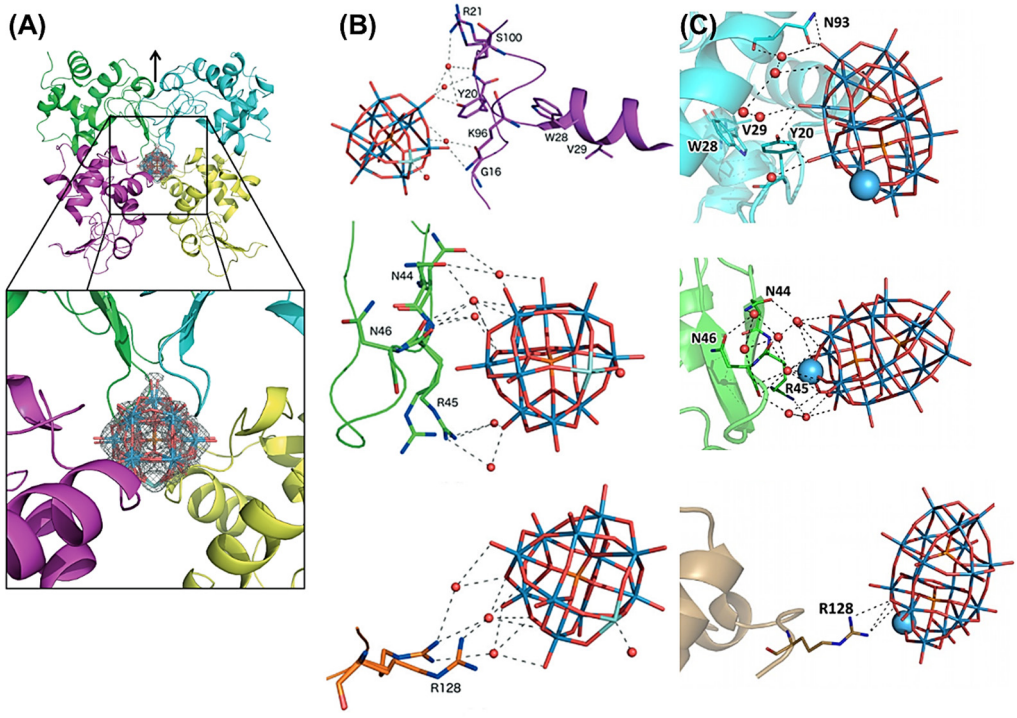

Figure 1.8 | (A) Crystal structure of four units of HEWL protein (displayed in different colors) surrounding a Zr–substituted Keggin anion, $[ZrPW_{11}O_{39}]^{3-}$. (B) and (C) Closer look to the three identified binding sites of HEWL for Zr–substituted Keggin and Hf–substituted Wells–Dawson anions, respectively. Adapted from ref. 62.

It is also worth mentioning that the formation of some POM structures has only been observed in co–crystals with proteins, since they are not stable in the absence of covalent linkages with amino acids from the protein. The most representative example is the molybdenum storage protein (MoSto), which can retain up to 100 Mo or W atoms from inorganic salts forming protein–stabilized clusters such as the $\{Mo_8O_{26}\}$ cluster covalently

connected to a glutamate and a histidine residue or the $\{W_3O_{10}\}$ cluster stabilized by coordination to three histidine nitrogen atoms.[68]

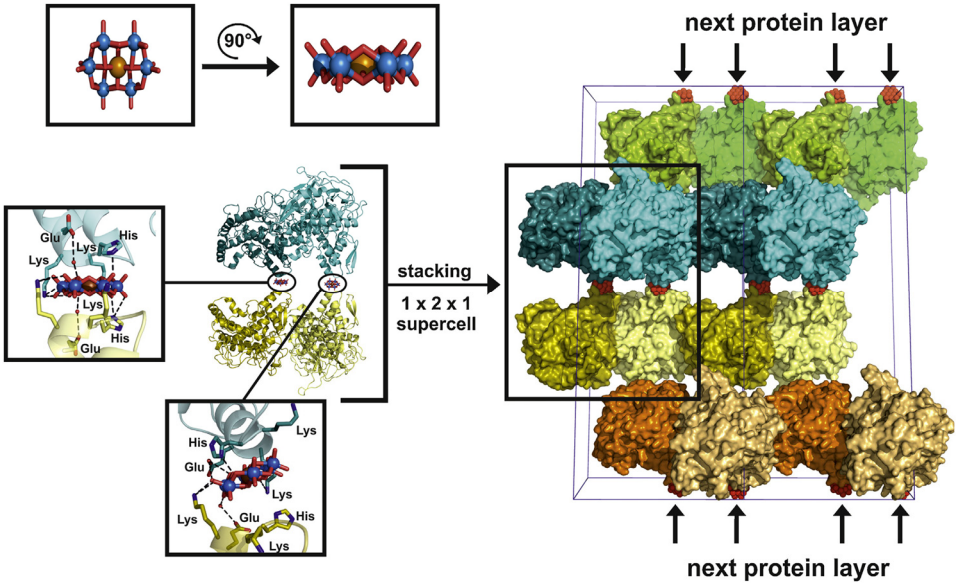

Figure 1.9 | Crystal packing of abPPO4 protein co–crystalized with $[TeW_6O_{24}]^{6-}$. The supercell shows how $[TeW_6O_{24}]^{6-}$ anions promote the arrangement of proteins in a layered fashion that enhances the crystal packing. Obtained from ref. 29.

1.2.3. Artificial metalloenzymes

More related to this thesis is the application of POMs as artificial metalloproteases. The group of Parac–Vogt initially reported the hydrolysis of peptide bonds in dipeptides by the monometallic oxomolybdate[69] and then, a series of TM–substituted POMs were synthesized and tested in the hydrolysis of small dipeptides.[70] Among the tested metals, only Zr^{IV}–, Ce^{IV}– and Hf^{IV}–substituted POMs showed hydrolytic activity towards peptide bonds. Since then, several Zr^{IV}–containing POM structures were successfully applied to the hydrolysis of a number of dipeptides and oligopeptides in mild conditions[71] and more importantly, to the selective hydrolysis of a wide range of proteins.[72] These results are indeed of paramount interest, since the selective peptide bond hydrolysis in proteins could serve to meet the demand of specific peptide sequences required for protein engineering and proteomics. Interestingly, different patterns of hydrolyzed sites were observed when moving from one protein to another. For instance, HHM is selectively hydrolyzed in the

presence of metal substituted POMs only at peptide bonds adjacent to an aspartate residue (Asp—X).[72d] However, the hydrolysis of HSA in the presence of POM–based proteases let to a different selectivity, since it occurs at four chemically disparate cleavage sites: Cys392–Glu393, Ala257–Asp258, Lys313–Asp314 and Arg114–Leu115.[72b] A similar behavior was observed for HEWL, which is only hydrolyzed by TM–POMs at two peptide bonds and none of them contain an aspartate residue: Trp28–Val29 and Asn44–Arg45 (**Figure 1.10**).[72a] Conversely, HEWL is selectively hydrolyzed at Asp—X sites in the presence of oxomolybdate,[73] suggesting that embedding the hydrolytically active metal ion in a POM framework can modulate the selectivity.

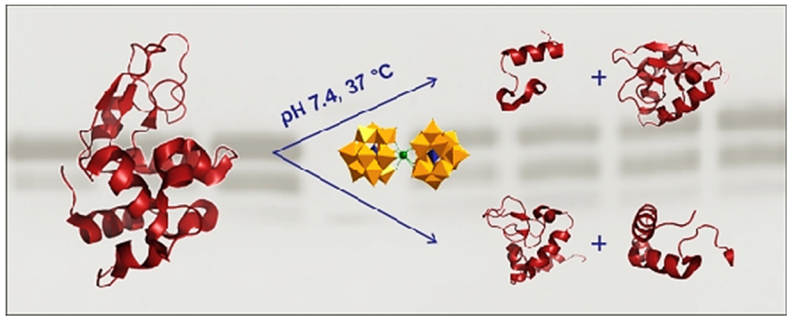

Figure 1.10 | Schematic representation of the selective peptide bond hydrolysis in HEWL promoted by the Ce^{IV}–substituted Keggin dimer $[Ce(PW_{11}O_{39})_2]^{10-}$. Obtained from ref. 72a.

Although the reasons for the reported selectivity are not fully understood, it was observed that the cleavage bonds in the protein structures were in all cases located at the vicinity of positively charged patches on the protein surface. In addition, several POM–protein co–crystals were obtained using HEWL,[62] which showed that the hydrolytically active POM complexes bind these positively charged regions nearby the cleavage sites in the solid state (first and second binding sites in **Figure 1.8**B and C). The most recent works in this field describe the selective hydrolysis of proteins by TM–POMs in the presence of surfactants, which can be used to modulate the cleavage sites, most likely due to the alteration of the protein structure upon interaction with surfactants.[74] During the preparation of this thesis, a new work from the Parac–Vogt group came out reporting the selective hydrolysis of Hemoglobin (Hb) at Asp—X sites by Zr–POMs.[75] This work was accompanied by docking studies that identified four positively charged binding sites on Hb surface nearby the hydrolyzed sites, as found previously for other proteins.[62] Furthermore, a DFT exploration of the reaction mechanism revealed that hydrolysis kinetics of Asp—X bonds is faster than those corresponding to X—Asp, X—

Glu and Glu—X bonds, explaining the preference of Zr–POMs to react with Asp—X sites over other carboxylate–containing ones.[75]

The hydrolysis process has been proposed to involve an initial coordination of the hydrolytically active metal ion to the amide oxygen atom of the peptide bond. This coordination polarizes carbonyl group, owing the Lewis acid nature of these metal ions and renders the carbon atom more susceptible to suffer a nucleophilic attack. Parac–Vogt, Pierloot and co–workers analyzed by means of DFT the mechanism responsible for the hydrolysis of dipeptides catalyzed by a tetrazirconium–containing sandwich POM. In this case, the most likely mechanism involves the nucleophilic attack of a solvent water molecule to the carbon of the peptide bond assisted by the carboxylate group of the C–terminus end acting as a Brönsted base.[71c] A few years later, a QM/MM study on the hydrolysis of HSA showed that the nucleophilic attack of the hydroxo ligand of the Zr ion is slightly more favorable than the outer–sphere attack of an external water molecule assisted by the Zr—OH group as Brönsted base.[76] Note that when the hydrolyzed dipeptide is embedded in the protein main chain, the carboxylate group assisting the outer–sphere nucleophilic attack in the hydrolysis of dipeptides is no longer available, unless the hydrolysis occurs at the end of the protein chain. According to the calculated mechanism, the nucleophilic attack is followed by the protonation of the amide nitrogen, which induces the C—N bond cleavage. In dipeptides, the initial nucleophilic attack was found to be the rate–determining step,[71c] while in HSA protein, the TS associated to the C—N bond cleavage is higher in energy and governs the kinetics of the overall process.[76] A very recent work proposed a novel mechanism for carboxylate–containing peptide bonds that consists in the nucleophilic attack of the carboxylate group onto the amide carbon to form a cyclic intermediate, from which the C—N bond cleavage can take place after protonating the N atom with POM ligands acting as Brönsted acid.[75] In this case, the reaction rate is determined by the free–energy difference between the covalent POM–protein complex and the TS associated to the C—N bond cleavage.

Scheme 1.1 | Overall reaction and proposed mechanisms for the peptide bond hydrolysis in dipeptides[71c] and proteins[76] catalyzed by Zr–containing POMs.

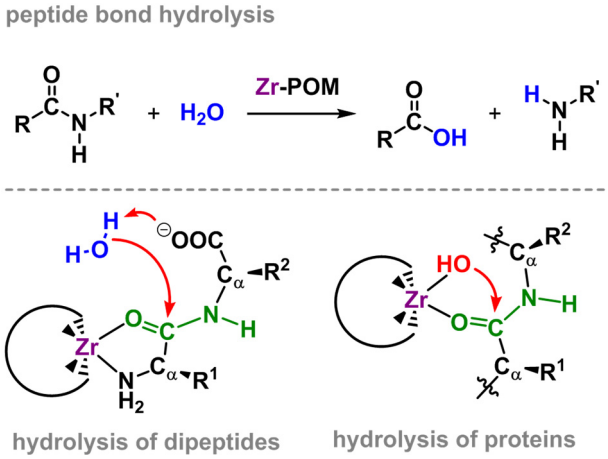

The group of Parac–Vogt also studied the role of POMs as artificial nucleases. Initially, polyoxovanadates and polyoxomolybdates ($[Mo_7O_{24}]^{6-}$ in particular) were used to hydrolyze the phosphoester bond in (p–nitrophenyl)phosphate (NPP) and bis(p–nitrophenyl)phosphate (BNPP) as tractable models of DNA and 2–hydroxypropyl–4–nitrophenyl phosphate (HPNP) as a model of RNA.[77] Later on, Zr and Ce–substituted POMs of Keggin and Wells–Dawson structure also showed hydrolytic activity towards phosphoester bonds in DNA and RNA model substrates[78] as well as in supercoiled plasmid pUC19 DNA.[79] Besides, the Zr–substitued Keggin anion was also active towards the hydrolysis of phosphoanhydride bonds in adenosine triphosphate (ATP);[80] and the archetypal single–addendum $[PW_{12}O_{40}]^{3-}$ was able to mimic sialidase enzymes that hydrolyze glycosidic bonds in sugars.[81]

In most of the cases, the employed POM structures consist in dimers such as the one represented in **Figure 1.10**, in which the embedded metal ion is coordinatively saturated. However, it is clear both from experimental results and from DFT calculations[62,78d] that dimeric POMs suffer hydrolysis at experimental conditions to yield the hydrolytically active TM–monosubstituted monomer that makes possible the coordination of the metal ion to functional groups of biomolecules.

1.2.4. Bio–imaging.

Another biomedical field in which POMs find application is bio–imaging. Magnetic resonance imaging (MRI) is a widely used noninvasive, medical imaging technique that usually requires the use of paramagnetic contrast agents to enhance the MRI signal and improve the quality of anatomical images. Gd^{III}–based complexes are generally contrast agents of choice because Gd^{III} has large paramagnetic moment and long electronic relaxation time. These features can shorten the longitudinal relaxation time of water protons at the surroundings of Gd^{III} and thus, improve the contrast and the bright of the image.[82] A variety of Gd–subsituted POMs of Keggin and Wells–Dawson structure exhibited higher ability to reduce relaxation time of proton nuclei than the Gadopentetic acid (Gd–DTPA), that is the contrast agent par excellence.[40,83] Specifically, the MRI signal was greatly enhanced for liver and kidney imaging. The next generation of POM–based contrast agents comprises self–assembled nanostructures that consist of Gd–POMs and positively charged organic molecules, which can increase the MRI signal up to three–fold.[84] The most recent advances include the use of Gd–POMs in conjunction with cationic dendrimers to form micellar structures that can also associate fluorescent dyes to be used for both MRI and Fluorescent imaging (FI), allowing the use of POMs as bimodal contrast agents.[85] Notably, in vivo experiments showed that these complexes are rather selective for the liver imaging and their metabolism can be achieved in about 24 hours.

1.3 POMs for Energy Storage.

Due to the high oxidation state of their metal ions, POMs can undergo several reversible redox processes in a relatively narrow potential range.[1] The reduction of POM clusters increases their basicity. For this reason, reduction processes can go along with the association of protons to the basic oxygens of the POM if the pH of the medium and the pK_a of the cluster permit it. Accordingly, cyclic voltammograms in the presence of protons usually show two–electron redox waves,[1] presumably due to proton–coupled electron transfer (PCET) steps.

Several groups have taken advantage of POMs as *electron reservoirs* for further use in the reduction of CO_2[86] or in the production of hydrogen.[87] This later is more related to the field of energy storage, in which POMs have emerged as potential candidates suitable for the construction of redox–flow batteries[88,89] and solid–state batteries[90,91] where POMs act

as electron carriers. Some of the reported POM–based batteries consist on devices where POMs are both used as negative and positive electrolytes. For example, Pratt and Anderson showed that aqueous solutions of A– and B–α–$[PV_3W_9O_{40}]^{6-}$ clusters can be placed at both sites of a membrane that permits the flow of protons and electrons to build up a redox–flow battery that involves three one–electron redox processes.[88a] Thus, the redox pairs at both sides of the cell are $[PV_3^{V}W_9^{VI}O_{40}]^{7-}$ / $[PV_3^{IV}W_9^{VI}O_{40}]^{10-}$ and $[PV_3^{IV}W_9^{VI}O_{40}]^{10-}$ / $[PV_3^{IV}W_3^{V}W_5^{VI}O_{40}]^{13-}$, as schematically represented in **Figure 1.11**. Other batteries only take advantage of POM redox properties in one of the electrolytes. For instance, Cronin and co–workers reported a battery in which an aqueous solution of $Li_6[P_2W_{18}O_{62}]$ acts as the negative electrolyte while the positive one is a solution of HBr.[89] Aiming to improve the charge transfer processes, some strategies are proposed in the literature, such as fixing the redox active POMs to single–wall carbon nanotubes (SWNTs) either via electrostatic interactions or covalent linkages.[92] These SWNTs are connected to the electrode and can successfully act as "wires" that can improve the specific capacity of the battery in up to ca. 460 $mAh{\cdot}g^{-1}$.[92c] Solid–state batteries are built up with the same philosophy, despite the fact that the redox components are found in the solid state. In this case, POMs are used as electrodes in combination with lithium or sodium ions.[90,91]

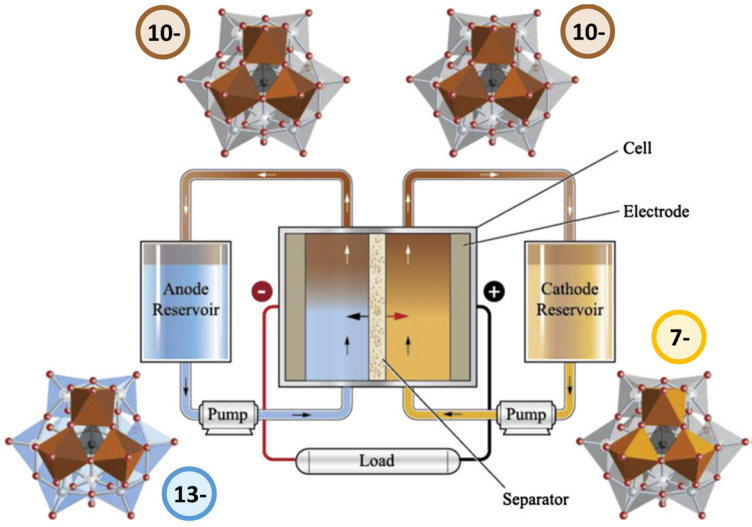

Figure 1.11 | Representation of a redox–flow battery during the discharging process. Black and blue polyhedra represent W^{VI} and W^{V} ions, while yellow and brown ones correspond to V^{V} and V^{IV}. Adapted from ref. 88a.

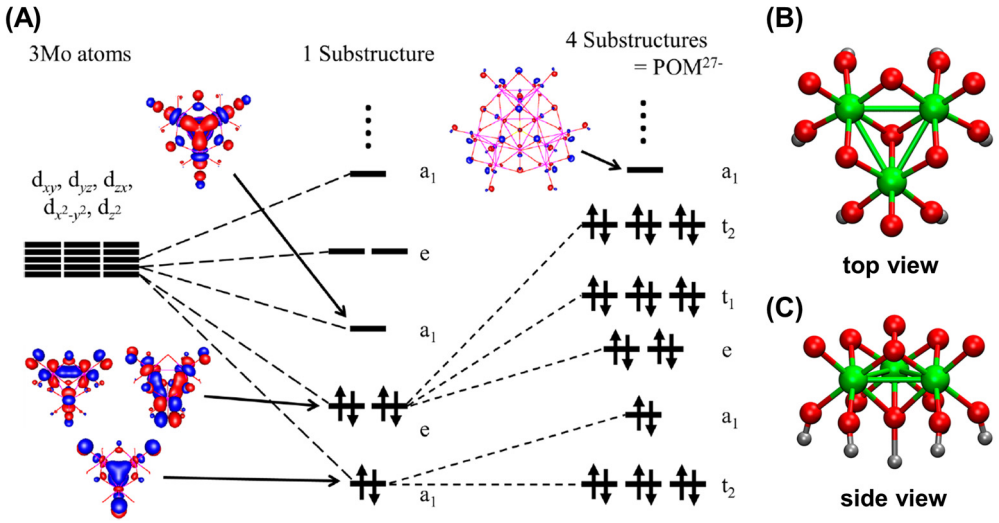

Figure 1.12 | (A) Frontier MO diagram showing the MO that accomodate the extra electrons inserted into the cluster upon reduction. Central panel represents a simplified triad model and righ panel accounts for the whole super reduced $[PMo_{12}O_{40}]^{27-}$ structure. (B) and (C) Top an side views of a $\{Mo_3\}$ triad exhibiting metal–metal bonds in the super reduced cluster. Adapted from ref. 95c.

Directly related to this thesis, the efficiency of POM–based systems as energy storage devices is tightly related to the number of reversible electrons that a POM can accept and store. For this reason, several studies have focused on exploiting the redox properties of POMs with the objective of injecting as many electrons as possible in their structure. Launay already reported in 1976 that the metatungstate anion $[H_2W_{12}O_{40}]^{6-}$ can accept up to 32 electrons in aqueous solution, which can be then reversibly extracted by reoxidation.[93] Further studies suggested that 26 of these electrons are localized in W—W bonds forming triangles within the $\{W_3\}$ triads, while the remaining ones are delocalized over the POM framework.[94] In addition, in the six–electron–reduced metatungstate, which presents three W—W bonds in one triad, the three terminal oxo groups in the reduced region were found to turn out into aqua ligands.[94] Polyoxomolybdates are also attractive candidates to store a large number of electrons.[95] The Wells–Dawson–type $[S_2Mo_{18}O_6]^{4-}$ was found to accept 18 electrons in aqueous solution,[95a] while the Keggin–type $[PMo_{12}O_{40}]^{3-}$ can be reduced with up to 24 electrons in the solid state with lithium cations.[95b] Interestingly, in operando EXAFS studies and *ab initio* methods revealed that, as proposed for the metatungstate anion, the super reduced $[PMo_{12}O_{40}]^{27-}$ cluster displays Mo^{IV}—Mo^{IV} bonds with intermetallic distances of ca. 2.6 Å (*vs.* ca. 3.5 Å in the fully oxidized structure),[95b,c] as shown in **Figure 1.12**. Very recently, Cronin and

co–workers reported the reduction of the Wells–Dawson phosphotungstate $[P_2W_{18}O_{62}]^{6-}$ with up to 18 electrons at highly concentrated aqueous solution in the presence of lithium counter cations.[89] Besides being suitable for the construction of redox–flow batteries (*vide supra*), the metastable solution of super–reduced Wells–Dawson anions featured spontaneous hydrogen evolution when diluted in water, releasing 14 of the 18 electrons as molecular hydrogen. This specific case has been studied in the Chapter 6 of this thesis.

1.4 POMs as Oxidation Catalysts.

Owing the oxidizing character of POMs, they have been extensively used as oxidation catalysts in a variety of reactions. A recent review by Weinstock et al.[96] collects dozens of examples in which POMs catalyze the oxidation of organic substrates making use of molecular oxygen as terminal oxidant. The most popular POMs for these purposes is the Keggin–type phosphovanadomolybdate $[PV_2Mo_{10}O_{40}]^{5-}$ (PV_2Mo_{10} for short), which combines high electron affinity with the strongly basic character of the vanadium–bound oxygen atoms. In oxidation reactions, PV_2Mo_{10} can take two well–differentiated roles, as described in ref. 96. On one hand, it can act as co–catalyst in chemical oxidations promoted by other metal complexes such as Pd^{II}– or Pt^{II}–based catalysts. For instance, Pd^{II} is usually reduced to Pd^0 after completing oxidative transformations such as the Wacker oxidation of alkenes to ketones. PV_2Mo_{10} can then regenerate the catalytically active Pd^{II} complex by accepting two electrons from the Pd^0 species that are accommodated in V atoms. Then, the fully oxidized POM can be recovered upon interaction with O_2 to yield water in the presence of protons that are generated during the oxidation of the organic moiety. On the other hand, PV_2Mo_{10} can catalyze several types of oxidative transformations itself. For instance, the dehydrogenation of dienes or alcohols can be achieved throughout the direct transfer of two electrons from the organic substrate to the POM. Another kind of oxidations, often termed as Mars–Van Krevelen–type oxidations, does not only involve this 2–electron redox process but also the transfer of an oxygen atom from the POM framework to the substrate. After completing these transformations, the POM catalyst can be regenerated with O_2 as described above. Other TM–substituted POMs have also been employed as oxidation catalysts. As a selected example, Co– and Cu–substituted Wells–Dawson phosphotungstates were found to promote the oxidative cleavage of C=C bonds to form the corresponding aldehydes in the presence of N_2O, giving NO as byproduct.[97]

Another oxidation strategy involves the activation of hydrogen peroxide (H_2O_2) with TM–substituted POMs to achieve the oxidation of sulfide groups in thioethers to sulfoxides and sulfones or the epoxidation of alkenes. These reactions are usually classified as *green oxidations* due to the environmentally friendly character of H_2O_2 that ideally, gives water as sole by–product, as shown in **Scheme 1.2**. Several POM structures came out as good candidates for the activation of H_2O_2 to afford the aforementioned transformations either in a stoichiometric or catalytic manner.[98] In particular, in this thesis we focused on the role of POMs as catalysts for alkene epoxidation, which is a process of both industrial and academic interest due to the valuable character of epoxides as intermediates in organic synthesis or for further application in the preparation of epoxy resines, paints or surfactants.

Scheme 1.2 | Global reaction equation for the alkene epoxidation with hydrogen peroxide.

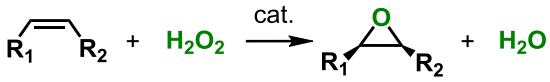

In the early 1980s, Venturello and co–workers reported that the phosphotungstic acid can activate H_2O_2 to form a peroxo–tungstate complex $[PO_4\{WO(O_2)_2\}_4]^{3-}$ (see **Figure 1.13**A). This complex was found to efficiently promote the epoxidation of alkenes in a highly selective manner.[99] Due to the possibility of isolating the peroxo intermediate, this was postulated to be the active species responsible for the oxygen–transfer to the alkene, which was identified as the rate–determining step. The reactivity of this complex was further studied during the following years by Venturello and Ishii[100] and for this reason, this catalytic structure is commonly known as the Venturello–Ishii complex. Lacunary polyoxotungstates presenting terminal oxygen groups in *cis* conformation are also active in the heterolytic activation of H_2O_2 and in the epoxidation of alkenes. Remarkably, the tetraprotonated form of a divacant silicodecatungstate $[\gamma\text{–}SiW_{10}O_{34}(H_2O)_2]^{4-}$ of Keggin structure exhibited higher yields than the Venturello–Ishii catalyst for the epoxidation of several alkenes with H_2O_2.[101]

The main side reaction in alkene epoxidation with H_2O_2 is the unproductive decomposition of the oxidant that produces non–desired products such as organic hydroperoxides, enols and enones (see **Scheme 1.3**). These are usually referred as *homolytic products* since the decomposition reaction is considered to proceed via homolytic cleavage of O—O bond in H_2O_2 to form radical species.[102] Seeking to avoid this side reaction and thus, improve the selectivity of the reaction towards the epoxide product,

several TM–substituted POMs (TM = Ti^{IV}, V^{V}, Nb^{V}, Mn^{II}, Zr^{IV}, among others) were synthesized and applied to the selective epoxidation of alkenes.[103]

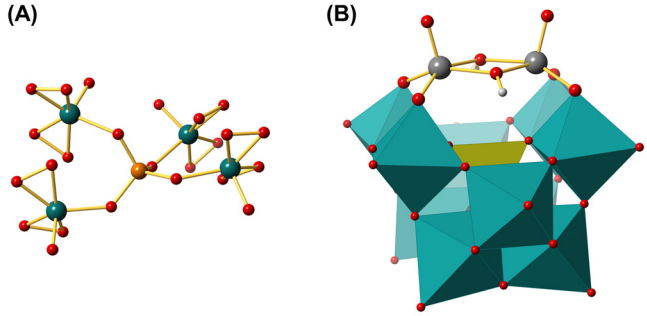

Figure 1.13 | 3D representation of the most popular POM–based catalysts for alkene epoxidation with hydrogen peroxide. (A) Venturello–Ishii catalyst with $[PO_4\{WO(O_2)_2\}_4]^{3-}$ structure[100] and (B) 1,2–divanadium–substituted γ–Keggin $[\gamma\text{–}1,2\text{–}H_2SiV_2W_{10}O_{40}]^{4-}$, sythesized by Mizuno and co–workers.[103b]

Scheme 1.3 | Main products formed in the alkene epoxidation reaction with H_2O_2.

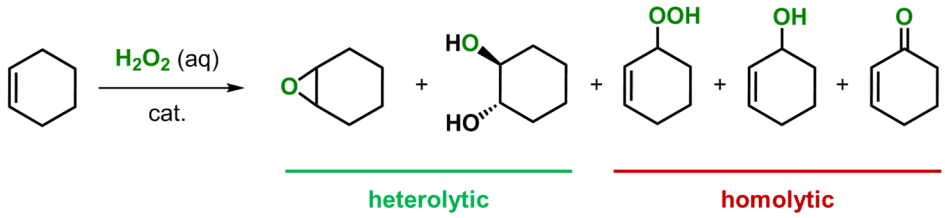

Apart from POMs, other frameworks have been used as supports for active TMs to build up single–site catalysts for the selective alkene epoxidation. One of the most relevant examples is the heterogeneous silica–supported Ti–containing TS–1 catalyst, developed by ENI in the 1980s.[104] This microporous catalyst resulted highly efficient in the epoxidation of light alkenes with H_2O_2 and prompted the development of novel mesoporous heterogeneous catalysts to allow the epoxidation of larger substrates.[105] For years, the group of Kholdeeva devoted itself to this research activity and moreover, they made use of TM–substituted POM systems as tractable molecular models of single–site heterogeneous catalysts to investigate kinetic aspects of the reaction or the nature of the involved intermediates.[106] Nevertheless, although POMs were initially used only as model systems, they turned out being rather efficient homogeneous catalysts themselves,

providing pretty decent conversion and selectivity. In fact, the catalytic activity of Ti–containing POMs has been directly compared to that of the heterogeneous TS–1.[106]

Guillemot, Proust and co–workers reported another strategy to model single–site silica supported catalysts for alkene epoxidation.[107] Their approach consists in hybrid silanol–functionalized lacunary polyoxotungstates that can accommodate the catalytically active metal ions in a ligand environment that fairly mimics those found in the silica–suppored catalysts. Using a bis–grafted $[PW_{10}O_{36}(^{t}BuSiO)_2VO(^{i}PrO)]^{3-}$ hybrid, they were able to model the oxidation of cyclic alkenes and allylic alcohols with *tert*–butyl hydroperoxide (TBHP) catalyzed by V^{V} ions dispersed onto silica.[107a] Another trilacunary Keggin–type POM scaffold, $[\alpha\text{–B–}SbW_9O_{33}(^{t}BuSiOH)_3]^{3-}$, can accommodate a Ti^{IV} center in a tetrahedral coordination environment provided by the silanol ligands leading to $[\alpha\text{–B–}SbW_9O_{33}(^{t}BuSiO)_3Ti(O^{i}Pr)]^{3-}$.[107b] It is worth noting that the structural parameters involving the Ti center in the X–ray structure of $[\alpha\text{–B–}SbW_9O_{33}(^{t}BuSiO)_3Ti(O^{i}Pr)]^{3-}$ derivative were found to be very similar to those reported for TS–1. Interestingly, this species let to selective epoxidation of allylic alcohols making use of of H_2O_2 as oxidant at room temperature, whereas no conversion was observed with non–functionalized alkenes. The reasons for the experimentally observed selectivity were investigated in Chapter 7 by means of computational methods.

From a computational perspective, several research groups have studied the alkene epoxidation reaction catalyzed by TM–containing POMs.[108–114] All them agree in the fact that the reaction mechanism involves two main steps: i) heterolytic activation of H_2O_2 on the metal ion to produce either a hydroperoxo (OOH) or a peroxo (OO) ligand; and ii) heterolytic O—O cleavage of the hydroperoxo or peroxo ligand to transfer an electrophilic oxygen to the double bond of the alkene. **Scheme 1.4** compiles the main mechanistic possibilities proposed so far, which vary in the nature of the epoxidizing species and in the oxygen atom transferred to the substrate. Two of them are proposed to take place from the metal–hydroperoxo intermediate (highlighted in green) and the third one consists on an oxygen transfer to the alkene from the peroxo intermediate (highlighted in purple). The same two–step mechanism was also found to apply for other oxidation reactions with H_2O_2 such as the hydroxylation of aromatic compounds or the oxidation of thioethers.[115]

In 2006, Musaev and co–workers reported the first mechanistic study of the alkene epoxidation with H_2O_2 catalyzed by POMs.[108] In this work, the authors analyzed the case

of the divacant γ–Keggin anion $[\gamma\text{–}SiW_{10}O_{34}(H_2O)_2]^{4-}$, which had emerged three years before as an outstanding catalytic structure.[101] The proposed mechanism consists in a hydroperoxo–mechanism in which the proximal α–oxygen of the W—OOH moiety is transferred to the alkene (analogous to pathway *ii* in **Scheme 1.4**).[108] Also, they highlighted that presence of protons at the terminal tungsten–oxo groups has a crucial role in reactivity allowing the formation of metal–hydroperoxo groups. Other computational studies with the Se–containing divacant γ–Keggin suggested a peroxo–type mechanism (path *iii* in **Scheme 1.4**).[109] Regardless the working mechanism, the oxygen–transfer step was identified in all cases as the rate–determining step, probing the postulated by Venturello and colleagues on the basis of experimental observations.[99]

Scheme 1.4 | Proposed Mechanisms for Alkene Epoxidation with H_2O_2 catalyzed by Ti–Substituted POMs.

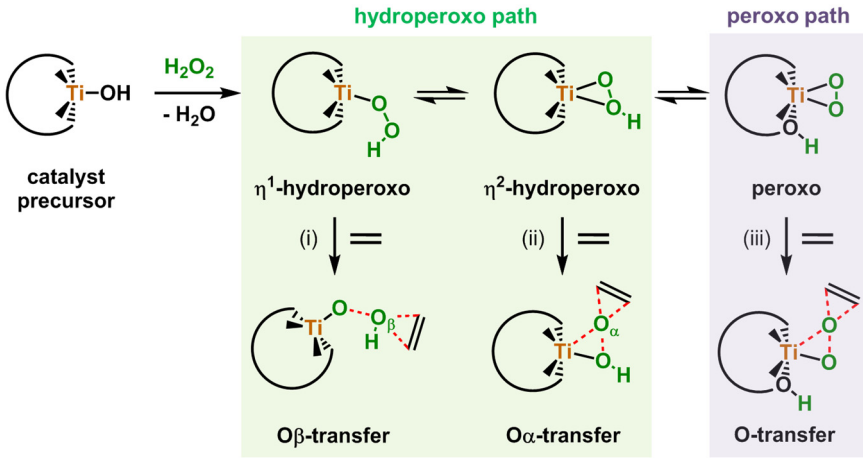

Nakagawa and Mizuno studied computationally the epoxidation of alkenes by the 1,2–divanadium–substituted γ–Keggin $[\gamma\text{–}1,2\text{–}H_2SiV_2W_{10}O_{40}]^{4-}$ (shown in **Figure 1.13**B).[110] This catalyst displays a {OV–(μ–OH)$_2$–VO} core that upon interaction with H_2O_2, generates a dihapto bridging peroxo ligand {OV–(μ–η^2:η^2–OO)–VO}. This latter was identified as the epoxidizing species, which transfers an electrophilic oxygen atom from the peroxo group (activated by the cooperative effect of both V^V ions) to the alkene via peroxo path.

In collaboration with the experimental group of Prof. Kholdeeva, our group has comprehensively studied by means of computational methods the epoxidation of alkenes catalyzed by Ti^{IV}–substituted polyoxometalates.[111–114] The analyzed Ti–POM structures

include the Ti–monosubstituted Keggin anion $[PTi(OH)W_{11}O_{39}]^{4-}$ and the "sandwich"–type dititanium 19–tungstodiarsenate(III) $[Ti_2(OH)_2As_2W_{19}O_{67}(H_2O)]^{8-}$. In both cases, the Ti–hydroperoxo species was found to be more reactive than the end–on peroxo complex Ti–(η^2–OO) protonated at the Ti—O—W site, although this latter is more stable because of the highly basic character of the protonated oxygen sites. In agreement with the early studies by Tantanak and Karlsen,[116] the non–protonated α–oxygen of the Ti–OOH moiety resulted more electrophilic than the distal and protonated β–oxygen because the σ^*_{O-O} orbital is polarized towards O_α. Thus, the attack of the alkene is electronically preferred at the O_α site (pathway *ii*, **Scheme 1.4**).[111] However, the transfer of the β–oxygen (pathway *i*, **Scheme 1.4**) prevails in complexes where the Ti center is strongly sterically hindered or found in a rigid environment that hampers the geometrical distortion required for the O_α–transfer.[114]

As an initial approach to understand the influence of the catalytically active metal ion in the reactivity, the electronic energy barriers for the hydroperoxo and peroxo paths were compared in **Figure 1.14** for a series of TM–substituted Keggin anions.[111] Although information about the H_2O_2 activation step and the relative stability of the reaction intermediates is still missing, this study allowed establishing some reactivity trends. When going down in the periodic table, the O–transfer barriers for both the hydroperoxo and the peroxo path decrease, although the latter does it more significantly. Moving from the left to the right in the periodic table revealed opposite trends in the peroxo and hydroperoxo paths. The barrier for the peroxo path is strongly decreased due to the higher oxidation state of the metal ion that renders the peroxo group more electrophilic. On the contrary, the barrier associated to the hydroperoxo path slightly increases. This latter trend was ascribed to the enhanced orbital mixing between the occupied p(O) orbitals of the hydroperoxo group and the empty d(TM) orbitals that strengthens the TM—O_α bonds and thus, increases the height of the barrier. Furthermore, it was found that increasing the electrophilicity of the Ti–OOH moiety via protonation of the POM framework has a positive effect in the reactivity, significantly decreasing the height of the energy barriers for the O–transfer step.[113] Based on the latest experimental results obtained by Kholdeeva and co–workers, we have analyzed in Chapter 7 of this thesis the reactivity of Nb^V–substituted POMs and compared it to that of widely studied Ti–containing POMs.

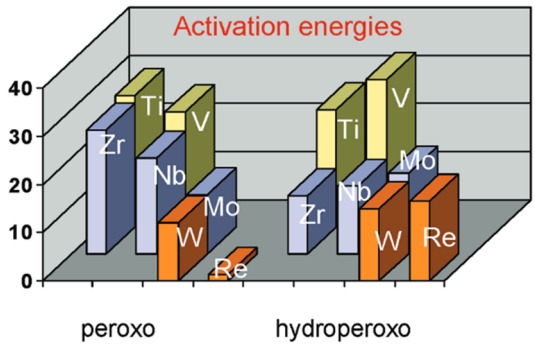

Figure 1.14 | Activation energies (kcal·mol^{-1}) associated to the oxygen transfer step computed for TM– substituted Keggin–type phosphotungstates in gas phase. Reproduced from ref. 111.

1.5 Computational Modeling of POMs.

In the last decades, computational chemistry has become an essential tool for rationalizing experimental outcomes and understanding molecular properties derived from their electronic structure. Nevertheless, it must be pointed out that strictly as experimental science needs to be backed by theoretical analyses, computational results also require experimental evidences to validate the models and methodologies employed for the calculations. For these reasons, synergies between experimental and computational chemistry represent nowadays a standard working protocol for going ahead in chemical research. The chemistry of POMs is not an exception, despite the fact that the relatively large size of POM structures has made their computational modeling tedious and expensive, but challenging at the same time. This section exposes how the computational modeling of POMs emerged and grew since the 1980s to nowadays, highlighting some selected contributions with the aim of defining the current state of the art.

The first calculations on POMs were carried out by Taketa et al. in the mid–1980s and were devoted to the electronic structure analysis of the Keggin–type phosphomolybdate anion[117] and other molybdates[118] to understand their reduction mechanism from a MO perspective. The main features of the frontier MOs were described by means of the Model Potential Xα method,[119] which is based on the LCAO–MO approximation and combines core effective potentials with Slater–type potentials. In $[PMo_{12}O_{40}]^{3-}$ anion, the HOMO was found to be composed by 2p orbitals from bridging oxygen atoms in up to 95 %, whereas the LUMO has $\pi^*_{W=O}$ character, combining the contribution from $2p(O_{bridging})$

and 4d(Mo) atomic orbitals. This electronic structure description can be extended to other POM structures and as shown in **Figure 1.15**, it is still valid nowadays. These early works preceded a number of studies using semi–empirical methods[120–123] that chiefly focused on understanding features related to the molecular and electronic structure of POMs, such as relative stability of species, [122] the position and coordination mode of a Cu^{II} ion in a Cu–containing Keggin POM,[120] or the electron localization in a reduced V–containing polyoxomolybdate.[121] Notably, semi–empirical methods permitted the first studies concerning the reactivity of POMs that were published in the early 1990s.[123] Specifically, these studies analyzed the photodimerization of alkanes and alkenes promoted by the decatungstate anion, and reported the first TSs involving POMs, which correspond to proton–transfer processes. Thanks to the increase of computational power, more accurate Hartree–Fock calculations became affordable for POM systems. Using the fully *ab initio* wave function granted by this method, Bénard and co–workers studied electronic properties of polyoxovanadates, getting special insights into the relative basicity of external oxygen sites and the ability of polyoxovanadates to accommodate small and medium–sized guests inside them.[124] Basic properties of diniobium and divanadium–substituted Lindqvist–type polyoxotungstates were also analyzed by means of HF methods.[125]

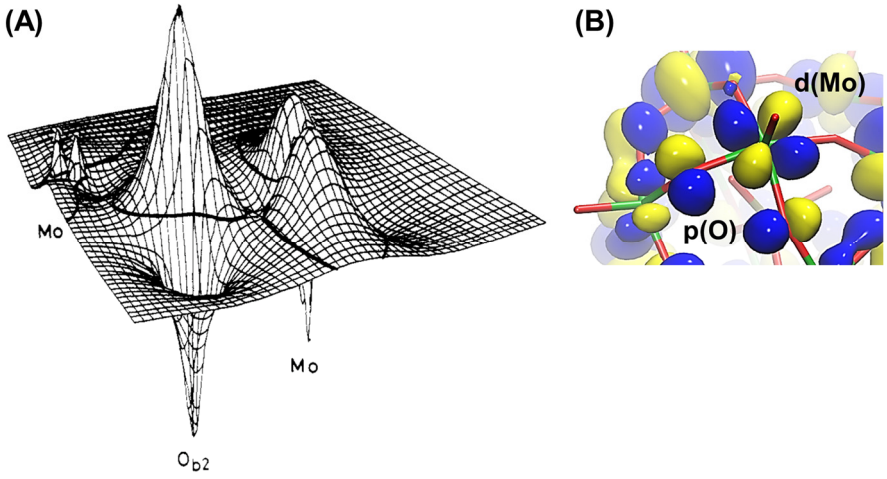

Figure 1.15 | (A) First LUMO representation of the $[PMo_{12}O_{40}]^{3-}$ anion.[117] (B) 3D representation of the same MO obtained from DFT for comparison.

The implementation of DFT[126] methods and continuum solvent models[127] represented a revolution in the field of computational chemistry in general and in the modeling of

POMs in particular, permitting the accurate description of large and highly anionic structures such as POMs at an affordable computational cost. A complete survey of POM chemistry employing DFT methods and implicit solvation has been conducted during the last two decades, tackling from electronic structure studies, redox properties and basicity investigations to more complex aspects such as spectroscopic properties, NMR chemical shifts, magnetism or reactivity. Poblet, Bo and co–workers collected the most recent advances on the computational modeling of POMs in some reviews.[128–130]

In 2002, Bridgeman and Cavigliasso reported a full description of the electronic structure of $[Nb_6O_{19}]^{8-}$, $[Ta_6O_{19}]^{8-}$, $[Mo_6O_{19}]^{2-}$, and $[W_6O_{19}]^{2-}$ anions and the one electron– and two electron–reduced Mo– and W–based systems.[131] The same year, Li reported a very similar study, highlighting the stabilizing nature of conjugated σ and π–type orbitals forming cycles that confer POMs a *quasi–aromatic* nature.[132] These studies classified the set of occupied orbitals in three well–separated blocks. The deepest one corresponds to different nonbonding combinations of s–type oxygen orbitals, which is followed by nonbonding combinations of p–type orbitals. Finally, there is a set of σ and π–type bonding orbitals involving combinations of p(O) and d(TM) that extend until the HOMO. A gap of ca. 3.1 eV in tungstates and 2.5 eV in molybdates separate the array of occupied orbitals from the virtual ones. Due to the C_{4v} symmetry around metal ions, the LUMO and the first set of virtual MOs correspond to d_{xy}(M) orbitals, followed by the d_{xz} and d_{yz} that are higher in energy and degenerated; and the e_g–type ones, found above, as represented in **Scheme 1.5**. Also, these initial studies already showed that the extra electrons in reduced species are not localized in a specific metal ion but delocalized over the whole structure, since the spin density is equally distributed over the six symmetry–equivalent metal centers. Furthermore, the accurate description of the electronic structure provided by DFT methods gave rise to the use of HOMO–LUMO gap as a stability–related descriptor for POM complexes.

Scheme 1.5 | Splitting of d(TM) molecular orbitals in the crystal field induced by the POM environment. Obtained from ref. 129.

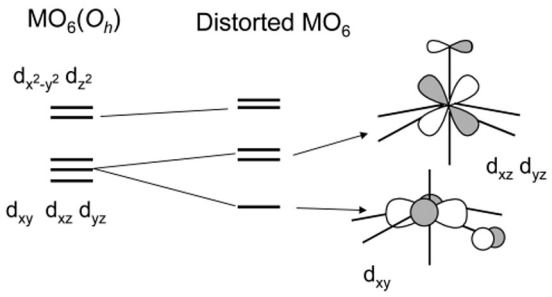

Following studies were devoted to analyze the redox properties of several Keggin, Wells–Dawson and Preyssler structures, getting insights into the electron (de)localization effects also in mixed–addenda structures.[133,134] At the same time, the acid/base properties of POM structures were tackled through DFT methods.[133b,134,135] Protonation energies along with representations of molecular electrostatic potentials (MEPs) served to unveil the most likely protonation sites in several POM structures, which usually correspond to bridging oxygen sites. In case of TM–polysubstituted structures, there is a clear preference for TM—O—TM sites, followed by TM—O—W sites or terminal TM—O ones depending on the nature of the TM. For example, Mo or V centers do not tend to promote protonation at terminal sites due to the double bond nature of TM=O bonds. However, POMs containing Nb or Ti are usually protonated at the terminal TM—O sites due to the lower bond order of the TM—$O_{terminal}$ bonds. Interestingly, both protonation energies and oxidizing power of POMs were found to correlate linearly with the charge per metal ratio (q/M) as a measure of the charge density of the anion; that is the higher the q/M value, the more favorable the protonation (see **Figure 1.16**) and the harder to reduce.[130] Further DFT calculations allowed to study the encapsulation of monoatomic cations by large POM structures such as the Preyssler anion,[134] as well as the origin of alternated bond distances within POM frameworks caused by a second order Jahn–Teller effect.[136] The most recent electronic–structure studies concern novel POM structures[137] and mixed–valent polyoxovanadate cages such as $\{V_{18}O_{40}\}$ or $\{V_{22}O_{54}\}$, which can encapsulate from small (e.g. I^-) to medium–sized (e.g. SCN) guests.[138] Most of these studies were performed with pure DFT functionals such as PBE[139] or BP86[140] by means of the ADF code, which uses of Slater–type basis functions, in contrast with other quantum chemistry packages that operate with Gaussian functions or plane waves. Since geometry optimizations with hybrid functionals are too computationally demanding within the ADF

code, a quite common computational approach consists in performing geometry optimizations with a pure functional followed by single–point calculations with a hybrid functional to obtain energies or other wave function–derived properties.

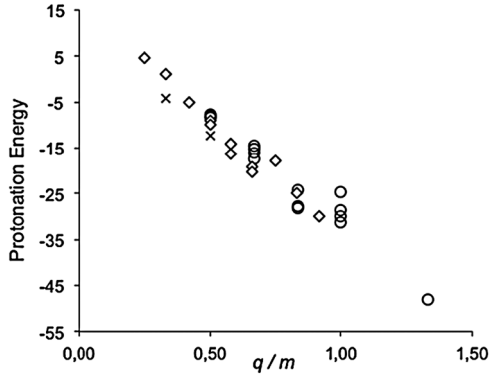

Figure 1.16 | Relationship between DFT–calculated protonation energies (kcal·mol^{-1}) at W—O—W sites and the *q/M* parameter. Protonation energies are relative to that of the $[W_6O_{19}]^{2-}$ anion. Diamonds, circles and crosses represent Keggin, Lindqvist and Dawson anions, respectively. Obtained from ref. 130.

As exemplified in the previous section, DFT methods have been also used to study chemical transformations involving POMs.[130] In the field of acid catalysis, some computational studies have analyzed the catalytic role of POMs in alcohol dehydration or ether hydrolysis processes, in which protonated POMs act as Brönsted acids.[141] Other remarkable theoretical analyses provided insights into the role of POMs as oxidation (*vide supra*)[111–115,144] or water splitting catalysts.[145] For studying the reactivity of POMs, B3LYP functional[142] together with continuum solvent models is usually the computational procedure of choice, since it often provides accurate geometries and energy barriers with a high degree of consistency with experimental kinetic parameters. The meta–GGA hybrid M06 functional[143] has been also applied to the modeling of POM reactivity, [144,146] although its use is much less common than that of B3LYP. Aside from discrete molecular systems, the implementation of DFT methods in quantum chemistry codes for periodic calculations allowed studying the interaction of POMs with metal surfaces and the physicochemical properties of POM–containing nano–composites.[147]

Beyond DFT, post–HF wave function methods such as CASPT2[148] or DDCI[149] have been applied to the study of the magnetic behavior reduced POMs containing more than one *d* electron.[150–152] Importantly, these calculations were able to nicely reproduce the

diamagnetic behavior of 2 electron–reduced polyoxometalates. Using these highly accurate techniques, Coronado and co–workers were able to determine local electron transfer parameters between W atoms in model systems of the Keggin–type phosphotungstate anion.[150] Later on, Poblet and co–workers studied the electronic structure of two–electron–reduced hexamolybdate, hexatungstate and several mixed–addenda Lindqvist–type clusters[151] using the variational DDCI method. Bigger anions with a larger number of unpaired electrons such as the $[PMo_8V_4O_{40}(VO)_4]^{5-}$ anion with 10 *d* electrons could also be studied at CASSCF level, giving a description of the electronic structure comparable to that obtained from hybrid DFT functionals.[152] It must be pointed out that although these methods bring an accurate description of the electronic structure in systems with unpaired electrons, they are highly computationally demanding and their systematic use is still prohibitive.

In general, static *ab initio* calculations can provide deep understanding at atomistic and electronic level of processes in which POMs are involved. However, studying some of their features in solution requires an explicit and dynamic description of the POM environment. Molecular Dynamics (MD) is a deterministic simulation method based on the integration of the Newton's equations of motion for a many–body system to compute a *trajectory*, that is the evolution of atomic positions and velocities as function of time.[153] Therefore, unlike static calculations based on molecular properties on a single point of the PES, MD allows the analysis of how molecular and even supramolecular properties evolve over time. We usually differentiate between *classical* and *ab initio* MD depending on the nature of the computed forces used in Newton's equations. Classical forces are usually obtained from Molecular Mechanics (MM) methods and arise from an empirical description of the energy as defined within the expressions of a force field. Differently, quantum forces are obtained from energies derived from an approximation to the Schrödinger equation in which electrons are treated explicitly. Thus, classical MD simulations can be applied to the study of large systems (many thousands of atoms) due to their lower computational cost, but their main limitation is that they cannot be used to study bond–formation or bond–breaking processes, since there is no explicit description of electrons. Therefore, one should move to more accurate (and expensive) *ab initio* simulation methods for studying reactivity, although they only allow simulations with a few hundreds of atoms at this moment. Reactive force fields such as ReaxFF[154] have been developed to study reactivity in large systems from a classical point of view. However, these force fields are usually available only for a limited set of systems for which they are parameterized. Another approach to tackle reactivity in large systems is the use of hybrid

QM/MM potentials,[155] in which the reactive region of the system is treated at high–level QM methods such as DFT, while the rest of the system is described with faster MM methods. The interaction between both sub–systems is usually attained through mechanical embedding through bonds that are simultaneously described by both methods and electronic embedding, which account for the polarization of the QM wave function by the set of MM charges through the space.

During the last two decades, a large number processes involving POMs have been successfully studied by means of both classical and *ab initio* MD methods. The pioneers in this field were Tsujimichi et al., which reported in 1995 the first simulation of a $[PMo_{12}O_{40}]^{3-}$ in water with 3 potassium cations.[156] In this study, the POM was empirically described by a force field previously developed for metal oxides, although the authors pointed out that it could be treated as a rigid body. Due to computational limitations, the simulation time consisted only in of a few picoseconds and therefore, it was not possible to perform a statistical analysis of the distribution of solvent and counter cations around the POM structure. However, this work demonstrated that MD techniques can be employed to study the explicit dynamic environment of POMs in solution and encouraged further MD simulations with POM systems. Ten years later, López et al. reported the first atomistic description of the solvation shell of a Keggin–type phosphotungstate $[PW_{12}O_{40}]^{3-}$ anion surrounded by 1000 water molecules and 3 Na^+ cations.[157] Unlike the early studies by Tsujimichi et al., the simulation time in this case was much longer (accounting for 2 ns in all) due to the important increase of computational power and the higher efficiency of the employed simulation codes. In this case, phosphorus and tungsten atoms were described with parameters obtained from the respective alkali cations, whereas inorganic oxygen atoms of the POM were described by the Lennard–Jones parameters of fluoride anion. The authors analyzed how the POM solvation shell is reproduced by several charge models, benchmarking the obtained results with experimental diffusion coefficients. The set of atomic charges derived from the electrostatic potential were found to be those providing the most reliable solvent distribution whereas other charge models such as Mulliken led to a too loose solvation shell with scarcely defined peaks in the POM···water radial distribution functions (**Figure 1.17**). This methodology was then adopted by other authors as well as in the simulations reported in this thesis, although other FFs for describing POM structures were also proposed in the literature.[158]

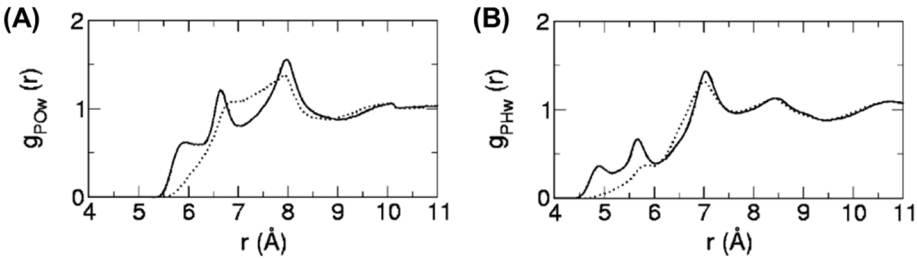

Figure 1.17 | Radial disftibution functions (RDFs) between the POM center of mass and water oxygen (A) and hydrogen (B) atoms. Solid and dashed lines represent the ChelpG and Mulliken charge models, respectively. Adapted from ref. 157.

Shortly later, Leroy et al. studied systematically ion–pairing processes between three Keggin–type polyoxotungstates of different charge and three different alkali cations, and how they affect the mobility of the anion in solution.[159] Specifically, the computed diffusion coefficients were found to strongly depend on the ability to form ion pairs and on the first and second solvation shells of the anion, which in turn are affected by the POM charge. Also related to ion–pairing processes, the most likely positions for cations to interact with the doughnut–shaped $[H_3Mo_{57}V_6(NO)_6O_{183}(H_2O)_{18}]^{21-}$ anion were successfully predicted by classical MD simulations.[160] More recently, Volkmer et al. analyzed the dynamic behavior of a dendrimer–encapsulated $[(Zn(H_2O))_3(SbW_9O_{33})_2]^{12-}$ anion[161] and Bo, Ávalos and co–workers analyzed the distribution of water and cations around (and inside) giant Keplerate structures.[162]

Chaumont and Wipff moved from MD analyses on single POMs to more ambitious MD studies in which several polyoxoanions (up to 20) were simulated together with their respective counter cations in a periodic simulation box full of explicit solvent molecules.[163] These simulations were carried out with the aim of studying the supramolecular agglomeration between Keggin anions in solution and at interphases of biphasic systems. In addition, they systematically analyzed how agglomeration was affected by several parameters, such as the charge of the POM, the nature of the solvent and counter cations or the concentration of POM salt. Notably, POM agglomeration was found to be very sensitive to the nature of the cations and related to this, two main interaction modes were identified to mediate the contacts between POMs: cation–mediated interactions and water–mediated contacts in which a "crown" of solvent water molecules is persistently attached to two POM units simultaneously. Other authors extended this work to MD studies on agglomeration processes in ionic liquids and solvent mixtures[164] or to other

POM structures such as lacunary polyoxotungstates or polyoxovanadate clusters.[165] Also, MD simulations of Dawson–type anions at high salt concentrations were able to reproduce the initial steps of a crystal nucleation process observed experimentally.[166]

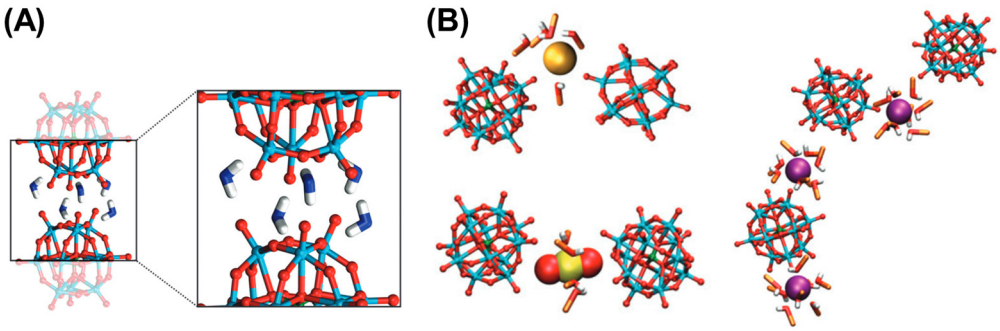

Figure 1.18 | Representative snapshots of POM agglomeration mediated by the solvent (A) or by Cs^{+} (left, top), UO_2^{2+} (left, bottom)and Eu^{3+} (right) cations in methanol solution (B). Adapted from ref. 163a.

In addition, *ab initio* simulation methods (AIMD) have been applied to the study of processes in which chemical bonds are formed or broken. The most representative case is mechanism of POM formation, studied by Poblet and co–workers during the late 2000s by means of Car–Parrinello MD simulations and static DFT calculations. Initial studies concerned the stability and speciation of small precursors and intermediates in the formation of the hexatungstate anion $[W_6O_{19}]^{2-}$.[167] Notably, the $[WO_3(OH)]^{-}$ complex was found to expand its coordination sphere at low pH, leading the hexa–coordinated $[WO_2(OH)_2(OH_2)_2]$ species, which can auto–condensate to grow POM structures. Then, the initial nucleation steps were studied through CPMD simulations using the metadynamics approach as enhanced sampling technique (**Figure 1.19**A).[168] Finally, the scope of this work was extended to include the formation of hexamolybdate,[169] the Keggin–type phosphotungstate[170] or $\{Mo_{132}\}$ Keplerate–type structures.[171] Related to the formation mechanism, Cameron et al. also performed metadynamics simulation to study the isomerism of a $[SiW_{10}O_{36}]^{8-}$ structure via a rotational transformation (**Figure 1.19**B).[172]

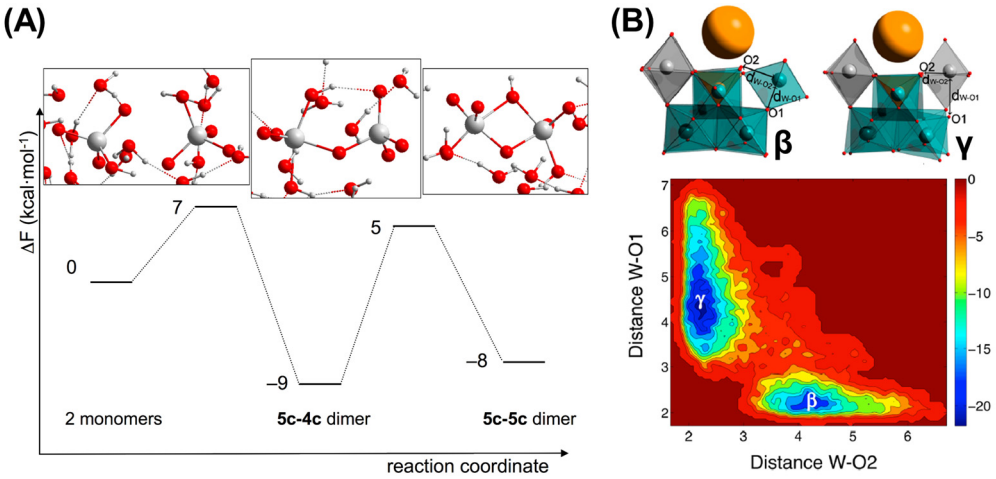

Figure 1.19 | Two examples of the application of metadynamics for studying POM chemistry. (A) Initial nucleation mechanism for the formation of POMs. Taken from ref. 168. (B) Free–energy landscape along the isomerization pathway of the $[SiW_{10}O_{36}]^{8-}$ cluster. Adapted from ref. 172.

Other researchers used *ab initio* simulations to study the conformational variability of systems of interest. For instance, Kachmar et al. studied a dicarboxylate encapsulated in a molybdenum oxysulfide ring[173] and Piccinin et al. analyzed the geometrical distortions of the tetraruthenium–containing POM–based WOC in the presence of explicit solvent.[174] In our group we also evaluated the stability of the fully reduced $[IV_{18}O_{40}]^{13-}$ anion in water as well as the fluctuations in their structural parameters in the presence of explicit solvent.[165b] Recently, CPMD simulations were carried out to study the speciation of a Zr–subsituted Lindqvist anion under different pH conditions, which was necessary to understand the assembly mechanism of TM–substituted POMs to form dimers and larger self–assemble structures.[175] In most of the cases, *ab initio* simulations were performed using the Car–Parrinello method, in which the wave function is iteratively optimized in the first step and propagated along the simulation by integrating the equations of motion derived from the Car–Parrinello Lagrangian.[176] On the basis of the available literature, Born–Oppenheimer MD (BOMD) simulations are more rarely applied to the dynamic simulation of POMs.

1.6 Novel Challenges in Computational POM Modeling.

In this thesis we have tackled two novel aspects of computational POM chemistry: the interaction and reactivity with biological systems, and the reactivity of POMs involving single electron transfer (SET) processes.

1.6.1 Interaction with biological systems.

As mentioned in previous sections, the molecular interaction of POMs with biological systems governs the biological activity of POMs in most cases. Before this doctoral thesis, however, the theoretical description of these interactions was limited to several docking studies exploring the binding locations for POMs with proteins; but the characterization of the physicochemical foundation to these interactions was still lacking. Biological systems are usually large organic molecules with a huge number of degrees of freedom. This causes the free–energy surface associated to their conformational space to have many different minima separated by small energy barriers. Thus, a static description of the interaction between POMs and proteins using a single protein conformation can only provide a very limited description of the interaction process. For this reason, atomistic MD simulations were used herein to study POM···protein interactions, since they allow getting a dynamic picture of these interactions, accounting for the conformational variability of the protein system and also for that of the solvent and counter ions around. Although some dynamic properties of POMs such as solvation or collective behavior have been successfully assessed by means of dynamic methods, this is the first time that these techniques are used to analyze their interaction with biological systems.

MD methods are very popular in the world of computational biology or bioinformatics, and therefore, there are plenty of force fields to describe the protein system. In contrast, inorganic POMs represent non–standard fragments for which force field parameters need to be defined. Nevertheless, previous MD studies already proposed a computational protocol for obtaining FF parameters for POMs (*vide supra*).[157] First, the geometry of the POM is fully optimized including solvent effects through a continuum solvent model. Then, the set of atomic charges are calculated in vacuum at the same level of theory. Specifically, ChelPG atomic charges derived from the molecular electrostatic potential were found to be those that reproduce the best the distribution of water molecules around the POM. The van der Waals parameters were also taken from a previous work[157] and force constants associated to bonding parameters were set to a value of the same order of magnitude than the strongest bond in the force field, in order to reproduce the rigidity of

the POM framework. In addition, proteins were described in our simulations with the widely employed AMBER99 force field,[177] which atomic charges are also derived from the electrostatic potential. Therefore, since electrostatic interactions account for the most important part of the interactions between charged fragments, it is reasonable to think that the strength of POM···protein interactions will be properly described within this computational approach.

Chemical reactivity in biological systems was studied through two different approaches: the cluster model[178] and hybrid QM/MM calculations.[155] The cluster model approach consists in performing calculations on a simplified model of the protein, which is the reactive region of the real system taken either from X–ray crystal structures or from a snapshot of a MD simulation, capped usually with hydrogen atoms or methyl groups. To account for the influence of the protein chain strain, the relative position of these capping groups is usually constrained during geometry optimizations. Also, if reactivity occurs in the hydrophobic core of the biological system, a continuum solvent model with a low dielectric constant (usually $\varepsilon = 4$) can be used to model the hydrophobic environment. The reactions analyzed in this thesis take place at the solvent–accessible surface of the biological systems so that the dielectric constant of the solvent was set to 78.4, which corresponds to water medium. Here, QM/MM calculations and classical MD simulations were also used to analyze the influence of the explicit environment of the protein in some key steps of the analyzed processes.

1.6.2 Electron transfer processes: Marcus Theory.

Conventional reactivity of POMs involving bond–breaking and bond–formation processes has been successfully studied in many occasions by means of static DFT calculations and *ab initio* molecular dynamics. Nevertheless, POM reactivity involving electron transfer process remained unexplored to date. In this thesis, we evaluated the free energy barriers associated to single electron transfer (SET) steps making use of the Marcus Theory of the electron transfer as adapted by Vaissier et al.[179]

In 1952, William F. Libby explained the experimental isotopic self–exchange reactions between small charged species in solution as electron transfer processes, which were rationalized in terms of the Frank–Condon principle.[180] Thus, it was initially assumed that electron transfer processes occur through vertical excitations from the equilibrium geometries. Some years later, Rudolph A. Marcus noticed that electron transfer processes also take place in the dark, what would be in disagreement with the previous postulate due

to the energy conservation principle. Therefore, Marcus proposed a novel scheme for SET processes involving reorganization of the solvent surrounding the redox species to allow the electron transfer in non–equilibrium geometries.[181] These non–equilibrium conditions also apply for polyatomic solutes; whose molecular structure must become distorted to transfer or accept an electron.

In addition, Marcus proposed a handy strategy for studying the kinetics of the electron transfer process based on the determination of the free–energy variation from the reactants to a "transition state" for the SET. This "transition state" corresponds to a situation in which the geometries of both reactants and their respective solvation shells are distorted and ready to transfer or accept an electron to or from its redox partner. This set of atomic positions also corresponds to the crossing point between the free–energy surfaces describing the electronic states of the reactants and the products (see **Figure 1.20**). Note that the reaction coordinate in **Figure 1.20** does not only include the atomic coordinates of the solute but also those of the solvent. Two main assumptions, though, need to be done. First, one needs to assume that the free–energy wells of the reactants and the products are both described by symmetric parabolas of the same width. Second, the electron transfer is treated as a diabatic process, since this theory relate kinetics with a crossing point between the potential energy surfaces neglecting spin–orbit coupling (SOC) effects. According to this formalism, the free energy barrier associated to a single electron transfer process (ΔG^*) can be estimated by means of equation 1.1, where ΔG_r° and λ represent the reaction free energy and the reorganization energy, respectively. Both parameters are graphically represented in **Figure 1.20**. This latter accounts for the reorganization of the nuclei in the two molecules directly involved in the electron transfer, as well as the change in the polarization of the solvent required to promote the electron transfer process.

$$\Delta G^* = \frac{(\lambda + \Delta G_r^\circ)^2}{4\lambda} \qquad (1.1)$$

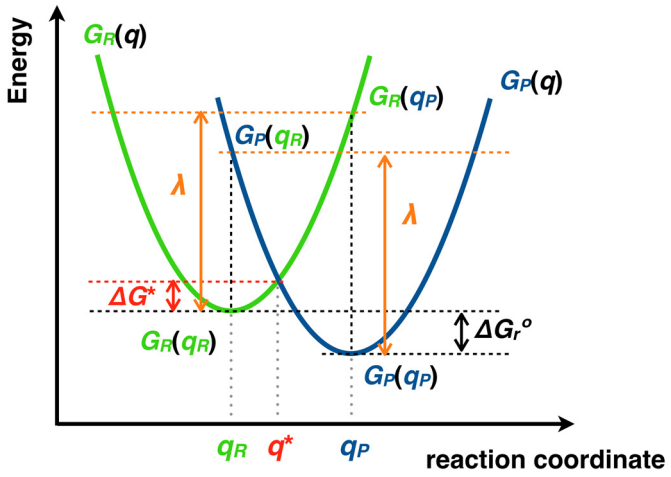

Figure 1.20 | Schematic representation of the potential free energy surfaces for the reactants (green parabola) and the products (blue parabola) of a SET process, highlighting the key parameters employed in equation 1.1 to calculate the free energy barrier (ΔG^*) associated to the electron transfer that brings reactants to products.

In practice, the reorganization energy (λ) was calculated as shown in **Figure 1.20** and **Figure 1.21**. Thus, the reorganization energy of a molecule (λ_i) corresponds to the energy difference in a given electronic state between its equilibrium geometry and the equilibrium geometry on the surface of its reduced/oxidized counterpart, in such a way that $\lambda_i = ½ \{[G_R(q_P) - G_R(q_R)] + [G_P(q_R) - G_P(q_P)]\}$; and the overall λ displayed in equation 1.1 is the sum of the individual λ_i computed for both molecules participating in the redox process. Since equilibrium geometries also include the grid of point charges of the solvent cavity, we used the non–equilibrium conditions as implemented in Gaussian09 (*NonEq* keyword)[182] to model the polarization of the solvent using the IEF–PCM continuum solvent model,[183] as done by Vaissier et al.[179]

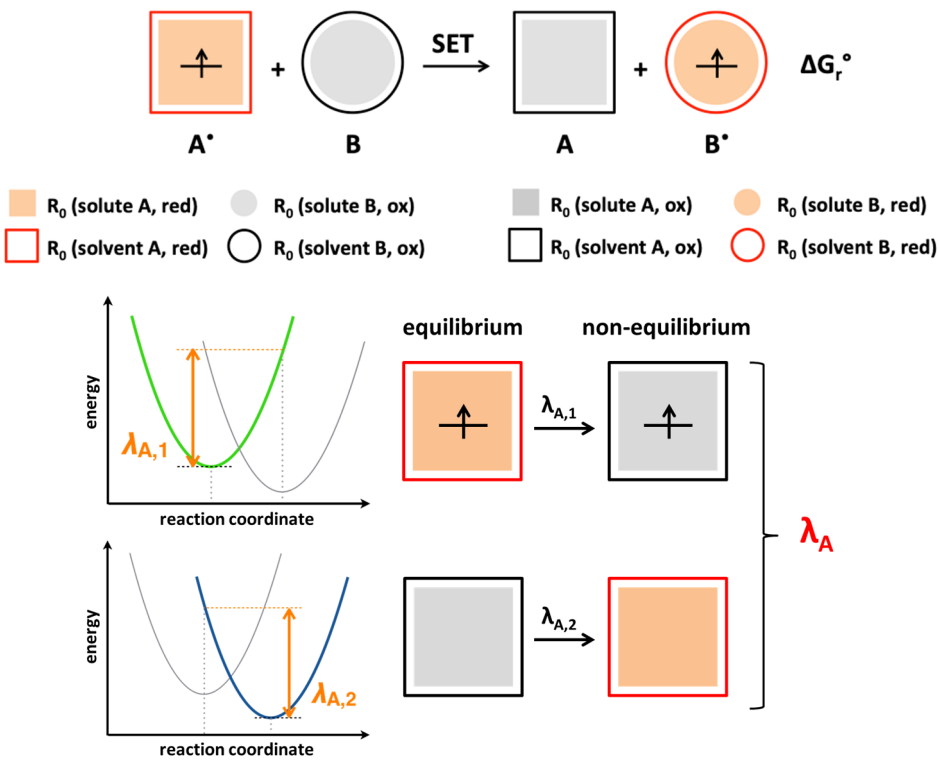

Figure 1.21 | Conceptual procedure used to calculate the reorganization energy associated to solute **A** in the SET processes represented on the top of the figure. The same procedure has to be followed for solute **B** to obtain $\lambda_{B;}$ in such a way that the overall reorganization energy in equation 1.1 is: $\lambda = \lambda_A + \lambda_B$.

References

1. Pope, M. T. *Heteropoly and isopoly oxometalates*, Springer–Verlag, New York, 1983.
2. Nymann, M. *Dalton Trans.* **2011**, *40*, 8049–8058.
3. Monakhov, K. Y.; Bensch, W.; Kögerler, P. *Chem. Soc. Rev.* **2015**, *44*, 8443–8483.
4. Müller, A.; Gouzerh, P. *Chem. Soc. Rev.* **2012**, *41*, 7431–7463
5. Song, Y.–F.; Tsunashima, R. *Chem. Soc. Rev.* **2012**, *41*, 7384–7402.
6. Wang, Y.; Weinstock, I. A. *Chem. Rev.* **2012**, *41*, 7479–7496.
7. Wang, S.–S.; Yang, G.–Y. *Chem. Rev.* **2015**, *115*, 4893–4962.
8. Proust, A.; Matt, B.; Villanneau, R.; Guillemot, G.; Gouzerh, P.; Izzet, G. *Chem. Soc. Rev.* **2012**, *41*, 7605–7622.
9. See for instance: Rinfray, C.; Renaudineau, S.; Izzet, G.; Anna Proust, A. *Chem. Commun.* **2014**, *50*, 8575–8577.
10. a) Izzet, G.; Abécassis, B.; Brouri, D.; Piot, M.; Matt, B.; Serapian, S. A.; Bo, C.; Proust, A. *J. Am. Chem. Soc.* **2016**, *138*, 5093–5099; b) Nikoloudakis, E.; Karikis, K.; Laurans, M.; Kokotidou, C.; Solé–Daura, A.; Carbó, J. J.; Charisiadis, A.; Charalambidis, G.; Izzet, G.; Mitraki, A.; Douvas, A. M.; Poblet, J. M.; Proust, A.; Coutsolelos, A. G. *Dalton Trans.* **2018**, *47*, 6304–6313; c) Zhang, B.; Pradeep, C. P.; Cronin, L.; Tianbo Liu, T. *Chem. Commun.* **2015**, *51*, 8630–8633.
11. Matt, B.; Fize, J.; Moussa, J.; Amouri, H.; Pereira, A.; Artero, V.; Izzet, G.; Proust, A. *Energy Environ. Sci.* **2013**, *6*, 1504–1508.
12. For some examples, see: a) Bijelic, A.; Aureliano, M.; Rompel, A. *Angew. Chem. Int. Ed.* **2018**, *58*, 2980–2999; b) Lei, F.; Hanqin, G.; Mei, Y.; Shouzhu, L.; Xinyu, L.; Zhifei, D.; Shaoqin, L. *Small* **2015**, *11*, 2938–2945; c) She, S.; Bian. S.; Huo, R.; Chen, K.; Huang, Z.; Zhang, J.; Hao, J.; Wei, Y. *Sci. Rep.* **2016**, *6*, doi: 10.1038/srep33529.
13. Gouzerh, P; Che, M. *L'actualité Chimique* **2006**, *298*, 9–22.
14. Hill, C. L. *Chem. Rev.* **1998**, 98, 1–2.
15. Kondinski, A.; Parac–Vogt, T. N. *Front. Chem.* **2018**, *6 (346)*: 1–7.
16. Scheele, C. W. Hermbstädt D.S.F., Sämtliche Physische und Chemische Werke, ed. Martin Sändig, Niederwalluf/Wiesbaden, **1971**, *1*, 185 (reprint: original **1793**).
17. Berzelius, J. J. *Pogg. Ann.* 1826, *6*, 369–380.
18. Galissard de Marignac J.–C. *Ann. Chim. & Phys.* **1864**, *3*, 1.
19. Miolati, A.; Pizzighelli, P. *J. Prakt. Chem.* **1908**, *77*, 417–456.
20. Pauling, L. C. *J. Am. Chem. Soc.* **1929**, 51, 2868–2880
21. Keggin, J. F. *Nature* **1933**, *131*, 908–909.
22. a) Anderson, J. S. Nature 1937, 140, 850–851; b) Wells, A. F. Lond. Edinb. Dubl. Phil. Mag. **1940**, 30, 103–134; c) Evans, H. T. Jr. *J. Am. Chem. Soc.* **1948**, *70*, 1291–1292; d) Dawson, B. *Acta Crystallogr.* **1953**, *6*, 113–126.
23. Pope, M. T.; Müller, A. *Angew. Chem. Int. Ed.* **1991**, *30*, 34–48.
24. Long, D.–L.; Tsunashima, R.; Cronin, L. *Angew. Chem. Int. Ed.* **2010**, *49*, 1736–1758.
25. Long, D.–L.; Burkholder, E.; Cronin, L. *Chem. Soc. Rev.* **2007**, *36*, 105–121.
26. Cronin, L.; Müller, A. *Chem. Soc. Rev.* **2012**, *41*, 7333–7334.

27. Omwoma, S.; Chen, W.; Tsunashima, R.; Song, Y.–F. *Coord. Chem Rev.* **2014**, *258*, 58–71.
28. Rhule, J. T.; Hill, C. L.; Judd, D. A. *Chem. Rev.* **1998**, *98*, 327–357.
29. Bijelic. A.; Rompel, A. *Coord. Chem. Rev.* **2015**, *299*, 22–38.
30. Ji, Y.; Huang, L.; Hu, J.; Streb, C.; Song, Y.–F. *Energy Environ. Sci.* **2015**, *8*, 776–789.
31. Yamase, T. *Chem. Rev.* **1998**, *98*, 307–325.
32. Streb, C. *Dalton Trans.* **2012**, *41*, 1651–1659.
33. Wang, X.; Wang, J.; Tsunashima, R.; Pan, K.; Cao, B.; Song Y.–F. *Ind. Eng. Chem. Res.* **2013**, *52*, 2598–2603.
34. Proust, A.; Thouvenot, R.; Gouzerth, P. *Chem. Commun.* **2008**, 1837–1852.
35. Dolbecq, A.; Dumas, E.; Mayer, C. R.; Mialane, P. *Chem. Rev.* **2010**, *110*, 6009–6048.
36. Bijelic, A.; Aureliano, M.; Rompel, A. *Chem. Commun.* **2018**, *54*, 1153–1169.
37. Arefian, M.; Mirzaei, M.; Estiagh–Hosseni, H.; Frontera, A. *Dalton Trans.* **2017**, *46*, 6812–6829.
38. Gao, P. Wu, Y.; Wu, L. *Soft Matter* **2016**, *12*, 8464–8479.
39. Van Rompuy, L. S.; Parac–Vogt, T. N. *Curr. Opin. Biotechnol.* **2019**, *58*, 92–99.
40. Wu, L.; Liang, J. in *Supramolecular Chemistry of Biomimetic Systems*, Springer Nature Singapore Pte Ltd 2012, pp 311–352.
41. Prudent, R.; Moucadel, V.; Laudet, B.; Barette, C.; Lafanechère, L.; Hasenknopf, B.; Li, J.; Bareyt, S.; Lacôte, E.; Thorimbert, S.; Malacria, M.; Gouzerh, P.; Cochet, C. *Chem. Biol.* **2008**, *15*, 683–692.
42. a) Nakae, T.; Ishii, J.; Tokunaga, M. *J. Biol. Chem.* **1979**, *254*, 1457–1461; b) Boyd, D. W.; Kustin, K.; Niwa, M. *BBA–Protein Struct. M.* **1985**, *827*, 472–475.
43. a) van Huijsduijnen, R. H.; Sauer, W. H. B.; Bombrun, A.; Swinnen, D. *J. Med. Chem.* **2004**, *47*, 4142–4146; b) Messmore, J. M.; Raines, R. T. *ArchBiochem. Biophys.* **2000**, *381*, 25–30.
44. Yamase, T. *J. Mater. Chem.* **2005**, *15*, 4773–4782.
45. Fischer, J.; Ricard, L.; Weiss, R. *J. Am. Chem. Soc.* **1976**, *98*, 3050–3052.
46. Wang, S.; Sun, W.; Hu, Q.; Yan, H.; Zeng, Y. *Bioorg. Med. Chem. Lett.* **2017**, *27*, 2357–2359.
47. a) Yang, P.; Lin, Z.; Bassil, B. S.; Alfaro–Espinoza, G.; Ullrich, M. S.; Li, M. X.; Silvestru, C.; Kortz, U. *Inorg. Chem.* **2016**, *55*, 3718–3720; b) Yang, P.; Bassil, B. S.; Lin, Z.; Haider, A.; Alfaro–Espinoza, G.; Ullrich, M. S.; Silvestru, C.; Kortz, U. *Chem. Eur. J.* **2015**, *21*, 15600–15606.
48. See for instance: a) Li, J. F.; Chen, Z. J.; Zhou, M. C.; Jing, J. B.; Li, W.; Wang, Y.; Wu, L. X.; Wang, L. Y.; Wang, Y. Q.; Lee, M. *Angew. Chem. Int. Ed.* **2016**, *55*, 2592–2595; b) Daima, H. K.; Selvakannan, P. R.; Kandjani, A. E.; Shukla, R.; Bhargava, S. K.; Bansal, V. *Nanoscale* **2014**, *6*, 758–765.
49. Sakamoto, A.; Unoura, K.; Nabika, H. *J. Phys. Chem. C* **2018**, *122*, 1404–1411.
50. Inoue, M.; Suzuki, T.; Fujita, Y.; Oda, M.; Matsumoto, N.; Yamase, T. *J. Inorg. Biochem.* **2006**, *100*, 1225–1233.
51. a) Pu, F.; Wang, E.; Jiang, H.; Ren, J. *Mol. BioSyst.* **2013**, *9*, 113–120; b) Qiang, W.; Ju, W.; Ling, Z.; An, H.; Jinsong, R. *Angew. Chem. Int. Ed.* **2005**, *44*, 4048–4052.
52. a) El Moll, H.; Zhu, W.; Oldfield, E.; Rodriguez–Albelo, L. M.; Mialane, P.; Marrot, J.; Vila, N.; Mbomekalle, I. M.; Riviere, E.; Duboc, C.; Dolbecq, A. *Inorg. Chem.* **2012**, *51*, 7921–7931; b) Shah, H. S.; Al–Oweini, R.; Haider, A.; Kortz, U.; Iqbal, J. *Toxicol. Rep.* **2014**, *1*, 341–352; c) Qi, W.; Zhang, B.; Qi, Y.; Guo, S.; Tian, R.; Sun, J.; Zhao, M. *Molecules* **2017**, *22*, 1535.

53. a) Yanagie, H.; Ogata, A.; Mitsui, S.; Hisa, T.; Yamase, T.; Eriguchi, M. *Biomed. Pharmacother.* **2006**, *60*, 349–352; b) Zhang, Z. M.; Duan, X. P.; Yao, S.; Wang, Z. S.; Lin, Z. K.; Li, Y. G.; Long, L. S.; Wang, E. B.; Lin, W. B. *Chem. Sci.* **2016**, *7*, 4220–4229.
54. a) Li, H.; Jia, Y.; Wang, A. H.; Cui, W.; Ma, H. C.; Feng, X. Y.; Li, J. B. *Chem. Eur. J.* **2014**, *20*, 499–504; b) Fu, L.; Gao, H. Q.; Yan, M.; Li, S. Z.; Li, X. Y.; Dai, Z. F.; Liu, S. Q. *Small* **2015**, *11*, 2938–2945; c) Sun, T. D.; Cui, W.; Yan, M.; Qin, G.; Guo, W.; Gu, H. X.; Liu, S. Q.; Wu, Q. *Adv. Mater.* **2016**, *28*, 7397–7404.
55. Yamin, G.; Ono, K.; Inayathullah, M.; Teplow, D. *Curr. Pharm. Design* **2008**, *14*, 3231–3246.
56. a) Geng, J.; Li, M.; Ren, J. S.; Wang, E. B.; Qu, X. *Angew. Chem. Int. Ed.* **2011**, *50*, 4184–4188; b) Gao, N.; Sun, H. J.; Dong, K.; Ren, J. S.; Duan, T. C.; Xu, C.; Qu, X. *Nat. Commun.* **2014**, *5*, doi: 10.1038/ncomms4422.
57. a) Zhou, Y.; Zheng, L.; Han, F.; Zhang, G.; Ma, Y.; Yao, J.; Keita, B.; de Oliveira, P.; Nadjo, L. *Colloids Surf. A* **2011**, *375*, 97–101; b) Chen, Q.; Yang, L.; Zheng, C.; Zheng, W.; Zhang, J.; Zhouband, Y.; Liu, J. *Nanoscale* **2014**, *6*, 6886–6897.
58. a) Gao, N.; Dong, K.; Zhao, A.; Sun, H.; Wang, Y.; Ren, J.; Qu, X. *Nano Res.* **2016**, *9*, 1079–1090; b) Li, M.; Guan, Y.; Zhao, a.; Ren, J.; Qu, X. *Theranostics* **2017**, *7*, 2996–3006; c) Li, M.; Xu, C.; Wu, L.; Ren, J. S.; Wang, E. B.; Qu, X. *Small* **2013**, *9*, 3455–3461.
59. Gao, N.; Du, Z.; Guan, Y.; Dong, K.; Ren, J.; Qu, X. *J. Am. Chem. Soc.* **2019**, *141*, 6915–6921.
60. Hauptman, H. A. In: *Electron Crystallography*; Dorset, D. L.; Hovmöller, S.; Zou, X. Eds.; Springer, Dordrecht, 1997; p. 131.
61. a) Thygesen, J.; Weinstein, S.; Francesci, F.; Yonath, A. *Structure* **1996**, *4*, 513–518; b) Schluenzen, F.; Tocilj, A.; Zarivach, R.; Harms, J.; Gluehmann, M.; Janell, D.; Bashan, A.; Bartels, H.; Agmon, I.; Franceschi, F.; Yonath; A. *Cell* **2000**, *102*, 615–623; c) Pioletti, M.; Schlünzen, F.; Harms, J.; Zarivach, R.; Glühmann, M.; Avila, H.; Bashan, A.; Bartels, H.; Auerbach, T.; Jacobi, C.; Hartsch, T.; Yonath, A.; Franceschic, F.; *EMBO J.* **2001**, *20*, 1829–1839; d) Tocilj, A.; Schlünzen, F.; Janell, D.; Glühmann, M.; Hansen, H. A. S.; Harms, J.; Bashan, A.; Bartels, H.; Agmon, I.; Franceschi, F.; Yonath, A. *Proc. Natl. Acad. Sci.* **1999**, *96*, 14252–14257.
62. a) Sap, A.; De Zitter, E.; Van Meervelt, L.; Parac–Vogt, T. N. *Chem. Eur. J.* **2015**, *21*, 11692–11695; b) Vandebroek, L.; De Zitter, E.; Ly, H. G. T.; Conić, D.; Mihaylov, T.; Sap, A.; Proost, P.; Pierloot, K.; Van Meervelt, L.; Parac–Vogt, T. N. *Chem. Eur. J.* **2018**, *24*, 10099–10108; c) Vandebroek, L.; Mampaey, Y.; Antonyuk, S.; Van Meervelt, L.; Parac–Vogt, T. N. *Eur. J. Inorg. Chem.* **2019**, *3*, 506–511.
63. Vandebroek, L.; Van Meervelt, L.; Parac–Vogt, T. N. *Acta Crystallogr. C* **2018**, *74*, 1348–1354.
64. a) Bijelic, A.; Rompel, A. *ChemTexts* **2018**, *4:10*, 1–27; b) Bijelic, A.; Rompel, A. *Acc. Chem. Res.* **2017**, *50*, 1441–1448.
65. a) Mauracher, S. G.; Molitor, C.; Al–Oweini, R.; Kortz, U.; Rompel, A. *Acta Crystallogr., Sect. D: Biol. Crystallogr.* **2014**, *70*, 2301–2315; b) Molitor, C.; Bijelic, A.; Rompel, A. *Chem. Commun.* **2016**, *52*, 12286–12289.
66. Bijelic, A.; Molitor, C.; Mauracher, S. G.; Al–Oweini, R.; Kortz, U.; Rompel, A. *ChemBioChem* **2015**, *16*, 233–241.
67. Breibeck, J.; Bijelic, A.; Rompel, A. *Chem. Commun.* **2019**, DOI: 10.1039/c9cc05818d.

68. a) Kowalewski, B.; Poppe, J.; Demmer, U.; Warkentin, E.; Dierks, T.; Ermler, U.; Schneider, K. *J. Am. Chem. Soc.* **2012**, *134*, 9768–9774; b) Schemberg, J.; Schneider, K.; Demmer, U.; Warkentin, E.; Muller, A.; Ermler, U. *Angew. Chem. Int. Ed.* **2007**, *46*, 2408–2413.
69. Ho, P. H.; Stroobants, K.; Parac–Vogt. T. N. *Inorg. Chem.* **2011**, *50*, 12025–12033.
70. Absillis G.; Parac–Vogt, T. N. *Inorg. Chem.* **2012**, *51*, 9902–9910.
71. See for instance: a) Giang T. L. H.; Absillis G.; Parac–Vogt, T. N. *Dalton Trans.* **2013**, *42*, 10929–10938; b) Sap, A.; Absillis, G.; Parac–Vogt, T. N. *Dalton Trans.* **2015**, *44*, 1539–1548; c) Ly, H. G. T.; Mihaylov, T.; Absillis, G.; Pierloot, K.; Parac–Vogt, T. N. *Inorg. Chem.* **2015**, *54*, 11477–11492.
72. For some examples, see: a) Stroobants, K.; Moelants, E.; Ly, H. G. T.; Proost, P.; Bartik K.; Parac–Vogt, T. N. *Chem. Eur. J.* **2013**, *19*, 2848–2858; b) Stroobants, K.; Absillis, G.; Moelants, E.; Proost P.; Parac–Vogt, T. N. *Chem. Eur. J.* **2014**, *20*, 3894–3897; c) Stroobants, K.; Goovaerts, V.; Absillis, G.; Bruylants, G.; Moelants, E.; Proost P.; Parac–Vogt, T. N. *Chem. Eur. J.* **2014**, *20*, 9567–9577; d) Ly, H. G. T.; Absillis, G.; Janssens, R.; Proost, P.; Parac–Vogt, T. N. *Angew. Chem. Int. Ed.* **2015**, *54*, 7391–7394; e) Sap, A.; Van Tichelen, L.; Mortier, A.; Proost, P.; Parac–Vogt, T. N. *Eur. J. Inorg. Chem.* **2016**, *32*, 5098–5105.
73. Stroobants, K.; Ho, P. H.; Moelants, E.; Proost, P.; Parac–Vogt, T. N. *J. Inorg. Biochem.* **2014**, *136*, 73–80.
74. Quanten, T.; De Mayaer, T.; Shestakova, P.; Parac–Vogt, T. N. *Front. Chem.* **2018**, *6*:372, DOI: 10.3389/fchem.2018.00372.
75. Ly, H. G. T.; Mihaylov, T. T.; Proost, P.; Pierloot, K.; Harvey, J. N.; Parac–Vogt, T. N. *Chem. Eur. J.* **2019**, DOI:10.1002/chem.201902675.
76. Jayasinghe–Arachchige, V. M.; Hu, Q.; Sharma, G.; Paul, T. J.; Lundberg, M.; Quinonero, D.; Parac–Vogt, T. N.; Prabhakar, R. *J. Comp. Chem.* **2019**, *40*, 51–61.
77. a) Cartuyvels, E.; Absillis, G.; Parac–Vogt, T. N. *Chem. Commun.* **2008**, 85–87; b) Absillis, G.; Cartuyvels, E.; Van Deun, R.; Parac–Vogt, T. N. *J. Am. Chem. Soc.* **2008**, *130*, 17400–17408; c) Steens, N.; Ramadan, A. M.; Absillis, G.; Parac–Vogt, T. N. *Dalton Trans.* **2010**, *39*, 585–592.
78. See for instance: a) Vanhaecht, S.; Absillis, G.; Parac–Vogt, T. N. *Dalton Trans.* **2012**, *41*, 10028–10034; b) Luong, T. K. N.; Shestakova, P.; Mihaylov, T. T.; Absillis, G.; Pierloot, K.; Parac–Vogt, T. N. *Chem. Eur. J.* **2015**, *21*, 4428 – 4439; c) Luong, T. K. N.; Absillis, G.; Shestakovaa, P.; Parac–Vogt, T. N. *Dalton Trans.* **2015**, *44*, 15690–15696; d) Luong, T. K. N.; Mihaylov, T. T.; Absillis, G.; Shestakova, P.; Pierloot, K.; Parac–Vogt, T. N. *Inorg. Chem.* **2016**, *55*, 9898–9911.
79. Luong, T. K. N.; Govaerts, I.; Robben, J.; Shestakova, P.; Parac–Vogt, T. N. *Chem. Commun.* **2017**, *53*, 617–620.
80. Luong, T. K. N.; Shestakova, P.; Absillis, G.; Parac–Vogt, T. N. *Inorg. Chem.* **2016**, *55*, 4864–4873.
81. Van Rompuy, L. S.; Parac–Vogt, T. N. *Chem. Commun.* **2017**, *53*, 10600–10603.
82. De León–Rodríguez, L. M.; Martins, A. F.; Pinho, M. C.; Rofsky, N. M.; Sherry, A. D. *J. Magn. Reson. Imaging.* **2015**, *42*, 545–565.
83. a) Feng, J. H.; Li, X. J.; Pei, F. K.; Sun, G. Y.; Zhang, X.; Liu, M. L. *Magn. Reson. Imaging* **2002**, *20*, 407–412; b) Li, Z. F.; Li, W. S.; Li, X. J.; Pei, F. K.; Li, Y. X.; Lei, H. *Magn. Reson. Imaging* **2007**, *25*, 412–417.
84. Caravan, P. *Chem. Soc. Rev.* **2006**, *5*, 512–523.
85. Zhang, S. M.; Zheng, Y. M.; Yin, S. Y.; Sun, J. Z.; Li, B.; Wu, L. X. *Chem. Eur. J.* **2017**, *23*, 2802–2810.

86. For some examples, see: a) Ettedgui, J.; Diskin–Posner, Y.; Weiner, L.; Neumann, R. *J. Am. Chem. Soc.* **2011**, *133*, 188–190; b) Xie, S.–L.; Liu, J.; Dong, L.–Z.; Li, S.–L.; Lan, Y.–Q.; Su, Z. M. *Chem. Sci.* **2019**, *10*, 185–190.
87. For some examples, see: a) Zhang, G.–H.; Yang, W.–B.; Wua, W.–M.; Wua, X.–Y.; Zhang, L.; Kuang, X. F. *J. Catalysis* **2019**, *369*, 54–59; b) Paille, G.; Boulmier, A.; Bensaid, A.; Ha–Thi, M.–H.; Tran, T.–T.; Pino, T.; Marrot, J.; Rivière, E.; Hendon, C. H.; Oms, O.; Gomez–Mingot, M.; Fontecave, M.; Mellot–Draznieks, C.; Dolbecq, A.; Mialane, P. *Chem. Commun.* **2019**, *55*, 4166–4169; c) Matt, B.; Fize, J.; Moussa, J.; Amouri, H.; Pereira, A.; Artero, V.; Izzet, G.; Proust, A. *Energy Environ. Sci.* **2013**, *6*, 1504–1508.
88. a) Pratt, H. D. III; Anderson, T. M. *Dalton Trans.* **2013**, *42*, 15650–15655; b) Pratt, H. D. III; Hudak, N. S.; Fang, X; Anderson, T. M. *J. Power Sources* **2013**, *236*, 259–264.
89. Chen, J.–J.; Symes, M. D.; Cronin, L. *Nat. Chem.* **2018**, *10*, 1042–1047.
90. a) Wang, H.; Hamanaka, S..; Nishimoto, Y.; Irle, S.; Yokoyama, T.; Yoshikawa, H.; Awaga, K. *J. Am. Chem. Soc.* **2012**, *134*, 4918–4924; b) Nishimoto, Y.; Yokogawa, D.; Yoshikawa, H.; Awaga, K.; Irle, S. *J. Am. Chem. Soc.* **2014**, *136*, 9042–9052.
91. a) Chen, J.–J.; Symes, M. D.; Fan, S.–C.; Zheng, M.–S.; Miras, H. N.; Dong, Q.–F.; Cronin, L.*Adv. Mater.* **2015**, *27*, 4649–4654; b) Chen, J.–J.; Ye, J.–C.; Zhang, X.–G.; Symes, M. D.; Fan, S.–C.; Long, D.–L.; Zheng, M.–S.; Wu, D.–Y.; Cronin, L.; Dong, Q.–F. *Adv. Energy Mater.* **2017**, *7*, 1701021
92. a) Ji, Y.; Huang, L.; Hu, J.; Streb, C.; Song, Y.–F. *Energy Environ. Sci.* **2015**, *8*, 776–789; b) Kawasaki, N.; Wang, H. Nakanishi, R. Hamanaka, S. Kitaura, R. Shinohara, H. Yokoyama, T. Yoshikawa H. Awaga, K. *Angew. Chem. Int. Ed.* **2011**, *50*, 3471–3474; c) Ma, D. Liang, L. Chen, W. Liu H. Song, Y.–F. *Adv. Funct. Mater.* **2013**, *23*, 6100–6105.
93. Launay, J. P. *J. Inorg. Nucl. Chem.* **1976**, *38*, 807–816.
94. a) Jeannin, Y.; Launay, J. P.; Seid Sedjadi, M. A. *Inorg. Chem.* **1980**, *19*, 2933–2935; b) Piepgrass, K.; Pope, M. T. *J. Am. Chem. Soc.* **1987**, *109*, 1586–1587; c) Boskovic, C.; Sadek, M.; Brownlee, R. T. C.; Bond, A. M.; Wedd, A. G. *J. Chem. Soc., Dalton Trans.* **2001**, *2001*, 187–196.
95. a) Way, D. M.; Bond, A. M.; Wedd, A. G. *Inorg. Chem.* **1997**, *36*, 2826–2833; b) Wang, H.; Hamanaka, S..; Nishimoto, Y.; Irle, S.; Yokoyama, T.; Yoshikawa, H.; Awaga, K. *J. Am. Chem. Soc.* **2012**, *134*, 4918–4924; c) Nishimoto, Y.; Yokogawa, D.; Yoshikawa, H.; Awaga, K.; Irle, S. *J. Am. Chem. Soc.* **2014**, *136*, 9042–9052.
96. Weinstock, I. A.; Schreiber, R. E.; Neumann, R. *Chem. Rev.* **2018**, *118*, 2680–2717.
97. Rubinstein A.; Jiménez–Lozanao, P.; Carbó, J. J.; Poblet, J. M.; Neumann, R. *J. Am. Chem. Soc.* **2014**, *136*, 10941–10948.
98. Mizuno, N.; Yamaguchi, K.; Kamata, K.; Nakagawa, Y. Activation of Hydrogen Peroxide by Polyoxometalates In *Mechanisms in Homogeneous and Heterogeneous Epoxidation Catalysis*; Oyama, S. T.; Elsevier B.V., Amsterdam, 2008, pp. 155–176.
99. Venturello, C.; Alneri, E.; Ricci, M. *J. Org. Chem.* **1983**, *48*, 3831–3833.
100. a) Venturello, C.; D'Aloisio, R.; Bart, J. C. J.; Ricci, M. *J. Mol. Catal.* **1985**, *32*, 107–110; b) Ishii, Y.; Yamawaki, K.; Yoshida, T.; Ura, T.; Ogawa, M. *J. Org. Chem.* **1987**, *52*, 1868–1870; c) Sakaguchi, S.; Nishiyama, Y.; Ishii, Y. *J. Org. Chem.* **1996**, *61*, 5307–5311.
101. Kamata, K.; Yonehara, K.; Sumida, Y.; Yamaguchi, K.; Hikichi, S.; Mizuno, N. *Science* **2003**, *300*, 964–966.

102. Fraile, J. M. Solid Catalysts for Epoxidation with Dilute Hydrogen Peroxide In *Encyclopedia of Inorganic and Bioinorganic Chemistry*; John Wiley & Sons Inc., Chichester, 2016, pp. 1–9.
103. For some examples, see: a) Goto, Y.; Kamata, K.; Yamaguchi, K.; Uehara, K.; Hikichi, S.; Mizuno, N. *Inorg. Chem.* **2006**, *45*, 2347–2356; b) Nakagawa, Y.; Kamata, K.; Kotani, M.; Yamaguchi, K.; Mizuno, N. *Angew. Chem. Int. Ed* **2005**, *44*, 5136–5141; c) Bösing, M.; Nöh, A.; Loose, I.; Krebs, B. *J. Am. Chem. Soc.* **1998**, *120*, 7252–7259; d) Maksimchuk, N. V.; Maksimov, G. M.; Evtushok, V. Yu.; Ivanchikova, I. D.; Chesalov, Yu. A.; Maksimovskaya, R. I.; Kholdeeva, O. A.; Solé–Daura, A.; Poblet, J. M.; Carbó, J. J. *ACS Catal.* **2018**, *8*, 9722–9737; e) Maksimchuk, N. V.; Ivanchikova, I. D.; Maksimov, G. M.; Eltsov, I. V.; Evtushok, V. Y.; Kholdeeva, O. A.; Lebbie, D.; Errington, J.; Solé–Daura, A.; Poblet, J. M.; Carbó, J. J. *ACS Catal.* **2019**, *9*, 6262–6275; f) Aoto, H.; Matsui, K.; Sakai, Y.; Kuchizi, T.; Sekiya, H.; Osada, H.; Yoshida, T.; Matsunaga, S.; Nomiya, K. *J. Mol. Catal. A Chem.* **2014**, *394*, 224–231.
104. a) Taramasso, M.; Perego, G.; Notari, B. Preparation of Porous Crystalline Synthetic Material Comprised of Silicon and Titanium Oxides. *US Patent* 4 410 501, 1983; b) Perego, C.; Carati, A.; Ingallina, P.; Mantegazza, M. A.; Bellussi, G. *Appl. Catal. A: General* **2001**, 221, 63–72; c) Clerici, M. G.; Domine, M. E. In: *Liquid Phase Oxidation via Heterogeneous Catalysis: Organic Synthesis and Industrial Applications*; Clerici, M. G., Kholdeeva O. A. Eds.; Wiley: Hoboken, 2013; p. 21.
105. See for instance: Kholdeeva, O. A. *Catal. Sci. Technol.* **2014**, *4*, 1869–1889.
106. Kholdeeva, O. A. *Top. Catal.* **2006**, *40*, 229–243; b) Kholdeeva, O. A. *Eur. J. Inorg. Chem.* **2013**, *2013*, 1595–1605.
107. a) Guillemot, G.; Matricardi, E.; Chamoreau, L–M.; Thouvenot, R.; Proust, A. *ACS Catal.* **2015**, *5*, 7415–7423; b) Zhang, T.; Mazaud, L.; Chamoreau, L–M.; Paris, C.; Proust, A.; Guillemot, G. *ACS Catal.* **2018**, *8*, 2330–2342.
108. Prabhakar, R.; Morokuma, K.; Hill C. L.; Musaev, D. G. *Inorg. Chem.* **2006**, *45*, 5703–5709.
109. Kamata, K.; Hirano, T.; Kuzuya, S.; Mizuno, N. *J. Am. Chem. Soc.* **2009**, 131, 6997–7004.
110. a) Nakagawa Y.; Mizuno, N.; *Inorg. Chem.* **2007**, *46*, 1727–1736; b) Kamata, K.; Sugahara, K.; Yonehara, K.; Ishimoto R.; Mizuno, N. *Chem. Eur. J.* **2011**, *17*, 7549–7559.
111. Antonova, N.; Carbó, J. J.; Kortz, U.; Kholdeeva, O.A.; Poblet, J. M. *J. Am. Chem. Soc.* **2010**, *132*, 7488–7497.
112. Donoeva, B. G.; Trubitsina, T. A.; Antonova, N. A.; Carbó, J. J.; Poblet, J. M.; Al–Kadamany, G.; Kortz, U.; Kholdeeva, O. A. *Eur. J. Inorg. Chem.* **2010**, *2010*, 5312–5317.
113. Jiménez–Lozano, P.; Ivanchikova, I. D.; Kholdeeva, O. A.; Poblet, J. M.; Carbó, J. J. *Chem. Commun.* **2012**, *48*, 9266–9268.
114. Jiménez–Lozano, P.; Skobelev, I. Y.; Kholdeeva, O. A.; Poblet, J. M.; Carbó, J. J. *Inorg. Chem.* **2016**, *55*, 6080–6084.
115. a) Skobelev, I. Y.; Evtushok, V. Y.; Kholdeeva, O. A.; Maksimchuk, N. V.; Maksimovskaya, R. I.; Ricart, J. M.; Poblet, J. M.; Carbó, J. J. *ACS Catal.* **2017**, *7*, 8514–8523; b) Skobelev, I. Y.; Zalomaeva, O. V.; Kholdeeva, O. A.; Poblet, J. M.; Carbó, J. J. *Chem. Eur. J.* **2015**, *21*, 14496–14506.
116. a) Tantanak, D.; Vincent, M. A.; Hillier, I. H. *Chem. Commun.* **1998**, *1998*, 1031–1032; b) Karlsen, E.; Schöffel, K. *Catal. Today* **1996**, *32*, 107–114.
117. Taketa, H.; Katsuki, S.; Eguchi, K.; Seiyama, T.; Yamazoe, N. *J. Phys. Chem.* **1986**, *90*, 2959–2962.
118. Eguchi, K.; Seiyama, T.; Yamazoe, N.; Katsuki, S.; Taketa, H. *J. Catal.* **1988**, *111*, 336–344.
119. Bonifacio, V.; Huzinaga, S. *J. Chem. Phys.* **1974**, *60*, 2779–2786.

120. a) Scholz, G.; Luck, R.; Stosser, R.; Lunk H. J.; Ritschl, F. *J. Chem. Soc., Faraday Trans.* **1991**, *87*, 717–772; b) Scholz, G.; Stosser, R.; Ritschl, F.; Luck, R. *Z. Chem* **1990**, *30*, 183–184.
121. Ritschl F.; Fricke, R. *J. Chem. Soc., Faraday Trans. 1* **1987**, *83*, 1041–1053.
122. a) Wang, S. H.; Jansen, S. A. *Chem. Mater.* **1994**, *6*, 2130–2137; b) Wang, S. H.; Jansen, S. A.; Singh, D. J. *J. Catal.* **1995**, *154*,137–150; c) Jansen, S. A.; Wang, S. H.; Eddowes, A. D. *Supramol. Sci.* **1997**, *4*, 51–58; d) Calhorda, M. J. *J. Organomet. Chem.* **1994**, *475*, 149–155.
123. a) Awad, M. K.; Anderson, A. B. *J. Am. Chem. Soc.* **1990**, *112*,1603–1606; b) Jen, S. F.; Anderson, A. B.; Hill, C. L. *J. Phys. Chem.* **1992**, *96*,5658–5662.
124. Rohmer, M. M.; Ernenwein, R.; Ulmschneider, M.; Wiest, R.; Bénard, M. *Int. J. Quantum Chem.* **1991**, *40*, 723–744.
125. Maestre, J. M.; Sarasa, J. P.; Bo, C.; Poblet, J. M. *Inorg. Chem.* **1998**, *37*, 3071–3077.
126. Parr, R. G.; Yang, W. *Density Functional Theory of Atoms and Molecules*; Oxford University Press: New York, 1989.
127. Tomasi, J.; Mennucci, B.; Cammi, R. *Chem. Rev.* **2005**, *105*, 2999–3094.
128. Poblet, J. M.; López, X.; Bo, C. *Chem. Soc. Rev.* **2003**, *32*, 297–308.
129. López, X.; Miró, P.; Carbó, J. J.; Rodríguez–Fortea, A.; Bo, C.; Poblet, J. M. *Theor. Chem. Acc.* **2011**, 128, 393–404.
130. López, X.; Carbó, J. J.; Bo, C.; Poblet, J. M. *Chem. Soc. Rev.* **2012**, *41*, 7537–7571.
131. Bridgeman, A. J.; Cavigliasso, G. *Inorg. Chem.* **2002**, *41*, 1761–1770.
132. Li, J. *J. Cluster Sci.* **2002**, *13*, 137–163.
133. For some examples: a) López, X.; Maestre, J. M.; Bo C.; Poblet, J. M. *J. Am. Chem. Soc.* **2001**, *123*, 9571–9576; b) López, X.; Bo, C.; Poblet, J. M. *J. Am. Chem. Soc.* **2002**, *124*, 12574–12582; c) López, X.; Fernández, J. A.; Poblet, J. M. *Dalton Trans.* **2006**, 1162–1167; d) Guan, W.; Yan, L. K.; Su, Z. M.; Liu, S. X.; Zhang, M.; Wang, X. H. *Inorg. Chem.* **2005**, *44*, 100–107.
134. Fernández, J. A.; López, X.; Bo, C.; de Graaf, C.; Baerends, E. J.; Poblet, J. M. *J. Am. Chem. Soc.* **2007**, *129*, 12244–12253.
135. For some examples: a) Dolbecq, A.; Guirauden, A.; Fourmigue, M.; Boubekeur, K.; Batail, P.; Rohmer, M. M.; Bénard, M.; Coulon, C.; Salle, M.; Blanchard, P. *J. Chem. Soc., Dalton Trans.* **1999**, 1241–1248; b) Fernández, J. A.; López, X.; Poblet, J. M. *J. Mol. Catal. A: Chem.* **2007**, *262*, 236–242; c) Bardin, B. B.; Davis, R. J.; Neurock, M. *J. Phys. Chem. B* **2000**, *104*, 3556–3562.
136. Yan, Y.; López, X.; Carbó, J. J.; Sniatynsky, R.; Duncan, D. C.; Poblet, J. M. *J. Am. Chem. Soc.* **2008**, *130*, 8223–8233.
137. See for instance: a) Busche, C.; Vilà–Nadal, L.; Yan, J.; Miras, H. N.; Long, D.–L.; Georgiev, V. P.; Asenov, A.; Pedersen, R. H.; Gadegaard, N.; Mirza, M. M.; Paul, D. J.; Poblet, J. M.; Cronin, L. *Nature* **2014**, *515*, 545–549; b) Zhang, T.; Solé–Daura, A.; Hostachy, S.; Blanchard, S.; Paris, C.; Li, Y.; Carbó, J. J.; Poblet, J. M.; Proust, A.; Guillemot, G. *J. Am. Chem. Soc.* **2018**, *140*, 14903–14914; c) Fujimoto, S.; Cameron, J. M.; Wei, R.–J.; Kastner, K.; Robinson, D.; Sans, V.; Newton, G. N.; Oshio, H. *Inorg. Chem.* **2017**, *56*, 12169–12177.
138. a) Notario–Estévez, A.; Kozłowski, P.; Linnenberg, O.; de Graaf, C.; López, X.; Monakhov, K. Y. *Phys. Chem. Chem. Phys.* **2018**, 20, 17847–17858; b) Solé–Daura, A.; Notario–Estévez, A.; Carbó, J. J.; Poblet, J. M.; De Graaf, C.; Monakhov, K. Y.; López, X. *Inorg. Chem.* **2019**, *58*, 3881–3894.
139. Perdew, J. P.; Burke, K.; Ernzerhof, M. *Phys. Rev. Lett.* 1996, 77, 3865–6388.

140. a) Perdew, J. P.*Phys. Rev. B: Condens. Matter Mater. Phys.***1986**, *33*, 8822–8824; b) Perdew, J. P. *Phys. Rev. B: Condens. Matter Mater. Phys.* **1986**, *34*, 7406; c) Becke, A. D. *Phys. Rev. A: At., Mol., Opt. Phys.* **1988**, *38*, 3098–3100.
141. a) Macht, J.; Janik, M. J.; Neurock, M.; Iglesia, E. *Angew. Chem., Int. Ed.* **2007**, *46*, 7864–7868; b) Macht, J.; Carr, R. T.; Iglesia, E. *J. Catal.* **2009**, *264*, 54–66; c) Macht, J.; Janik, M. J.; Neurock, M.; Iglesia, E. *J. Am. Chem. Soc.* **2008**, *130*, 10369–10379; d) Janik, M. J.; Macht, J.; Iglesia, E.; Neurock, M. *J. Phys. Chem. C* **2009**, *113*, 1872–1885.
142. a) Lee, C.; Yang, W.; Parr, R. G. *Phys. Rev. B: Condens. Matter Mater. Phys.* **1988**, *37*, 785–789; b) Becke, A. D. *J. Chem. Phys.* **1993**, *98*, 5648–5652; c) Stephens, P. J.; Devlin, F. J.; Chabalowski, C. F.; Frisch, M. J. *J. Phys. Chem.* **1994**, *98*, 11623–11627.
143. Zhao, Y.; Truhlar, D. G. *Theor. Chem. Acc.* **2006**, *120*, 215–241.
144. a) Efremenko, I.; Neumann, R. *J. Am. Chem. Soc.* **2012**, *134*, 20669–20680; b) Sarma, B. B.; Efremenko, I.; Neumann, R. *J. Am. Chem. Soc.* **2015**, *137*, 5916–5922.
145. a) Kuznetsov, A. E.; Geletii, Y. V.; Hill, C. L.; Morokuma, K.; Musaev, D. G. *J. Am. Chem. Soc.* **2009**, *131*, 6844–6854; b) Piccinin, S.; Fabris, S. *Phys. Chem. Chem. Phys.* **2011**, *13*, 7666–7674; c) Soriano–López, J.; Musaev, D. G.; Hill, C. L.; Galán–Mascarós, J. R.; Carbó, J. J.; Poblet, J. M. *J. Catal.* **2017**, *350*, 56–63.
146. Khenkin, A. M.; Efremenko, I.; Weiner, L.; Martin, J. K. L.; Neumann, R. *Chem. Eur. J.* **2010**, *16*, 1356–1364.
147. a) Aparicio–Anglès, X.; Miró, P.; Clotet, A.; Bo, C.; Poblet, J. M. *Chem. Sci.* **2012**, *3*, 2020–2027; b) Grinenval, E.; Rozanska, X.; Baudouin, A.; Berrier, E.; Delbecq, F.; Sautet, P.; Basset, J. M.; Lefebvre, F. *J. Phys. Chem. C* **2010**, *114*, 19024–19034; c) Lang, Z.; Aparicio–Anglès, X.; Weinstock, I.; Clotet, A.; Poblet, J. M. *Inorg. Chem.* **2017**, *56*, 3961–3969; d) Linnenberg, O.; Moors, M.; Notario–Estévez, A.; López, X.; de Graaf, C.; Peter, S.; Baeumer, C.; Waser, R.; Monakhov, K. Y. *J. Am. Chem. Soc.* **2018**, *140*, 16635–16640.
148. Andersson, K.; Malmqvist, P.–A.; Roos, B. O. J. *Chem. Phys.* **1992**, *96*, 1218–1226.
149. Miralles, J.; Castell, O.; Caballol, R.; Malrieu, J.–P. *Chem. Phys.* **1993**, *172*, 33–43.
150. a) Borrás–Almenar, J. J.; Clemente–Juan, J. M.; Coronado, E.; Tsukerblat, B. S.; *Chem. Phys.* **1995**, *195*, 1–15; b) Suaud, N.; Gaita–Ariño, A.; Clemente–Juan, J. M.; Sánchez–Marín, J.; Coronado, E. *J. Am. Chem. Soc.* **2002**, *124*, 15134–15140.
151. a) de Graaf, C.; Caballol, R.; Romo, S.; Poblet, J. M. *Theor. Chem. Acc.* **2009**, *123*, 3–10; b) Suaud, N.; López, X.; Ben Amor, N.; Bandeira, N. A. G.; de Graaf, C.; Poblet, J. M. *J. Chem. Theory Comput.* **2015**, *11*, 550–559;
152. López, X.; de Graaf, C.; Maestre, J. M.; Bénard, M.; Rohmer, M.–M.; Bo, C.; Poblet, J. M. *J. Chem. Theory Comput.* **2005**, *1*, 856–861.
153. a) McCammon, J. A.; Gelin, B. R.; Karplus, M. *Nature* **1977**, *267*, 585–590; b) Hospital, A.; Goñi. J. R.; Orozco, M.; Gelpí, J. L. *Adv. Appl. Bioinform. Chem.* **2015**, *8*, 37–47.
154. van Duin, A. C. T.; Dasgupta, S.; Lorant, F.; Goddard, W. A. *J. Phys. Chem. A* **2001**, *105*, 9396–9409.
155. a) Warshel, A.; Levitt, M. *J. Mol. Biol.* **1976**; *103*, 227–249; b)Field, J. M.; Bash, P. A.; Karplus, M. *J. Comput. Chem.* **1990**, *11*, 700–7333.
156. Tsujimichi, K.; Kubo, M.; Vetrivel, R.; Miyamoto, A. *J. Catal.* **1995**, *157*, 569–575.
157. López, X.; Nieto–Draghi, C.; Bo, C.; Ávalos, J. B.; Poblet, J. M. *J. Phys. Chem. A* **2005**, *109*, 1216–1222.

158. a) Menke, C.; Diemann, E.; Müller, A. *J. Mol. Struct.* **1997**, *437*, 35–47; b) Torok, B.; Torok, M.; Rozsa–Tarjani, M.; Palinko, I.; Horvath, L. I.; Kiricsi, I.; Molnar, A. *Inorg. Chim. Acta* **2000**, *298*, 77–83; c) Brodbeck, R.; Tonsing, T.; Andrae, D.; Volkmer, D. *J. Phys. Chem. B* **2008**, *112*, 5153–5162; d) Courcot, B.; Bridgeman, A. J. *J. Comput. Chem.* **2011**, *32*, 3143–3153.
159. Leroy, F.; Miró, P.; Poblet, J. M.; Bo, C.; Bonet–Ávalos, J. *J. Phys. Chem. B* **2008**, *112*, 8591–8599.
160. a) Müller, A.; Sousa, F. L.; Merca, A.; Bogge, H.; Miró, P.; Fernández, J. A.; Poblet, J. M.; Bo, C. *Angew. Chem., Int. Ed.* **2009**, *48*, 5934–5937; b) Miró, P.; Poblet, J. M.; Bonet–Ávalos, J.; Bo, C. *Can. J. Chem.* **2009**, *87*, 1296–1301.
161. Volkmer, D.; Bredenkotter, B.; Tellenbroker, J.; Kögerler, P.; Kurth, D. G.; Lehmann, P.; Schnablegger, H.; Schwahn, D.; Piepenbrink, M.; Krebs, B. *J. Am. Chem. Soc.* **2002**, *124*, 10489–10496.
162. a) Garcia–Ratés, M.; Miró, P.; Müller, A.; Bo, C.; Ávalos, J. B. *J. Phys. Chem. C* **2014**, *118*, 5545–5555; b) Watfa, N.; Melgar, D.; Haouas, M.; Taulelle, F.; Hijazi, A.;Naoufal, D.; Ávalos, J. B.; Floquet, S.; Bo, C.; Cadot, E. *J. Am. Chem. Soc.* **2015**, *137*, 5845–5851.
163. a) Chaumont, A.; Wipff, G. *Phys. Chem. Chem. Phys.* **2008**, *10*, 6940–6953; b) Chaumont, A.; Wipff, G. *J. Phys. Chem. C* **2009**, *113*, 18233–18243; c) Chaumont, A.; Wipff, G. *C. R. Chim.* **2012**, *15*, 107–117; d) Chaumont, A.; Wipff, G. *Eur. J. Inorg. Chem.* **2013**, *2013*, 1835–1853.
164. a) Mei, Y.; Huang, W.; Yang, Z.; Wang, J.; Yang, X. *Fluid Phase Equilib.* **2016**, *425*, 31–39; b) Nikoloudakis, E.; Karikis, K.; Laurans, M.; Kokotidou, C.; Solé–Daura, A.; Carbó, J. J.; Charisiadis, A.; Charalambidis, G.; Izzet, G.;Mitraki, A.; Douvas, A. M.; Poblet, J. M.; Proust, A.; Coutsolelos, A. G. *Dalton Trans.* **2018**, *47*, 6304–6313.
165. a) Serapian, S. A.; Bo, C. *J. Phys. Chem. B* **2016**, *120*, 12959–12971; b) Linnenberg, O.; Moors, M.; Solé–Daura, A.; López, X.; Bäumer, C.; Kentzinger, E.; Pyckhout–Hintzen, W.; Monakhov, K. Y. *J. Phys. Chem. C* **2017**, *121*, 10419–10429; c) Solé–Daura, A.; Notario–Estévez, A.; Carbó, J. J.; Poblet, J. M.; De Graaf, C.; Monakhov, K. Y.; López, X. *Inorg. Chem.* **2019**, *58*, 3881–3894.
166. Schreiber, R. E.; Houben, L.; Wolf, S. G.; Leitus, G.; Lang, Z.–L.; Carbó, J. J.; Poblet, J. M.; Neumann, R. *Nat. Chem.* **2017**, *9*, 369–373.
167. a) Vilà–Nadal, L.; Rodríguez–Fortea, A.; Poblet, J. M. *Inorg. Chem.* **2008**, *47*, 7745–7750; b) Vilà–Nadal, L.; Rodríguez–Fortea, A.; Poblet, J. M. *Eur. J. Inorg. Chem.* **2009**, 5125–5133.
168. Vilà–Nadal, L.; Rodríguez–Fortea, A.; Yan, L.–K.; Wilson, E. F.; Cronin, L.; Poblet, J. M. *Angew. Chem. Int. Ed.* **2009**, *48*, 5452 –5456.
169. Vilà–Nadal, L.; Wilson, E. F.; Miras, H. N.; Rodríguez–Fortea, A.; Cronin, L.; Poblet, J. M. *Inorg. Chem.* **2011**, *50*, 7811–7819.
170. Vilà–Nadal, L.; Mitchell, S. G.; Rodríguez–Fortea, A.; Miras, H. N.; Cronin, L.; Poblet, J. M. *Phys. Chem. Chem. Phys.* **2011**, *13*, 20136–20145.
171. Biswas, S.; Melgar, D.; Srimany, A.; Rodríguez–Fortea, A.;Pradeep, T.; Bo, C.; Poblet, J. M.; Roy, S. *Inorg. Chem.* **2016**, *55*, 8285–8291.
172. Cameron, J. M.; Vilà–Nadal, L.; Winter, R. S.; Iijima, F.; Murillo, J. C.; Rodríguez–Fortea, A.; Oshio, H.; Poblet, J. M.; Cronin, L. *J. Am. Chem. Soc.* **2016**, *138*, 8765–8773.
173. Kachmar, A.; Bénard, M.; Rohmer, M. M.; Boero, M.; Massobrio, C. *J. Phys. Chem. A* **2009**, *113*, 9075–9079.
174. Piccinin, S.; Fabris, S. *Phys. Chem. Chem. Phys.* **2011**, *13*, 7666–7674.

175. a) Jiménez–Lozano, P.; Carbó, J. J.; Chaumont, A.; Poblet, J. M.; Rodríguez–Fortea, A.; Wipff, G. *Inorg. Chem.* **2014**, *53*, 778–786; b) Jiménez–Lozano, P.; Solé–Daura, A.; Wipff, G.; Poblet, J. M.; Chaumont, A.; Carbó, J. J. *Inorg. Chem.* **2017**, *56*, 4148–4156.
176. Car, R.; Parrinello, M. *Phys. Rev. Lett.* **1985**, *55*, 2471–2474.
177. Wang, J.; Cieplak, P.; Kollman, P. A. *J. Comput. Chem.* **2000**, *21*, 1049–1074.
178. Himo F, Siegbahn P. E. M. *Chem. Rev.* **2003**, *103*, 2421–2456.
179. Vaissier, V.; Barnes, P.; Kirkpatrick, J.; Nelson J. *Phys. Chem. Chem. Phys.*, **2013**, *15*, 4804–4814.
180. Libby, W. F. *J. Phys.Chem.* **1952**, *56*, 893.
181. a) Marcus, R. A. *J. Chem. Phys.* **1956**, *24*, 966–978; b) Marcus, R. A. *Angew. Chem., Int. Ed. Engl.* **1993**, *32*, 1111–1121.
182. Frisch, M. J.; Trucks, G. W.; Schlegel, H. B.; Scuseria, G. E.; Robb, M. A.; Cheeseman, J. R.; Scalmani, G.; Barone, V.; Mennucci, B.; Petersson, G. A.; Nakatsuji, H.; Caricato, M.; Li, X.; Hratchian, H. P.; Izmaylov, A. F.; Bloino, J.; Zheng, G.; Sonnenberg, J. L.; Hada, M.; Ehara, M.; Toyota, K.; Fukuda, R.; Hasegawa, J.; Ishida, M.; Nakajima, T.; Honda, Y.; Kitao, O.; Nakai, H.; Vreven, T.; Montgomery, J. A., Jr.; Peralta, J. E.; Ogliaro, F.; Bearpark, M.; Heyd, J. J.; Brothers, E.; Kudin, K. N.; Staroverov, V. N.; Kobayashi, R.; Normand, J.; Raghavachari, K.; Rendell, A.; Burant, J. C.; Iyengar, S. S.; Tomasi, J.; Cossi, M.; Rega, N.; Millam, J. M.; Klene, M.; Knox, J. E.; Cross, J. B.; Bakken, V.; Adamo, C.; Jaramillo, J.; Gomperts, R.; Stratmann, R. E.; Yazyev, O.; Austin, A. J.; Cammi, R.; Pomelli, C.; Ochterski, J. W.; Martin, R. L.; Morokuma, K.; Zakrzewski, V. G.; Voth, G. A.; Salvador, P.; Dannenberg, J. J.; Dapprich, S.; Daniels, A. D.; Farkas, Ö.; Foresman, J. B.; Ortiz, J. V.; Cioslowski, J.; Fox, D. J. Gaussian 09, revision D.01; Gaussian, Inc.: Wallingford, CT, 2009.
183. Cancès, E.; Mennucci, B.; Tomasi, J. *J. Chem. Phys.* **1997**, *107*, 3032–3041.

UNIVERSITAT ROVIRA I VIRGILI
NEW HORIZONS IN COMPUTATIONAL MODELING OF POLYOXOMETALATES:
BIOLOGICAL ACTIVITY, ENERGY STORAGE AND SUSTAINABLE CATALYSIS.
Albert Solé Daura

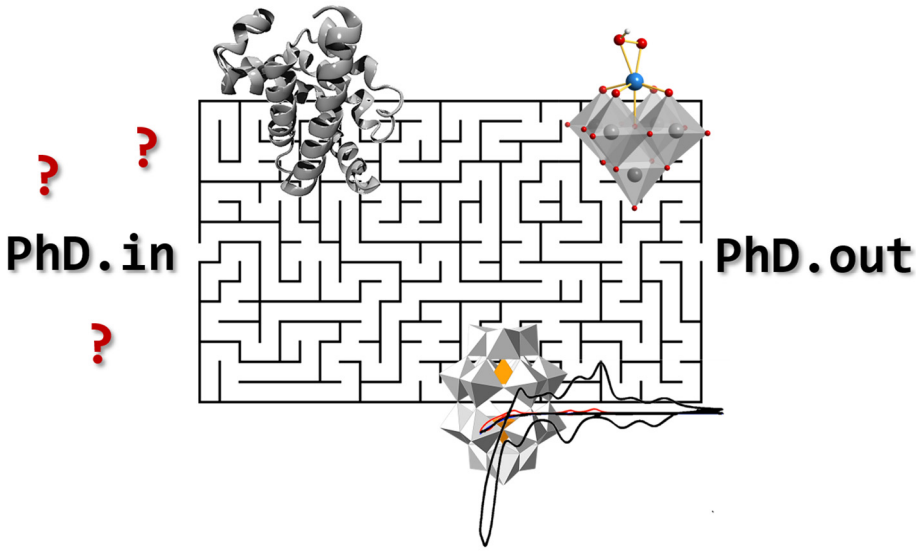

Chapter 2

Goals of the Thesis

UNIVERSITAT ROVIRA I VIRGILI
NEW HORIZONS IN COMPUTATIONAL MODELING OF POLYOXOMETALATES:
BIOLOGICAL ACTIVITY, ENERGY STORAGE AND SUSTAINABLE CATALYSIS.
Albert Solé Daura

CHAPTER 2

Goals of the Thesis

Herein we summarize the main goals of this thesis separated by chapters. Some of them were clearly defined from the very beginning of the Ph. D. but some others rose from the need of giving explanation to experimental evidences observed either by our collaborators or in the literature. The first three chapters (3–5) are tightly related and concern the investigation of the POM activity towards biological systems. Chapter 6 deals with the analysis of unusual POM redox properties and Chapter 7 convenes computational studies of alkene epoxidation reactions catalyzed by POM systems. Overall, we aim to extend the understanding of several outstanding aspects of POM chemistry by means of computational tools, exploring the limits of computational modeling for these systems.

Chapter 3: Probing the Interaction between Polyoxometalates and Proteins using Molecular Dynamics Simulations.

Using as a reference the experimental work of the group of Parac–Vogt on the interaction of Zr^{IV}–, Ce^{IV}– and Hf^{IV}–substituted POMs with hen egg–white lysozyme (HEWL) protein, we aim to explore the interactions between POMs and proteins at atomistic level by means of Molecular Dynamics (MD) simulations. The study includes the following specific objectives:

- Characterize the nature of the interactions between POMs and biological systems at atomistic level using as a reference the experimentally tested case of HEWL and classical MD simulations.
- Identify and characterize the different types of interactions between the POM and the amino acids of the protein.
- Evaluate the influence of the POM structure into the POM···protein interactions.

Chapter 4: Structure–Activity Relationships for the Affinity of Chaotropic Polyoxometalate Anions towards Proteins.

Despite several attempts of relating the POM structure to their affinity to biological systems are reported in the literature, their joint analysis does not provide unambiguous

trends, most likely due to the difficulty of performing systematic analyses experimentally varying one single parameter of the POM structure at a time. In this regard, our goal is to use computational modeling, which readily allows evaluating the influence of individual parameters making possible this kind of fundamental studies. With this information in hand, the specific goals of this chapter are the following:

- Understand how different parameters of the POM structure such as the charge, the size or the shape influence their affinity to biological systems, aiming to establish clear structure–activity relationships.
- Build a multivariate regression model relating the protein affinity of POMs with the aforementioned parameters using time–derived, response variables obtained from MD simulations.

Chapter 5: Modeling the Reactivity of Polyoxometalates towards Biological Systems.

The previous chapters of this thesis are dedicated to understand the formation of non–covalent POM···protein adducts. In a more ambitious project, in this chapter we wish to move a step forward studying chemical transformations in proteins promoted by POM structures. In particular, we have analyzed the origin of selectivity in the hydrolysis of peptide bonds in proteins catalyzed by Zr^{IV}–substituted POMs, and the reduction of disulfide bonds using POMs with *d*–electrons, which finds application in the clinical diagnosis of preeclampsia. Specifically, the studies encompassed in this chapter are aimed to:

- Understand the molecular mechanism and the origin of selectivity for the hydrolysis of peptide bonds in proteins catalyzed by Zr–substituted POMs.
- Characterize the reaction mechanism for the reduction of DTNB with the one electron reduced Keggin–type phosphotungstate.
- Propose a POM structure capable of cleaving more kinetically inert S—S bonds with aliphatic substituents, as more realistic model substrates of biological disulfides.
- Evaluate the feasibility of the disulfide bond reduction in angiotensinogen protein, that is a system of biomedical interest.

Chapter 6: Modeling Super–Reduced Polyoxometalates for Energy Storage.

The experimental group of Prof. Cronin has recently reported the ability of the classical Wells–Dawson anion $[P_2W_{18}O_{62}]^{6-}$ to be reversibly reduced with up to 18 electrons in aqueous solution under certain conditions. Considering that the regular redox behavior of this anion involves 6 electrons as much, these findings are of great interest and define new horizons in the use of POMs as electron reservoirs in chemical reactions or as redox carriers in batteries. Aiming to shed some light onto the factors governing this process, we carried out a computational study focused on achieving the following goals:

- Give an explanation to the super–reduction process observed at experimental conditions.
- Evaluate the influence of the size of the alkali counter cation in the redox properties of $[P_2W_{18}O_{62}]^{6-}$.
- Propose a plausible molecular and electronic structure for the 18 electron–reduced POM.

Chapter 7: Computational Studies on Alkene Epoxidation Catalyzed by Early Transition Metal–Substituted Polyoxometalates.

For years, transition metal–substituted POMs have been used as tractable molecular models to study catalytic processes occurring on their single–site silica–supported heterogeneous catalysts. Specifically, in the alkene epoxidation reaction with hydrogen peroxide, POMs have shown ability to efficiently mimic the catalytic activity and selectivity of their heterogeneous counterparts. Aiming to support the latest experimental results from our experimental collaborators working on this topic, the goals of this chapter are:

- Characterize the mechanism of the alkene epoxidation with hydrogen peroxide catalyzed by Nb–substituted Lindqvist catalysts and compare their reactivity with that of their Ti–containing analogues.
- Evaluate the influence of the POM scaffold and unveil the origin of selectivity towards allylic alcohols for the hybrid Ti–containing tris–silanol functionalized polyoxotungstate catalyst.
- Propose a plausible mechanism for the hydrogen peroxide decomposition side reaction.

UNIVERSITAT ROVIRA I VIRGILI
NEW HORIZONS IN COMPUTATIONAL MODELING OF POLYOXOMETALATES:
BIOLOGICAL ACTIVITY, ENERGY STORAGE AND SUSTAINABLE CATALYSIS.
Albert Solé Daura

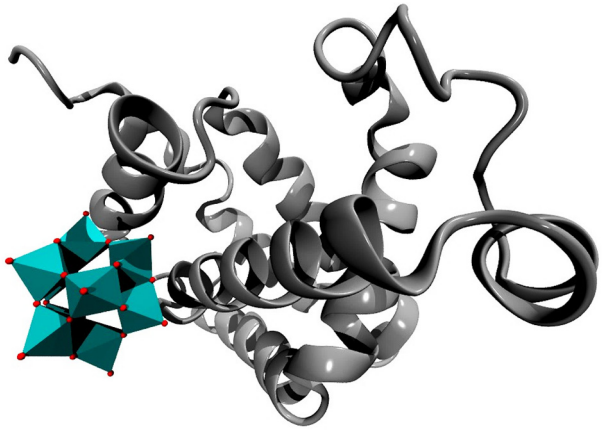

Chapter 3

Probing the Interaction between Polyoxometalates and Proteins Using Molecular Dynamics Simulations

UNIVERSITAT ROVIRA I VIRGILI
NEW HORIZONS IN COMPUTATIONAL MODELING OF POLYOXOMETALATES:
BIOLOGICAL ACTIVITY, ENERGY STORAGE AND SUSTAINABLE CATALYSIS.
Albert Solé Daura

CHAPTER 3

Probing the Interaction between Polyoxometalates and Proteins Using Molecular Dynamics Simulations

*In this chapter we describe the first atomistic MD simulations devoted to characterize the non–bonding interactions between POMs and biological systems. We selected the experimental tested case of Hen Egg–White Lysozyme (HEWL); which is selectively hydrolyzed at the peptide bonds Trp28–Val29 (site I) and Asn44–Arg45 (site II) in the presence of the Ce^{IV}–substituted Keggin anion $[PW_{11}O_{39}Ce(OH_2)_4]^{3-}$ (**CeK**). These simulations served to characterize the physicochemical nature of POM···protein interactions and to identify two cationic regions of the protein that could be related with the observed selectivity. The analysis of **CeK** was compared with the Ce^{IV}–substituted Keggin dimer $[(PW_{11}O_{39})_2Ce]^{10-}$ (**CeK$_2$**) and the Zr^{IV}–substituted Lindqvist anion $[W_5O_{18}Zr(OH_2)(OH)]^{3-}$ (**ZrL**) in order to evaluate how POM features such as the shape, the size, the charge or the type of incorporated metal ion can influence the POM···protein interactions.*

This work was carried out in collaboration with the experimental group of Prof. T. N. Parac–Vogt, from KU Leuven (Belgium) and with the group of Prof. J. D. Hirst, based in University of Nottingham (U.K.).

3.1 Background

In recent years Parac–Vogt *et al.* have studied the POM hydrolytic activity towards the highly inert peptide bond in biomolecules such as dipeptides and oligopeptides,[1] and more importantly, reported the first examples of selective hydrolysis of proteins by POMs.[2–6] The active POMs include different structures of Ce^{IV}– Hf^{IV}– and Zr^{IV}–substituted anions, which initially were applied to the hydrolysis of hen egg–white lysozyme (HEWL),[2] and more recently to human serum albumin (HSA),[3] myoglobin (HHM),[4] cytochrome c (Cyt C)[5] and ovalbumin (OVA).[6] It was observed that the peptide bond cleavage sites are close to positively charged protein surface patches. Therefore, it was postulated that the electrostatic interactions with the negatively charged POM structures lead to the selective

hydrolysis in an enzyme–like recognition scheme.[2–6] Nevertheless, so far no direct proof for the electrostatic nature of these POM···protein interactions has been presented.

Understanding the physicochemical foundations of the interactions between POMs and biomolecules might have important implications for medical and biochemical applications of POMs beyond selective peptide hydrolysis. In this regard, computational simulations could facilitate the understanding of the molecular properties that govern the interaction in order to further develop metal–substituted POMs with specific interaction properties. Although these tools have been largely employed to study POM chemistry,[7] the study of POM–protein interactions at molecular level is still a largely unexplored area. There have been a number of docking studies exploring the binding locations for POMs with proteins, but due to the intrinsic limitations of this methodology little was revealed about the driving forces that are responsible for the specific interactions.[8] These studies proposed that POMs interact mainly with positively charged amino acids such as Lys, His or Arg, or with polar uncharged ones such as Asn, Ser, Cys, Thr or Gln. For example, Hill *et al.* showed that Nb–containing POMs inhibit HIV–1 protease by binding to a cationic pocket of lysine residues away from the active site.[8g] Similar findings were derived from experimental studies, which identified electrostatic effects as the main factor in the interaction of POMs with biomolecules based on luminescence of Eu–substituted POMs, the fluorescence of tryptophan residues, isothermal titration calorimetry (ITC), and NMR and circular dichroism (CD) spectroscopy.[2–6,8–10] For example, Qu *et al.* proposed that POMs bind to the positively charged His13–Lys16 cluster region of amyloid β–peptides associated with Alzheimer's disease.[9d] It was also observed that the POMs can bind sufficiently tightly to cause structural change in basic fibroblast growth factor (bBGF).[9b] More specifically, recent studies using model amino acids and peptides attributed the mechanism of interactions with biomolecules to electrostatic interactions and hydrogen bonds between amino acids and the negative charges of POMs.[10]

Interestingly, Qu *et al.* found an apparent trend related to POM composition: the larger negative charge, the higher the binding affinity, and the stronger the inhibitory effect.[9d] However, if one considers the charge density of the anion instead of the overall charge, the inactive POMs are not only the least charged but also the smallest anion carrying one of the highest charge densities among the series. Thus, we suspect that binding might require cooperation of electrostatic (high negative charge) and hydrophobic (accessible surface) forces. Moreover, hydrophobic and electrostatic interactions in the most general sense are non–specific effects that would not explain by themselves the specificity of interaction

sites, the selective enzyme–like recognition, nor the dependence on POM size and shape. Therefore, we believe that it is necessary to analyze the factors underlying the interaction of POMs with biomolecules beyond size–specific electrostatic effects in order to obtain a full picture of the physicochemical foundations in these processes.

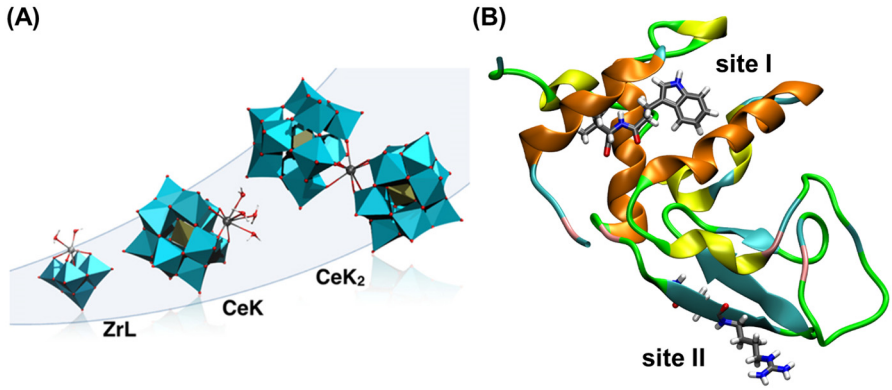

Figure 3.1 | (A) Polyhedral representation of the anions $[PW_{11}O_{39}Ce(OH_2)_4]^{3-}$ (**CeK**), $[Ce(PW_{11}O_{39})_2]^{10-}$ (**CeK₂**) and $[W_5O_{18}Zr(OH_2)(OH)]^{3-}$ (**ZrL**). (B) Secondary structure of HEWL protein (q = 8+) highlighting the experimentally hydrolyzed sites labeled as site I (Trp28–Val29) and site II. (Asn44–Arg45)

Herein, we performed molecular dynamics (MD) simulations of three different POM structures with HEWL in aqueous solution. The three POMs are Ce–substituted Keggin–type anion $[PW_{11}O_{39}Ce(OH_2)_4]^{3-}$ (**CeK**) the corresponding 1:2 dimer $[Ce(PW_{11}O_{39})_2]^{10-}$ (**CeK₂**) and the Zr–substituted Lindqvist–type anion $[W_5O_{18}Zr(OH_2)(OH)]^{3-}$ (**ZrL**), which differ in the overall charge, the size, the shape and the type of substituted metal (see **Figure 3.1**, left). Lysozyme represents a simple model protein for fundamental studies, but more importantly, it has been demonstrated that Ce–substituted POM acted as a selective protease cleaving HEWL at the peptide bonds Trp28–Val29 (site I) and Asn44–Arg45 (site II). **Figure 3.1** (right) shows the location of both cleavage sites in the secondary structure of HEWL. Both Eu^{III} luminescence and tryptophan fluorescence studies indicated that the POM binds the protein near these cleavage sites.[6] Moreover, Sap et al. reported the co–crystallization of a non–covalent complex between lysozyme and the analogous Zr–substituted Keggin–type anion and its characterization via X–ray analysis.[11] After the publication of the results presented in this chapter, other crystal structures appeared in the literature; all of them displaying similar features.[12,13] The simulations of **CeK** with HEWL protein performed in this work should provide additional information regarding the dynamics of the interaction and the relative

binding strengths of individual amino acids. Moreover, direct comparison between POMs will shed light on the structural factors governing the interactions between the POMs and the biomolecules.

3.2 Computational Details

The systems were simulated by classical MD using the GROMACS 4.5.4 software[14] and the AMBER99 force field,[15] which has been successfully employed to study the aggregation behavior of POMs in solution by Chaumont and Wipff.[16] The potential energy U is empirically described by a sum of bond, angle, and dihedral deformation energies and pair–wise additive 1–6–12 (electrostatic and van der Waals) interactions between non bonded atoms or between those separated by more than three bonds.

The parameters for the Ce–substituted POMs were obtained following the procedure of Bonet–Avalos, Bo, Poblet et al.[17] We used CHELPG atomic charges derived from the electrostatic potential. They were obtained with the Gaussian09 package[18] at the DFT level (BP86 functional)[19] using the LANL2DZ basis set[20] for W, O and H atoms, and the MWB28 basis set[21] for Ce. Solvent effects were included in geometry optimizations by using the IEF–PCM model[22] as implemented in Gaussian09 package.[18] The set of Lennard–Jones parameters for W and O atoms were taken from previous work,[17] and those for Ce were taken from UFF force field.[23] Parameters for **ZrL** were taken from previous studies.[24] The geometry of the 8+ charged HEWL was taken from protein data bank (PDB) database (PDB ID: 3IJV).[25] For the MD simulations with **CeK**, the protein was embedded in a water solvent box of dimensions 73.1 × 68.8 × 77.1 Å, one POM molecule (q = 3–) and five chloride ions to neutralize the system. MD simulations with **ZrL** were performed in a water solvent box of dimensions 75.7 × 78.4 × 79.1 Å, one POM molecule (q = 3–) and five chloride atoms to neutralize the system. For simulations with **CeK_2** the size of the box was 75.7 × 78.4 × 79.1 Å for the runs starting at the vicinity of protein site I and 73.1 × 68.8 × 77.1 Å for those of site II. One POM molecule (q = 10–) and two Na^+ ions were added to neutralize the system.

Water was represented with the TIP3P model.[26] All simulations were performed with 3D–periodic boundary conditions using an atom cutoff of 14 Å for 1–4 van der Waals and of 10 Å for 1–4 Coulombic interactions and corrected for long–range electrostatics by using the particle–particle mesh Ewald (PME) summation method.[27] The simulations

were performed at 300 K starting with random velocities. The temperature was controlled by coupling the system to a thermal bath using the Berendsen algorithm[28] with a relaxation time of 0.5 ps to keep the NVT canonical conditions throughout the simulation. Newton equations of motion were integrated using the leap–frog algorithm,[29] and a time step of 1 fs. The bonds with hydrogens were restrained using the LINCS algorithm.[30] Starting either at the vicinity of site I or site II, we run 5 independent simulations of 20 ns for each POM at each site. Before the production runs, the systems were equilibrated with 5000 steps of energy minimization followed by simulations of 250 ps at constant volume (NVT).

3.3 Results and Discussion

3.3.1 MD study of $[PW_{11}O_{39}Ce(OH_2)_4]^{3-}$ anion with HEWL in solution.

Initially, we simulated the monomeric Ce–substituted Keggin–type anion $[PW_{11}O_{39}Ce(OH_2)_4]^{3-}$ (**CeK**) with HEWL in aqueous solution. Experimentally, the 1:2 dimeric structure $[Ce(PW_{11}O_{39})_2]^{10-}$ (**CeK_2**) was in fact the complex employed in the selective hydrolysis.[2] However, this species is a highly unlikely catalyst because the coordination sphere of Ce^{IV} is fully saturated by coordination to oxygen atoms of the POM framework. Since hydrolysis requires the binding of the Ce metal acting as a Lewis acid to the amide carbonyl, it was proposed that the interaction with protein induces dissociation of the dimeric species **CeK_2** to the monomeric **CeK** POM. Some posterior evidence has supported this hypothesis. The analogous **EuK_2** dimer was shown to dissociate leading to monomeric **EuK**, which is able to bind to amino acids.[6a] Similarly, when the analogous Zr dimer **ZrK_2** was used for co–crystallization with HEWL, the resulting crystal structure showed exclusively the presence of the Zr–substituted monomeric species, **ZrK**.[11,12] The same behavior was reported afterwards for several TM–substituted Wells–Dawson dimers (TM = Hf^{IV}, Zr^{IV}, Co^{II}, Ni^{II}, Cu^{II}).[13]

We performed two sets of simulations starting with the **CeK** anion placed at the vicinity of each of the known cleavage sites of HEWL (I and II). **Figure 3.2** plots the classical non–bonding energy for the interactions of the **CeK** anion with the protein (blue line), the solvent (red line) and the whole system (green line) along a representative trajectory of 20 ns (see Appendix for the other trajectories). The graphs in **Figure 3.3** collect the analysis of the interaction of **CeK** with the individual amino acids averaged over 100 ns of dynamics trajectories: the average energy strength in bars and the percentage hydrogen

bond lifetimes in lines. These simulations allowed us to identify the direct **CeK**···HEWL interaction, to characterize and evaluate the interactions with individual amino acids and their nature.

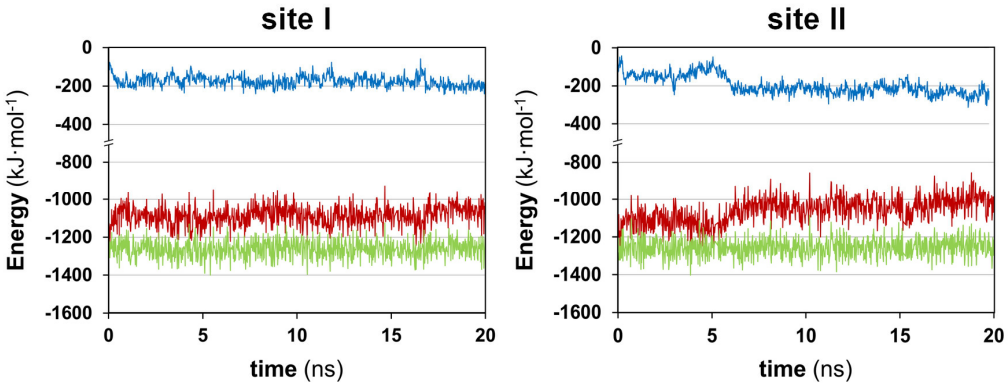

Figure 3.2 | Non–bonding interaction energies (in kJ·mol^{-1}) of the **CeK** anion with HEWL (blue line), with the solvent (red line), and with the whole system (green line) as a function of the time (ns) for simulations starting at vicinity of site I (left) and II (right). Representative 20 ns run.

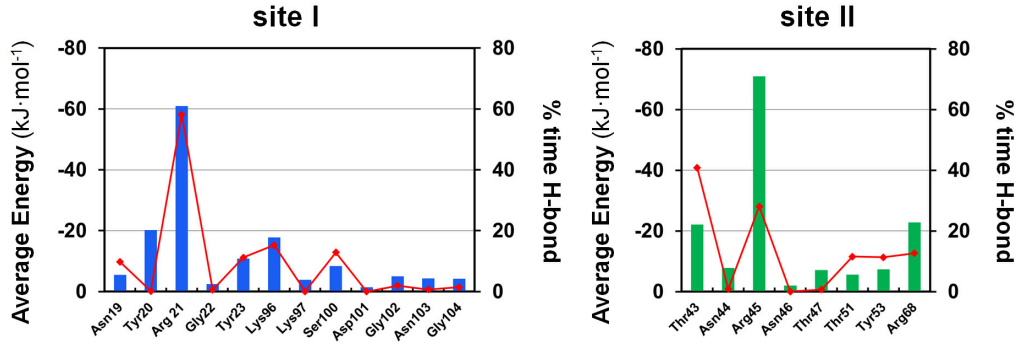

Figure 3.3 | Analysis of amino acid specific interaction between the **CeK** anion and selected individual AAs of HEWL. Average non–bonding interaction energies in kJ·mol^{-1} (bars), and percentage of hydrogen bond persistences for acidic hydrogens of amide bond and side chains (lines) along the simulations starting at vicinity of site I (left) and II (right). The values are quantified at every 4 ps time frame over 100 ns MD trajectories.

For all the runs performed the interaction between the **CeK** anion and the HEWL is appreciable and remains present during most of the simulation time with non–bonding interaction energies averaging –178 kJ·mol^{-1} for site I and –161 kJ·mol^{-1} for site II (see **Figure 3.2** and **Figures A3.1** and **A3.2** in Appendix). As a general trend, as the interaction with the protein strengthens, the solvent interaction energy lowers because the **CeK** anion

has to remove the solvation shell to access protein surface. This can be seen in **Figure 3.2**, where blue and red lines represent protein and solvent interaction energies, respectively. From the evolution of the interaction energy, we could also identify different time periods corresponding to different interactions modes of the **CeK** anion. In the simulations starting at the vicinity of site I, the **CeK** anion interacts at the α–helical part of the structure outside of an entrance channel to cleavage site I that is buried in a hydrophobic pocket of the protein. As **Figure 3.3** shows, the most strongly interacting amino acid is Arg21; the interaction is present during the whole 100 ns sampling. Then the **CeK** anion can interact with Ser100 and with either amino acids on the left– or the right–hand side of the entrance channel (Lys96 and Lys97 or Tyr23, respectively). **Figure 3.4** shows a representation of the two portions of the protein surface that interact with the **CeK** anion, and **Figures 3.5** and **3.6** show illustrative snapshots of the **CeK**···HEWL interactions at the two different regions close to site I. Thus, the Arg21 anchors the **CeK** anion acting as a flexible hinge that places the POM at the one or the other side of the protein surface, or more embedded in the solvent.

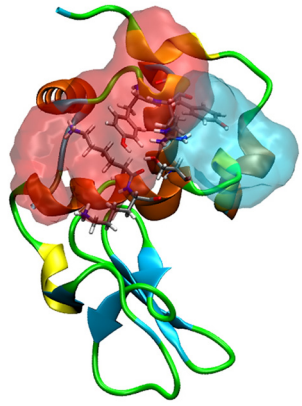

Figure 3.4 | Representation of the volumetric density for the **CeK** anion contact with HEWL (POM···protein distance < 3.5 Å) along the 100 ns trajectories. Two protein surface regions differentiated by colors. Red area involving Lys96 and Lys97 and blue area involving Tyr23. Residues Arg21 and Ser100 are common in both areas.

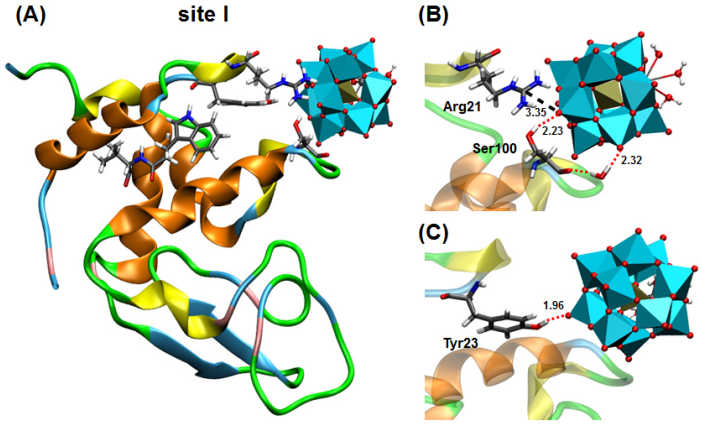

Figure 3.5 | Illustrative snapshots of **CeK**···HEWL interaction at the vicinity of site I involving Tyr23 (red area in **Figure 3.4**) taken at 17066 ps of run 1 (interaction energy –237 kJ·mol^{-1}). (A) Interacting amino acids and cleavage site I (Trp28 and Val29). (B,C) Closer look at the interaction between **CeK** and amino acids Arg21, Ser100 and Tyr23 (–71, –47 and –38 kJ·mol^{-1}). Distances in Å.

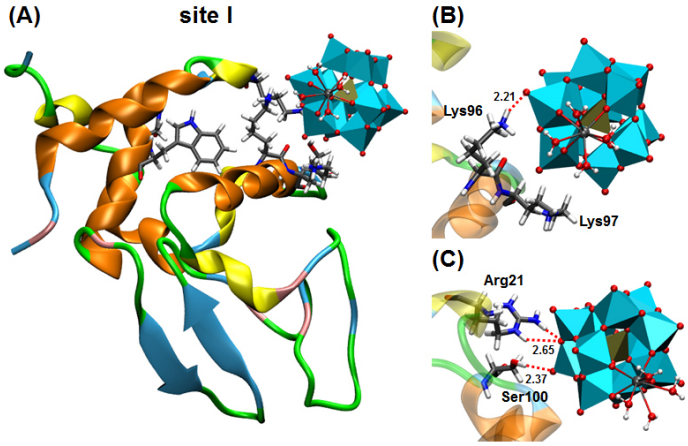

Figure 3.6 | Illustrative snapshot of **CeK**···HEWL interaction at the vicinity of site I involving Lys96 and Lys97 (blue area in **Figure 3.4**) taken at 19384 ps of run 5 (interaction energy –304 kJ·mol^{-1}). (A) Interacting amino acids and cleavage site I (Trp28 and Val29). (B,C) Closer look at the interaction between **CeK** and amino acids Arg21, Lys97, Lys96 and Ser100 (–104, –88, –76 and –37 kJ·mol^{-1}). Distances in Å.

In the simulation at the vicinity of site II, the **CeK** anion adsorbs onto the protein surface, interacting directly with the amino acids of cleavage site II, which are exposed to the solvent in the β–strand region. In fact, the most strongly interacting amino acid in this set of simulations is Arg45 belonging to cleavage site II (see **Figure 3.3**, right panel). This

interaction persists for most of the simulation, and some additional ones can occur simultaneously with amino acids such as Arg68, Tyr53, Thr43 and Thr51 (**Figure 3.3**, right panel) that contribute to the stability of the **CeK**···HEWL complex. **Figure 3.7** shows an illustrative snapshot in which this additive interaction can be observed: strong interaction with positively charged amino acids Arg45 and Arg68 at different protein regions, and with polar amino acids Tyr53, Thr43 and Thr51. In both cases, the **CeK** anion interacts mostly through the POM framework, with the hydrophilic $Ce(H_2O)_4$ moiety pointing towards the solvent. The binding sites and the orientation of **CeK** anion revealed by dynamic simulations fully agree with the positions of the TM–substituted Keggin– and Dawson–type anions co–crystallized with HEWL.[11–13]

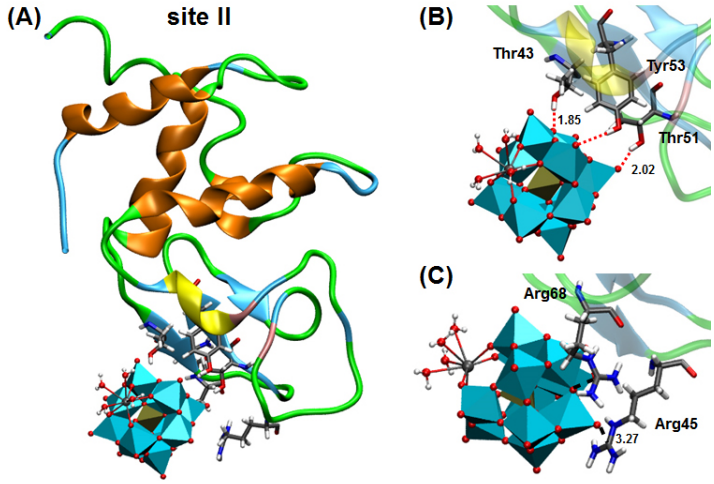

Figure 3.7 | Illustrative snapshot of **CeK**···HEWL interaction at the vicinity of site I involving Lys96 and Lys97 (blue area in **Figure 3.4**) taken at 19384 ps of run 5 (interaction energy –304 kJ·mol^{-1}). Left panel highlights interacting amino acids and cleavage site I (Trp28 and Val29). Right panels: closer look at the interaction between **CeK** and amino acids Arg21, Lys97, Lys96 and Ser100 (–104, –88, –76 and –37 kJ·mol^{-1}). Distances in Å.

As illustrative snapshots in **Figures 3.5**, **3.6** and **3.7** show, the **CeK** anion can be in direct contact with the protein surface forming hydrogen bonds with the amino acids side chains through the most basic oxygen atoms of the POM framework. Several amino acids of different sections of the protein structure interact simultaneously with the anion in an additive manner, and both the terminal and the bridging oxygen atoms act as hydrogen acceptors. For example, in the first snapshot of site I (**Figure 3.5**), the side chains of Ser100 and Tyr23 form hydrogen bonds with the terminal oxo groups of the POM

framework (O–H···O_{POM} distances = 2.23 and 1.96 Å, respectively), while for positively charged Arg21 we observe an electrostatic contact. In the other snapshot of site I (**Figure 3.6**), the **CeK** anion forms a double–hydrogen bonding interaction with two of the guanidinium N–H groups of Arg21 involving a bridging oxygen of POM framework. The NH_3^+ amino group of Lys96 forms a hydrogen bond with the POM, whereas the analogous Lys97 is bound via an electrostatic–type interaction showing N–H–O_{POM} angles < 108°. Similarly, for site II (**Figure 3.7**), the **CeK** complexation occurs via multiple binding interactions such as hydrogen bonding with Thr43, Thr51 and Tyr53 (O–H···O_{POM} distances ranging from 1.85 to 2.42 Å), and electrostatic with Arg45 and Arg68. Within these snapshots, the polar uncharged amino acids serine tyrosine, and threonine show computed interaction energies ranging from –37 to –47 kJ·mol^{-1}, which lie within the typical energy range for *normal* hydrogen bonds.[14] For the positively charged arginines and lysines, the obtained interaction energies are two–fold higher (ranging from –71 to –104 kJ·mol^{-1}) and lie in the range of typical *strong* hydrogen bonds, which include the *positively charge assisted hydrogen bonds* X^+–H···A.[14]

We have analyzed the formation of hydrogen bonds along the whole simulation in more detail. **Figure 3.3** shows the simulated hydrogen bond persistences as a percentage of the trajectory (lines). For each residue we quantified the number of snapshots showing H–bonding to **CeK** whose value was normalized by the total number of snapshots and used as representation of the overall **CeK**···HEWL H–bond statistics. The H–bond criteria comprise a distance (< 3.5 Å) and an angle (X–H–O_{POM} > 130°) constraint. This parameter provides information on the most strongly interacting amino acids and the nature of their interaction, complementing the average energies reported in **Figure 3.3**. The longest–lasting and the strongest interactions are with Arg21 for site I and Arg45 and Arg68 for site II. This agrees with previous NMR results showing resonance shifts for arginine side chains in the presence of POM.[2] The interaction with these amino acids combines electrostatic and hydrogen–bonding contributions. For example, although the interaction with Arg21 is present during the whole simulation, the persistence represents only the 57%. The affinity of the **CeK** anion increases by additional hydrogen bonding with the side chains of Ser100 and Tyr23 in site I and Thyr53 and Thr43 in site II, with percentage persistence ranging from 20 to 40%. We could also identify other non–polar amino acids, such as, glycine and alanine that interact appreciably with **CeK**, via the N–H amide group, the most outstanding being Gly102 and Gly104 with percentage persistence between 10 and 20% (see **Figure 3.3**). It should be noted that although it had been

proposed that hydrogen–bonding might be an interaction force in POMs binding to biomolecules, [10,32] this is the first time that these interactions have been quantified.

In the crystal structure of the non–covalent POM···protein complex, the Zr–substituted $[PW_{11}O_{39}Zr(OH_2)_n]^{3-}$ anion showed direct hydrogen–bond interactions with HEWL, and also, water–mediated interactions, in which a layer of water molecules connected the **CeK** anion and the protein.[11] There are other X–ray structures in which the interactions between the POMs and the protein are partially mediated by the solvent.[33] For example, the octamolybdate and the hexatungstotellurate anions interact partially via water molecules with uncharged polar amino acids such as glutamine and threonine in the molybdenum storage protein[33a] and abPPO4 mushroom tyrosinase,[33b] respectively. Since the interaction of the POM with the solvent decreases as the interaction with the protein increases, the optimal situation might be the water–mediated contact in which the **CeK** anion keeps the first solvation shell and there is still a non–bonding electrostatic interaction with the positively charged amino acids. **Figure 3.8** presents a sequence of snapshots taken during the approach of **CeK** anion to site II as illustrated by the evolution of interaction energies in **Figure 3.2**. In the frames of **Figure 3.8**, we can observe different water–mediated interactions with Arg45, Arg68 and Thr43; and how the successive removal of the water layer surrounding the POM reduces the **CeK**···water interaction energy, which is balanced by the increase of the direct contact with the protein residues. Overall, both experiments and simulations indicate that electrostatic–based water–mediated interactions are quite favorable. However, in the dynamic process the **CeK** anion can easily remove the solvation shell to reach the protein surface, stabilized via hydrogen bonding with polar and positively charged amino acids. Analogously, other X–ray structures have shown that the POMs are also able to interact directly with the protein. Rompel et al.[34] have co–crystallized HEWL with the Anderson–Evans–type hexatungstotellurate $[TeW_6O_{24}]^{6-}$ anion which binds to positively charged (Arg and Lys) or polar uncharged residues (Asn and Gln) similarly to **CeK** anion in our simulations. Interestingly, they identified a specific cationic site formed by Arg45 and Arg68 where the hexatungstate binds similarly to **CeK** at site II. Also the analogous anion $[W_{12}O_{40}H_2]^{6-}$ binds NTPDase1 directly interacting with Lys, Asn and Gln.[35]

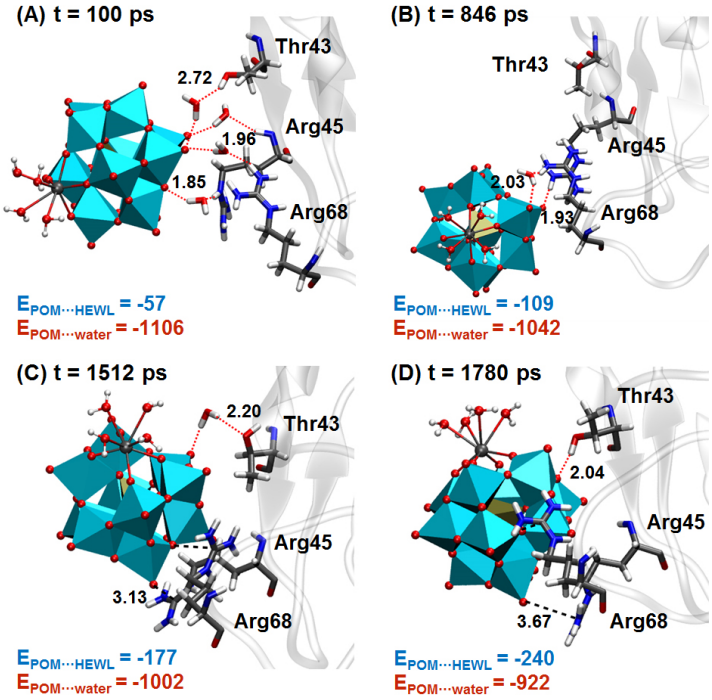

Figure 3.8 | Snapshots taken during the approach of **CeK** anion to protein site II. For clarity, only selected water molecules are shown. Distances in Å and energies in kJ·mol^{-1}.

The **CeK** anion interaction does not induce any conformational change in the HEWL structure and we only observed small geometrical differences in the side chains. This agrees with crystal structures indicating that HEWL structure is preserved upon binding to the analogous Keggin–type Zr–substituted anion.[11] Thus, for the available simulation times, we cannot expect to observe a direct interaction of **CeK** with site I (Trp28–Val29) site which would involve a modification of protein secondary structure. However, the observed binding site at Arg21 might be related to an entrance channel to the solvent–inaccessible site I via secondary structure decrease of the α–helix. For site II, the long and strong interaction with Arg45 is quite noteworthy because it belongs to the cleavage site II. As in the X–ray structures, the catalytically active Ce^{IV} center points towards the solvent due to the hydrophilicity of the Ce^{IV}–aqua moiety. Consequently, the dynamic hydrolysis process should involve anion reorganization to bind the amide oxygen with the corresponding energy penalty. Nevertheless, the direct interaction of **CeK** to cleavage site II revealed in this study is consistent with the hydrolytic selectivity observed at Asn44–Arg45 bond.

3.3.2 Influence of POM structure on the POM···protein interactions.

To get further insight into how POM features such as the shape, the size, the charge, the kind of incorporated metal ion and ligands can affect the interaction between POMs and proteins, we compared the behaviour of the **CeK** anion with the Ce^{IV}–substituted Keggin dimer $[Ce(PW_{11}O_{39})_2]^{10-}$ (**CeK_2**), and the Zr^{IV}–substituted Lindqvist anion, $[W_5O_{18}Zr(OH_2)(OH)]^{3-}$ (**ZrL**). The dimeric **CeK_2** anion is in fact the species used for peptide hydrolysis, and it differs from **CeK** anion in that it carries greater negative charge and is larger and more extended. It also plaussible that the enzyme–like recognition of the POM occurs before the dimeric **CeK_2** species dissociates into **CeK**, and then interaction with protein promotes the hydrolysis of **CeK_2**.[13] The **ZrL** species represents a POM structure with smaller size and a different transition–metal substitution, which was also active towards the peptide bond hydrolysis in proteins.[1c,3–4,7c] Moreover, in POM chemistry the charge/metal ratio parameter (q/M) has been used to set structure activity relationships because it reflects better charge density distribution on the oxide structure.[7,36] For the three selected POMs, the values are: 0.25, 0.43 and 0.50 for **CeK**, **CeK_2** and **ZrL**, respectively.

Our simulations showed that POMs bind proteins mainly by electrostatic interactions; however, we anticipated that the interaction with the solvent, as well as the size of the system allowing several interactions to occur simultaneously, also need to considered. In fact, Nadjo *et al.* have recognized that the overall charge of the cluster is not the single parameter governing the binding process when comparing the binding of Human Serum Albumin (HSA) with POMs of different atomistic composition: $[P_2W_{17}O_{61}]^{10-}$, $[CuP_2W_{17}O_{61}]^{8-}$, $[NiP_2W_{17}O_{61}]^{8-}$, $[H_2W_{12}O_{40}]^{6-}$ and $[NaP_5W_{30}O_{110}]^{14-}$.[37] **Table 3.1** compares the simulated percentage of POM···HEWL interaction persistence for the three POMs which reflects their binding affinity to the protein. We quantified the number of snapshots in which the POM is closer than 3.5 Å to the protein and normalized by the total number of snapshots. Roughly, the higher the charge density (q/M ratio), the lower the binding affinity of the POM, indicating that the hydrophobic character of the anion might favour its protein affinity in water solution. In fact, the q/M ratio correlates with the computed POM solvation energies per solvent–accessible atom (**Table 3.1**), measured as the average non–bonding interactions with the solvent when the POM is not in contact with the protein. The solvent–accessible atoms consist of the terminal and bridging oxygen atoms of the POM, and the ligands on the imbedded metal. **Table 3.1** also compares the *interaction strengths*, measured as the average of POM···HEWL interaction

energies when the POM is in contact with the protein (POM···HEWL distance < 3.5 Å). The **CeK** anion shows higher affinity for HEWL than **CeK_2** and **ZrL** anions. The highly hydrophilic and small **ZrL** anion exhibits shorter persistence values (56 and 69% for site I and II) compared to **CeK** because the solvation energy becomes higher while the *interaction strength* with HEWL remains similar (**Table 3.1**). The protein affinity of **CeK_2** anion lies in an intermediate situation with persistence values (90 and 95% for site I and II) closer to **CeK** anion. The computed solvation energy of **CeK_2** is significantly higher due to its hydrophilicity, which however, is partially balanced by the stronger *interaction strength* due to the increase of interactions with multiple residues (*vide infra* for more details).

Table 3.1 | Comparison of the HEWL affinity of the three POMs **CeK**, **CeK_2**, and **ZrL**.[a]

			% *time binding*		**interaction strength**	
anions	***q/M***	E_{solv}	**site I**	**site II**	**site I**	**site II**
$[PW_{11}Ce]^{3-}$ (**CeK**)	0.25	–27	99%	99%	–178	–161
$[Ce(PW_{11})_2]^{10-}$ (**CeK_2**)	0.43	–43	90%	95%	–260	–224
$[W_5Zr]^{3-}$ (**ZrL**)	0.50	–54	56%	69%	–168	–187

[a] Estimated from the percentage of POM···HEWL contact persistence, interaction strength during the contact and the non–bonding interaction with the solvent per solvent–accessible atom. Energies in kJ·mol^{-1}. The values are sampled every 4 ps from the 100 ns MD trajectories.

Figure 3.9 compares the average interaction energies of the POMs with the individual amino acids. For **CeK_2** and **ZrL** anions, the most strongly interacting residues are also Arg21, Lys96 and Lys97 for simulations at site I and Arg45 and Arg68 for simulations at site II. In general, the **CeK_2** anion shows the higher average interaction energies (green bars) than those for **CeK** anion (yellow bars) and much higher than those for **ZrL** (blue bars). Their interactions with the proteins involve mainly hydrogen bond–mediated direct contacts with the side chains of positively charges amino acids such as arginine and lysine, and polar ones such as serine and tyrosine (see **Figures 3.10 and 3.11** for representative interactions of **CeK_2** and **ZrL**). Therefore, these electrostatic interactions in the form of hydrogen bonding might be generalized in the binding of POMs to proteins, as recent reviews on the use of POMs in protein crystallography indicates.[38] Nevertheless among the POM series, we found remarkable differences on the extent, the strength and the type of interaction with protein that can be directly related to the POM composition.

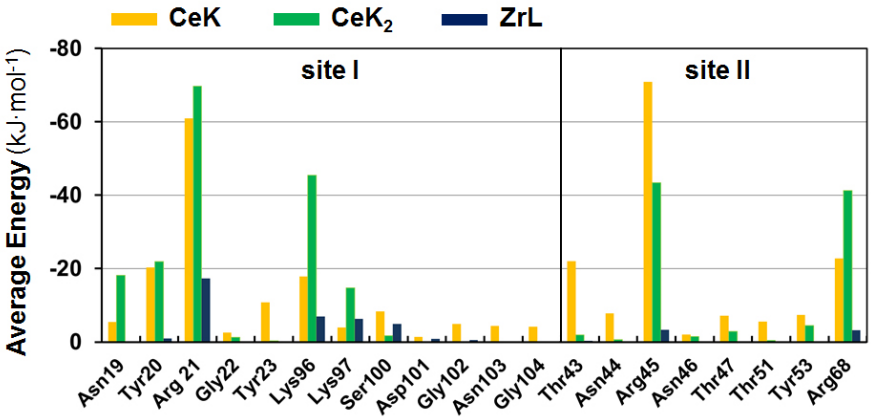

Figure 3.9 | Comparison of amino acid specific POM···HEWL interactions for **CeK** (yellow), **CeK_2** (green), and **ZrL** anions (blue). Average non–bonding interaction energies in kJ·mol^{-1} computed for snapshots taken every 4 ps from the 100 ns of sampling.

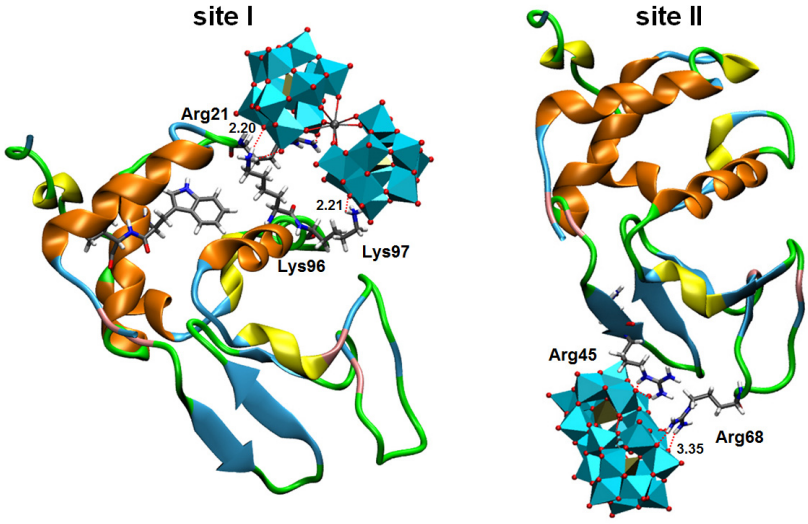

Figure 3.10 | Illustrative snapshots of **CeK_2**···HEWL interaction at site I and II taken at 10494 ps of run 1 and 11924 ps of run 1, respectively (interaction energies –408 and –283 kJ·mol^{-1}). Left: the most strongly interacting amino acids for simulation at site I: Arg21, Lys96, and Lys97 (–108, –88, and –120 kJ·mol^{-1}). Right: those for simulation at site II: Arg45 and Arg68 (–123 and –117 kJ·mol^{-1}). Distances in Å.

In the simulation of **CeK_2** anion at site I, the POM interacts mainly with Arg21 as it was observed for **CeK**, but because of its greater size additional strong interaction appears with

other amino acids such as Lys96 and Lys97 where the two Keggin units operate simultaneously (see **Figure 3.10** for representative snapshot). This makes the interaction strength significantly higher than that for **CeK** (–260 vs. –178 kJ·mol^{-1} in **Table 3.1**). Interestingly, the additive effect of the two Keggin units can induce some structural changes in the protein. At the POM binding site, the protein structure opens leading to a more accessible entrance channel to the cleavage site I (see **Figure 3.10**, left). **Figure 3.12** shows that the root mean square deviation (RMSD) of the backbone portion involving the residues directly interacting with the POMs at site I (Tyr20, Arg21, Gly22, Tyr23, Lys96 and Lys97) is significantly larger for **CeK$_2$** than for **CeK** and **ZrL**. This kind of conformational process might initiate a secondary structure decrease of the α–helical part required to expose the cleave site I to the hydrolysis catalyst. In the case of the simulation of the **CeK$_2$** anion at site II, the anion does not stay interacting with Arg45 as reflected in the low average interaction energy (**Figure 3.9**). Instead, the anion is released into the solution and/or it moves through protein surface interacting with other cationic sites. Compared to interaction occurring at the vicinity of site I, here the topology of the protein does not allow **CeK$_2$** anion interaction with the two Keggin units simultaneously. Consequently, the POM has a larger surface exposed to the solvent that pulls the whole POM towards the bulk of the solution. Thus, the *interaction strength* at site II (–224 kJ·mol^{-1}) is weaker than that of **CeK$_2$** for site I (–260 kJ·mol^{-1}).

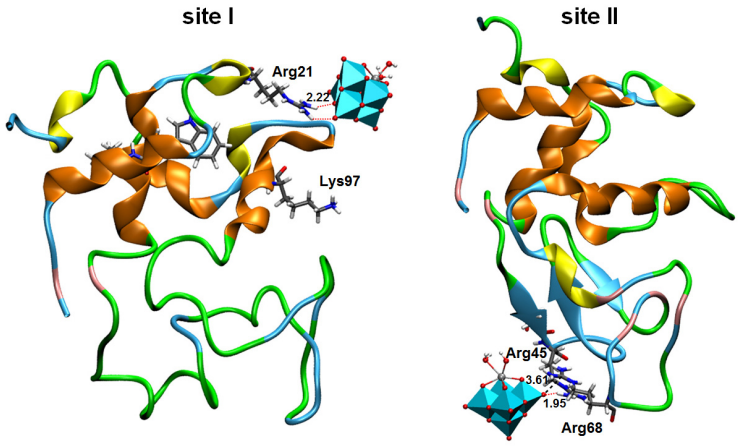

Figure 3.11 | Illustrative snapshots of **ZrL**···HEWL interaction at site I and II taken at 40 ps of run 1 and 560 ps of run1, respectively (interaction energies –120 and –195 kJ·mol^{-1}). Left: the most strongly interacting amino acids for simulation at site I: Arg21 (–85 kJ·mol^{-1}). Right: those for simulation at site II: Arg45 and Arg68 (–69 and –114 kJ·mol^{-1}). Distances in Å.

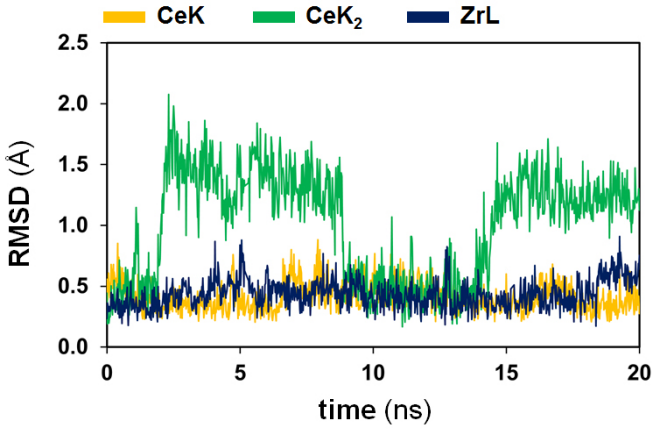

Figure 3.12 | RMSD values of the protein backbone involved in the interaction site I (residues: 20, 21, 22, 23, 96, 97) as a function of simulation time for a selected run of 20 ns. Simulations for **CeK** (yellow), **CeK_2** (green), and **ZrL** anions (blue).

The interaction mode of **ZrL** anion with the protein resembles that of **CeK**; the basic oxygen atoms of the POM framework form hydrogen bonds and the Zr–substituted moiety mostly points towards the solvent (see **Figure 3.11**). In line with this fact, a recent study showed the electrostatic POM···protein interactions are not influenced by the nature of the substituted metal ion, as four different ions embedded in the same POM archetype gave rise to isostructural POM···protein co–crystals.[13b] However, the persistence of the interactions is significantly shorter as reflected by the average interaction energies with individual residues in **Figure 3.9**. The smaller size of the anion does not allow **ZrL** to interact simultaneously with several residues so effectively. For example in site I, the anion interacts alternatively with Arg21 and Lys97 jumping from one residue to the other. However, the *interaction strength* of **ZrL** (–168 kJ·mol^{-1}) is similar to that of **CeK** (–178 kJ·mol^{-1}) because the higher charge density of **ZrL** atoms can lead to stronger interactions with individual amino acids.

3.4 Concluding Remarks

In this work we report for the first time the use of molecular dynamics (MD) simulations to analyze the interaction between proteins and polyoxometalates by using the specific case of hen egg–white lysozyme (HEWL) and three different POMs including 1:1

and 1:2 Ce^{IV}–monosubstituted Keggin POMs (**CeK** and **CeK_2**, respectively) and Zr^{IV}–monosubstituted Lindqvist POM (**ZrL**).

In the MD simulations with the **CeK** anion, we have identified two sites of the protein in which the POM interacts strongly that can be related to the observed selectivity in hydrolytic activity of Ce^{IV}– and Zr^{IV}–substituted POMs towards the Trp28–Val29 (site I) and Asn44–Arg45 (site II) bonds. The **CeK** anion interacts strongly with Arg21 at an entrance channel to the cleavage site I buried in a hydrophobic pocket, and with Arg45 directly at site II. Both interactions occur through the POM framework with the catalytically active Ce^{IV} center pointing towards the solvent. This is in full agreement with the X–ray structures obtained from co–crystallization of HEWL and a different TM–substituted POMs.[11–13] Thus, the modeling also established a relationship between the non–bonding electrostatic type interaction of the **CeK** anion with HEWL and the observed selectivity of the hydrolysis.

In general, the interaction of POMs with HEWL involves charge attraction and hydrogen boding of the basic oxygen atoms of POM framework with the side chains of positively charged amino acids (arginine and lysine) and of polar uncharged amino acids (tyrosine, serine and asparagine). The formation of hydrogen bonding with the N–H amide group of the main protein chain is also plausible, although its extent is less important. Moreover, depending on the size and shape of the polyoxoanion the cooperative effects, in which several amino acids interact simultaneously with the oxide framework, are enhanced or decreased.

The protein affinity of the **CeK** anion is higher than for **CeK_2** and **ZrL** anions. The Keggin–type **CeK** anion is less hydrophilic reducing the solvation energies and it has the right size and shape for accepting the additive effect of several amino acids simultaneously. The larger and more charged dimeric **CeK_2** anion has more charge density and larger solvent–accessible surface that increases its hydrophilicity and reduces its affinity to proteins. However, the **CeK_2** anion can interact very strongly with some sections of the protein through its two dimeric units at once, causing some structural changes in HEWL. They can include an opening of the entrance channel to cleavage site I that could expose the peptide bond to be hydrolyzed. The smaller **ZrL** anion has high charge density that increases its hydrophilicity, and in addition, its size and shape do not allow interaction with several amino acids simultaneously so effectively causing the lowest protein affinity among the series of studied POMs. Thus, these simulations demonstrated that an optimal

interaction POM···protein should balance charge and size. In addition, the study proves the feasibility of this computational approach, opening up new opportunities to study range of other POM···protein interaction and other chemical processes, as shown in the following chapters of this thesis.

3.5 Supplementary Material

Animations of some representative simulations discussed in this chapter can be accessed by scanning the following QR codes with a smartphone or though the URLs below.

CeK interacting at site I	**CeK** interacting at site II
https://youtu.be/WEXpx7JUmYo	https://youtu.be/GAvsmaSBXbg
CeK_2 interacting at site II	**ZrL** interacting at site I
https://youtu.be/LM_9irPW7us	https://youtu.be/8wm2F_F8fQk

References

1. a) Absillis G.; Parac–Vogt, T. N. *Inorg. Chem.* **2012**, *51*, 9902–9910; b) Giang T. L. H.; Absillis G.; Parac–Vogt, T. N. *Dalton Trans.* **2013**, *42*, 10929–10938; c) Giang, T. L. H.; Absillis, G.; Bajpe, S. R.; Martens, J. A.; Parac–Vogt, T. N. *Eur. J. Inorg. Chem.* **2013**, *26*, 4601–4611; d) Vanhaecht, S.; Absillis, G.; Parac–Vogt, T. N. *Dalton Trans.* **2013**, *42*, 15437–15446; e) Sap, A.; Absillis, G.; Parac–Vogt, T. N. *Dalton Trans.* **2015**, *44*, 1539–1548; f) Ly, H. G. T.; Absillis, G.; Parac–Vogt, T. N. *Eur. J. Inorg. Chem.* **2015**, *13*, 2206–2215; g) Ly, H. G. T.; Mihaylov, T.; Absillis, G.; Pierloot, K.; Parac–Vogt, T. N. *Inorg. Chem.* **2015**, *54*, 11477–11492.
2. Stroobants, K.; Moelants, E.; Ly, H. G. T.; Proost, P.; Bartik K.; Parac–Vogt, T. N. *Chem. Eur. J.* **2013**, *19*, 2848–2858.
3. a) Stroobants, K.; Absillis, G.; Moelants, E.; Proost P.; Parac–Vogt, T. N. *Chem. Eur. J.* **2014**, *20*, 3894–3897; b) Stroobants, K.; Goovaerts, V.; Absillis, G.; Bruylants, G.; Moelants, E.; Proost P.; Parac–Vogt, T. N. *Chem. Eur. J.* **2014**, *20*, 9567–9577.
4. Ly, H. G. T.; Absillis, G.; Janssens, R.; Proost, P.; Parac–Vogt, T. N. *Angew. Chem. Int. Ed.* **2015**, *54*, 7391–7394.
5. a) Quanten, T.; Mayaer, T. D.; Shestakova, P.; Parac–Vogt, T. N. *Front. Chem.* **2018**, *6*, 372; b) Sap, A.; Van Tichelen, L.; Mortier, A.; Proost, P.; Parac–Vogt, T. N. *Eur. J. Inorg. Chem.* **2016**, *32*, 5098–5105.
6. a) Goovaerts, V.; Stroobants, K.; Absillis G.; Parac–Vogt, T. N. *J. Inorg. Biochem.* **2015**, *150*, 72–80; b)Stroobants, K.; Saadallah, D.; Bruylants, G.; Parac–Vogt, T. N. *Phys. Chem. Chem. Phys.*, **2014**, *16*, 21778–21787; c) Ly, H. G. T.; Parac–Vogt, T. N. *ChemPhysChem* **2017**, *18*, 2451–2458.
7. a) López, X.; Carbó, J. J.; Bo, C.; Poblet, J. M. *Chem. Soc. Rev.*, **2012**, *41*, 7537–7571; b) López, X.; Miró, P.; Carbó, J. J.; Rodríguez–Fortea, A.; Bo, C.; Poblet, J. M. *Theor. Chem. Acc.* **2011**, *128*, 393–404.
8. a) Narasimhan, K.; Pillay, S.; Ahmad, N. R. B.; Bikadi, Z.; Hazai, E.; Yan, L.; Kolatkar, P. R.; Pervushin, K.; Jauch, R. *ACS Chem. Biol.* **2011**, *6*, 573–581; b) Prudent, R.; Sautel, C. F.; Cochet, C. *Biochim. Biophys. Acta* **2010**, *1804*, 493–498; c) Prudent, R.; Moucadel, V.; Laudet, B.; Barette, C.; Lafanechere, L.; Hasenknopf, B.; Li, J.; Bareyt, S.; Lacote, E.; Thorimbert, S.; Malacria, M.; Gouzerh, P.; Cochet, C. *Chem. Biol.* **2008**, *15*, 683–692; d) Hu, D.; Shao, C.; Guan, W.; Su, Z.; Sun, J. *J. Inorg. Biochem.* **2007**, *101*, 89–94; e) Tiago, T.; Martel, P.; Gutierrez–Merino, C.; Aureliano, M. *Biochim. Biophys. Acta* **2007**, *1774*, 474–480; f) Pezza, R. J.; Villarreal, M. A.; Montich, G. G.; Argaña, C. E. *Nucleic Acids Research* **2002**, *30*, 4700–4708 ; g) Judd, D. A.; Nettles, J. H.; Nevins, N.; Snyder, J. P.; Liotta, D. C.; Tang, J.; Ermolieff, J.; Schinazi, R. F.; Hill, C. L. *J. Am. Chem. Soc.* **2001**, *123*, 886–897; h) Sarafianos, S. G.; Kortz, U.; Pope, M. T.; Modak, M. J. *Biochem. J.* **1996**, *319*, 619–626.
9. a) Li, M.; Xu, C.; Ren, J.; Wang, E.; Qu, X. *Small* **2013**, *9*, 3455–3461; b) Pu, F.; Wang, E.; Jiang, H.; Ren, J. *Mol. BioSyst.* **2013**, *9*, 113–120; c) Nabika, H.; Inomata, Y.; Itoh, E.; Unoura, K. *RSC Adv.* **2013**, *3*, 21271–21274; d) Geng, J.; Li, M.; Ren, J.; Wang, E.; Qu, X. *Angew. Chem. Int. Ed.* **2011**, *50*, 4184–4188; e) Wu, Q.; Wang, J.; Zhang, L.; Hong, A.; Ren, J. *Angew. Chem., Int. Ed.* **2005**, *44*, 4048–4052.
10. a) Zhang, T.; Li, H. W.; Wu, Y.; Wang, Y.; Wu, L. *Chem. Eur. J.* **2015**, *21*, 9028–9033; b) Li, H. W.; Wang, Y.; Zhang, T.; Wu, Y.; Wu, L. *Chem PlusChem.* **2014**, *79*, 1208–1213.
11. Sap, A.; De Zitter, E.; Van Meervelt L.; Parac–Vogt, T. N. *Chem. Eur. J.* **2015**, *21*, 11692–11695.
12. Vandebroek, L.; Van Meervelt, L.; Parac–Vogt, T. N. *Acta Crystallogr. C* **2018**, *74*, 1348–1354.

13. a) Vandebroek, L.; De Zitter, E.; Ly, H. G. T.; Conić, D.; Mihaylov, T.; Sap, A.; Proost, P.; Pierloot, K.; Van Meervelt, L.; Parac–Vogt, T. N. *Chem. Eur. J.* **2018**, *24*, 10099–10108; b) Vandebroek, L.; Mampaey, Y.; Antonyuk, S.; Van Meervelt, L.; Parac–Vogt, T. N. *Eur. J. Inorg. Chem.* **2019**, *3*, 506–511.
14. a) Hess, B.; Kutzner, C.; Van Der Spoel, D.; Lindahl, E. *J. Chem. Theory Comput.* **2008**, *4*, 435–447; b) Van Der Spoel, D.; Lindahl, E.; Hess, B.; Groenhof, G.; Mark, A. E.; Berendsen, H. J. C. *J. Comput. Chem.* **2005**, *26*, 1701–1718; c) Berendsen, H. J. C.; Van Der Spoel, D.; van Drunen, R. *Comput. Phys. Commun.* **1995**, *91*, 43–56.
15. Wang, J. M.; Cieplak, P.; Kollman, P. A. *J. Comput. Chem.* **2000**, *21*, 1049–1074.
16. a) Chaumont, A.; Wipff, G. *Phys. Chem. Chem. Phys.* **2008**, *10*, 6940–6953; b) Chaumont, A.; Wipff, G. *J. Phys. Chem. C* **2009**, *113*, 18233–18243; c) Chaumont, A.; Wipff, G. *C. R. Chimie*, **2012**, *15*, 107–117.
17. a) Leroy, F.; Miró, P.; Poblet, J. M.; Bo, C.; Bonet Ávalos, J. *J. Phys. Chem. B* **2008**, *112*, 8591–8599; b) López, X.; Nieto–Draghi, C.; Bo, C.; Avalos, J. B.; Poblet, J. M. *J. Phys. Chem. A* **2005**, *109*, 1216–1222.
18. Frisch, M. J.; Trucks, G. W.; Schlegel, H. B.; Scuseria, G. E.; Robb, M. A.; Cheeseman, J. R.; Scalmani, G.; Barone, V.; Mennucci, B.; Petersson, G. A.; Nakatsuji, H.; Caricato, M.; Li, X.; Hratchian, H. P.; Izmaylov, A. F.; Bloino, J.; Zheng, G.; Sonnenberg, J. L.; Hada, M.; Ehara, M.; Toyota, K.; Fukuda, R.; Hasegawa, J.; Ishida, M.; Nakajima, T.; Honda, Y.; Kitao, O.; Nakai, H.; Vreven, T.; Montgomery, J. A., Jr.; Peralta, J. E.; Ogliaro, F.; Bearpark, M.; Heyd, J. J.; Brothers, E.; Kudin, K. N.; Staroverov, V. N.; Kobayashi, R.; Normand, J.; Raghavachari, K.; Rendell, A.; Burant, J. C.; Iyengar, S. S.; Tomasi, J.; Cossi, M.; Rega, N.; Millam, J. M.; Klene, M.; Knox, J. E.; Cross, J. B.; Bakken, V.; Adamo, C.; Jaramillo, J.; Gomperts, R.; Stratmann, R. E.; Yazyev, O.; Austin, A. J.; Cammi, R.; Pomelli, C.; Ochterski, J. W.; Martin, R. L.; Morokuma, K.; Zakrzewski, V. G.; Voth, G. A.; Salvador, P.; Dannenberg, J. J.; Dapprich, S.; Daniels, A. D.; Farkas, Ö.; Foresman, J. B.; Ortiz, J. V.; Cioslowski, J.; Fox, D. J. Gaussian 09, revision C.01; Gaussian, Inc.: Wallingford, CT, **2009**.
19. a) Becke, A. D. *Phys. Rev. A* **1988**, *38*, 3098–3100; b) Perdew, J. P. *Phys. Rev. B* **1986**, *33*, 8822–8824.
20. Hay, P. J.; Wadt, W. R. *J. Chem. Phys.* **1985**, *82*, 270–283.
21. a) Cao X.; Dolg, M. *J. Mol. Struct.* **2002**, *581*, 139–147; b) Dolg, M.; Stoll, H.; Preuss, H. *J. Chem. Phys.* **1989**, *90*, 1730–1734.
22. Cancès, E.; Mennucci B.; Tomasi, J. *J. Chem. Phys.* **1997**, *107*, 3032–3041.
23. Rappe, A. K.; Casewit, C. J.; Colwell, K. S.; Goddard, W. A.; Skiff, W. M. *J. Am. Chem. Soc.* **1992**, *114*, 10024–10035.
24. Jiménez–Lozano, P.; Carbó, J. J.; Chaumont, A.; Poblet, J. M.; Rodríguez–Fortea, A.; Wipff, G. *Inorg. Chem.* **2014**, *53*, 778–786.
25. Pechkova, E.; Tripathi S. K.; Nicolini, C. DOI: 10.2210/pdb2213ijv/pdb
26. Jorgensen, W. L.; Chandrasekhar, J.; Madura, J. D.; Impey, R. W.; Klein, M. L. *J. Chem. Phys.* **1983**, *79*, 926–935.
27. Darden, T.; York D.; Pedersen, L. *J. Chem. Phys.* **1993**, *98*, 10089–10092.
28. Berendsen, H. J. C.; Postma, J. P. M.; van Gunsteren, W. F.; DiNola, A.; Haak, J. R. *J. Chem. Phys.* **1984**, *81*, 3684–3690.
29. Hockney, R. W.; Goel, S. P.; Eastwood, J.; Quiet, J. *J. Comp. Phys.* **1974**, *14*, 148–158.
30. Hess, B.; Bekker, H.; Berendsen, H. J. C.; Fraaije, J. G. E. M. *J. Comp. Chem.* **1997**, *18*, 1463–1472.
31. Steiner, T. *Angew. Chem. Int. Ed.* **2002**, *41*, 48–76.

32. Zhou, Y.; Zheng, L.; Han, F.; Zhang, G.; Ma, Y.; Yao, J.; Keita, B.; de Oliveira, P.; Nadjo, L. *Colloids Surf. A* **2011**, *375*, 97–101.
33. a) Kowalewski, B.; Poppe, J.; Demmer, U.; Warkentin, E.; Dierkes, T.; Ermler, U.; Schneider, K. *J. Am. Chem. Soc.* **2012**, *134*, 9768–9774; b) Mauracher, S. G.; Molitor, C.; Al–Oweini, R.; Kortz, U.; Rompel, A. *Acta Crystallogr. Sect. D* **2014**, *70*, 2301–2315.
34. Bijelic, A.; Molitor, C.; Mauracher, S. G.; Al–Oweini, R.; Kortz, U.; Rompel, A. *ChemBioChem* **2015**, *16*, 233–241.
35. Zebisch, M.; Krauss, M.; Schafer, P.; Strater, N. *Acta Crystallogr. D* **2014**, *70*, 1147–1154.
36. López, X.; Fernández, J. A.; Poblet, J. M. *Dalton Trans.* **2006**, *2006*, 1162–1167.
37. a) Zhang, G.; Keita, B.; Craescu, C. T.; Miron, S.; de Oliveira, P.; Nadjo, L. *Biomacromolecules*, **2008**, *9*, 812–817; b) Zhang, G.; Keita, B.; Craescu, C. T.; Miron, S.; de Oliveira, P.; Nadjo, L. *J. Phys. Chem. B* **2007**, *111*, 11253–11259.
38. a) Bijelic, A.; Rompel, A. *Coord. Chem. Rev.* **2015**, *299*, 22–38; b) Bijelic, A.; Rompel, A. *Acc. Chem. Res.* **2017**, *50*, 1441–1448.

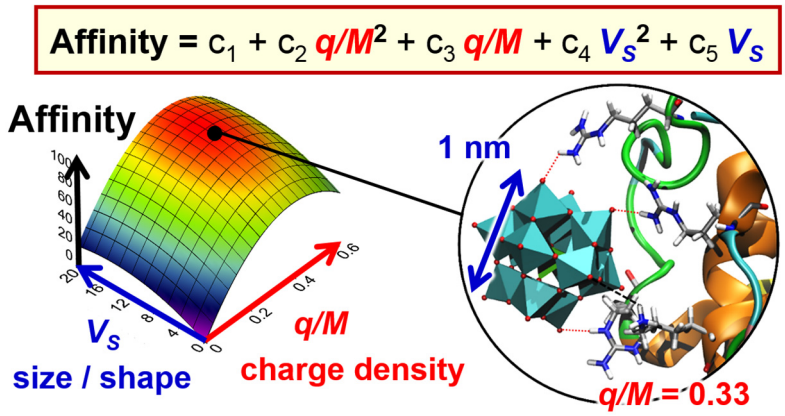

Chapter 4

Structure–Activity Relationships for the Affinity of Chaotropic Polyoxometalate Anions towards Proteins

UNIVERSITAT ROVIRA I VIRGILI
NEW HORIZONS IN COMPUTATIONAL MODELING OF POLYOXOMETALATES:
BIOLOGICAL ACTIVITY, ENERGY STORAGE AND SUSTAINABLE CATALYSIS.
Albert Solé Daura

CHAPTER 4

Structure–Activity Relationships for the Affinity of Chaotropic Polyoxometalate Anions towards Proteins

Prompted by the results discussed in the previous chapter, here we studied the influence of the POM composition into their affinity to biological systems by means of atomistic Molecular Dynamics (MD) simulations. The variations in the affinity to hen egg–white lysozyme (HEWL) were analyzed along two series of POMs whereby the charge or the size and shape of the metal cluster are modified systematically, aiming to evaluate the individual effect of each parameter. The former comprises five POMs of the same size and shape but different charges: $[X^{n+}W_{12}O_{40}]^{(8-n)-}$ *(*$X = S^{VI}$, P^{V}, Si^{IV}, Al^{III}, Zn^{II}*). The second series is constituted by four POM structures differing in size and shape but featuring similar charge densities:* $[W_6O_{19}]^{2-}$, $[SiW_{12}O_{40}]^{4-}$, $[P_2W_{18}O_{62}]^{6-}$ *and* $[HThP_5W_{30}O_{110}]^{10-}$ *with Lindqvist–, Keggin–, Wells–Dawson– and Preyssler–type structure, respectively. In addition, we developed a quantitative multidimensional model for protein affinity with predictive ability (*$r^2 = 0.97$; $q^2 = 0.88$*) using two molecular descriptors that account for the charge density (charge per metal atom ratio; q/M) and the size and shape of the POM (shape weighted–volume;* V_S*).*

4.1 Background

It is widely accepted that the biological activity of POMs depends largely on their ability to establish non–bonding interactions with peptides and proteins.[1] In turn, these interactions were recognized to be influenced by the electrostatic charge of the POM, its size and shape in host–guest interactions, and its composition.[1–16] Recently, the affinity of POMs towards biomolecules have been attributed to the *superchaotropic* character of the POM anion, providing a broader description of the physicochemical foundations of POM–protein interactions.[5] In chaotropic anions, typically large and charge–delocalized, the ion–dipole interaction with the solvent is less directional, and therefore, the desolvation process upon binding does not change the bulk water structure in large extent reducing the entropy penalty. For example, Nadjo and co–workers found this thermodynamic fingerprint in the binding of Keggin $[H_2W_{12}O_{40}]^{6-}$ anion to human serum albumin (HSA) protein, where the binding reaction is enthalpically driven (ΔH = –50

kJ·mol^{-1}) with a small, unfavourable entropy component ($T\Delta S$ = –12 kJ·mol^{-1}) due to the minimal dehydration entropy change.[6]

Several attempts to set empirical structure–activity trends relating the activity of POMs to their composition have been reported in the literature,[2,4,6,7,11,12,15,16] however, they do not provide an unambiguous picture. Due to limitations in POM stability under experimental conditions, the number of analyzed structures is usually too low to set clear relationships. It is also common that tested POMs differ in more than one feature at a time, hampering the interpretation of the results. In this regard, computational modeling would allow performing systematic variations on single parameters of well–defined POM structures and thus making possible this type of fundamental studies. In a previous contribution, we provided a computational, atomistic description of the POM–protein interactions based on molecular dynamics simulations (MD).[17] The study was backed by experimentally reported systems formed by model hen egg–white lysozyme (HEWL) protein and experimentally reported Ce^{IV}– and Zr^{IV}–substituted POMs.[18–20] Simulations revealed that POMs interact mainly with the side chains of the positively charged and polar uncharged residues via charge attraction and hydrogen bonding of the basic oxygen atoms of POM framework.[17] Then, Prabhakar and co–workers have computationally characterized interactions of the same nature between POMs and HSA protein.[21]

Herein, we study how the affinity to HEWL protein varies along two series of POMs in which the charge and the size of the POM are systematically modified (**Figure 4.1**). Aiming to understand the influence of each individual POM feature, we analyze at atomic level the interaction of POMs with both the protein and the solvent. Finally, we are able to build a multidimensional correlation between the POM structure and its protein affinity by using two molecular descriptors: the charge per metal ratio[17,22] and the novel descriptor *shape–weighted volume* (V_S).

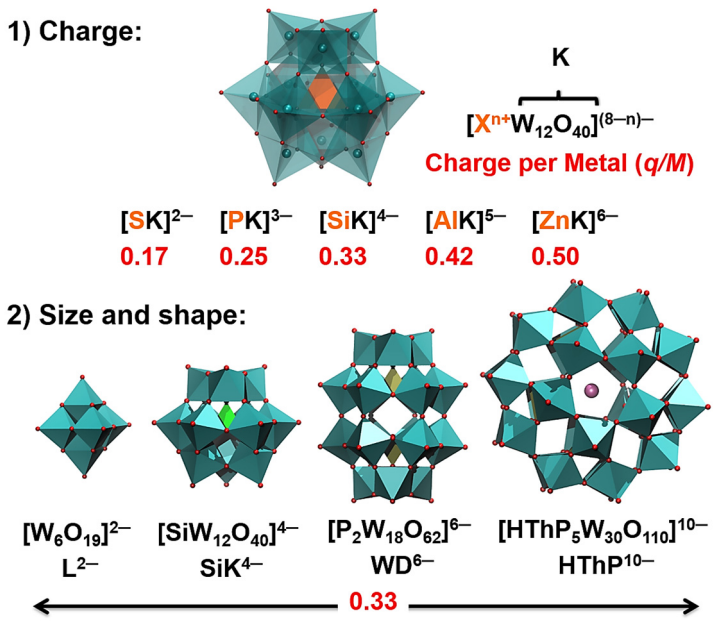

Figure 4.1 | Polyhedral representation of the model POM structures used to evaluate the influence of the charge (top) and the size and shape (bottom) of the POM on POM···protein interactions.

4.2 Computational Details

The methodology used for classical simulations is analogous to that explained in Chapter 3. Lennard–Jones parameters for W and O atoms of the POMs were taken from previous works,[17,23,24] and those for Al^{III}, Si^{IV} and Th^{IV} were taken from the UFF force field.[25] CHelpG atomic charges for the different POM structures were obtained using the same computational approach described in Chapter 3.

For the MD simulations, the protein was embedded in a cubic solvent box in which 1 POM was inserted randomly, and the initial POM position was kept for all the runs. The box size was set to keep the same V_{POM}/V_{total} in all the simulations and roughly, the molal concentration of POM ($g_{POM} \cdot L_{water}^{-1}$). In particular, when simulating POMs of different sizes, it is of great importance to maintain the same volume ratio in order to avoid overestimations in quantifying the interaction of bulkier POMs or underestimate it for smaller ones. Cl^- or Na^+ counter ions were added to neutralize the system. Detailed information of each simulated system can be found in **Table 4.1**.

Before the production runs, all the systems were equilibrated by 1000 steps of energy minimization followed by a 250 ps simulation fixing the solute molecules in order to relax the solvent around them. Then, a 250 ps at constant volume (NVT) with the solvent relaxed, a 500 ps simulation at constant temperature (300 K) and pressure (1 atm) to stabilize the pressure and thus the density and a last 250 ps simulation (NVT). Finally, five independent runs of 20 ns dynamics were performed at constant volume and at 300 K for each system. For the sake of comparison, some NVT simulations were repeated using the velocity rescaling algorithm[26] and found that results do not vary significantly.

Table 4.1 | Main characteristics of the simulated systems to study the effect of the charge and the size of the polyoxoanion.[a]

system	box size (Å^3)	N_{water}	C_{POM} (g·L^{-1})
1 $[SW_{12}O_{40}]^{2-}$ (**SK^{2-}**) + 6 Cl^-	79.5^3	15845	9.51
1 $[PW_{12}O_{40}]^{3-}$ (**PK^{3-}**) + 5 Cl^-	79.4^3	15846	9.54
1 $[SiW_{12}O_{40}]^{4-}$ (**SiK^{4-}**) + 4 Cl^-	79.5^3	15847	9.50
1 $[AlW_{12}O_{40}]^{5-}$ (**AlK^{5-}**) + 3 Cl^-	79.4^3	15848	9.53
1 $[ZnW_{12}O_{40}]^{6-}$ (**ZnK^{6-}**) + 2 Cl^-	79.4^3	15849	9.66
1 $[W_6O_{19}]^{2-}$ (**L^{2-}**) + 6 Cl^-	62.6^3	7488	9.51
1 $[P_2W_{18}O_{62}]^{6-}$ (**WD^{6-}**) + 2 Cl^-	91.4^3	24481	9.49
1 $[HThP_5W_{30}O_{110}]^{10-}$ (**HThP^{10-}**) + 2 Na^+	110.4^3	43542	9.45

[a] All systems contain 1 HEWL protein (q = 8+).

4.3 Results and Discussion

4.3.1 Influence of the POM charge.

To understand how the POM charge affects their interaction with proteins, we initially simulated HEWL protein in solution with five different POMs of the same size and shape but different overall charges. The selected POM structures are represented in **Figure 4.1** (top) and comprise five Keggin–like anions of general formula $[X^{n+}W_{12}O_{40}]^{(8-n)-}$ with X^{n+} = S^{VI}, P^{V}, Si^{IV}, Al^{III} and Zn^{II}, labeled as **SK^{2-}**, **PK^{3-}**, **SiK^{4-}**, **AlK^{5-}** and **ZnK^{6-}**, respectively. This array of POMs allowed covering a range of charges from 2–, for the least charged

SK^{2-} to 6– for **ZnK**$^{6-}$. For every polyoxoanion, we performed a set of five independent MD runs of 20 ns each. The POM trajectories are graphically represented in the Appendix (**Figure A4.1**) as color evolution of their center of mass around the protein.

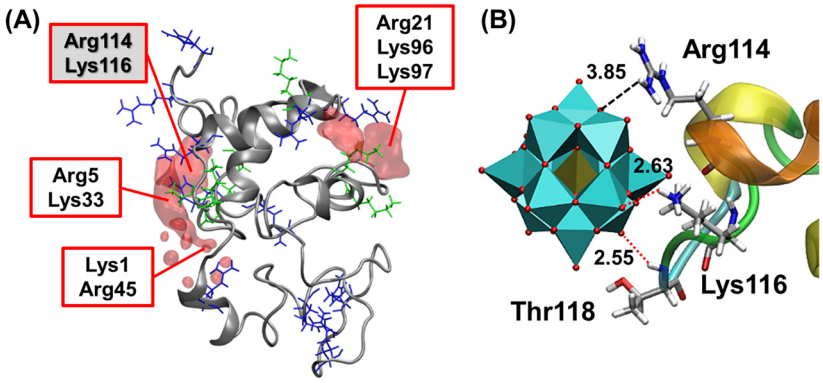

Figure 4.2 | (A) Volumetric density of the **PK**$^{3-}$ contacts on the protein surface (POM···protein distance ≤ 3.5 Å) averaged over 100 ns of MD trajectories. Positively charged arginine and lysine residues are depicted in blue and green sticks, respectively. (B) Typical snapshot of the interaction of **PK**$^{3-}$ at a positively charged patch on HEWL surface, comprising Arg114, Lys116, and Thr118. Red dotted lines and black dashed lines represent H–bonds and purely electrostatic contacts, respectively. Distances in Å.

To illustrate the specific interactions of Keggin anions with positively charged and polar amino acids of HEWL, we selected the archetypal **PK**$^{3-}$ anion. The volumetric density map in **Figure 4.2**A represents the protein regions interacting with the POM, which mostly involve positively charged amino acids such as arginines and lysines. Notably, the two binding sites containing Arg21 and Arg45, respectively, had been actually observed in crystal X–ray structures of noncovalent complexes with different transition metal–substituted Keggin and Wells–Dawson anions.[18,20] In addition, these two positive patches on the protein surface were related to the selective peptide bond hydrolysis catalyzed by Lewis acid metal–substituted POMs.[17,27] X–ray studies have identified an additional binding site containing Arg128, which is placed at a C–terminus end of the HEWL protein.[18,19] This is an unstructured region of the protein, whose interaction with the POMs was suggested to induce a higher degree of structural stability in the solid state,[20a] explaining why the interaction of **PK**$^{3-}$ anion is scarcely observed in the simulations in solution. **Figure 4.2**B shows a selected snapshot with representative interactions between the oxygen atoms of POM framework and the amino acids of HEWL. As it had been computationally characterized[17] and experimentally observed,[18–20] the nature of these

interactions comprises mainly electrostatic interactions, hydrogen bonding and water–mediated interactions with positively–charged and polar amino acids.

Inspection of the trajectories reveals well–differentiated behaviors of POMs over the protein surface (see **Figure A4.1** in the Appendix). Depending on the charge, the anion is set in a specific cationic pocket or it moves over the protein surface and in and out of the solution. To evaluate the affinity of the POMs to the protein, the persistence of POM···protein contacts was quantified in terms of *% time binding*. This parameter was calculated for each individual POM anion as the number of snapshots in which the POM is closer than 3.5 Å to the protein and normalized by the total number of snapshots.[17] **Figure 4.3** plots the computed values of *% time binding* as a function of POM charge and **Table 4.2** collects the numerical values. The *% time binding* follows the same trend as the peak integration of POM units in the radial distribution function (RDF) between the POM and protein surface (see **Figure 4.4**), further supporting the use of this descriptor for evaluating POM affinity.

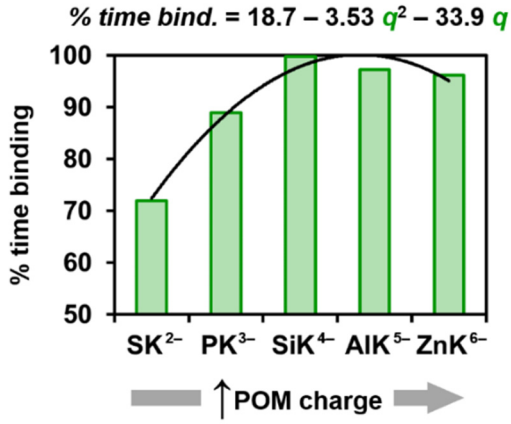

Figure 4.3 | Protein affinity, measured as percentage of simulated time in which POM interacts with HEWL protein (% *time binding*), as function of the POM charge in $[X^{n+}W_{12}O_{40}]^{(8-n)-}$. The relationship was fitted to a quadratic polynomial regression model ($r^2 = 0.98$): solid black curve and equation on the top.

Table 4.2 | Comparison of the HEWL affinity, and the protein and solvent interactions for the five Keggin–type POMs.[a]

anion	% time binding	$E_{POM\cdots HEWL}$	$E_{POM\cdots water}$	H–bonds 1st shell
$[SW_{12}O_{40}]^{2-}$ (**SK^{2-}**)	72.0	–360	–572	7.3
$[PW_{12}O_{40}]^{3-}$ (**PK^{3-}**)	88.9	–571	–823	9.4
$[SiW_{12}O_{40}]^{4-}$ (**SiK^{4-}**)	99.8	–777	–1153	12.9
$[AlW_{12}O_{40}]^{5-}$ (**AlK^{5-}**)	97.2	–1049	–1543	18.7
$[ZnW_{12}O_{40}]^{6-}$ (**ZnK^{6-}**)	96.2	–1216	–1986	23.7

[a] The *% time binding* averaged over 100 ns of MD trajectories sampling data every 4 ps. Interaction energies, $E_{POM\cdots HEWL}$ and $E_{POM\cdots water}$ in kJ·mol^{-1}, obtained from 50 ns simulation in the absence of solvent or protein, respectively. Number of H–bonds in the first solvation shell derived from the same MD simulations of POMs in water.

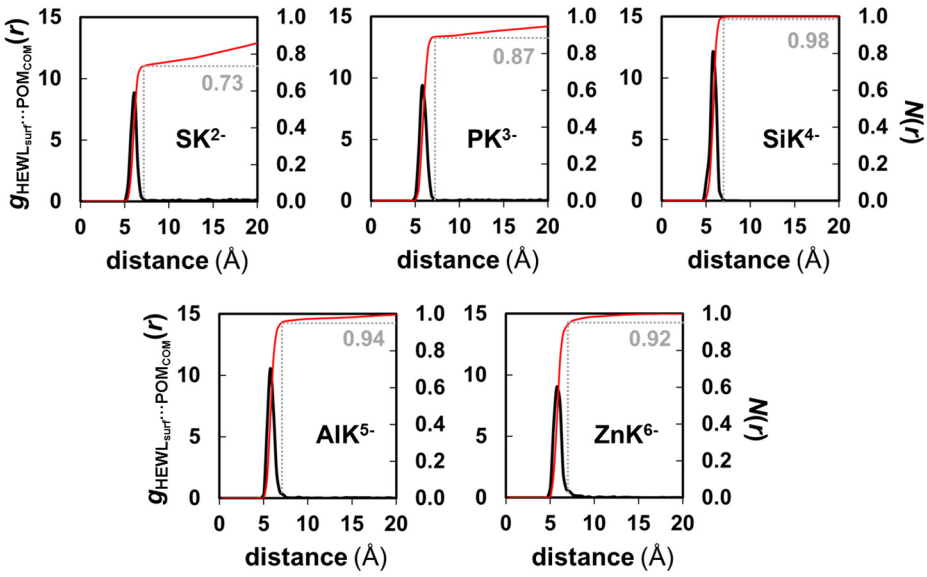

Figure 4.4 | Radial distribution functions (RDFs) between the center of mass of the different Keggin–type anions and the closest atom in HEWL averaged over 100 ns of MD simulation. Black and red solid lines represent the RDFs themselves and the coordination number $N(r)$, that is the integration of the RDF along the distance. The integrations of the peaks in the RDF are shown in gray numbers.

Interestingly, there is no linear relationship between POM charge and protein affinity. Instead, we found a quadratic polynomial correlation ($r^2 = 0.98$) in which the **SiK^{4-}** anion,

with an intermediate charge value of 4–, shows the highest protein affinity (see **Figure 4.3**). Experimentally, the higher POM charge had been correlated to larger binding affinity in the inhibition of amyloid β peptides,[7] and the selective precipitation of prions by the POM complexes.[14] This apparent charge–affinity relationship would only explain the increasing domain of the equation reported in **Figure 4.3**. However, we suspect that the analyzed datasets covered only a narrow range of charges within the same POM size, providing a partial description of the effect. In fact, analysis of the interaction between charged ligands and proteins had revealed that binding energy has a quadratic form on the charges of the ligand.[28,29] This complex picture was attributed to the delicate balance between two effects of opposite sign: protein–ligand electrostatic interaction and ligand desolvation incurred upon binding. Thus, too weak electrostatic protein–ligand interaction as well as too strong ligand–solvent interaction in the unbound state result in a sub–optimal binding. According to the quantitative model built by Sulea and Purisima, the intermolecular Coulomb interaction energy increases linearly with the charge while the desolvation energy upon binding has a parabolic form.[29] Moreover, for the analogous, chaotropic borane anions a quadratic relationship was observed between the binding affinity to estrogen receptor and their hydrophobiticy,[30] which can be viewed as the inverse of the charge. The effects governing these non–linear correlations are very intricate at the level of accurate molecular understanding and qualitative predictions; and their atomistic description is still lacking.

Figures 4.5, **4.6** and values of **Table 4.2** (columns 3rd – 5th) collect the results of further analysis of POM interactions with the protein and with water solvent as a function of the anion charge. As **Figure 4.5** shows, the POM···water interaction energy in the absence of the protein follows a quadratic growth with the POM charge, while the POM···protein interaction increases linearly if solvent effects are neglected, in agreement with the electrostatic model proposed by Sulea and Purisima.[29] Thus, the two competing interactions increase with the POM charge at different rates explaining why the POM affinity reaches a maximum at intermediate charge values.

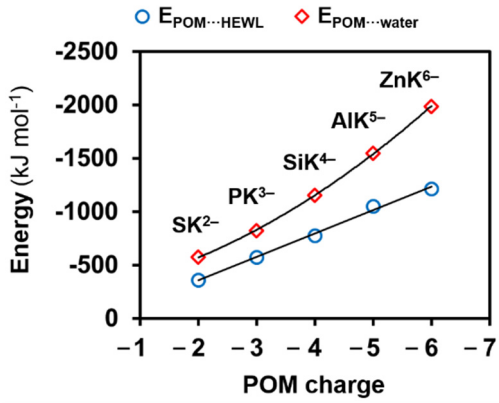

Figure 4.5 | Average POM···HEWL (blue circles) and POM···water (red diamonds) interaction energies (in kJ·mol^{-1}) for the differently charged Keggin–type anions. Simulations performed in the absence of solvent and of protein, respectively. The $E_{POM\cdots HEWL}$ and $E_{POM\cdots water}$ on the POM charge were fitted, respectively, to linear ($r^2 = 0.996$) and to a quadratic polynomial ($r^2 = 0.999$) regression models.

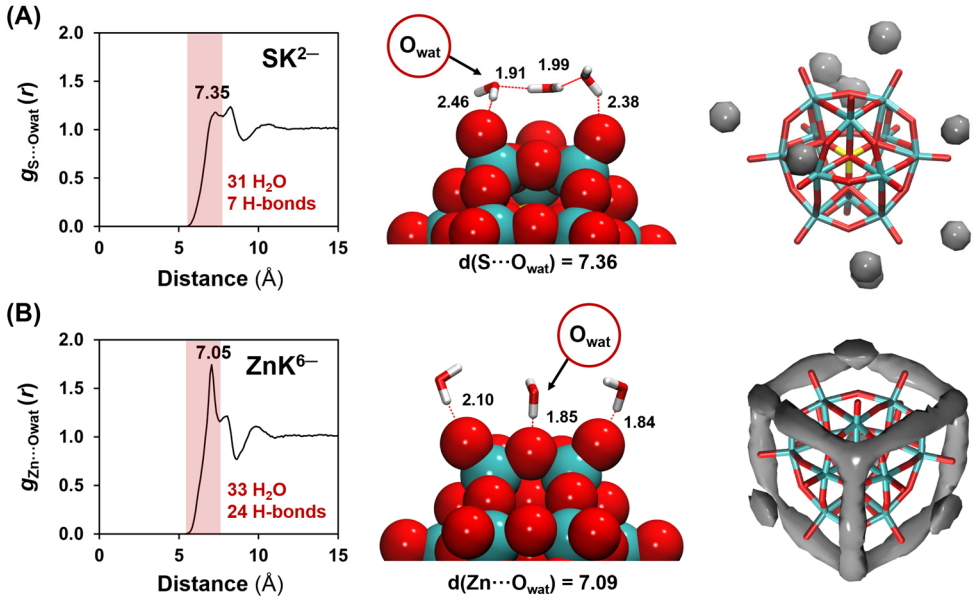

Figure 4.6 | Radial distribution function (RDF) between the POM center of mass and the oxygen atom of water molecules for **SK^{2-}** (A) and **ZnK^{6-}** (B) averaged over the last 20 ns of a 50 ns simulation carried out in the absence of protein. Each RDF is accompanied by a representative snapshot of the water distribution around each POM and a representation of the volumetric density of water molecules gathered in the first peak of each RDF.

To explain the counterintuitive non–linear relationship of the $E_{POM\cdots water}$ with the POM charge, we analyzed the solvation shells around the POM and the variation of hydrogen bonding patterns, which have been used to understand the difference between chaotropic (water–structure–breaking) and kosmotropic (water–structure–forming) properties of ions.[5,31,32] **Figure 4.6** compares the POM···water radial distribution functions (RDFs) for the two extreme charge cases $\mathbf{SK^{2-}}$ and $\mathbf{ZnK^{6-}}$ (see **Figure A4.2** for the other Keggin anions). In going from $\mathbf{SK^{2-}}$ to $\mathbf{ZnK^{6-}}$, there is an appreciable sharpening of the first RDF peak, similar to that observed for a series of polyoxovanadates with different charge.[33] Interestingly, for both POMs the first peak integrates to a similar number of water molecules per anion unit (31 for $\mathbf{SK^{2-}}$ *vs* 33 for $\mathbf{ZnK^{6-}}$), but the average number of anion–water hydrogen bonds increases dramatically, from 7.3 in $\mathbf{SK^{2-}}$ to 23.7 in $\mathbf{ZnK^{6-}}$ (see **Table 4.2** and **Figure 4.6**). **Figure 4.6** also shows typical snapshots illustrative of the difference in hydrogen bonding patterns. In $\mathbf{ZnK^{6-}}$, the first solvation shell of water molecules is more structured and the bridging oxygen of the POM participate more actively in the hydrogen bonding network (**Figures 4.6** and **A4.3**). The more organized water structure in $\mathbf{ZnK^{6-}}$ is reflected in the volumetric density of water molecules surrounding the each POM (**Figure 4.6**).

The first consequence of the change in hydrogen bonding pattern is that increasing the negative charge of the POMs, the strength and the number of hydrogen bonds with water solvent increase, leading to a quadratic growth of the $E_{POM\cdots water}$ interaction energy. Moreover, longer residence of the hydrogen bonds and more localized waters in $\mathbf{ZnK^{6-}}$ (**Figure 4.6**) can be related to slower water dynamics over the anion surface.[34] Therefore, less chaotropic (more kosmotropic) properties are expected for highly charged POMs resulting in larger desolvation energies, and consequently in less affinity towards proteins. On the other hand, for moderately charged POMs the first solvation shell is less structured and diffuses faster, resulting in lower desolvation energies. Overall, to enhance POM affinity towards proteins, one needs to balance the strength of POM···protein and POM···water interactions. For HEWL, this situation is found for the moderately charged $\mathbf{SiK^{4-}}$ anion, but depending on the topology of the biological system, the optimal POM charge might be shifted.

4.3.2 Influence of the POM size and shape.

Next, we varied systematically the size and shape of the POM keeping constant its charge density, using the charge per metal ratio (q/M) as a magnitude that correlates with

the charge density.[17,22] The selected structures with q/M = 0.33 are shown in **Figure 4.1** and comprise: the $[W_6O_{19}]^{2-}$ Lindqvist anion (**L**$^{2-}$), the $[SiW_{12}O_{40}]^{4-}$ Keggin anion (**SiK**$^{4-}$), the $[P_2W_{18}O_{62}]^{6-}$ Wells–Dawson anion (**WD**$^{6-}$), and the $[HThP_5W_{30}O_{110}]^{10-}$ Preyssler–like anion, (**HThP**$^{10-}$). Note that the **HThP**$^{10-}$ anion corresponds to a model structure in which one internal oxygen atom was protonated in order to ensure the same q/M ratio along the series. Moreover, the volume ratio V_{POM}/V_{water} was kept approximately constant, by adjusting the dimension of the simulated system (see **Figure 4.7**) in order to avoid the bias of concentration on POM···protein contacts (9.45 – 9.52 g·L^{-1} range).

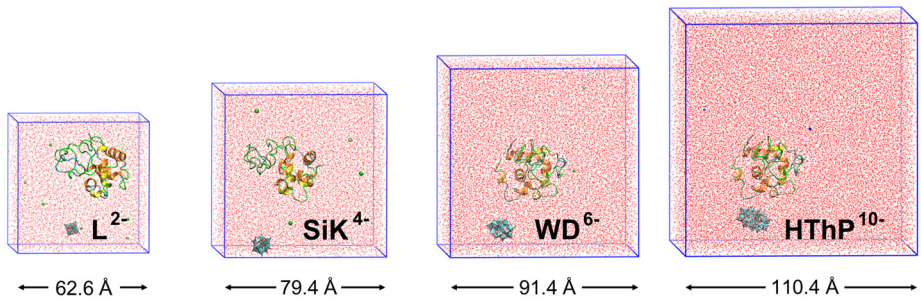

Figure 4.7 | Periodic cubic boxes used to simulate four different systems containing POMs of different size and shape but the same charge density (q/M = 0.33). The dimensions of the boxes were set to keep constant the V_{POM}/V_{water} ratio in such a way that the POM concentrations are, from the left to the right: 9.51, 9.52, 9.49 and 9.45 g·L^{-1}.

Table 4.3 | Comparison of the HEWL affinity and protein and solvent interaction of **L**$^{2-}$, **SiK**$^{4-}$, **WD**$^{6-}$, and **HThP**$^{10-}$ POMs having different size and shape ant the same charge density (q/M = 0.33).[a]

anion	% time binding	$E_{POM\cdots HEWL}$	$E_{POM\cdots water}$/atom	E_{desolv}
$[W_6O_{19}]^{2-}$ (**L**$^{2-}$)	94.2	–152	–34	+172
$[SiW_{12}O_{40}]^{4-}$ (**SiK**$^{4-}$)	99.8	–239	–32	+265
$[P_2W_{18}O_{62}]^{6-}$ (**WD**$^{6-}$)	99.4	–261	–32	+264
$[HThP_5W_{30}O_{110}]^{10-}$ (**HThP**$^{10-}$)	99.0	–325	–32	+267

[a] Interaction energies in kJ·mol^{-1}. $E_{POM\cdots water}$/atom corresponds to the interaction energy with water normalized per solvent–accessible atom, and E_{desolv} accounts for the loss of $E_{POM\cdots water}$ in going from the unbound to the bound situation. Data were sampled every 4 ps from the 100 ns MD trajectories.

Table 4.3 (second column) collects the values of the % *time binding* for the series of POMs with different sizes. All the anions display a high affinity to the protein, indicating

that the *q/M* ratio of 0.33 corresponds to the *optimal* charge density to interact with HEWL. Among the series, the smallest $\mathbf{L}^{2-}$ anion presents a less persistent interaction and it moves over the protein surface and in/out of the solution. Contrastingly, the other anions ($\mathbf{SiK}^{4-}$, $\mathbf{WD}^{6-}$, and $\mathbf{HThP}^{10-}$) interact persistently at a single cationic site at each MD run (see **Figure A4.4**). The sub–optimal interaction of $\mathbf{L}^{2-}$ can be ascribed to the fact that its size cannot interact with several amino acids simultaneously resulting in less efficient contacts with the protein than bigger anions.[17] The average values of anion–solvent interactions normalized by the number of solvent–accessible atoms have very similar values confirming that the differences in the protein affinity are due to the influence of the size, not biased by electrostatics (see **Table 4.3**, third column). There are several experiments that could be directly related to our findings for Lindqvist anion. For example, Parac–Vogt et al. reported that Lindqvist anions were less active than bigger structures in the hydrolysis of proteins.[2,3] Moreover, spectroscopic studies revealed that among several POMs with different structures, the smallest Lindqvist structure resulted the one affecting the protein structure the least.[4]

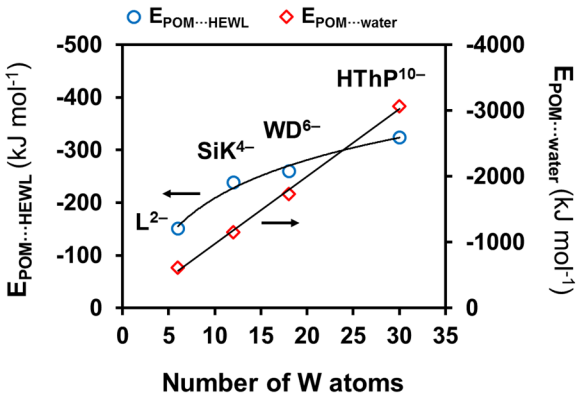

Figure 4.8 | Average POM···HEWL (blue circles) and POM···water (red diamonds) interaction energies (in kJ·mol^{-1}) as a function of the number of W atom in $\mathbf{L}^{2-}$, $\mathbf{SiK}^{4-}$, $\mathbf{WD}^{6-}$ and $\mathbf{HThP}^{10-}$ anions. $E_{POM\cdots HEWL}$ averaged for snapshots with POM···HEWL distance ≤ 3.5 Å. $E_{POM\cdots water}$ averaged from 20ns simulations in the absence of protein and fitted to a linear regression model ($r^2 = 0.99$).

The evolution of protein affinity with the size is similar to that found with charge density, that is, it increases until a maximum (Keggin structure) and then decreases less steeply (**Table 4.3**). Note however that in this case the dataset is not large enough to set a reliable quantitative relationship. To understand the origin of the observed time–dependence we analyzed separately the interaction of the POMs with the solvent and the

protein as a function of the size. **Figure 4.8** shows that the POM···water interaction energy ($E_{POM\cdots water}$) increases linearly with the number of addenda W atoms, because so does the number of solvent–accessible atoms, which support similar atomic charges. Differently, the POM···protein interaction energy ($E_{POM\cdots HEWL}$) grows logarithmically with the cluster size (see **Figure 4.8**). A closer look to the interaction mode of large anions revealed that the *non–spherical* Wells–Dawson (**WD**$^{6-}$) and Preyssler (**HThP**$^{10-}$) anions do not interact with HEWL using the largest possible surface area but they do it in an edgewise manner through their narrowest side (see **Figure 4.9** for representative snapshots of these interactions). Moreover, the computed volumetric density of POM···protein contacts for **WD**$^{6-}$ and **HThP**$^{10-}$ species confirms these interaction modes (**Figure 4.10**). Accordantly, the computed POM desolvation energies upon binding to HEWL (E_{desolv}) are very similar for **SiK**$^{4-}$, **WD**$^{6-}$ and **HThP**$^{10-}$ anions (see **Table 4.3** and **Table A4.1** for details). Thus, one can say that Wells–Dawson type **WD**$^{6-}$ and Preyssler–type **HThP**$^{10-}$ anions interact with HEWL in a *Keggin–like* manner, and therefore, not only POM size but also the shape is important to understand their interaction with biomolecules. An animation of a trajectory with the **HThP**$^{10-}$ anion, in which this *Keggin–like* interaction mode can be appreciated, can be accessed from the "Supplementary Material" section.

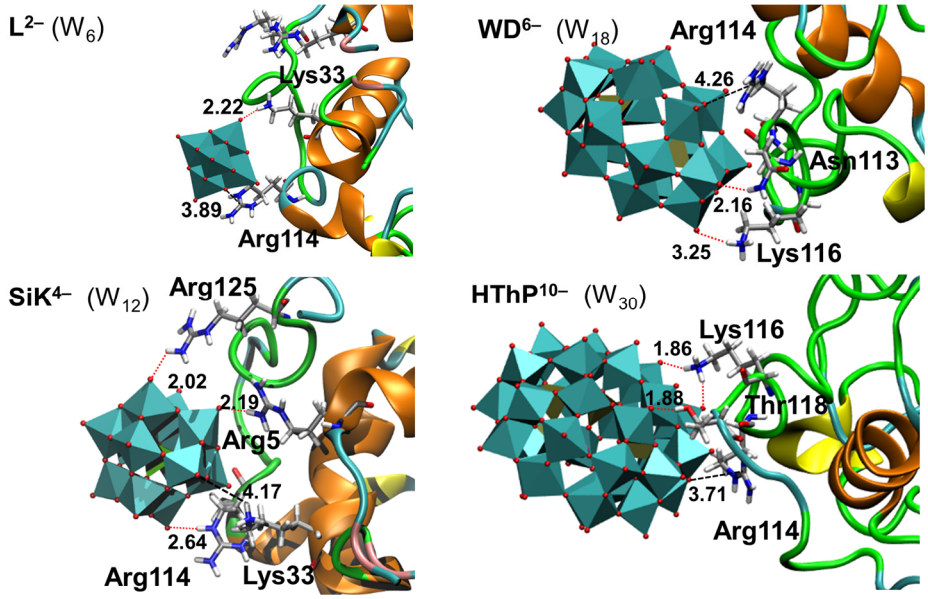

Figure 4.9 | Representative snapshots of the interaction between HEWL and four POMs with the same charge density (q/M) but different structure.

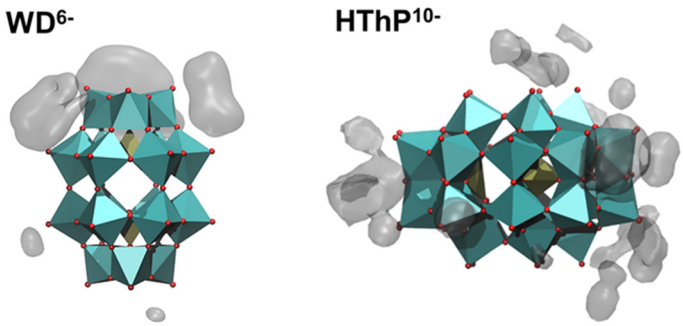

Figure 4.10 | Volumetric density of POM···protein contacts (d ≤ 3.5Å) around **WD^{6-}** and **HThP^{10-}** averaged over 100 of MD trajectories.

The origin of this *Keggin–like* interaction mode in larger anions with non–spherical shape may be related to the non–homogeneous charge distribution. Electrostatic repulsion within the POM causes the charge density to be higher at the most peripheral parts, accumulating larger negative charge at the most distal oxygen atoms (see **Figure 4.11**). Thus, these oxygen centers are expected to interact strongly with the protein. Conversely, we evaluate the importance of the size of cationic pockets at the HEWL protein by comparing simulations of **WD^{6-}** anion with new ones of the same Wells–Dawson structure setting all the atomic charges to zero, **WD^{0}**. The computed volumetric densities of the POM···protein contacts reveal that both species interact with HEWL protein through the same cap region (see **Figure 4.12**) indicating that charge distribution does not rule the directionality of the interaction. Finally, one should consider that for POMs bigger than Keggin structure (**WD^{6-}** and **HThP^{10-}**) the POM surface exposed to the solvent enlarges POM···water interactions. This increases the forces that pull the POMs towards the solvent bulk counterbalancing POM···protein interactions and explaining the smooth decrease in the *% time binding* (see **Table 4.3**). Overall these results indicate that in solution cationic pockets in HEWL are size–specific for Keggin–sized POMs (of about 1 nm of side length) determining the optimal size for POM affinity.

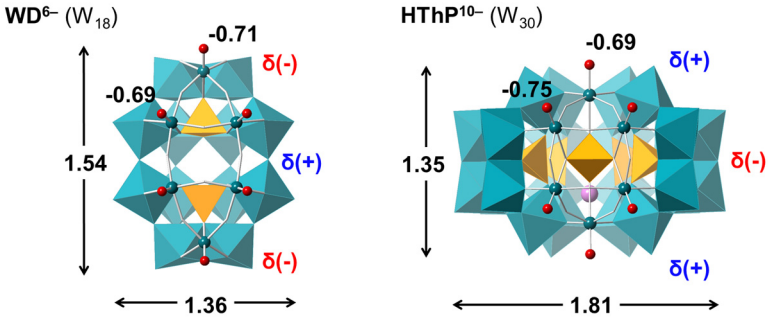

Figure 4.11 | Combined balls–and–sticks and polyhedral representation of **WD**$^{6-}$ and **HThP**$^{10-}$ with Wells–Dawson (left) and Preyssler (right) structures. The ChelPG atomic charges [e/K_BT] derived from molecular electrostatic potential are displayed for the terminal oxygen atoms belonging to the different regions of both POMs. The POM side lengths are shown in nm.

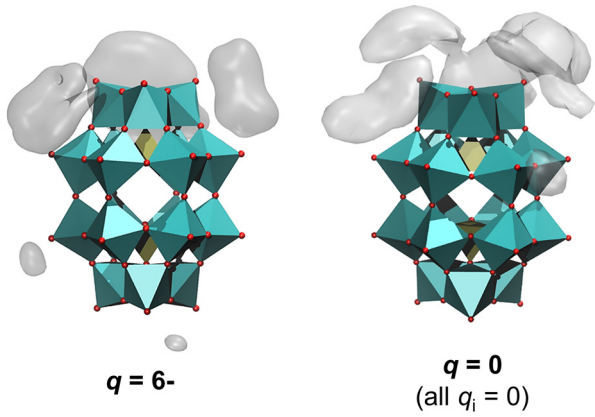

Figure 4.12 | Comparison of the volumetric density of POM···protein contacts around **WD**$^{6-}$ and the analogous structure in which all the atomic charges are set to zero, **WD**^{0}.

4.3.3 Development of a multidimensional model.

After analyzing the influence of different POM features separately, we sought to build a multidimensional mathematical model correlating protein affinity of POMs with their charge density and molecular size and shape. The dataset comprises previous simulated structures and five additional ones, including model systems, selected to balance the chemical space. Thus, we performed analogous simulations of HEWL protein in solution with the following five structures: the one electron–oxidized Lindqvist anion $[W_6O_{19}]^-$ (**L**$^-$), the one electron–reduced anion $[W_6O_{19}]^{3-}$ (**L**$^{3-}$), the tungstosulfate $[S_2W_{18}O_{62}]^{4-}$ (**SWD**$^{4-}$) and tungstosilicate $[Si_2W_{18}O_{62}]^{8-}$ (**SiWD**$^{8-}$) with Wells–Dawson structure and

the classical sodium–containing Preyssler anion $[NaP_5W_{30}O_{110}]^{14-}$ (**NaP^{14-}**). For each set of simulations, we evaluated the *% time binding* as a response variable associated to protein affinity. To describe the electrostatic features of the POMs we used the charge per metal ratio (q/M) as numerical parameter to account for the charge density of the anions. As discussed above, both the size and the shape have an influence on protein affinity. To describe simultaneously both geometric features we propose a novel descriptor, the shape–weighted volume (V_S). The V_S is calculated according to equation 4.1, where n_W are the number of addenda ions (W) and r_{max} represents the maximum side length in the POM structure in nm (see **Figure 4.13** for a graphical description). **Table 4.4** collects the values of the response variable (*% time binding*) and the descriptors (q/M and V_S) for the 13 structures of the dataset ordered in increasing values of the response variable.

$$V_S = \frac{n_W}{r_{max}} \tag{4.1}$$

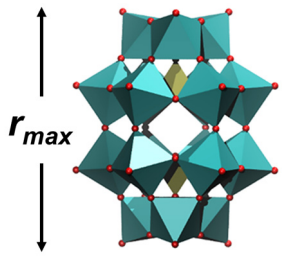

Figure 4.13 | Graphical representation of the r_{max} parameter used to calculate the shape–weighted Volume (V_S) molecular descriptor.

Table 4.4 | Classification of the simulated systems as a function of the *% time binding*, and values of molecular descriptors charge density (q/M) and shape–weighted volume (V_S).

classification	POM	q/M	V_S	% time binding[a]
Moderate interaction (< 90 %)	$\mathbf{L^{-}}$	0.17	6.8	69.7
	$\mathbf{SK^{2-}}$	0.17	11.4	72.0
	$\mathbf{L^{3-}}$	0.50	6.8	86.0
	$\mathbf{SWD^{4-}}$	0.22	11.7	87.0
	$\mathbf{PK^{3-}}$	0.25	11.4	88.9
Strong interaction (90–98 %)	$\mathbf{L^{2-}}$	0.33	6.8	94.2
	$\mathbf{ZnK^{6-}}$	0.50	11.4	96.2
	$\mathbf{AlK^{5-}}$	0.42	11.4	97.2
	$\mathbf{SiWD^{6-}}$	0.44	11.7	97.8
Persistent interaction (98–100 %)	$\mathbf{NaP^{14-}}$	0.47	16.6	98.9
	$\mathbf{HThP^{10-}}$	0.33	16.6	99.0
	$\mathbf{WD^{6-}}$	0.33	11.7	99.4
	$\mathbf{SiK^{4-}}$	0.33	11.4	99.8

[a] Values are sampled every 4 ps from the 100 ns MD trajectories.

The calculated *% time binding* is correlated to the descriptors q/M and V_S, and their second–order terms (q/M^2 and V_S^2), which account for quadratic dependence found above. Using partial least square (PLS) regression technique and the descriptors normalized to the highest values, we obtain a predictive model in which full leave–one–out (LOO) cross–validation leads to a value of r^2 for the fitting of 0.97 and a predictive ability q^2 of 0.88 with three PLS. In quantitative structure–activity relationship (QSAR) modeling, a model is considered to be predictive when the value of q^2 is higher than 0.5, which is halfway between perfect prediction (1.0) and no model at all (0.0). **Figure 4.14** shows the measured affinities plotted against the fitted values and the multidimensional QSAR equation. To further evaluate the prediction ability of our model, the dataset is divided into test (3 POMs of different protein affinity class) and training subsets (10 POMs) to develop an externally validated QSAR model. New QSAR models are generated with the training subsets and predictions were made for the test subsets (see

Table A4.2 for details). We repeated the procedure 5 times obtaining good predictive models for the training set in all cases (q^2 ranging from 0.78 to 0.92). From the 15 externally validated samples, 8 are excellently predicted with errors < 2 %, and average error ranges from 2.1 to 4.9%. The poorest predictions are obtained for $\mathbf{L}^{2-}$ (7.6 %) $\mathbf{SK}^{2-}$ (6.0 %) and $\mathbf{ZnK}^{6-}$ (5.9 %), which correspond to species with structural features close to the limits of the analyzed chemical space. However, the overall validation supports the reliability of the QSAR model and quantitative (or semi–quantitative) ability to predict the affinity of POMs to HEWL proteins.

$$\%\ time\ bind. = -6.8 - 135.1\ q/M^2 + 210.2\ q/M - 35.5\ V_S^2 + 61.7\ V_S$$

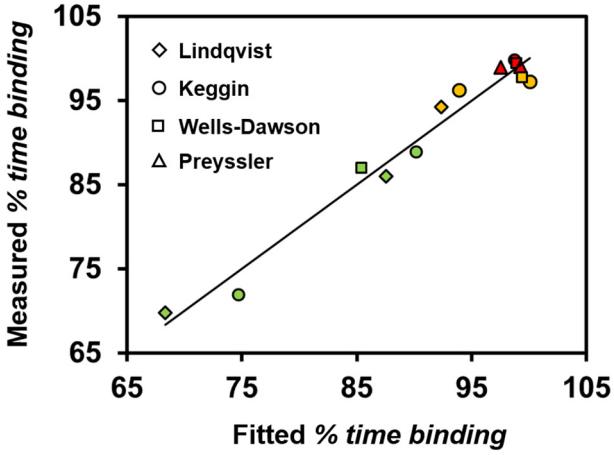

Figure 4.14 | Measured versus fitted *% time binding* for the 13 POMs species using a linear regression model with q/M, V_S, q/M^2 and V_S^2 descriptors, and the resulting QSAR equation. Diamonds, circles, squares and triangles correspond to Lindqvist, Keggin, Wells–Dawson and Preyssler structures, respectively. Green for moderate, yellow for strong and red for persistent interactions.

The use of normalized, chemically–meaningful descriptors allows to extract some (bio)chemical information from the QSAR equation depicted in **Figure 4.14**. Both the charge density and the geometry of the POM have a non–lineal correlation with protein affinity. The significant weight of second–order terms indicates that protein affinity has a quadratic–like dependence of both properties. This is the result of a delicate balance between POM···protein and POM···solvent interactions. Moreover, the higher absolute values of the q/M coefficients compared to those V_S indicate that the protein affinity is mainly governed by the charge density of the polyoxoanion and it is less affected by its bulkiness or its shape. **Table A4.5** compiles the values of the normalized descriptors and

the QSAR equation with non–normalized coefficients for its direct application is found below:

$$\%\ time\ binding = -6.8 - 540.5\ q/M^2 + 420.3\ q/M - 0.13\ V_S^2 + 3.72\ V_S$$

Finally, **Figure 4.15** shows the response surface predicted by the QSAR model as function of the POM molecular descriptors (see **Figure A4.5** for a 2D contour map). Within the analyzed chemical space, the map allows identifying a region (dark red) in which the POM···protein interactions are maximized.

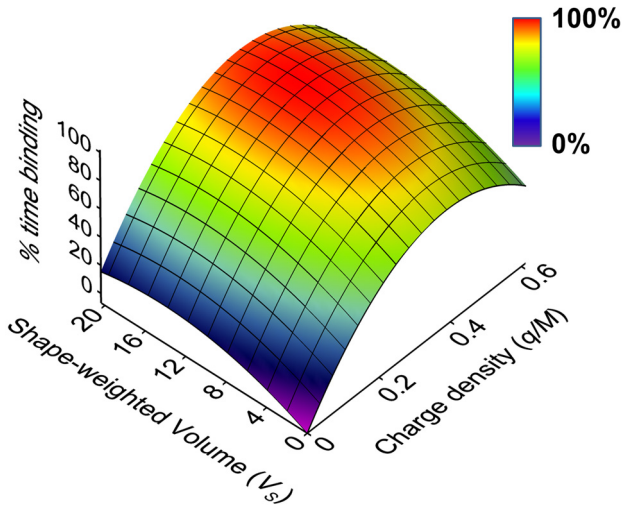

Figure 4.15 | Three–dimensional response surface of the *% time binding* as function of the charge density (q/M) and the shape–weighted volume (V_S) of the POMs using QSAR model. Red regions represent the most persistent interactions, and thus, the highest protein affinities.

4.4 Concluding Remarks

A systematic Molecular Dynamics (MD) study allowed setting structure–activity relationships between the molecular composition of chaotropic polyoxometalate (POM) anions and their affinity to biomolecules, using hen egg–white lysozyme (HEWL) as a model protein. When the charge of the POM is varied systematically keeping the same size and shape ($[X^{n+}W_{12}O_{40}]^{(8-n)-}$; $X^{n+} = S^{VI}$, P^{V}, Si^{IV}, Al^{III} and Zn^{II}), the protein affinity shows a quadratic dependence with a maximum at charge 4– (X = Si^{IV}, $q/M = 0.33$). The effects governing this non–linear correlation are very intricate and depend on the delicate balance

between the POM···protein and the POM···water interactions. While the POM···protein interaction energy increases linearly with the POM charge, the POM···water interaction showed a parabolic growth. Highly charged POM anions have less chaotropic (more kosmotropic) character that results in a more structured solvation shell of water molecules, in which the strength and number of hydrogen bonds increases. This accurate atomistic description of the change in hydrogen bonding pattern revealed that POMs with high charges have larger desolvation energies, and consequently, less affinity towards proteins. When the size and shape of the POM is varied keeping its charge density (number of W = 6, 12, 18 and 30; q/M = 0.33), simulations indicate that POM interactions with proteins are size–specific, being the size of Keggin–type anion (~1 nm length; W = 12) optimal for the cationic pockets in HEWL. Smaller structures such as the Lindqvist (W = 6) have sub–optimal interaction with the protein because they cannot interact with several amino acids simultaneously. Shape is also important since larger non–spherical anions such as the Wells–Dawson (W = 18) and the Preyssler (W = 30) interact in an edgewise (*Keggin–like*) manner exposing a large part of their oxide surface to the solvent, which pulls the POMs towards the bulk.

Finally, we were able to build a multidimensional model with predicting ability (r^2 = 0.97 and q^2 = 0.88) that correlates quantitatively the protein affinity expressed as the *% time binding* and two handy molecular descriptors accounting for the charge density of the POM (charge per metal atom ratio; q/M) and its size and shape (shape–weighted volume; V_S). The QSAR model indicates that the charge density of POMs influences their affinity to proteins in a larger extent than their molecular size and shape. Furthermore, this study evinces the capability of atomistic simulations to set structure–affinity relationships for the binding of inorganic clusters such as POMs to biological systems using time–derived variables.

4.5 Supplementary Material

The animation of a representative simulation discussed in this chapter can be accessed by scanning the following QR code with a smartphone or though the URL below.

HThP^{10-} interacting with HEWL

https://youtu.be/mPGncMtoRuc

References

1. Arefian, M.; Mirzaei, M.; Eshtiagh–Hosseini, H.; Frontera, A. *Dalton Trans.* **2017**, *46*, 6812–6829.
2. Stroobants, K.; Absillis, G.; Moelants, E.; Proost P.; Parac–Vogt, T. N. *Chem. Eur. J.* **2014**, *20*, 3894–3897.
3. Ly, H. G. T.; Absillis, G.; Janssens, R.; Proost, P.; Parac–Vogt, T. N. *Angew. Chem. Int. Ed.* **2015**, *54*, 7391–7394.
4. Ly, H. G. T.; Parac–Vogt, T. N. *ChemPhysChem* **2017**, *18*, 2451–2458.
5. Assaf, K. I.; Nau, W. M. *Angew. Chem. Int. Ed.* **2018**, 57, 13968–13981.
6. Zhang, G.; Keita, B.; Craescu, C. T.; Miron, S.; de Oliveira, P.; Nadjo, L. *J. Phys. Chem. B* **2007**, *111*, 11253–11259.
7. Geng, J.; Li, M.; Ren, J.; Wang, E.; Qu, X. *Angew. Chem. Int. Ed.* **2011**, *50*, 4184–4188.
8. Shigeta, S.; Mori, S.; Watanabe, J.; Baba, M.; Khenkin, A. M.; Hill, C. L.; Schinazi, R. F. *Antiviral Chem. Chemother.* **1995**, *6*, 114–122.
9. Shigeta, S.; Mori, S.; Watanabe, J.; Yamase, Y.; Schinazi, R. F. *Antiviral Chem. Chemother.* **1996**, *7*, 346–352.
10. Zhang, T.; Fu, D.; Wu, Y.; Wang, Y.; Wu, L. *Dalton Trans.* **2016**, *45*, 15457–15463.
11. Prudent, R.; Moucadel, V.; Laudet, B.; Barette, C.; Lafanechère, L.; Hasenknopf, B.; Li, J.; Bareyt, S.; Lacôte, E.; Thorimbert, S.; Malacria, M.; Gouzerh, P.; Cochet, C. *Chem. Biol.* **2008**, *15*, 683–692.
12. Zhang, G.; Keita, B.; Craescu, C. T.; Miron, S.; de Oliveira, P.; Nadjo, L. *Biomacromolecules* **2008**, *9*, 812–817.
13. Zhou, Y.; Zheng, L.; Han, F.; Zhang, G.; Ma, Y.; Yao, J.; Keita, B.; de Oliveira, P.; Nadjo, L. *Colloids Surf. A* **2011**, *375*, 97–101.
14. a) Lee, I. S.; Long, J. R.; Prusiner, S. B.; Safar, J. G. *J. Am. Chem. Soc.* **2005**, *127*, 13802–13803; b) Wille, H.; Shanmugam, M.; Murugesu, M.; Ollesch, J.; Stubbs, G.; Long, J. R.; Safar, J. G.; Prusiner, S. B. *PNAS*, **2009**, *106*, 3740–3745.
15. a) Müller, C. E.; Iqbal, J.; Baqi, Y.; Zimmermann, H.; Röllich, A.; Stephan, H. *Bioorg. Med. Chem. Lett.* **2006**, *16*, 5943–5947; b) Lee, S.–Y.; Fiene, A.; Li, W.; Hank, T.; Brylev, K. A.; Fedorov, V. E.; Lecka, J.; Haider, A.; Pietzsch, H.–J.; Zimmermsnn, H.; Sévigny, J.; Kortz, U.; Stephan, H.; Müller, C. E. *Biochem. Pharmacol.* **2015**, *93*, 171–181.
16. a) Gumerova, N.; Krivosudský, L.; Franqueza, G.; Breibeck, J.; Al–Sayed, E.; Tanuhadi, E.; Bijelic, A.; Fuentes, J.; Aureliano, M.; Rompel, A. *Metallomics*, **2018**, *10*, 287–295; b) Bijelic, A.; Aureliano, M.; Rompel, A. *Chem. Commun.* **2018**, *54*, 1153–1169.
17. Solé–Daura, A.; Goovaerts, V.; Stroobants, K.; Absillis, G.; Jiménez–Lozano, P.; Poblet, J. M.; Hirst, J. D.; Parac–Vogt, T. N.; Carbó, J. J. *Chem. Eur. J.* **2016**, *22*, 15280–15289.
18. Sap, A.; De Zitter, E.; Van Meervelt, L.; Parac–Vogt, T. N. *Chem. Eur. J.* **2015**, *21*, 11692–11695.
19. Vandebroek, L.; Van Meervelt, L.; Parac–Vogt, T. N. *Acta Crystallogr. C* **2018**, *74*, 1348–1354.
20. a) Vandebroek, L.; De Zitter, E.; Ly, H. G. T.; Conić, D.; Mihaylov, T.; Sap, A.; Proost, P.; Pierloot, K.; Van Meervelt, L.; Parac–Vogt, T. N. *Chem. Eur. J.* **2018**, *24*, 10099–10108; b) Vandebroek, L.; Mampaey, Y.; Antonyuk, S.; Van Meervelt, L.; Parac–Vogt, T. N. *Eur. J. Inorg. Chem.* **2019**, *3*, 506–511.

21. a) Paul, T. J.; Parac–Vogt, T. N.; Quiñonero, D.; Prabhakar, R. *J. Phys. Chem. B* **2018**, *122*, 7219–7232; b) Jayasinghe–Arachchige, V. M.; Hu, Q.; Sharma, G.; Paul, T. J.; Lundberg, M.; Quiñonero, D.; Parac–Vogt, T. N.; Prabhakar, R. *J. Comp. Chem.* **2019**, *40*, 51–61.
22. a) López, X.; Carbó, J. J.; Bo, C.; Poblet, J. M. *Chem. Soc. Rev.* **2012**, *41*, 7537–7571; b) López, X.; Miró, P.; Carbó, J. J.; Rodríguez–Fortea, A.; Bo, C.; Poblet, J. M. *Theor. Chem. Acc.* **2011**, *128*, 393–404; c) López, X.; Fernández, J. A.; Poblet, J. M. *Dalton Trans.* **2006**, *2006*, 1162–1167.
23. a) Leroy, F.; Miró, P.; Poblet, J. M.; Bo, C.; Bonet Ávalos, J. *J. Phys. Chem. B* **2008**, *112*, 8591–8599; b) López, X.; Nieto–Draghi, C.; Bo, C.; Avalos, J. B.; Poblet, J. M. *J. Phys. Chem. A* **2005**, *109*, 1216–1222.
24. Jiménez–Lozano, P.; Carbó, J. J.; Chaumont, A.; Poblet, J. M.; Rodríguez–Fortea, A.; Wipff, G.; *Inorg. Chem.* **2014**, *53*, 778.
25. Rappe, A. K.; Casewit, C. J.; Colwell, K. S.; Goddard, W. A.; Skiff, W. M. *J. Am. Chem. Soc.* **1992**, *114*, 10024–10035.
26. Bussi, G.; Donadio, D.; Parrinello, M. *J. Chem. Phys.* **2007**, *126*, 014101.
27. a) Stroobants, K.; Moelants, E.; Ly, H. G. T.; Proost, P.; Bartik, K.; Parac–Vogt, T. N. *Chem. Eur. J.* **2013**, *19*, 2848–2858; b) Stroobants, K.; Goovaerts, V.; Absillis, G.; Bruylants, G.; Moelants, E.; Proost, P.; Parac–Vogt, T. N. *Chem. Eur. J.* **2014**, *20*, 9567–9577.
28. a) Kangas, E.; Tidor, B. *J. Phys. Chem. B* **2001**, 105, 880–888; b) Lee, L.–P.; Tidor, B. *Nat. Struct. Biol.* **2001**, *8*, 73–76; c) Lee, L.–P.; Tidor, B.; *Protein Sci.* **2001**, *10*, 362–377.
29. a) Sulea, T.; Purisima, E. O. *Biophys. J.* **2003**, *84*, 2883–2896; b) Sulea, T.; Purisima, E. O. *J. Phys. Chem. B.* **2001**, *105*, 889–899.
30. Endo, Y.; Yamamoto, K.; Kagechika, H. *Bioorg. Med. Chem. Lett.* **2003**, *13*, 4089–4092.
31. Collins, K. D.; Washabaugh, M. W. Q. *Rev. Biophys.* **1985**, *18*, 323–422.
32. Marcus, Y. *Chem. Rev.* **2009**, *109*, 1346–1370.
33. Solé–Daura, A.; Notario–Estévez, A.; Carbó, J. J.; Poblet, J. M.; de Graaf, C.; Monakhov, K. Y.; López, X. *Inorg. Chem.* **2019**, *58*, 3881–3894.
34. Sharma, B.; Chandra, A. *J. Phys. Chem. B* **2018**, *122*, 2090–2101.

UNIVERSITAT ROVIRA I VIRGILI
NEW HORIZONS IN COMPUTATIONAL MODELING OF POLYOXOMETALATES:
BIOLOGICAL ACTIVITY, ENERGY STORAGE AND SUSTAINABLE CATALYSIS.
Albert Solé Daura

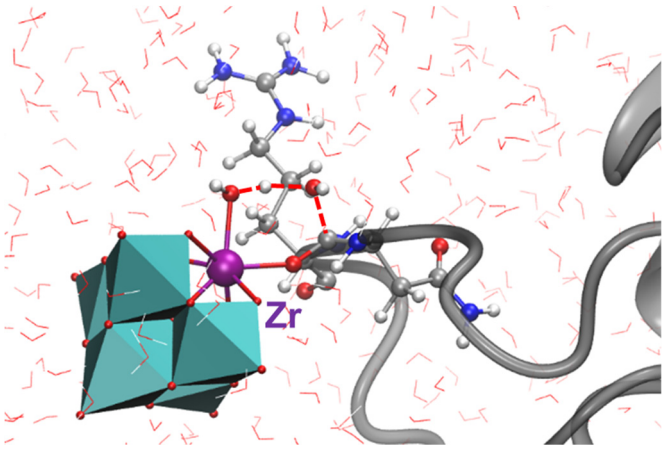

Chapter 5

Modeling the Polyoxometalate Reactivity towards Biological Systems

UNIVERSITAT ROVIRA I VIRGILI
NEW HORIZONS IN COMPUTATIONAL MODELING OF POLYOXOMETALATES:
BIOLOGICAL ACTIVITY, ENERGY STORAGE AND SUSTAINABLE CATALYSIS.
Albert Solé Daura

CHAPTER 5

Modeling the Polyoxometalate Reactivity towards Biological Systems

This chapter is devoted to the study of POM–mediated transformations in biological systems. Specifically, we have analyzed two different reactions: the selective hydrolysis of peptide bonds in proteins by Zr–substituted POMs and the disulfide bond reduction by POMs with d electrons. The origin of selectivity in protein hydrolysis has been investigated using a variety of computational techniques, including classical MD simulations, static DFT and hybrid QM/MM calculations. On the other hand, we studied the reduction mechanism of DTNB, as model system of angiotensinogen protein by the one–electron reduced Keggin–type phosphotungstate $[PW_{12}O_{40}]^{4-}$ and proposed a POM structure to attain the reduction of more realistic models of angiotensinogen consisting on dicysteine–based polypeptides. Moreover, MD simulations and DFT calculations on the protein using a cluster model approach were applied to evaluate the feasibility of the S—S bond reduction in angiotensinogen.

Part of the first project was carried out during a nearly four–months stay in the group of Prof. J. D Hirst (University of Nottingham, U.K.), and in collaboration with Dr. D. Robinson (Nottingham Trent University, U.K.). The project was funded by the URV and the Fundació Obra Social "La Caixa" (ARES program). The same stay gave rise to the second collaboration project related to the reduction of disulfide bonds. Besides the Hirst group, this project was developed in collaboration with the experimental groups of Dr. G. N. Newton and Dr. N. J. Mitchell; both based in the University of Nottingham.

5.1 Origin of Selectivity in Protein Hydrolysis Promoted by Zr–Substituted POMs.

5.1.1 Background.

The selective hydrolysis of peptide bonds is a process of particular interest, finding application in the fields of biochemistry and biomedicine, including proteomics, protein engineering or the digestion of pathogenic proteins.[1] Nevertheless, peptide bonds in

proteins are highly kinetically inert, with an estimated half–time of 600 years at 25 ºC and neutral pH,[2] which makes mandatory the use of catalysts to achieve their hydrolysis. In nature, there is a family of hydrolytic enzymes called hydrolases or proteases that accelerate this reaction effectively. However, they are usually expensive, provide low selectivity and can only operate in a narrow range of pH and temperature.[1] To overcome these issues, many research groups have devoted themselves to the development of artificial metalloproteases.[3] Among them, the group of Parac–Vogt probed the hydrolytic activity of Zr^{IV}–, Ce^{IV} and Hf^{IV}–substituted polyoxometalates (POMs) towards dipeptides and oligopeptides,[4,5] and more importantly, towards peptide bonds in proteins in a highly selective manner.[6–12]

Zr–substituted POMs (**Figure 5.1**A) were found to hydrolyze horse heart myoglobin (HHM)[9] and hemoglobin (Hb)[12] only at peptide bonds of Asp—X topology, where X is any other amino acid. In contrast, other proteins such as human serum albumin (HSA)[7] or hen egg–white lysozyme (HEWL)[6] were found to be selectively hydrolyzed at chemically different sites. Specifically, HEWL is hydrolyzed in the presence of Zr–POMs at only two peptide bonds located between Trp28 and Val29 and between Asn44 and Arg45, labeled site I and site II, respectively.[6] For this protein, our previous molecular dynamics (MD) simulations[14] (Chapter 3) and crystallographic studies[15–17] identified two positively charged regions on its surface located at the vicinity of the cleavage sites where POMs can establish persistent interactions. Later, a combined docking and MD study described similar findings for HSA protein,[18] for which four binding sites were identified nearby the four chemically distinct cleavage sites. Therefore, it was hypothesized that these positively charged patches could be related to the observed selectivity. However, in a more recent MD study with HEWL, we showed that other regions of the protein exhibit persistent interactions with POMs, besides those at the vicinity of the cleavage sites (Chapter 4).[19] Thus, although these simulations provide insight into the nature of the non–covalent POM···protein interactions, they cannot unequivocally explain the origin of selectivity in peptide hydrolysis.

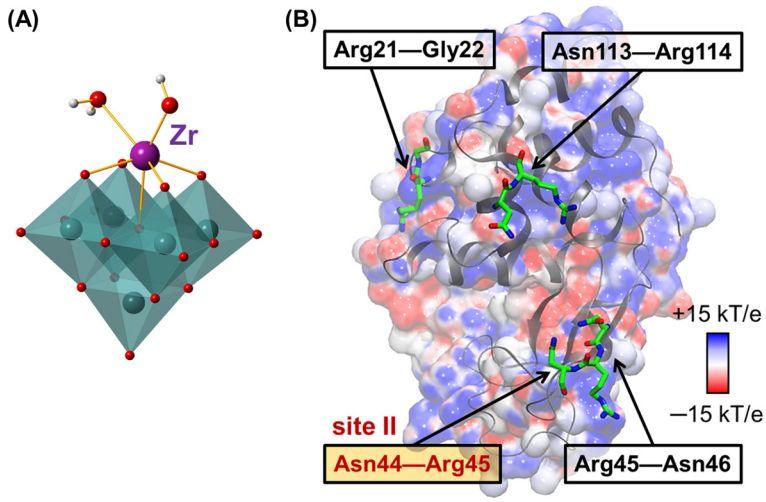

Figure 5.1 | (A) Combined balls–and–sticks and polyhedral representation of the hydrolytically active $[Zr(H_2O)(OH)W_5O_{18}]^{3-}$ anion (**ZrL**) with Lindqvist structure. (B) Molecular electrostatic potential (MEP) of hen egg–white lysozyme (HEWL; $q = 8+$) showing in green sticks the amino acids belonging to the four analyzed peptide bonds. The experimentally hydrolyzed site II (Asn44—Arg45) is highlighted with a red label. Blue coloring represents positively charged regions on HEWL surface, while red represents the negatively charged ones. The MEP was obtained by means of the PDB2PQR on–line server.[13]

Scheme 5.1 compiles different reaction mechanisms analyzed computationally for the peptide hydrolysis by Zr–substituted POMs,[5,12,20] and by other transition metal–based systems.[21–29] Once the Zr^{IV} ion coordinates to the amide oxygen of the peptide bond, the mechanisms can be classified as follows: the inner–sphere attack of the hydroxo ligand of Zr (i); the outer–sphere nucleophilic attack of an external water molecule assisted by the ZrOH moiety (ii) or by a carboxylate group of a neighboring residue (iii); and the direct attack of a carboxylate group nearby (iv). Earlier studies by Pierloot and co–workers on the hydrolysis of dipeptides found that the most likely pathway resembles mechanism (*iii*) in **Scheme 5.1**, but with a nucleophilic attack is assisted by the C–terminus carboxylate group acting as a Brönsted base.[5] Prabhakar and co–workers analyzed mechanisms (*i*) and (*ii*) for the hydrolysis of four different peptide bonds in HSA by Zr–POM using static quantum mechanics / molecular mechanics (QM/MM) calculations in the full molecular system.[20] The authors concluded that the inner–sphere nucleophilic attack of the hydroxo ligand of Zr (*i*) is somewhat preferred over the outer–sphere mechanism (*ii*). Although this study shed some light onto the reaction mechanism, the reasons for the experimentally observed selectivity remained unexplored.

Scheme 5.1 | Proposed mechanisms for peptide bond hydrolysis by Zr–substituted POMs.

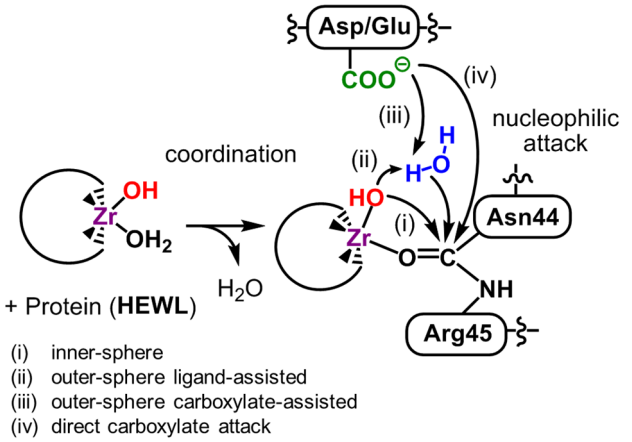

Very recently, a static DFT study using model tripeptides discussed the origin of selectivity for specific Asp—X bonds in Hb.[12] The proposed mechanism involves the direct nucleophilic attack of the carboxylate side chain of Asp residue on the amide carbon with formation of a cyclic anhydride (mechanism *iv*), which shows a lower activation energy than the structurally related Glu–X bond.[12] Although these results nicely explain the preference for hydrolyzing Asp–X sites, experimentally not all the Asp–X bonds in Hb are hydrolyzed, and therefore, the authors recognize that positive patches on protein surface might also influence the selectivity.[12] Moreover, as noted above for HSA and HEWL the selective hydrolysis was observed at non–carboxylate containing sites, while Asp–X bonds are also present. Thus, we suspect that dynamic protein arrangements around the negatively charged polyoxometalate cluster occurring along the reaction mechanism are crucial to explain the observed selectivity. Here, we select the model HEWL protein and the Zr–substituted Lindqvist anion $[Zr(H_2O)(OH)W_5O_{18}]^{3-}$ (**ZrL**, in **Figure 5.1**A) as catalyst, and compare the observed hydrolysis of the Asn44—Arg45 peptide bond with those of the structurally analogous Asn113—Arg114, Arg45—Asn46, and Arg21—Gly22 ones (**Figure 5.1**B). We employ a combination of DFT calculations in cluster models with MD simulations and hybrid QM/MM calculations to evaluate the effect of protein structure and POM···protein non–covalent interactions on the reaction mechanism and the selectivity.

5.1.2 Computational Details.

DFT calculations were performed at B3LYP level[30] using Gaussian09 rev. A02 quantum chemistry package.[31] Ti and W centers were described using the LANL2DZ basis set with the corresponding pseudopotential,[32] while the Pople 6–31G(d,p) basis set[33] was used for the remaining atoms. Solvent effects of water ($\varepsilon = 78.3553$) were included in the geometry optimizations and energy calculations by means of the IEF–PCM continuum solvent model[34] as implemented in Gaussian09. To describe the cleavage site within a *cluster model* approach,[35] the C_αCO—Asn44(**ZrL**)—Arg45—NHC_α fragment was taken from the protein structure and the alpha carbons were capped with hydrogens. Also, the position of these alpha carbons was constrained during the geometry optimizations in order to reproduce the strain imposed by the main chain of the protein into the peptide bond. Frequency calculations confirmed the nature of the stationary points on the potential energy surface for all minima and transition state structures. For the latter, the unique imaginary frequency is associated to the normal mode of vibration connecting reactants and products. The standard state correction of +8 kJ·mol^{-1} (from ideal gas at 1 atm to 1 mol L^{-1} at 298.15 K) was applied to the free energy of all the species except water molecules. For them, the standard state corresponds to a higher concentration as water acts as solvent in this reaction. Thus, according to the water density of 0.997 g cm^{-3}, the correction becomes +18 kJ·mol^{-1} for the free energy of water molecules.[36]

MD simulations were performed with the same methodology described in previous chapters. For constrained simulations, a fictitious bond between the Zr center of the POM and the O atom of the protein was defined with a force constant of 7.5×10^5 kJ·mol^{-1}·nm^{-2}. Also, angle parameters involving the Zr—O bond were described with a force constant of 7.5×10^3 kJ·mol^{-1}·degree^{-2}, with equilibrium values that correspond to those in the DFT–optimized geometry of the POM—GlyGly complex, calculated at the level of theory defined above. In all cases, simulations were carried out in a periodic simulation box of dimensions $75.7 \times 78.4 \times 79.8$ Å^3 filled with one HEWL protein ($q = 8+$), 1 **ZrL** anion ($q = 3-$), 5 Cl$^-$ anions to neutralize the charge and a number of water molecules close to 14650, with slight variation from one simulation to another.

Static, hybrid QM/MM calculations were performed with the Qchem(4.2)[37]–CHARMM(41b2)[38] interface, describing the QM region at same level of theory as in static DFT calculations, whereas the low layer was described with the CHARMM36 force field.[39] The system was generated with CHARMM–GUI[40] and contains one HEWL—ZrL complex obtained from previous constrained simulations,

8834 water molecules, 24 K^+ cations and 29 Cl^- anions embedded in a periodic truncated–octahedral box with dimensions of a = b = c = 74 Å and $\alpha = \beta = \gamma = 109.47^o$. The high–level region (represented in **Figure 5.2**) includes, besides the POM, the main chain of the dipeptide to be cleft (from N_{Asn44} to C_{Arg45}). In calculations related to the outer–sphere mechanism, one solvent water molecule was also included in the QM subsystem. The four QM/MM borders crossing chemical bonds were treated with the single link atom (SLA) approach[41] and the EXGR method[42] to exclude QM/MM electrostatic interactions that involve MM host groups. The through–space partition was described by the electronic embedding scheme, in which the set of MM Gaussian–delocalized charges[43] with a finite width of 1.5 Å polarize the QM wave function. Replica–path[44] calculations were carried out with 16 images. Those corresponding to the reactants and the products were obtained from QM/MM optimizations and those in between were initially generated by linear interpolation of Cartesian coordinates. For each replica, we initially performed 80 steps of QM/MM steepest descent (SD) optimization followed by 80 additional steps using the Average–Basis Newton Raphson (ABNR) algorithm. Geometry optimizations along the replica path were carried freezing the position of all atoms further than 6 Å from the QM region, and constraining the distance between adjacent replicas with a force constant (k_{RMS}) of 2.5×10^6 kJ·mol^{-1}·Å^{-2} that induces an energy penalty through a Hooke's Law–like expression. To control the linearity of the reaction path, we used a force constant (k_{angle}) of 836 kJ·mol^{-1}. This applies an angle energetic penalty upon deviation from linearity through the law of cosines, which permits a maximum value for $\cos(\Theta)$ of 0.975 before applying any penalty (where Θ is the angle defined by replicas *i*, *i*±1 and *i*±2 on the potential energy surface). Also, an additional energy penalty ($k_{max} = 2.5 \times 10^6$ kJ·mol^{-1}·Å^{-2}) is applied if one point moves further than 0.1 Å from their neighbors during the replica–path minimization. For more details on the constraints used in replica–path calculations, see ref. 44.

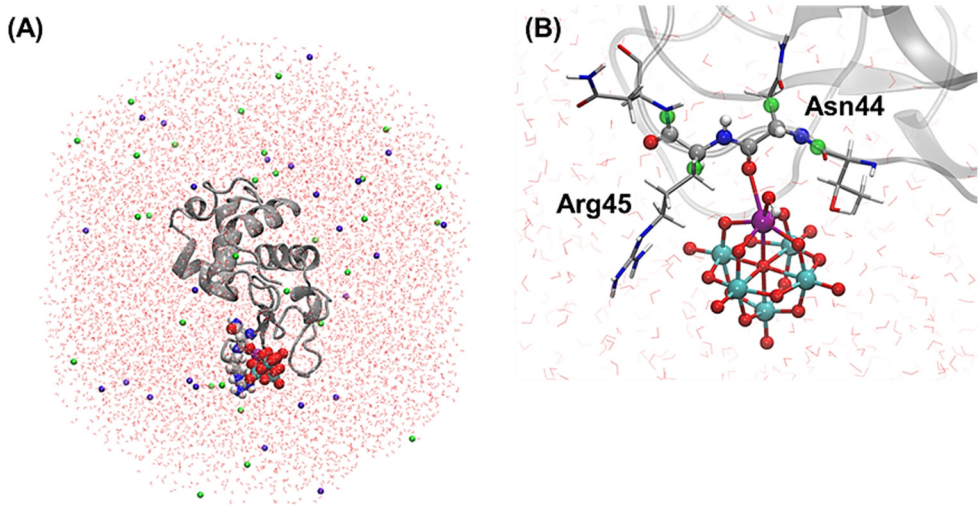

Figure 5.2 | System used for QM/MM calculations. (A) complete view of the periodic box, where the reactive region of the protein is highlighted in spheres, and the potassium and chloride ions are represented as violet and green spheres, respectively. (B) Closer look to the reactive region. QM part is represented in balls and sticks, whereas neighboring MM atoms are shown as sticks. The rest are omitted for clarity. Green spheres denote the position of hydrogen link atoms at the border between high– and low–level regions. In calculations on the outer–sphere mechanism, an additional water molecule from the solvent, hydrogen–bonded to the Zr—OH moiety, was also included in the QM region.

5.1.3 Results and Discussion.

5.1.3.1 Characterization of the reaction mechanism.

Initially, we studied the reaction mechanism for the hydrolysis of the Asn44—Arg45 peptide bond combining static DFT calculations within the *cluster model* approach[35] and MD simulations. Then we compared the results for this site with other sites that showed resistance to hydrolysis experimentally (Asn113—Arg114, Arg45—Asn46, and Arg21—Gly22). **Figure 5.3** shows the free–energy profile computed for the hydrolysis of Asn44—Arg45 peptide bond by **ZrL** via mechanisms (*i*) and (*ii*) (**Scheme 5.1**); and **Figure 5.4** shows the optimized geometries of the most representative TSs. The reaction mechanisms can be divided into four main steps: (1) the coordination of **ZrL** to the amide oxygen of the peptide bond, (2) the nucleophilic attack of the Zr–hydroxo group (inner–sphere, *i*) or an external water (assisted outer–sphere, *ii*) on the amide carbon, (3) the proton–transfer to the amide nitrogen, and (4) the final C—N bond cleavage to yield the products and regenerate the catalyst.

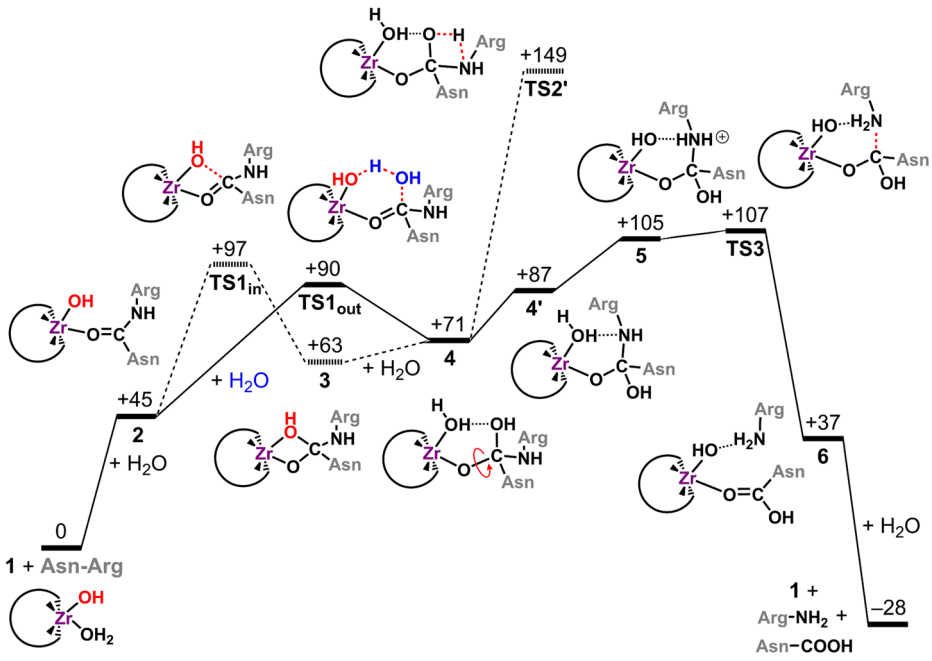

Figure 5.3 | Free–energy profile (kJ·mol^{-1}) for the hydrolysis of Asn44—Arg45 peptide bond by **ZrL** using a cluster model.

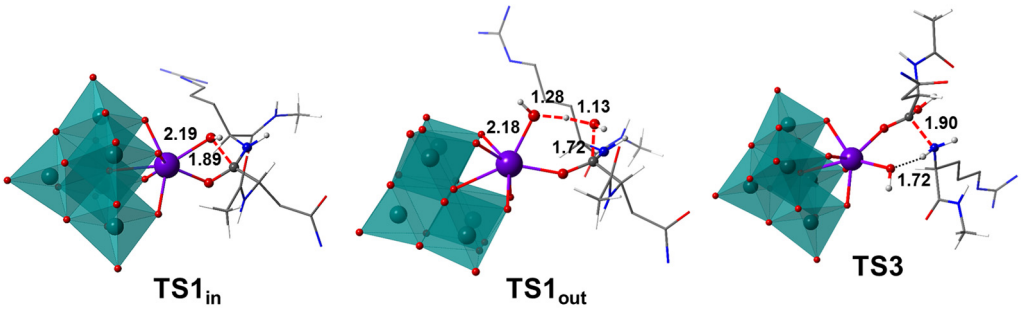

Figure 5.4 | B3LYP–optimized geometries of key transition states are shown at the right omitting side–chain hydrogens for clarity. Selected distances in Å.

The first coordination step was computed to be endergonic by 45 kJ·mol^{-1}. Note that the geometry for the cluster model was generated from restricted MD simulations fixing the Zr–oxygen bond (*vide infra*). The coordinated Zr^{IV} ion acts as a Lewis acid activating the amide carbon for the subsequent nucleophilic attack, which can occur through different pathways (**Scheme 5.1**). Our calculations indicate that the outer–sphere nucleophilic attack (**TS1$_{out}$**) is slightly more favorable than the inner–sphere one (**TS1$_{in}$**)

[$\Delta G^{\ddagger}$ (2→TS) of 45 *vs* 52 kJ·mol^{-1}]. This is ascribed to the less strained six–membered ring in **TS1$_{out}$**. Nevertheless, the small free–energy difference suggests that both mechanisms could be operative. This result differs slightly from that found for the hydrolysis of HSA by $[PW_{11}O_{39}Zr(OH)]^{4-}$ where the inner–sphere mechanism was energetically preferred.[20] In fact, our calculations initially pointed towards inner–sphere mechanism, but introducing the entropy corrections to the ideal gas thermochemistry analysis of standard DFT codes resulted in a slight preference of the associative process of the outer–sphere mechanism (*ii*) (see Computational Details). The inner–sphere mechanism leads the four–membered ring intermediate **3** that lies 63 kJ·mol^{-1} above the reactants, while the outer–sphere one results in intermediate **4** which is 8 kJ·mol^{-1} less stable. The interconversion between **3** and **4** requires the incorporation or release of an aqua ligand in the coordination sphere of Zr, which is expected to be fast due to the lability of water coordination to Zr^{IV} ion.[45]

From **4**, we propose a step–wise process that involves an intramolecular rearrangement via bond rotation to yield **4'**, a proton transfer from the aqua ligand to the amide nitrogen to give **5**, and final C—N bond cleavage (see **Figure 5.3**). This process goes uphill in energy until it reaches the transition state for the C–N bond cleavage, in line with that proposed for hydrolysis of dipeptides by Zr–containing POMs.[12] The proton transfer (see **Figure A5.1** in the appendix for further details) results in the thermodynamically and kinetically unstable intermediate **5** from which the C—N cleavage proceeds through a very small free–energy barrier of 2 kJ·mol^{-1}. Thus, the existence of intermediate **5** might depend on the specific conditions transforming the step–wise hydrogen transfer then C—N bond cleavage in a concerted process. Finally, transition state **TS3** yields intermediate **6** with the release of the amine product and the Zr–coordinated carboxylic acid, which then is exchanged by a water molecule recovering the catalyst and providing the thermodynamic driving force of the reaction (–28 kJ·mol^{-1}). Additionally, we analyzed direct hydrogen transfer from the carboxylic acid group in **4** which is concomitant with the C—N bond cleavage, as proposed for the hydrolysis of HSA protein by Zr–substituted POM.[20] However, the corresponding four–membered ring transition state (**TS2'** in **Figure 5.3**; geometry displayed in **Figure 5.5**) is significantly higher in energy (149 kJ·mol^{-1} vs. 107 kJ·mol^{-1} for **TS3**).

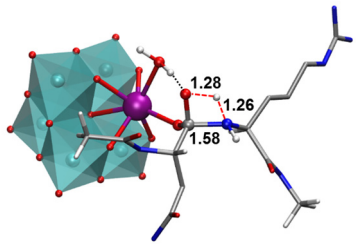

Figure 5.5 | DFT optimized structure of the four–membered ring transition state for the proton transfer step to induce the C—N cleavage (**TS2'**). Distances are shown in Å.

The overall activity of the hydrolysis reaction is governed by the energy cost to reach the transition state for C—N bond cleavage from the reactants (**1** + protein → **TS3**) since the reaction proceeds uphill in energy along the process (see **Figure 5.3**). Thus, it is not crucial for the understanding of the activity and selectivity to determine the preference for the inner–sphere pathway (*i*) or the outer–sphere (*ii*), both converging in intermediate **4** before reaching **TS3**. Nevertheless, we have analyzed in more detail the different nucleophilic attack of both mechanisms using a QM/MM approach in conjunction with the replica–path method.[44] The potential energy curves (see **Figure 5.6**) show that both mechanisms are feasible, and that there is any clear preference for any of the two mechanisms within the protein environment. The large radius of the Zr atom makes the strained four–membered ring transition state to be close in energy to the six–membered ring TS of outer–sphere. It must be pointed out that within the used computational protocol, the geometries of all the replicas are not fully relaxed. However, the aim of this calculations is to qualitatively assess the feasibility of mechanism (*i*) and (*ii*) of **Scheme 5.1** in the real system.

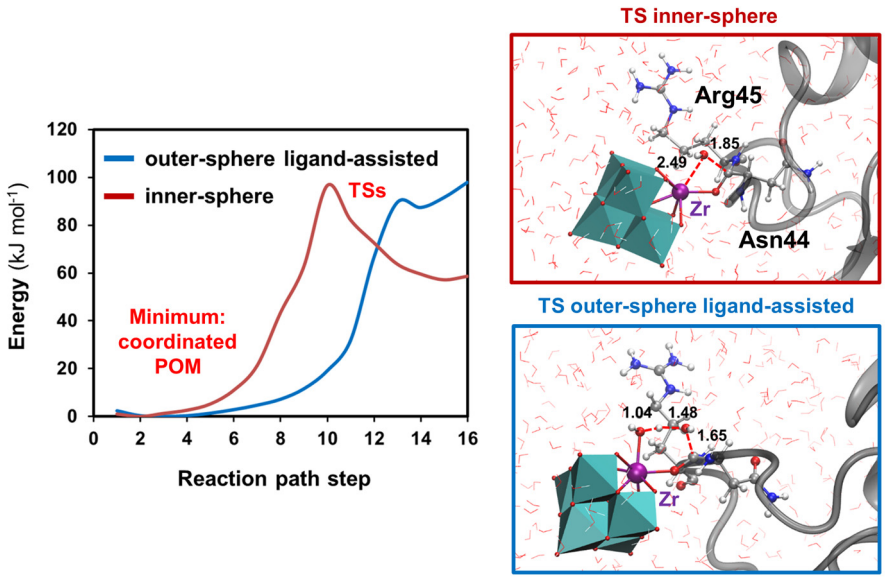

Figure 5.6 | Electronic energy profiles obtained from the QM/MM replica–path study in the real system of the proposed mechanisms for the nucleophilic attack step. Right panels show the geometry corresponding to the maxima of the curves, in which main distances are given in Å.

We have also evaluated the feasibility of the carboxylate–assisted mechanisms (*iii*) and (*iv*) by analyzing the distribution of aspartate and glutamate residues around site II along the MD simulation on the coordinated POM—protein complex. Distance analysis identifies Asp52 as the closest carboxylate–containing residue to the Asn44—Arg45 peptide bond (see **Figure 5.7**A). Thus, we analyzed the density of water molecules surrounding the COO^- moiety (green density) and the carbonyl group of the peptide bond (red density) as shown in **Figure 5.7**B. The gap between both densities suggests that the probability of finding one water molecule close enough from both groups to react via mechanism *iii* (**Scheme 5.1**) is low. Even so, it is possible to find snapshots of the dynamics in which a water molecule is simultaneously hydrogen–bonded to the carboxylate of Asp52 and the amide oxygen of Asn44. From one of these snapshots we generated a new cluster model with three residues (Asn44, Arg45 and Asp52, see **Figure 5.8**) in order to evaluate the energy cost of the nucleophilic attack of an external water molecule assisted by the carboxylate group. The free–energy barrier associated to this process (105 $kJ{\cdot}mol^{-1}$) is higher than those for the nucleophilic attacks to amide carbon associated to mechanisms (*i*) and (*ii*) (90 and 97 $kJ{\cdot}mol^{-1}$). Overall, the carboxylate–assisted mechanism (*iii*) is unlikely because of the higher energy barrier and

the low occurrence (0.4 %) of conformations with short enough distances between the amide carbonyl and the carboxylate. On the other hand, the MD trajectory does not provide any geometry suitable for modeling a TS geometry for the direct attack of the carboxylate group, and therefore, we concluded that mechanism (*iv*) is also not likely to occur.

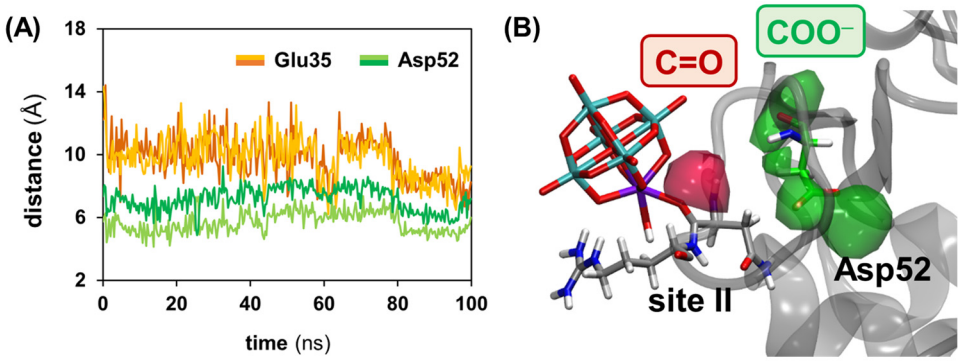

Figure 5.7 | (A) Evolution of the distance (in Å) between the carbon atom of the peptide bond in site II (C_{Asn44}) and the oxygen atoms of the nearest carboxylate groups, that are those in the side chain of Glu35 (dark and light orange) and Asp52 (dark and light green), along 100 ns of MD simulation. (B) Representation of the volumetric density of water molecules at a distance ≤3.5 Å from the carbonyl group of site II (CO; red density) and from the carboxylate group of Asp52 (COO^-; green density). Densities were averaged over 100 ns of MD run from which data were sampled every 4 ps.

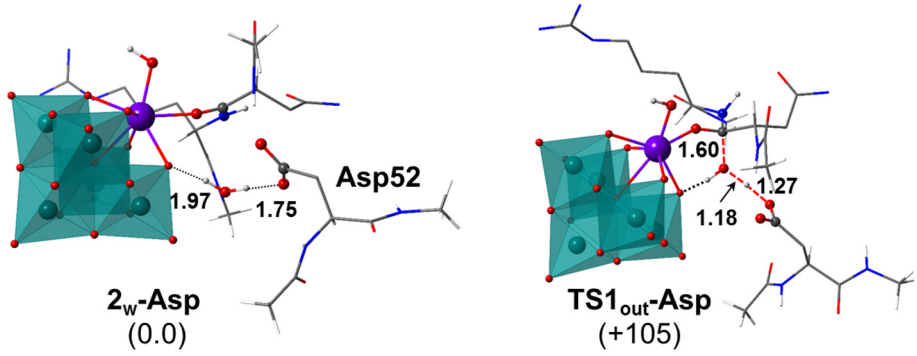

Figure 5.8 | DFT optimized structures of species involved in the *outer–sphere carboxylate–assisted* mechanism for the nucleophilic attack of an external water molecule to the peptide bond. Relative free energies are given in $kJ{\cdot}mol^{-1}$ and main distances are shown in Å.

5.1.3.2 Influence of protein conformation on reactivity.

Considering that the highest–energy TS corresponds to a bond cleavage in the protein main chain, we suspect that the conformational variability of the protein may influence the reaction kinetics, as observed in other biological systems.[46–50] To assess this point, we analyzed the free–energy barrier associated to the rate–determining process ($\Delta G^{\ddagger}_{overall}$) for a set snapshots taken from different stages of the MD simulation (**Table 5.1**). Indeed, the conformation of the protein was found to play an important role in its reactivity since the array of computed barriers is rather broad, comprising values from 88 to 143 kJ·mol^{-1}. Therefore, the reaction kinetics should not only be studied on a single protein conformation but on a thermodynamic ensemble. Interestingly, we found a correlation between the free energy barriers and the distance between capping alpha carbons ($r_{C\alpha\cdots C\alpha}$). This relationship is represented graphically in **Figure 5.9** and shows that the longer the $C_\alpha\cdots C_\alpha$ distance, the lower the barrier and thus, the faster hydrolysis. We attributed this trend to the fact that longer distances may increase the strain incurred to the peptide bond to facilitate the cleavage of the C—N bond, which is the step that controls the reaction rate. **Figure 5.9** also displays the distribution of $C_\alpha\cdots C_\alpha$ distances computed over 100 ns of MD simulation with the POM coordinated to the cleavage site. The abundance of each $C_\alpha\cdots C_\alpha$ distance value is expressed as the % of simulated time that is reported. The $C_\alpha\cdots C_\alpha$ distances show an almost symmetric unimodal distribution centered at 9.90 Å, which is the most likely distance accounting for the 18.6 % of the simulated time. As the dependence of $\Delta G^{\ddagger}_{overall}$ on $r_{C\alpha\cdots C\alpha}$ can be fitted to a linear regression, we could determine the free–energy barrier for each protein conformation ($C_\alpha\cdots C_\alpha$ distance) using the linear equation (see **Table A5.1** in the Appendix). Then, the average free–energy barrier can be estimated from this set of values weighted with the abundance of each conformation. This approach leads to an average free–energy barrier of 121 kJ·mol^{-1} for the hydrolysis of Asn44—Arg45. Importantly, this value lies within the range of values derived from experimental rate constants (113–134 kJ·mol^{-1}; **Table A5.2**).[4,7,9,10] In addition, this value corresponds to that computed at the most likely $C_\alpha\cdots C_\alpha$ distance (see snapshot 4 in **Table 5.1**) and it is very close to the fitted one at the same distance (123 kJ·mol^{-1} in **Table A5.1**).

Table 5.1 | Dependence of the free–Energy barriers on the protein conformation.[a]

snapshot	$r_{Cα\cdots Cα}$ (Å)	$\Delta G^{‡}_{overall}$ (kJ·mol^{-1})
1	9.97	107
2	10.0	124
3	10.15	102
4	9.91	121
5	9.95	134
6	10.45	88
7	9.46	143
8	9.81	137

[a]Snapshots were taken from a 100 ns MD simulation in which the distance between the Zr of the POM and the carbonylic oxygen of site II was constrained to 2.33 Å.

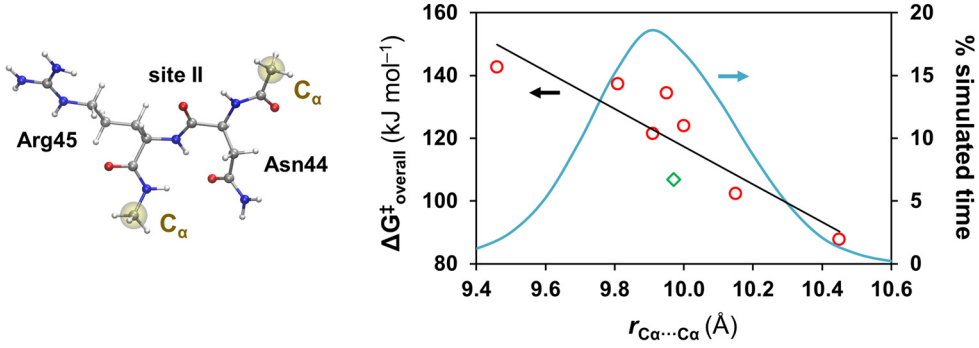

Figure 5.9 | Overall free–energy barrier for the hydrolysis of Asn44—Arg45 as a function of the distance between alpha carbons, $r_{Cα\cdots Cα}$ (highlighted in yellow in the balls–and–sticks representation) using different snapshots of the 100 ns MD simulation. The green diamond represents the snapshot used for computing the free–energy profile of **Figure 5.3**, whereas red circles account for seven additional snapshots. Values were fitted to a linear regression model (r^2 =0.78). The abundance of each $r_{Cα\cdots Cα}$ value is expressed as the % of simulated time (blue line).

5.1.3.3 Origin of selectivity in peptide hydrolysis.

Initially, we analyzed how the energy barrier for the peptide bond cleavage varies at different protein sites and whether this effect governs the selectivity. **Table 5.2** compares the computed, overall free–energy barriers (**1** + protein → **TS3**) at hydrolyzed site II

(Asn44–Arg45) with those at structurally–related, non–hydrolyzed sites (Asn113–Arg114, Arg21–Gly22, and Arg45–Asn46). For each site, we selected a cluster model derived from the most likely protein conformation, which is obtained from the analysis of the $C_\alpha \cdots C_\alpha$ distance abundance along the simulation. In all cases, the $C_\alpha \cdots C_\alpha$ distances describe unimodal distributions analogous to that depicted in **Figure 5.9** that are rather symmetric around the maximum (see **Figure 5.10**), justifying the use of a single conformation as representative of the distribution. All four peptide bonds exhibited very similar $\Delta G^{\ddagger}_{overall}$ values within a range of 4 kJ·mol^{-1}. This indicated that there is no intrinsic preference for hydrolyzing site II over other sites and therefore, we hypothesized that the origin of selectivity might lie in the enzyme–like recognition of **ZrL** anion at the protein region of the hydrolyzed peptide bond. One may note that although the preferred $C_\alpha \cdots C_\alpha$ distance differs significantly from one site to another (see **Figure 5.10**), the obtained barriers are pretty much alike. We ascribed this to the secondary structure of the protein regions where the peptide bonds are located. Thus, the hydrolysis kinetics of Asn44—Arg45, located in a β–strand region, might be more sensitive to the protein conformation than that of Asn113—Arg114, found in an α–helix that is more flexible *per se*.[51] Accordingly, the calculated barriers for Asn113—Arg114 present less dispersion than those in **Figure 5.9**, lying between 120 and 135 kJ·mol^{-1} in a $C_\alpha \cdots C_\alpha$ distance range of ~1.1 Å (from 6.13 to 7.26 Å).

Table 5.2 | Comparison of free–energy barriers for the hydrolysis of several peptide bonds in HEWL.[a]

cleavage site	$r_{C\alpha \cdots C\alpha}$ **distribution maximum**	$r_{C\alpha \cdots C\alpha}$ **selected snapshot**	$\Delta G^{\ddagger}_{overall}$
Asn44—Arg45 (*site II*)	9.90	9.91	121
Asn113—Arg114	6.80	6.77	124
Arg21—Gly22	5.40	5.36	124
Arg45—Asn46	7.00	7.00	120

[a]Free–energy barriers are given in kJ·mol^{-1} and distances in Å.

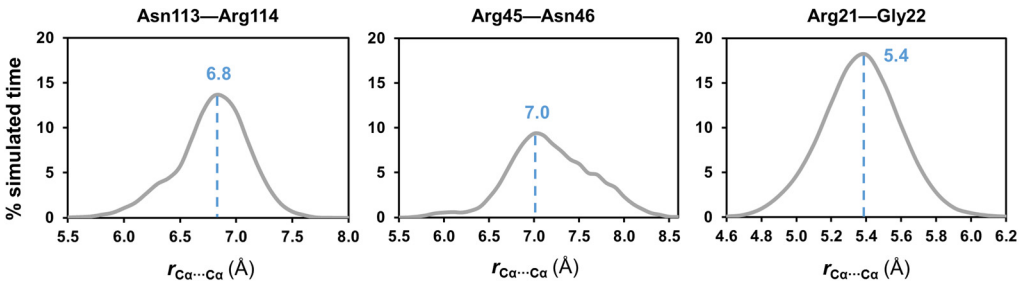

Figure 5.10 | Abundance of distances between alpha carbons adjacent to the analyzed dipeptide fragment ($r_{C\alpha\cdots C\alpha}$) expressed as the % of simulated time, computed over 100 ns of MD simulation.

Next we analyzed the effect of protein arrangements around the polyoxometalate on the selectivity by comparing the non–covalent POM···protein interactions at the four different sites highlighted in **Figure 5.1**B. These interactions should be present from the early stages of the reaction, that is the Zr ion coordination to the amide oxygen. Thus, we performed constrained MD simulations, in which the $Zr_{POM}\cdots O_{protein}$ distance ($r_{Zr\cdots O}$) was initially set to the non–coordination length of 5.50 Å and decreased successively every 250 ps of simulation until 2.33 Å. This latter value corresponds to the bond equilibrium distance predicted by DFT (see Computational Details section for further details). The procedure was repeated along five parallel runs for each site to sample the most likely POM···protein interactions.

Figure 5.11 displays the time evolution of POM···protein interaction ($E_{POM\cdots protein}$) and the Zr···O distance for a selected run of each site (analogous data for the remaining MD runs are compiled in **Figures A5.2–A5.5**); and **Figure 5.12** collects the $E_{POM\cdots protein}$ energies averaged over the five independent MD runs at different $Zr_{POM}\cdots O_{protein}$ distances. The four selected sites contain positively charged arginine residues which can interact with the negatively charged POM framework. Consequently, **Figure 5.11** and **5.12** show attractive POM···protein interactions along the simulated coordination process in all the cases. However, we observed remarkable differences between the sites which can explain the experimental selectivity. Most importantly, the interaction energies at the hydrolyzed site (Asn44–Arg45 in **Figure 5.11**A) are significantly stronger than for the other sites. Visual analysis of the trajectories revealed that during the coordination **ZrL** interacts simultaneously with Arg45 and with Arg68 located nearby, as illustrated by the snapshot of **Figure 5.11**A. **Figure A5.6** (Appendix) provides the averaged, non–covalent interaction energies of **ZrL** with individual amino acids, confirming the simultaneous interaction of Arg45 and Arg68. Additional hydrogen bonding interactions with polar

residues Thr43, Thr51 and Tyr53 were also characterized, being analogous to those of previous MD simulation on noncovalent adducts.[14,18,19] Moreover, close contacts of the guanidine groups of Arg45 and Arg68 with Zr–substituted POMs had been actually observed in crystal X–ray structures of non–covalent complexes.[15,17]

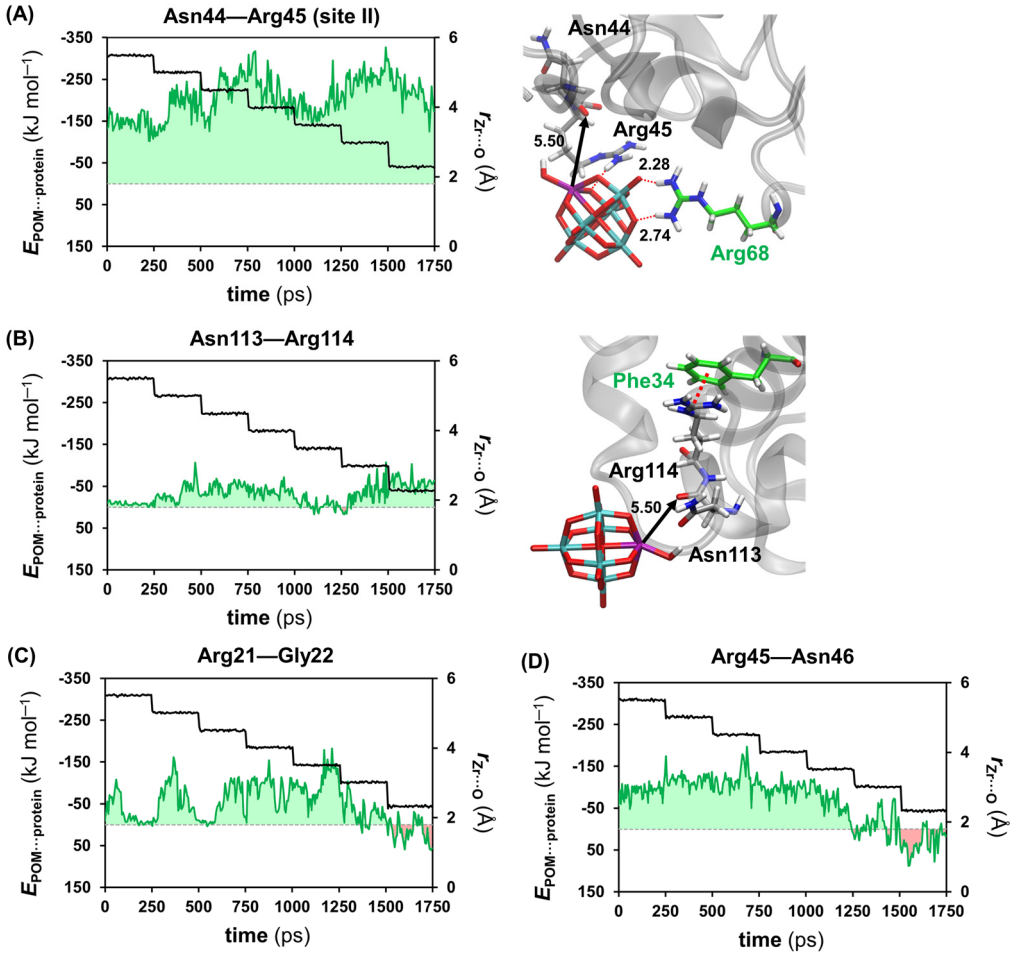

Figure 5.11 | Evolution of the POM···protein non–covalent interaction energies in kJ·mol^{-1} (green lines) and the $Zr_{POM}\cdots O_{protein}$ distance in Å (black lines) along simulated coordination processes to four different sites: hydrolyzed site II Asn44—Arg45 (A), and the non–hydrolyzed sites Asn113—Arg114 (B), Arg21—Gly22 (C) and Arg45—Asn46 (D). Selected 1750 ps runs of restricted MD simulations. Typical snapshots of **ZrL**···protein interaction for simulations A and B.

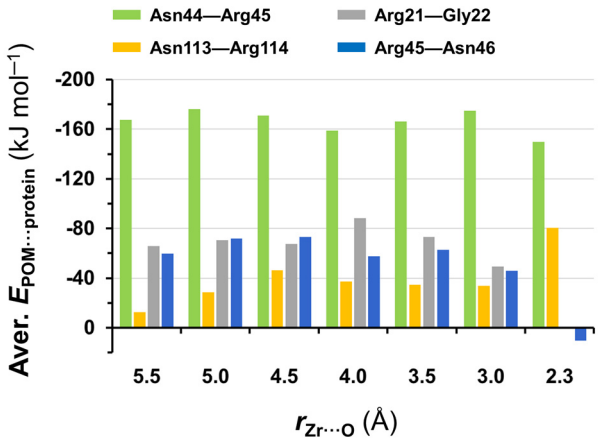

Figure 5.12 | Average non–covalent interaction energies between the **ZrL** POM and the protein ($E_{POM\cdots protein}$) as function of the $Zr_{POM}\cdots O_{protein}$ distance during the coordination of **ZrL** to Asn44—Arg45, Asn113—Arg114, Arg21—Gly22 and Arg45—Asn46 (green, yellow, gray and blue bars, respectively). Data were sampled every 2 ps and averaged over the 5 runs.

Moving from simulations at site Asn44–Arg45 to the consecutive Arg45–Asn46 site, we only observed a significant stabilizing interaction between the **ZrL** anion and Arg45 that vanishes as the zirconium–oxygen distance shortens (**Figure A5.9**). As a result, the overall non–covalent POM···protein interaction is significantly weaker for the Arg45–Asn46 site, becoming even slightly repulsive at the estimated Zr–O coordination distance (**Figure 5.11**D and **5.12**). The coordination to either of these consecutive sites places the POM at different regions of the protein causing a differentiated pattern of non–covalent interactions (see **Figure 5.13**). For the Asn113–Arg114 site, which is chemically equivalent to the hydrolyzed Asn44–Arg45 site, the stabilizing interactions are even weaker than in Arg45–Asn46 site (**Figures 5.11**B and **5.12**). Besides the lack of efficient cooperative effects at non–reactive sites, POM···protein interactions are often hampered by neighboring amino acids that compete with the POM for interacting with the side chain of arginines. In this case, the Arg114 with a positively charged guanidine is *trapped* in a cation–π interaction with the phenyl ring of Phe34 residue (snapshot in **Figure 5.11**B, and Appendix for further discussion).

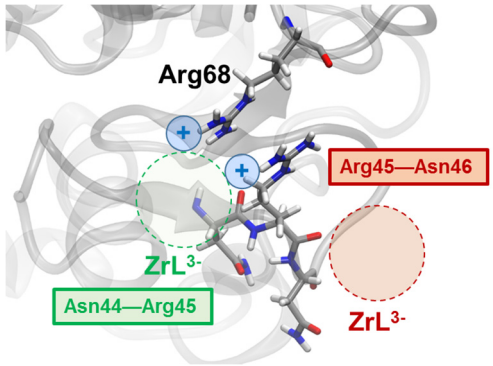

Figure 5.13 | Schematic representation showing the preference of **ZrL** to coordinate Asn44—Arg45 rather than Arg—Asn46 peptide bond.

To sum up, previous simulations have shown that POM anions can form persistent non–covalent interactions at different cationic patches of the HEWL protein surface (Chapters 3 and 4);[14,19] however, only specific peptide bonds of these sites are hydrolyzed. We propose that the observed selectivity is governed by non–covalent interactions occurring during the POM approach to the protein and the transition–metal coordination to the amide oxygen. In contrast to other sites, we observed for the selectively hydrolyzed site (Asn44–Arg45) that the side chains of two arginines (Arg45 and Arg68) clamp the POM and set stabilizing, non–covalent interactions with the POM during the whole coordination process, and presumably, along the whole reaction profile. This effect might be related to the observed selectivity as it can compensate to some extent the endothermicity of Zr coordination and prevent the inverse process that releases the Zr–substituted POM to the solvent. Although we have not characterized the whole process in the real system, we can speculate that the free–energy profiles of **Figure 5.14** could reflect the hydrolysis process of inert and reactive peptide bonds. DFT calculations suggested that the barriers required for carbon–nitrogen bond breaking are similar in both cases as denoted by red arrows in **Figure 5.14**. Nevertheless, in the reactive peptide bond the POM catalyst forms strong interactions with specific amino acids of the protein during the coordination process that might reduce the energy expense related to the reorientation of the POM to coordinate the peptide bond and in addition, shift the energy profile down ($\Delta\Delta G$ in **Figure 5.14**). Thus, the combination of both effects could accelerate the macroscopic hydrolysis rate of site II relative to other sites.

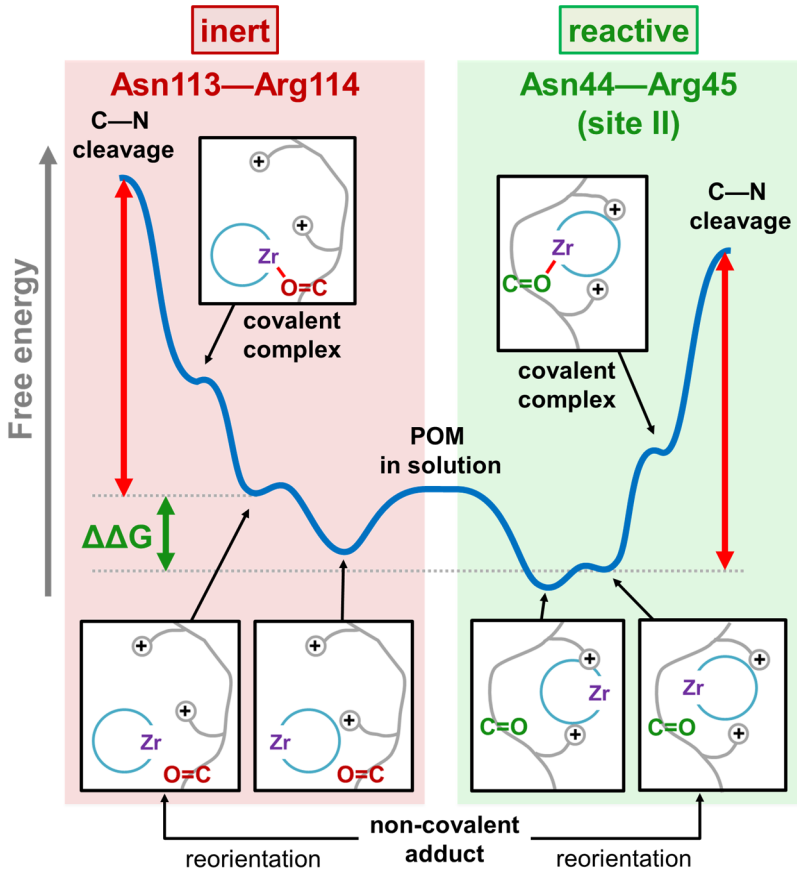

Figure 5.14 | Pictorial representation of the origin of selectivity in peptide bond hydrolysis in proteins by Zr–substituted POMs.

5.2 Reduction of Disulfide Bonds by Reduced Polyoxometalates

5.2.1 Motivation and Experimental Background.

Preeclampsia is a hypertensive disorder that complicates almost the 10 % of pregnancies from the 20th week on.[52] The main symptoms include high blood pressure, swelling, red blood cell breakdown and other dysfunctions affecting the liver, the kidney or the lungs, accounting for ca. 50,000 annual deaths worldwide.[53] Also, it increases the risk of premature delivery or even stillbirth, causing about 500,000 additional deaths per year.[54] The risk of developing preeclampsia has been related to the ratio of oxidized/reduced angiotensinogen (AGT) protein in blood.[55,56] Human AGT consists on a 453–residue

protein (represented in **Figure 5.15**) that is synthesized and delivered by the liver to participate in the renin–angiotensinogen system, which regulates blood pressure. The oxidized and reduced states of AGT differ from each other in the existence of a disulfide bridge between Cys18 and Cys138 (see **Figure 5.15**) that is present in the oxidized form (AGT_{ox}) but not in the reduced one (AGT_{red}). In healthy blood, AGT is found in a 40:60 ratio of the oxidized and the reduced form,[55] however, the levels of AGT_{ox} are higher in the blood of patients that are more prone to suffer hypertension.

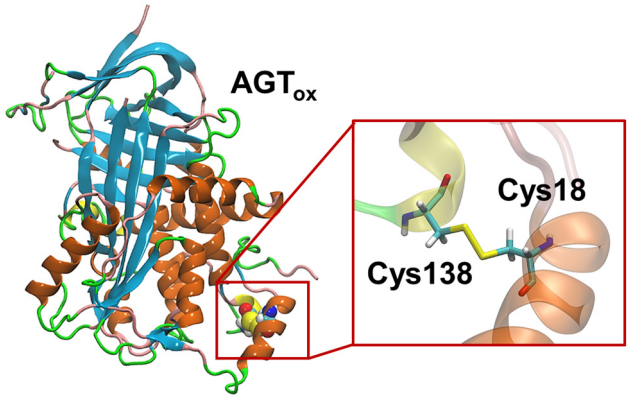

Figure 5.15 | Secondary structure of the oxidized form of angiotensinogen (AGT_{ox}), in which there is a disulfide bridge between Cys18 and Cys138.

Renin is a proteolytic enzyme secreted by the kidney that can only cleave AGT in its oxidized form at the N–terminus region to yield a decapeptide, namely Angiotensin I,[57] which in turn, can be further hydrolyzed by an enzyme produced at the lungs tissue, called angiotensin–converting enzyme (ACE).[58] Hydrolysis of angiotensin I results in angiotensin II, a polypeptide that is tightly related to hypertension due to its vasoconstrictive nature.[59] As in many other diseases, early detection of preeclampsia is crucial to reduce the risk of both maternal and infant mortality. Nowadays, Western blot techniques are used to determine the AGT_{ox}/AGT_{red} ratio in blood for clinical diagnosis of preeclampsia. However, these techniques are usually time–consuming, pseudo–quantitative and present low reproducibility.[60] Thus, there is a need for a new method for preeclampsia detection that is faster and more reliable. Our collaborators proposed a new strategy for preeclampsia detection based on a fast and easy–to–handle colorimetric analysis. Taking advantage of the redox properties of AGT, the percentage of oxidized protein in blood might be accurately quantified by reducing the disulfide bond

with a traceable redox mediator, in such a way that decrease in the absorbance can be attributed to the amount of oxidized protein in the initial sample.

POMs are potential candidates to act as reducing agents, since aqueous solutions of the fully oxidized anions are colorless but the reduced ones exhibit a deep blue coloration due to the presence of strong absorption bands in the visible region.[61] Initially, the one–electron reduced $[PW_{12}O_{40}]^{4-}$ anion labeled as **PW_{12}(1e)** was experimentally applied to the chemical reduction of 5,5'–dithiobis–(2–nitrobenzoic acid), DTNB (**1**, depicted in **Scheme 5.2**), as a model disulfide substrate. As shown in **Figure 5.16**, the addition of **1** to the charged solution of **PW_{12}(1e)** causes a quench of the absorbance, indicating that **PW_{12}(1e)** can accomplish the reduction of the disulfide bond in **1**. **Scheme 5.2** shows the proposed reaction equation, which involves a 1:2 stoichiometry, since the full reduction of a disulfide bond requires two electrons. However, the reduction of more inert, non–aromatic substrates containing dicysteine moieties using **PW_{12}(1e)** was unsuccessful. Aiming to understand this process, we performed a computational analysis of the reaction mechanism that allowed us to propose alternative POM species to promote the reduction of kinetically stable disulfides. With the gained knowledge, we also evaluated the feasibility of the S—S bond reduction in AGT_{ox}, which could be applied to diagnose preeclampsia in pregnants.

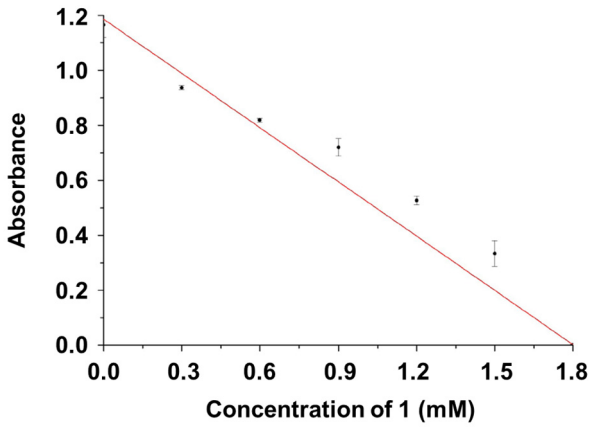

Figure 5.16 | Absorbance at 750 nm of a 0.6 mM solution of **PW_{12}(1e)** as function of the concentration of added **1**.

Scheme 5.2 | Proposed reaction equation for the reduction of **1** by $\mathbf{PW_{12}(1e)}$.

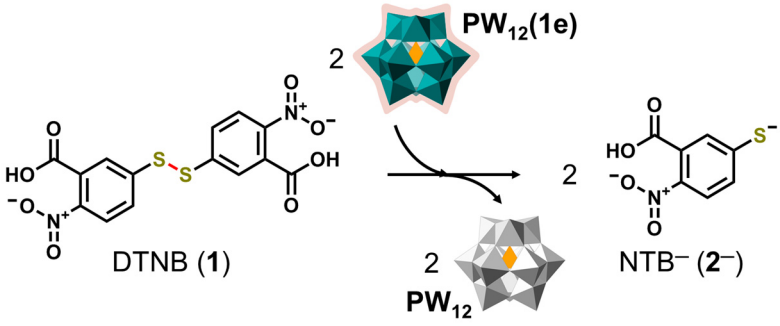

5.2.2 Computational Details.

The methodology used for these calculations is analogous to that used in the previous section. Single Electron Transfer (SET) steps were studied by means of the Marcus theory of the electron transfer, as explained in Chapter 1. The MD simulation to study the interaction between AGT_{ox} and $[H_2W_{12}O_{40}]^{7-}$ was carried out on a cubic solvent box of 97.4^3 Å^3 (28,395 H_2O molecules) that contains one AGT_{ox} protein (PDB ID: 2WXW),[62] one $[H_2W_{12}O_{40}]^{7-}$ anion and 18 Na^+ cations. FF parameters for the non–standard $[H_2W_{12}O_{40}]^{7-}$ were obtained as indicated in previous chapters.

5.2.3 Results and Discussion

5.2.3.1 Characterization of the reaction mechanism.

Initially, we analyzed the reaction mechanism for the reduction of **1** with $\mathbf{PW_{12}(1e)}$. Previous computational studies suggested two main mechanisms for the disulfide reduction promoted by external agents: i) the two–electron mechanism involving a S_N2 nucleophilic attack on a S atom to directly promote the S—S cleavage;[63] and ii) the outer–sphere electrochemical reduction in which the acceptance of two electrons by the substrate occurs in two different single electron transfer (SET) steps.[64,65] Radical–initiated mechanisms in which a homolytic C—H cleavage occurs on the C atom adjacent to S have been also proposed.[66] However, this option was ruled out due to the lack of an aliphatic carbon directly bonded to S in the structure of **1**.

Figure 5.17 shows the calculated outer–sphere free–energy profile that consists of three main steps: 1) the first one–electron reduction of the substrate to give a radical anion; 2) the S—S bond cleavage and 3) the second reduction of the NTB radical to yield the products. To study SET processes, we made use of the Marcus theory of the electron transfer,[67] which relates the free–energy barrier associated to the electron transfer with the reaction free energy and the reorganization energy of the system (including the solute and the solvent). Further details about this theory and its technical implementation are found in the Chapter 1 of this thesis. So far, Marcus theory has been successfully employed in the literature to study SET processes in organic and organometallic chemistry.[68] However, this is the first time to our knowledge that it is applied to processes in which POMs are involved. For this reason, we initially evaluated the applicability of this methodology by comparing, for the self–exchange reactions listed in **Table 5.3**,[69] the free–energy barriers obtained from experimental rate constants with those obtained computationally using the Marcus theory. Comparison of the rightmost columns in **Table 5.3** reveals rather good agreement between calculated and experimental free–energy barriers and therefore, we assumed that this approach is suitable for estimating the kinetic viability of the SET steps proposed in **Figure 5.17**.

Table 5.3 | Comparison between experimental and calculated free–energy barriers for self–exchange reactions of POMs of the same nature.

			ΔG* (kJ·mol^{-1})	
entry	**reaction**	**k_r[a] (M^{-1} s^{-1})**	**exp[b]**	**DFT[c]**
1	$PW_{12}^{4-} + PW_{12}^{3-} \rightarrow PW_{12}^{3-} + PW_{12}^{4-}$	$1.84\ 10^6$	37	37
2	$PW_{12}^{5-} + PW_{12}^{4-} \rightarrow PW_{12}^{4-} + PW_{12}^{5-}$	$3.80\ 10^4$	47	43

[a] Kozik et al.[69] reported rate constants at different ionic strengths. To compare with calculated ΔG*, we estimated the rate constant at zero ionic strength via extrapolation in the linear regression obtained from fitting $\ln(k_r)$ to the square root of the ionic strength.[70] [b] Experimental ΔG* were obtained from rate constants in the third column using the Eyring equation. [c] Calculated using the Marcus theory of the electron transfer using B3LYP–derived reorganization energies and reaction free energies.

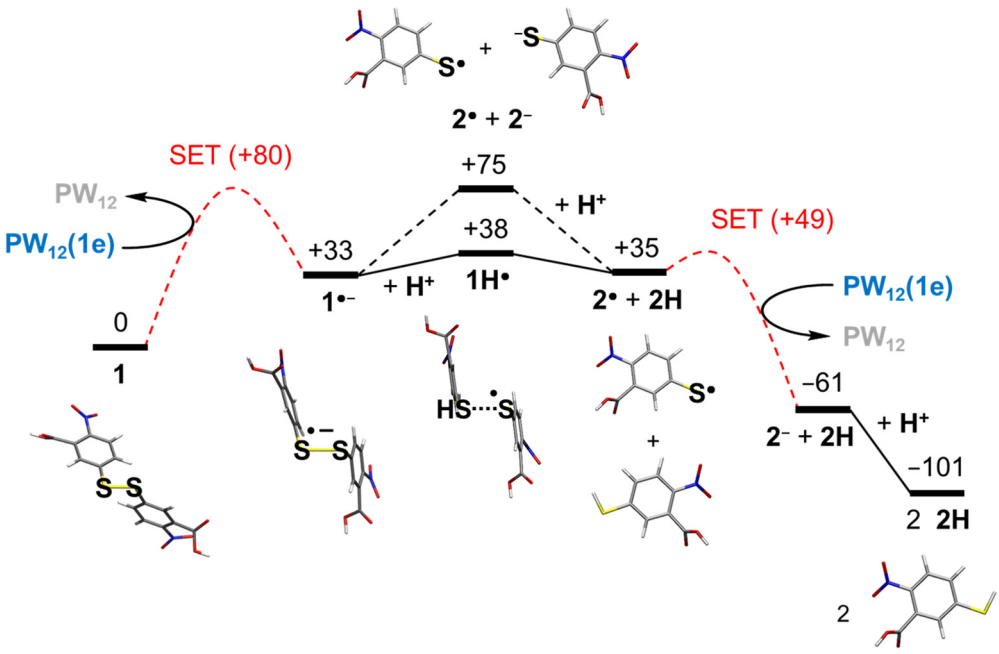

Figure 5.17 | Calculated Gibbs free–energy profile (kJ·mol^{-1}) for the reduction of DTNB (**1**) by 2 molecules of $[PW_{12}O_{40}]^{4-}$ anion, **PW_{12}(1e)**.

The outer–sphere SET from **PW_{12}(1e)** to **1** yields the radical anion species **1$^{\bullet-}$** and the oxidized POM and was found to be endergonic by 33 kJ·mol^{-1}. The estimated free–energy barrier of 80 kJ·mol^{-1} (see **Figure 5.17**) suggests that this SET step can be easily achieved at room temperature, in agreement with the fast quench in the absorbance observed experimentally. Notably, this reduction causes a non–negligible lengthening of the S—S distance from 2.07 Å in **1** to 2.80 Å in **1$^{\bullet-}$**, due to the population of a molecular orbital with S—S σ* character, as noted in previous computational studies.[64] Although the electronic structure of **1** shows two degenerated LUMOs mainly localized on the nitro groups (**Figure 5.18**), the spin density in the B3LYP–optimized geometry of **1$^{\bullet-}$** is localized on the S atoms, since the SOMO corresponds to the σ^*_{S-S} molecular orbital. Antonello *et* al. previously studied at Hartree–Fock level the reduction of several disulfides and identified two different minima for reduced nitroaryl disulfides (analogous to species **1$^{\bullet-}$**), which differ on the S—S bond length.[64b] At short S—S distance, the spin density is found in nitro groups while at long distances it is localized mainly on the sulfur atoms, similarly to what we obtained using the B3LYP functional (**Figure 5.18**). On the basis of the large gap between the LUMOs and the LUMO+2 orbital (see **Figure 5.18**), the

authors proposed an initial reduction at a π^* orbital (LUMO), followed by an internal conversion to populate the σ^*_{S-S} orbital upon elongation of the S—S bond.[64b] Unfortunately, we were not able to find the minimum with short S—S distance with B3LYP. Nevertheless, analysis of the PES with the M06–2X functional,[71] which includes a larger percentage of HF exchange, allowed us to locate a minimum for $\mathbf{1}^{\bullet-}$ with S—S distance of 2.10 Å. At M06–2X level, the formation of $\mathbf{1}^{\bullet-}$ with short S—S distance and spin density localized mainly in the nitro groups (**Figure 5.19**) is endothermic by 34 kJ·mol^{-1}; and the free–energy barrier associated to its formation was also found to be affordable (76 kJ·mol^{-1}). In fact, both values are rather close to those obtained with B3LYP considering the species with elongated S—S bond (**Figure 5.17**). This suggests that the potential energy surface of $\mathbf{1}^{\bullet-}$ along the S—S distance might be rather flat, involving more than one electronic state within a narrow range of energy. Thus, single–determinant methods might not be able to provide a detailed description of the reduction mechanism but can be useful to estimate the energy cost of the process. Regardless the mechanism, the computed barriers using the Marcus theory can be overcome at room temperature, which is supported by experimental results. Conversely, the two–electron pathway in which the POM performs a nucleophilic attack on the S—S bond was found to be prohibitively high in energy, since the products (see **Figure 5.20**) lie 187 kJ·mol^{-1} above the reactants. This was ascribed to the weak nucleophilic character of POM terminal oxygen.

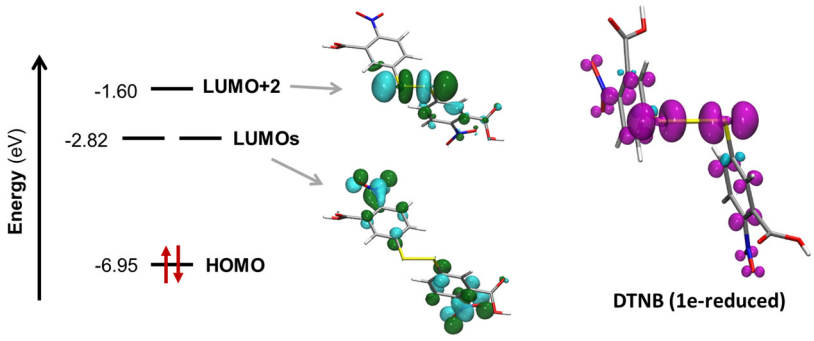

Figure 5.18 | Frontier molecular orbital diagram of the fully oxidized species **1** (left) and spin density of the B3LYP–optimized geometry of the one–electron reduced species $\mathbf{1}^{\bullet-}$, which displays a S—S distance of 2.80 Å (right).

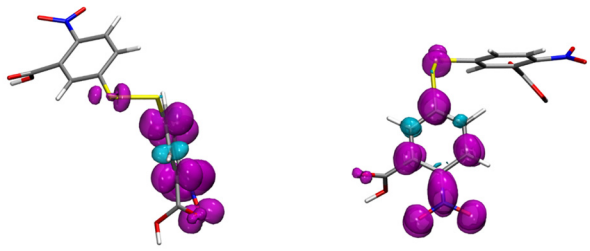

Figure 5.19 | Two views of the spin density distribution for the $\mathbf{1}^{\bullet-}$ species with short S—S distance (2.10 Å), obtained from geometry optimization with the M06–2X functional.

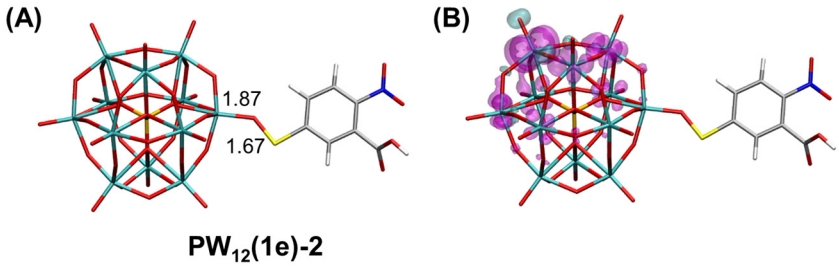

Figure 5.20 | (A) B3LYP–optimized structure resulting from the S_N2 attack of $\mathbf{PW_{12}(1e)}$ to **1** involving O—S bond formation ($\mathbf{PW_{12}(1e)–2}$). Main distances are shown in Å. (B) Representation of the spin density of $\mathbf{PW_{12}(1e)–2}$, which is delocalized over the POM framework.

From $\mathbf{1}^{\bullet-}$, we can envisage two possible pathways to proceed with the S—S cleavage: the direct cleavage to yield the radical and the anionic NTB fragments ($\mathbf{2}^{\bullet}$ and $\mathbf{2}^{-}$, respectively) or the proton–assisted process that involves the initial formation of the protonated species $\mathbf{1H}^{\bullet}$ (**Figure 5.17**). Before the reduction of **1**, the POM complex was reduced photochemically to generate $\mathbf{PW_{12}(1e)}$ using an excess of ascorbic acid as electron donor and therefore, it is reasonable to think that protons are readily available in the reaction medium. Thus, the negatively charged species $\mathbf{1}^{\bullet-}$ can become protonated to form $\mathbf{1H}^{\bullet}$ with a slight energy penalty of 5 kJ·mol^{-1}. Notably, the protonation elongates even more the S—S distance (up to 3.34 Å) resulting in a non–covalent S···S adduct in which the spin density is mostly localized on the non–protonated S atom. The structure of $\mathbf{1H}^{\bullet}$ might represent a fairly shallow minimum on the PES and dissociates into $\mathbf{2}^{\bullet}$ and the protonated product **2** through an exergonic and barrierless process. Note that owing the limitations of the employed methodology, it cannot be discarded that the formation of $\mathbf{1H}^{\bullet}$ from **1** occurs directly through a PCET process.

The alternative, direct dissociation of $\mathbf{1}^{\bullet-}$ into $\mathbf{2}^{\bullet}$ and $\mathbf{2}^{-}$ entails a significantly larger energy cost of 42 kJ·mol^{-1}. In agreement with the Morse–like potential energy functions reported by Antonello et al.,[64] the S—S cleavage in $\mathbf{1}^{\bullet-}$ was found to be barrierless. Overall, the protonation of $\mathbf{1}^{\bullet-}$ permits the disulfide cleavage through a smoother free–energy landscape, which in addition is consistent with the observed dependence on the pH of the decay rate of disulphide radical anions under acid conditions.[72]

It is also worth mentioning that Sohn *et* al. pointed out that the B3LYP functional commits a systematic error of *ca.* 8–10 kcal mol^{-1} (33–42 kJ·mol^{-1}) in the BDE of S—S bonds[66] and highlighted the better performances of meta–hybrid functionals such as BMK[73] or M06–2X.[71] **Table 5.4** shows that indeed, this error can be appreciated in the homolytic cleavage of the S—S bond in substrate **1** but not in the S—S cleavage of the reduced compound $\mathbf{1}^{\bullet-}$. Thus, we considered that B3LYP is suitable for describing the S—S cleavage shown in **Figure 5.17** ($\mathbf{1}^{\bullet-} \rightarrow \mathbf{2}^{\bullet} + \mathbf{2}^{-}$).

Table 5.4 | Comparison between the performances of B3LYP and meta–hybrid functionals in the determination of bond–dissociation energies (BDEs) of **1** and $\mathbf{1}^{\bullet-}$.

		BDE (kJ·mol^{-1})		
entry	**reaction**	**M06–2X**	**BMK**	**B3LYP**
1	$\mathbf{1} \rightarrow \mathbf{2}^{\bullet} + \mathbf{2}^{\bullet}$	+252	+262	+220
2	$\mathbf{1}^{\bullet} \rightarrow \mathbf{2}^{\bullet} + \mathbf{2}^{-}$	+63	+71	+72

Finally, the second reduction was found to be highly stabilizing (in almost 100 kJ·mol^{-1}) because it implies the reduction of the electron deficient radical species $\mathbf{2}^{\bullet}$ to form the corresponding anion. Consequently, this SET step occurs through a very smooth barrier of 14 kJ·mol^{-1}. The protonation of the resulting $\mathbf{2}^{-}$ anion places the reaction products 101 kJ·mol^{-1} below the reactants and renders irreversible the global reaction, being the reverse free–energy barrier higher than 150 kJ·mol^{-1}. Overall, the first reduction step of the DTNB substrate (**1**) is predicted to be the rate–determining step of the whole process. However, it is important to note that the S–S bond cleavage could become rate–determining in the absence of proton sources.

5.2.3.2 *Reducing dicysteine–like models.*

The reduction of DTNB (**1**) can be seen as a proof of concept for the reduction of S—S bonds with POMs, but the target disulphide bond in AGT does not have aromatic substituents to stabilize the radical anion intermediate but it connects two cysteine residues (Cys18 with Cys138), as shown in **Figure 5.15**. For this reason and with a more ambitious goal, the group of Dr. Mitchell synthesized polypeptide structures (depicted in **Scheme 5.3**) based on a dicysteine fragment to study more realistic models of AGT. Unfortunately, **PW_{12}(1e)** showed no reactivity towards these substrates and therefore, it might not be suitable neither for the reduction of AGT_{ox}.

Scheme 5.3 | Chemical structures of dicysteine–based polypeptides **3** and **4**.

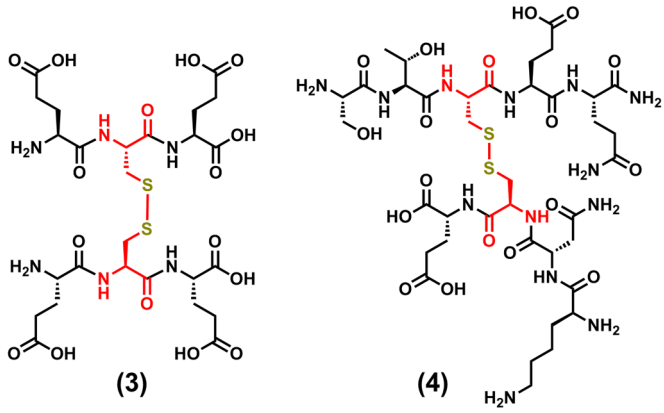

To model these substrates, we considered the zwitterionic forms (**3z** and **4z**) expected for a pH close to 7, that is the carboxylic groups in **Scheme 5.3** as negatively charged carboxylates and the terminal amines as positively charged ammonium groups in such a way that **3z** and **4z** bear overall charges of 4– and 2+, respectively (see **Figure 5.21**). For the sake of comparison, we also studied the reactivity of the neutral form of **3**. In line with the experimental lack of reactivity, the free–energy barriers associated to the first reduction of these substrates by **PW_{12}(1e)** were computed to be unaffordable (> 150 $kJ{\cdot}mol^{-1}$) as shown in fourth column of **Table 5.5**. The reduction of diaryl disulphides such as **1** has been proposed to be easier than other substrates due to partial delocalization of the unpaired electron over the phenyl rings (see spin density of $\mathbf{1}^{\bullet-}$ in **Figure 5.18**), which favors the electron transfer reducing the reorganization energy (λ) of the substrate,[64a] as well as the endothermicity of the electron transfer process. In agreement with these findings, the calculated reorganization energies for the non–aromatic substrates

are ca. 100 kJ·mol^{-1} larger (see column 2 in **Table 5.5**). Thus, we evaluated whether the reduction of highly kinetically stable substrates (**Scheme 5.3**) can be achieved by using stronger reductants obtained electrochemically. Potential candidates include the two–electron reduced $[PW_{12}O_{40}]^{5-}$, **PW_{12}(2e)**, the one–electron reduced silicon–containing Keggin anion $[SiW_{12}O_{40}]^{5-}$, labeled as **SiW_{12}(1e)** or the one–electron reduced metatungstate $[H_2W_{12}O_{40}]^{7-}$ anion, labeled as **H_2W_{12}(1e)**. **Table 5.5** collects the computed free–energy barriers for the first reduction of the analyzed substrates by the aforementioned POM structures. As expected, the height of the barriers decreases as the overall charge of the POM increases, because the energy of the molecular orbital of the POM that accommodates the electron to be transferred is proportional to the charge density of the cluster.[74] Thus, the barriers for the reduction of dicysteine substrates by **PW_{12}(2e)** and **SiW_{12}(1e)**, with q = 5– are lower than those for **PW_{12}(1e)** but still rather high (125–155 kJ·mol^{-1}) and those for the 7– charged **H_2W_{12}(1e)** are moderate (100–116 kJ·mol^{-1}). This suggests that, among the analyzed POM structures, **H_2W_{12}(1e)** is the only one that is likely to reduce disulfide bonds in dicysteine–based substrates. Prompted by these results, our collaborators attempted experimentally the reduction of substrate **4** with **H_2W_{12}(1e)** and indeed, mixing these species results in quenching of the absorbance. This validates our mechanistic proposal and more importantly, probes the ability of **H_2W_{12}(1e)** to reduce the highly stable S—S bond in a dicysteine–based substrate. Therefore, this anion could be suitable for the reduction of the S—S bond in AGT_{ox} and in turn, for the clinical diagnosis of preeclampsia.

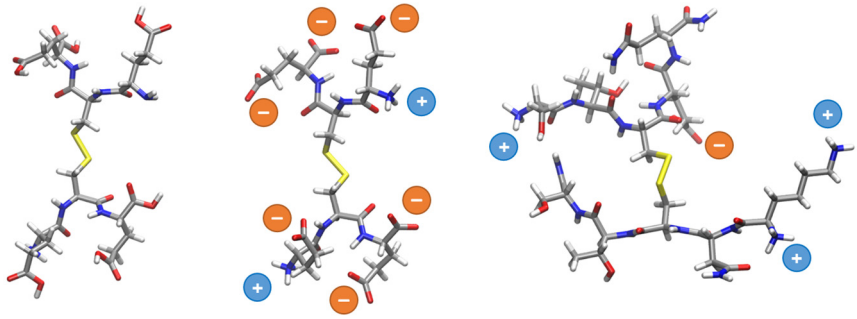

Figure 5.21 | B3LYP–optimized structures of neutral species **3** and zwitterionic complexes **3z** and **4z**.

It is interesting to note that the barriers reported for the neutral **3** are lower than those obtained for its zwitterionic form (**3z**) with a charge of 4–. Since the reorganization

energies for both species is rather similar, this fact was attributed to the energy cost of the reduction process, which increases with the negative charge of the organic substrate. In fact, **Table 5.5** shows that the height of the barriers correlates rather well with the reduction free–energy (ΔG_{red}), indicating that besides the reorganization energy, the stability of the formed radical anion is crucial for reactivity.

Table 5.5 | Free–energy barriers for the first SET process for the studied disulphide substrates and POM reductants.

Substrate (*q*)	**reorganization energy** ($\lambda_{substrate}$)	ΔG_{red}	ΔG^{*}_{SET} (kJ·mol^{-1})			
			$[PW_{12}O_{40}]^{4-}$ **PW_{12}(1e)**	$[PW_{12}O_{40}]^{5-}$ **PW_{12}(2e)**	$[SiW_{12}O_{40}]^{5-}$ **SiW_{12}(1e)**	$[H_2W_{12}O_{40}]^{7-}$ **H_2W_{12}(1e)**
1 (0)	176	−3.83	80	59	69	41
3 (0)	274	−2.99	156	129	140	105
3z (4−)	269	−2.71	172	143	155	116
4z (2+)	272	−2.97	152	125	136	100

[a] Reorganization energies ($\lambda_{substrate}$) and free–energy barriers are given in kJ·mol^{-1}, whereas reduction free–energies [$\Delta G_{red} = G_{red} - G_{ox}$] are given in eV. The reorganization energies for the different POM complexes (λ_{POM}) are rather alike, ranging from 73 to 105 kJ·mol^{-1}.

5.2.3.3 Reducing angiotensinogen protein (AGT_{ox}).

Finally, we sought to analyze if **H_2W_{12}(1e)** could promote the reduction of AGT_{ox} using a *cluster model*[35] of the Cys18—Cys138 fragment labeled as **Dicys**, taken from the X–ray crystal structure of AGT_{ox} (**Figure 5.15**). The obtained free–energy profile is represented in **Figure 5.22**. As for the model substrate **1**, the rate–limiting step of the whole process is the first SET from the POM to the disulfide bond, which accounts for an accessible barrier of 104 kJ·mol^{-1}. Although this barrier is higher than that for the reduction of DTNB by **PW_{12}(1e)** (80 kJ·mol^{-1}), the endothermicity is smaller due to high energy of the highly charged **H_2W_{12}(1e)** species. The S—S bond cleavage in **Dicys$^{\bullet-}$** is not as endergonic as in **1$^{\bullet-}$** because aliphatic groups are electron donating groups that can better stabilize the electron deficient radical species Cys$^{\bullet}$ (analogous to **2$^{\bullet}$**).[66] From this point on, the reaction goes steeply downhill with an estimated free–energy barrier for the second SET reduction of 31 kJ·mol^{-1}. Finally, the process yields the products that lie almost 300 kJ·mol^{-1} below the reactants and thus, their formation is strongly irreversible. We have also

determined the kinetics of the first reduction, which is rate–limiting, considering the dielectric constant of the solvent equal to 4, which is a common approach when studying enzymatic reactions within a truncated model to simulate the hydrophobic environment.[35] With this approach, the barrier increases from 104 to 129 kJ·mol^{-1}, which is near the limit of kinetically accessible reactions at room temperature. Nevertheless, as the disulfide bond in AGT$_{ox}$ is at the solvent accessible surface of the protein, we considered the values in water and in the hydrophobic environment as lower and upper limits for the actual free–energy barrier.

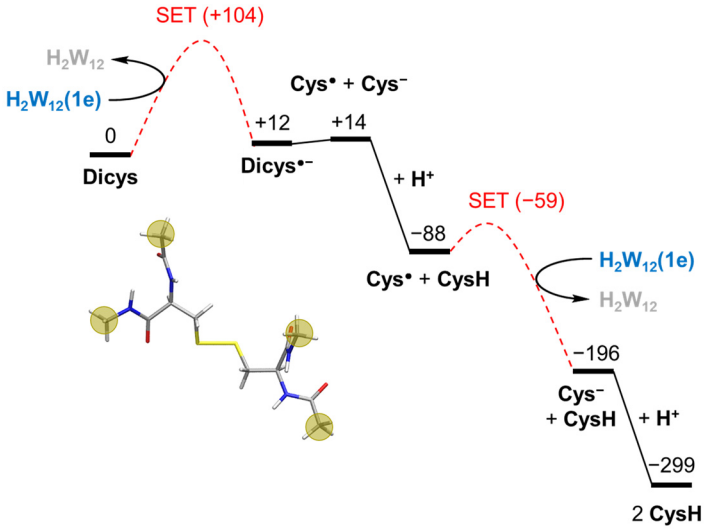

Figure 5.22 | Calculated Gibbs free–energy profile (kJ·mol^{-1}) for the reduction of the disulfide bond in the dicysteine fragment of AGT$_{ox}$ (**Dicys**) by **H$_2$W$_{12}$(1e)**. The snapshot shows the model system used for this study and highlights the positions that kept fixed during geometry optimizations to account for the strain imposed by the protein chains.

Aside from affordable kinetics, reactivity in biological systems is strongly dependent on the supramolecular recognition process, as discussed in the first part of this chapter. Thus, getting insight into the non–bonding interactions between **H$_2$W$_{12}$(1e)** and AGT$_{ox}$ in solution might be useful to rationalize hypothetical experimental outcomes in the future. To investigate the interaction of **H$_2$W$_{12}$(1e)** with the protein at the proximity of the disulfide bridge to promote its reduction, we have performed MD simulations starting from a configuration in which **H$_2$W$_{12}$(1e)** is close to the reactive site.[14]

Figure 5.23A shows the evolution of the distance between the centers of mass of the disulfide bond and the POM along 20 ns of simulation. During the first 10 ns the POM remains at a relatively short distance from the disulfide bond that is suitable for the electron transfer process.[75] During the simulation, the POM mainly interacts with positively charged lysine residues that are close to the S—S bond (Lys23, 28, 30 and 136) leading to POM···protein interactions that range, roughly, from −100 to −200 kJ·mol^{-1}. Specifically, we identified two interaction modes for which representative snapshots of these interactions can be appreciated in **Figure 5.23**B and C. In the first one (**Figure 5.23**B) the POM interacts with Lys23, 28 and 30 being at about 20 Å of the disulfide bond, while the second one involves Lys28 and 136 and permits shorter POM···SS distances of ca. 16 Å (the shortest being 12.4 Å). Note that these distances were measured taking as reference the centers of mass of both moieties, but as electrons are not located inside the POM but on W atoms, the effective distances between the electron donor and the acceptor are shorter. Importantly, both adducts might be able to promote the S—S reduction through an outer−sphere electron transfer, since charge transfer between redox partner proteins has been measured at intermolecular distance of up to 10 nm.[75a] After that, the POM moves through the protein surface to other regions where the POM···protein interactions are weaker until it leaves the protein surface to become fully solvated at t ≈ 15 ns. According to the high charge density of a Keggin−sized anion bearing a charge of 7−, $\mathbf{H_2W_{12}(1e)}$ exhibits poor chaotropic behavior[19] and therefore, its residence time in positively charged sites of AGT_{ox} accounts only for the 51.8 % of the simulated time (considering the same geometric criteria used in previous chapters). However, it has been demonstrated that $\mathbf{H_2W_{12}(1e)}$ can establish strong interactions at the vicinity of the disulfide bond in AGT_{ox} and therefore, it is a potential candidate to be used for the clinical diagnosis of preeclampsia.

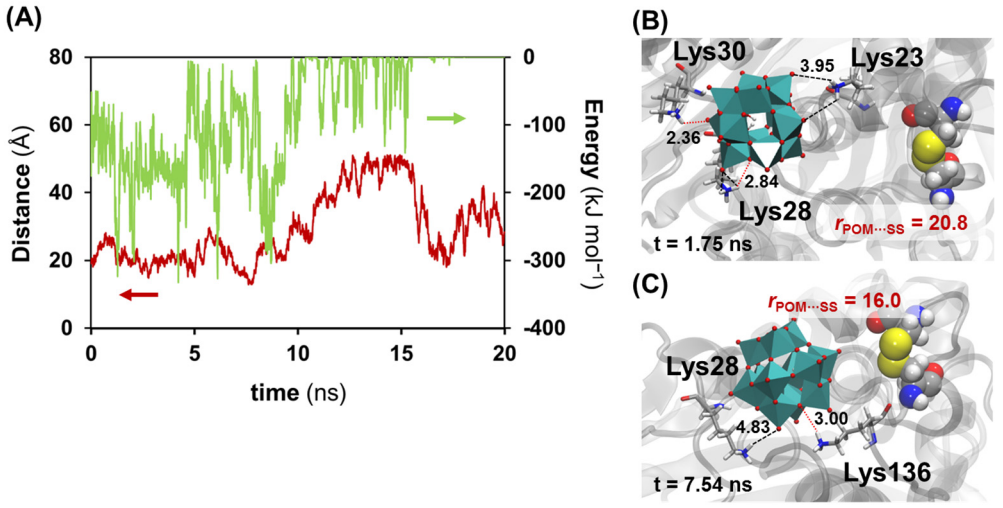

Figure 5.23 | (A) Evolution of the distance between the centers of mass of $\mathbf{H_2W_{12}(1e)}$ and the disulfide bond (red line), as well as the overall POM···protein interaction energy (green line) along 20 ns of MD simulation. (B) and (C) Representative snapshots of the non–covalent POM···protein interactions occurring at the vicinity of the disulfide bridge, with interaction energies of −153 and −104 kJ·mol^{-1}, respectively. Dashed black lines represent purely electrostatic contacts and hydrogen bonds are shown in red dotted lines (criteria for hydrogen bonds: XH···A distance ≤ 3.5 Å and X–H···A angle ≥ 130 ^{0}. Distances are given in Å.

5.3 Concluding remarks

In the first part of this chapter we report a detailed computational study of the origin of selectivity in protein hydrolysis promoted by Zr^{IV}–containing polyoxometalates. Specifically, we analyzed the observed selective hydrolysis in lysozyme using $[W_5O_{18}Zr(H_2O)(OH)]^{3-}$ (**ZrL**) as an artificial protease; and compared the Asn44—Arg45 cleavage site with three structurally similar, non–reactive peptide bonds. Using DFT calculations on cluster models derived from MD simulations, we propose a reaction mechanism consisting of four main steps: i) coordination of the Zr center to the amide oxygen; ii) nucleophilic attack of either the hydroxo ligand of Zr or an external water molecule assisted by the ZrOH group as general base; iii) protonation of the amide nitrogen and iv) C–N bond cleavage. The reaction goes uphill in energy until it reaches the transition state for C–N bond cleavage, and therefore the overall activity is governed by the energy cost to reach this transition state from the reactants. We also found that the overall free–energy barrier of the hydrolysis is very sensitive to the protein conformation

but it shows a linear correlation with the length of the dipeptide section. The computed $\Delta G^{\ddagger}_{overall}$ for Asn44—Arg45 peptide bond, averaged over protein conformation (121 kJ·mol^{-1}), agrees very well with the values derived from the experimental rate constants (113–134 kJ·mol^{-1}).

The origin of selectivity cannot be ascribed to the intrinsic differences on the protein backbone because computed overall free–energy barriers for other chemically analogous peptide bonds (Asn113–Arg114, Arg21–Gly22 and Arg45–Asn46) are very similar. Instead, MD simulations show that unlike other sites, the experimentally hydrolyzed Asn44–Arg45 is surrounded by an array of positively charged and polar amino acids that can trap the POM in an *enzyme–like* recognition process and interact with it during the coordination process. This might hold together the reactants (the POM and the O=C fragment) and reduce the energy expense of POM reorientation and coordination to Asn44–Arg45 resulting in the acceleration of the hydrolysis rate with respect to other sites.

We have also characterized the reduction mechanism of DTNB (**1**), as model system of the oxidized form of angiotensinogen protein (AGT_{ox}) by the one–electron reduced Keggin–type phosphotungstate $[PW_{12}O_{40}]^{4-}$, **PW_{12}(1e)**. The most likely reaction mechanism involves an initial outer–sphere SET from a molecule of **PW_{12}(1e)** to **1** to yield an oxidized POM and the radical anion **1**$^{\bullet-}$ in which the S—S has been weakened due to partial occupation of the $\sigma^*_{S—S}$ orbital. Protonation of **1**$^{\bullet-}$ promotes the S—S bond cleavage to give the protonated NTB product (**2**) and a radical NTB (**2**$^{\bullet}$), which can be easily reduced to **2**$^{-}$ by a second molecule of **PW_{12}(1e)** to yield the final products after the exothermic protonation of **2**$^{-}$. The initial reduction of **1** was identified as the rate–determining step of the reaction, indicating that the reaction rate mainly depends on the reductant power of the employed POM and the ability of the disulfide bond to accept an electron. For **1**, the overall free–energy barrier accounts for 80 kJ·mol^{-1}, in agreement with the fast quench of the **PW_{12}(1e)** solution upon addition of **1**. Also, a computationally–aided study allowed the experimental reduction of more realistic models of angiotensin consisting on dicysteine–based polypeptides using the one–electron reduced metatungstate anion $[H_2W_{12}O_{40}]^{7-}$, **H_2W_{12}(1e)**. Unlike **H_2W_{12}(1e)**, **PW_{12}(1e)** and other less charged anions exhibit SOMOs too deep in energy to promote an electron transfer to non–aromatic disulfides, which are more kinetically stable than **1** due to the larger reorganization energies involved in the SET process and the less stable character of the formed radical anion. Furthermore, MD simulations and DFT calculations on AGT_{ox}

using a cluster model approach suggested that the reduction of the dicysteine group in the protein is feasible, since $\mathbf{H_2W_{12}(1e)}$ can interact favorably in a region close to the S—S bond site, and the predicted barrier for the electron transfer is affordable, lying between 104 and 129 kJ·mol^{-1}.

5.4 Supplementary Material

The animation of a representative simulation discussed in this chapter can be accessed by scanning the following QR code with a smartphone or though the URL below.

Constrained MD — Coordination of **ZrL** to site II

https://youtu.be/Ffq8F41Of1E

References

1. See this review and references therein: Grant, K. B.; Kassai, M. *Curr. Org. Chem.* **2006**, *10*, 1035–1049.
2. Radzicka, A.; Wolfenden, R. *J. Am. Chem. Soc.* **1996**, *118*, 6105–6109.
3. See for instance: Wezynfeld, N. E.; Frączyk, T.; Bal, W. *Coord. Chem. Rev.* **2016**, *327–328*, 166–187.
4. Absillis G.; Parac–Vogt, T. N. *Inorg. Chem.* **2012**, *51*, 9902–9910.
5. Ly, H. G. T.; Mihaylov, T.; Absillis, G.; Pierloot, K.; Parac–Vogt, T. N. *Inorg. Chem.* **2015**, *54*, 11477–11492.
6. Stroobants, K.; Moelants, E.; Ly, H. G. T.; Proost, P.; Bartik K.; Parac–Vogt, T. N. *Chem. Eur. J.* **2013**, *19*, 2848–2858.
7. Stroobants, K.; Absillis, G.; Moelants, E.; Proost P.; Parac–Vogt, T. N. *Chem. Eur. J.* **2014**, *20*, 3894–3897.
8. Stroobants, K.; Goovaerts, V.; Absillis, G.; Bruylants, G.; Moelants, E.; Proost P.; Parac–Vogt, T. N. *Chem. Eur. J.* **2014**, *20*, 9567–9577.
9. Ly, H. G. T.; Absillis, G.; Janssens, R.; Proost, P.; Parac–Vogt, T. N. *Angew. Chem. Int. Ed.* **2015**, *54*, 7391–7394.
10. Sap, A.; Van Tichelen, L.; Mortier, A.; Proost, P.; Parac–Vogt, T. N. *Eur. J. Inorg. Chem.* **2016**, *32*, 5098–5105.
11. Quanten, T.; Mayaer, T. D.; Shestakova, P.; Parac–Vogt, T. N. *Front. Chem.* **2018**, *6*, 372
12. Ly, H. G. T.; Mihaylov, T. T.; Proost, P.; Pierloot, K.; Harvey, J. N.; Parac–Vogt, T. N. *Chem. Eur. J.* **2019**, DOI:10.1002/chem.201902675.
13. a) Dolinsky, T. J.; Czodrowski, P.; Li, H.; Nielsen, J. E.; Jensen, J. H.; Klebe, G.; Baker, N. A. *Nucleic Acids Res.* **2007**, *35*, W522–W525; b) Dolinsky, T. J.; Nielsen, J. E.; McCammon, J. A.; Baker, N. A. *Nucleic Acids Res.*, **2004**, *32*, W665–W667; c) Baker, N. A.; Sept, D.; Joseph, S.; Holst, M. J.; McCammon, J. A. *Proc. Natl. Acad. Sci. U. S. A.* **2001**, *98*, 10037–10041.
14. Solé–Daura, A.; Goovaerts, V.; Stroobants, K.; Absillis, G.; Jiménez–Lozano, P.; Poblet, J. M.; Hirst, J. D.; Parac–Vogt, T. N.; Carbó, J. J. *Chem. Eur. J.* **2016**, *22*, 15280–15289.
15. Sap, A.; De Zitter, E.; Van Meervelt, L.; Parac–Vogt, T. N. *Chem. Eur. J.* **2015**, *21*, 11692–11695.
16. Vandebroek, L.; De Zitter, E.; Ly, H. G. T.; Conić, D.; Mihaylov, T.; Sap, A.; Proost, P.; Pierloot, K.; Van Meervelt, L.; Parac–Vogt, T. N. *Chem. Eur. J.* **2018**, *24*, 10099–10108.
17. Vandebroek, L.; Mampaey, Y.; Antonyuk, S.; Van Meervelt, L.; Parac–Vogt, T. N. *Eur. J. Inorg. Chem.* **2019**, *3*, 506–511.
18. Paul, T. J.; Parac–Vogt, T. N.; Quiñonero, D.; Prabhakar, R. *J. Phys. Chem. B* **2018**, *122*, 7219–7232.
19. Solé–Daura, A.; Poblet, J. M.; Carbó, J. J. (*submitted*); publication related to Chapter 4 of this thesis.
20. Jayasinghe–Arachchige, V. M.; Hu, Q.; Sharma, G.; Paul, T. J.; Lundberg, M.; Quinonero, D.; Parac–Vogt, T. N.; Prabhakar, R. *J. Comp. Chem.* **2019**, *40*, 51–61.
21. a) Zhang, T.; Zhu, X.; Prabhakar, R. *J. Phys. Chem. B.* **2014**, *118*, 4106–4114; b) Zhang, T.; Ozbil, M.; Barman, A.; Paul, T. J.; Bora, R. P.; Prabhakar, R. *Acc. Chem. Res.* **2015**, *48*, 192–200; c) Zhang, T.; Sharma, G.; Paul, T. J.; Hoffmann, Z.; Prabhakar, R. *J. Chem. Inf. Model.* **2017**, *57*, 1079–1088.
22. Pelmenschikov, V.; Blomberg, M. R. A.; Siegbahn, P. E. M. *J. Biol. Inorg. Chem.* **2002**, *7*, 284–298.
23. Bora, R. P.; Barman, A.; Zhu, X.; Ozbil, M.; Prabhakar, R. *J. Phys. Chem. B.* **2010**, *114*, 10860–10875.
24. Blumberger, J.; Lamoureux, G.; Klein, M. L. *J. Chem. Theory Comput.* **2007**, *3*, 1837–1850.
25. Brás, N. F.; Fernandes, P. A.; Ramos, M. J. *ACS Catal.* **2014**, *4*, 2587–2597.
26. Díaz, N.; Suárez D. *J. Phys. Chem. B* **2008**, *112*, 8412–8424.
27. Paul, T. J.; Barman, A.; Ozbil, M.; Bora, R. P.; Zhang, T.; Sharma, G.; Hoffmann, Z.; Prabhakar, R. *Phys. Chem. Chem. Phys.* **2016**, *18*, 24790–24801.
28. Leopoldini, M.; Russo, N.; Toscano, M. *J. Am. Chem. Soc.* **2007**, *129*, 7776–7784.

29. Alberto, M. E.; Leopoldini, M.; Russo, N. *Inorg. Chem.* **2011**, *50*, 3394–3403.
30. a) Lee, C.; Yang, W.; Parr, R. G. *Phys. Rev. B: Condens. Matter Mater. Phys.* **1988**, *37*, 785–789; b) Becke, A. D. *J. Chem. Phys.* **1993**, *98*, 5648–5652; c) Stephens, P. J.; Devlin, F. J.; Chabalowski, C. F.; Frisch, M. J. *J. Phys. Chem.* **1994**, *98*, 11623–11627.
31. Frisch, M. J.; Trucks, G. W.; Schlegel, H. B.; Scuseria, G. E.; Robb, M. A.; Cheeseman, J. R.; Scalmani, G.; Barone, V.; Mennucci, B.; Petersson, G. A.; Nakatsuji, H.; Caricato, M.; Li, X.; Hratchian, H. P.; Izmaylov, A. F.; Bloino, J.; Zheng, G.; Sonnenberg, J. L.; Hada, M.; Ehara, M.; Toyota, K.; Fukuda, R.; Hasegawa, J.; Ishida, M.; Nakajima, T.; Honda, Y.; Kitao, O.; Nakai, H.; Vreven, T.; Montgomery, J. A., Jr.; Peralta, J. E.; Ogliaro, F.; Bearpark, M.; Heyd, J. J.; Brothers, E.; Kudin, K. N.; Staroverov, V. N.; Kobayashi, R.; Normand, J.; Raghavachari, K.; Rendell, A.; Burant, J. C.; Iyengar, S. S.; Tomasi, J.; Cossi, M.; Rega, N.; Millam, J. M.; Klene, M.; Knox, J. E.; Cross, J. B.; Bakken, V.; Adamo, C.; Jaramillo, J.; Gomperts, R.; Stratmann, R. E.; Yazyev, O.; Austin, A. J.; Cammi, R.; Pomelli, C.; Ochterski, J. W.; Martin, R. L.; Morokuma, K.; Zakrzewski, V. G.; Voth, G. A.; Salvador, P.; Dannenberg, J. J.; Dapprich, S.; Daniels, A. D.; Farkas, Ö.; Foresman, J. B.; Ortiz, J. V.; Cioslowski, J.; Fox, D. J. Gaussian 09, revision A.02; Gaussian, Inc.: Wallingford, CT, 2009.
32. Hay, P. J.; Wadt, W. R. *J. Chem. Phys.* **1985**, *82*, 270–283.
33. a) Francl, M. M.; Pietro, W. J.; Hehre, W. J.; Binkley, J. S.; Gordon, M. S.; DeFrees, D. J.; Pople, *J. J. Chem. Phys.* **1982**, *77*, 3654–3665; b) Hehre, W. J.; Ditchfield, R.; Pople, J. A. *J. Chem. Phys.* **1972**, *56*, 2257–2261; c) Hariharan, P. C.; Pople, J. A. *Theoret. Chim. Acta* **1973**, *28*, 213–222.
34. Cancès, E.; Mennucci, B.; Tomasi, J. *J. Chem. Phys.* **1997**, *107*, 3032–3041.
35. The cluster model approach consists on taking a fragment from a biological system to perform calculations constraining the relative position of the capping groups during the geometry optimizations to mimic the strain in the real system (see also Computational Details section). For an example of its successful application, see: Himo F, Siegbahn P. E. M. *Chem. Rev.* **2003**, *103*, 2421–2456.
36. Pliego, J. R., Jr.; Riveros, J. M. *J. Phys. Chem. A* **2001**, *105*, 7241–7247.
37. Shao, Y.; Gan, Z.; Epifanovsky, E.; Gilbert, A. T. B.; Wormit, M.; Kussmann, J.; Lange, A. W.; Behn, A.; Deng, J.; Feng, X.; *et al. Mol. Phys.* **2015**, *113*, 184–215.
38. Brooks, B. R.; Brooks, C. L. 3rd; Mackerell, A. D. Jr.; Nilsson, L.; Petrella, R. J.; Roux, B.; Won, Y.; Archontis, G.; Bartels, C.; Boresch, S.; Caflisch, A.; Caves, L.; Cui, Q.; Dinner, A. R.; Feig, M.; Fischer, S.; Gao, J.; Hodoscek, M.; Im, W.; Kuczera, K.; Lazaridis, T.; Ma, J.; Ovchinnikov, V.; Paci, E.; Pastor, R. W.; Post, C. B.; Pu, J. Z.; Schaefer, M.; Tidor, B.; Venable, R. M.; Woodcock, H. L.; Wu, X.; Yang, W.; York, D. M.; Karplus, M. *J. Comput. Chem.* **2009**, *30*, 1545–1614.
39. a) MacKerell, A. D., Jr., Feig, M. and Brooks, III, C. L. *J. Am. Chem. Soc.* **2004**, *126*, 698–699; b) MacKerell, Jr., A. D.; Bashford, D.; Bellott, M.; Dunbrack Jr., R.L.; Evanseck, J. D.; Field, M. J.; Fischer, S.; Gao, J.; Guo, H.; Ha, S.; Joseph–McCarthy, D.; Kuchnir, L.; Kuczera, K.; Lau, F. T. K.; Mattos, C.; Michnick, S.; Ngo, T.; Nguyen, D. T.; Prodhom, B.; Reiher, III, W. E.; Roux, B.; Schlenkrich, M.; Smith, J.C.; Stote, R.; Straub, J.; Watanabe, M.; Wiorkiewicz–Kuczera, J.; Yin, D.; Karplus, M. *J. Phys. Chem. B*, **1998**, *102*, 3586–3616.
40. Jo, S.; Kim, T.; Iyer, V. G.; Im, W. *J. Comput. Chem.* **2008**, *29*,1859–1865.
41. a) Vasilyev, V. V. *J. Mol. Struct. (Theochem)* **1994**, *110*, 129–141; b) Waszkowycz, B.; Hillier, I. H.; Gensmantel, N.; Payling, D. W. *J. Chem. Soc. Perkin Trans. 2* **1991**, *2*, 225–231.
42. Singh, U. C.; Kollman, P. A. *J. Comput. Chem.* **1986**, *7*, 718–730.
43. Das, D.; Eurenius, K. P.; Billings, E. M. *J. Chem. Phys.* 2002, *117*, 10534–10547.
44. Woodcock, H. L.; Hodošček, M.; Sherwood, P.; Lee, Y. S.; Schaefer III, H. F.; Brooks, B. R. *Theor. Chem. Acc.* **2003**, *109*, 140–148.

45. Jiménez–Lozano, P.; Carbó, J. J.; Chaumont, A.; Poblet, J. M.; Rodríguez–Fortea, A.; Wipff, G. *Inorg. Chem.* 2014, **53**, 778–786.
46. Ferrer, S.; Tuñón, I.; Martí, S.; Moliner, V.; Garcia–Viloca, M.; González–Lafont, À.; Lluch, J. M. *J. Am. Chem. Soc.* **2006**, *128*, 16851–16863.
47. Hu, P.; Zhang, Y. *J. Am. Chem. Soc.* **2006**, *128*, 1272–1278.
48. Lodola, A.; Mor, M.; Zurek, J.; Tarzia, G.; Piomelli, D.; Harvey, J. N.; Mulholland, A. J. *Biophys. J.* **2007**, *92*, L20–L22.
49. Benkovic, S. J.; Hammes, G. G.; Hammes–Schiffer, S. *Biochemistry* **2008**, *47*, 3317–3321.
50. a) Ribeiro, A. J.; Ramos, M. J.; Fernandes, P. A. *J. Am. Chem. Soc.* **2012**, *134*, 13436–13447; b) Ribeiro, A. J. M.; Santos–Martins, D.; Russo, N.; Ramos, M. J.; Fernandes, P. A. *ACS Catal.* **2015**, *5*, 5617–5626.
51. Perticaroli, S.; Nickels, J. D.; Ehlers, G.; O'Neill, H.; Zhang, Q.; Sokolov, A. P. SoftMatter, **2013**, *9*, 9548–9556.
52. a) Redman C. W.; Sargent, I. L. *Science* **2005**, *308*, 1592–1594; b) Eiland, E.; Nzerue, C.; Faulkner, M. *J. Pregnancy* **2012**, doi:10.1155/2012/586578; c) Al–Jameil, N.; Khan, F. A.; Khan, M. F.; Tabassum, H.; *Clin. Med. Res.* **2014**, *6*, 1–7; d) Steegers, E. A. P.; von Dadelszen, P.; Duvekot, J. J.; Pijnenborg. R. *Lancet* **2010**, *376*, 631–644.
53. a) Al–Jameil, N.; Khan, F. A.; Khan M. F.; Tabassum, H.; *J. Clin. Med. Res.* **2014**, *6*, 1–7; b) Roberts, J. M.; August, P. A.; Bakris, G.; Barton, J. R.; Bernstein, I. M.; Druzin, M.; Gaiser, R. R.; Granger, J. P.; Jeyabalan, A.; Johnson, D. D.; Anath–Karumanchi, S.; Lindheimer, M.; Owens, M. Y.; Saade, G. R.; Sibai, B. M.; Spong, C. Y.; Tsigas, E.; Joesph, G. E.; O'Reilly, M.; Politzer, A.; Son S.; Ngaiza, K. *Obstet. Gynecol.* **2013**, *122*, 1122–1131; c) Duley, L. *Semin. Perinatol.* **2009**, *33*, 130–137; d) WHO Recommendations for Prevention and Treatment of Preeclampsia and Eclampsia, WHO Department of Maternal and Child Health, Geneva, Switzerland, **2011**.
54. a) English, F. A.; Kenny L. C.; McCarthy, F. P. *Integr. Blood Pressure Control* **2015**, *8*, 7–12; b) CESDI. Confidential Enquiry into Stillbirths and Death in Infancy. 5th Annual Report. London, UK: Maternal and Child Health Research Consortium; **1998**.
55. Zhou, A.; Carrell, R. W.; Murphy, M. P.; Wei, Z.; Yan, Y.; Stanley, P. L. D.; Stein, P. E.; Pipkin, f. B.; Read, R. J. *Nature* **2010**, *468*, 108–111.
56. Sigmund, C. D. *Nature* **2010**, *468*, 46–47.
57. Griendling, K. K.; Murphy T. J.; Alexander, R. W. *Circulation* **1993**, *87*, 1816–1828.
58. Golan, D.; Tashjian, A.; Armstrong, E.; Armstrong, A. (15 December 2011). *Principles of Pharmacology – The Pathophysiologic Basis of Drug therapy.* Lippincott Williams & Wilkins. A Wolters Kluwer business., Philadelphia, 2011; p. 335.
59. Yee, A. H.; Burns, J. D.; Wijdicks, E. F. *Neurosurg. Clin. N. Am.* **2010**, *21*, 339–352.
60. a) Mishra, M.; Tiwari S.; Gomes, A. V. *Expert. Rev. Proteomics* **2017**, *14*, 1037–1053; b) Berglund, L.; Bjorling, E.; Oksvold, P.; Fagerberg, L.; Asplund, A.; Szigyarto, C. A.; Persson, A.; Ottosson, J.; Wernerus, H.; Nilsson, P.; Lundberg, E.; Sivertsson, A.; Navani, S.; Wester, K.; Kampf, C.; Hober, S.; Ponten F.; Uhlen, M. *Mol. Cell. Proteomics* **2008**, *7*, 2019–2027; c) Begley C. G.; Ellis, L. M. *Nature* **2012**, *483*, 531–533.
61. Varga, G. M.; Papaconstantinou, E.; Pope, M. T. *Inorg. Chem.* **1970**, *9*, 662–667.
62. Zhou, A.; Carrell, R. W.; Murphy, M. P.; Wei, Z.; Yan, Y.; Stanley, P. L. D.; Stein, P. E.; Pipkin, F. B.; Read, R. J. *Nature* **2010**, *468*, 108–111.
63. a) David, C.; Enescu M. *J. Phys. Chem. B* **2010**, *114*, 3020–3027; b) Dmitrenko, O.; Thorpe, C.; Bach R. D. *J. Org. Chem.* **2007**, *72*, 8298–8307; c) Carvalho, A. T. P.; Swart, M.; van Stralen, J. N. P.; Fernandes, P. A.; Ramos, M. J.; Bickelhaupt F. M. *J. Phys. Chem. B* **2008**, *112*, 2411–2523; d) Neves, R. P. P.; Fernandes, P. A. Ramos M. J. *PNAS* **2017**, *114*, E4724–E4733.

64. a) Antonello, S.; Benassi, R.; Gavioli, G.; Taddei, F.; Maran F. *J. Am. Chem. Soc.* **2002**, 124, 7529–7538; b) Antonello, S.; Daasbjerg, K.; Jensen, H.; Taddei, F.; Maran F. *J. Am. Chem. Soc.* **2003**, 125, 14905–14916.
65. Limburg, B.; Hilbers, M.; Brouwer, A. M.; Bouwman, E.; Bonnet S. *J. Phys. Chem. B* **2016**, 120,12850–12862.
66. Sohn, C. H.; Gao, J.; Thomas, D. A.; Kim, T.; Goddard, W. A.; Beauchamp J. L. *Chem. Sci.* **2015**, *6*, 4550–4560.
67. a) Marcus, R. A.; Sutin, N. *Biochim. Biophys. Acta Bioenerg.* **1985**, *811*, 265–322; b) Marcus, R. A. *Angew. Chem. Int. Ed.* **1993**, *32*, 1111–1121.
68. a) VandeVondele, J.; Ayala, R.; Sulpizi, M.; Sprik M. *J. Electroanal. Chem.* **2007**, *607*, 113–120; b) Kazemiabnavi, S.; Dutta, P.; Banerjee S. *Phys. Chem. Chem. Phys*. **2015**, *17*, 11740–11751; c) Guardia, J. J.; Moral, M.; Granadino–Roldán, J. M.; Garzón A. *Comput. Theor. Chem.* **2016**, *1077*, 113–118; d) Funes–Ardoiz, I.; Nelson, D. J.; Maseras F. *Chem. Eur. J.* **2017**, *23*, 16728–16733; e) Fernández–Alvarez, V. M.; Nappi, M.; Melchiorre, P.; Maseras F. *Org. Lett.* **2015**, *17*, 2676–2679; f) Hu, Y.; Solé–Daura, A.; Yao, Y.–R.; Liu, X.; Liu, S.; Yu, A.; Peng, P.; Poblet, J. M.; Rodríguez–Fortea, A.; Echegoyen, L.; Li, F.–F. *Chem. Eur. J.* **2019**, DOI: 10.1002/chem.201904854.
69. Kozik, M.; Baker L. C. W. *J. Am. Chem. Soc.* **1990**, *112*, 7604–4611.
70. Van Leeuween, J. W.; Mofers, F. J. M.; Veerman, E. C. I. *Biochim. Biophys. Acta* **1981**, *635*, 434–439.
71. Zhao, Y.; Truhlar, D. G. *Theor. Chem. Acc.* **2006**, *120*, 215–241.
72. Hoffman, M. Z.; Hayon E. *J. Am. Chem. Soc.* **1972**, *94*, 7950–7957.
73. Boese, A. D.; Martin, J. M. L. *J. Chem. Phys.* **2004**, *121*, 3405–3416.
74. López, X.; Carbó, J. J.; Bo, C.; Poblet, J. M. *Chem. Soc. Rev.* **2012**, *41*, 7537–7571
75. a) Lagunas, A.; Guerra–Castellano, A.; Nin–Hill, A.; Díaz–Moreno, I.; De la Rosa, M. A.; Samitier, J.; Rovira, C.; Gorostiza, P. *Nature Commun.* **2018**, *9*, DOI: 10.1038/s41467–018–07499; b) Díez–Pérez, I., Güell, A. G., Sanz, F. & Gorostiza, P. *Anal. Chem.* **2006**, *78*, 7325–7329; c) Gray, H. B.; Winkler, J. R. *Proc. Natl. Acad. Sci. U.S.A*, **2005**, *102*, 3534–3539.

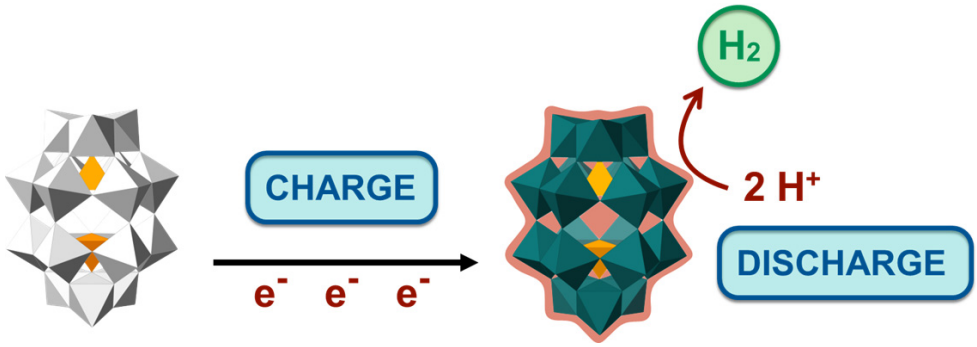

Chapter 6

Modeling Super–Reduced Polyoxometalates for Energy Storage

UNIVERSITAT ROVIRA I VIRGILI
NEW HORIZONS IN COMPUTATIONAL MODELING OF POLYOXOMETALATES:
BIOLOGICAL ACTIVITY, ENERGY STORAGE AND SUSTAINABLE CATALYSIS.
Albert Solé Daura

CHAPTER 6

Modeling Super–Reduced Polyoxometalates for Energy Storage

This chapter concerns the redox properties of aqueous solutions of Wells–Dawson polyoxotungstate $[P_2W_{18}O_{62}]^{6-}$, which under certain conditions be reversibly reduced by 18 electrons per anion, in contrast with the classical redox behavior that involves six electrons as much. Interestingly, this phenomenon was found to be counter cation and concentration dependent. The main goal of this chapter is to unveil the reasons for the super–reduction process and the role of the counter cations in the POM salt. Also, we aim to understand the metastable nature of the super reduced POMs, as well as to propose a plausible molecular and electronic structure for it.

All the results discussed in this chapter are part of an ongoing project in collaboration with the experimental group of Prof. L. Cronin from University of Glasgow (U.K.).

6.1 Experimental background.

As explained in Chapter 1, one of the most attractive features of POMs are their fascinating redox properties, that allow them to accept and storage several electrons for further use in catalysis or energy production.[1] Recently, Cronin and co–workers reported the ability of the Wells–Dawson–type phosphotungstate $[P_2W_{18}O_{62}]^{6-}$ ($\mathbf{W_{18}}$) to accept up to 18 electrons.[2] In addition, these electrons can be reversely recovered upon re–oxidation, what permitted the construction of a redox–flow battery with an energy density of 225 $Wh{\cdot}l^{-1}$, featuring the highest energy density in POM–based redox–flow batteries to date, since the most efficient one before this discovery displays an energy density of 15.4 $Wh{\cdot}l^{-1}$.[3] Indeed, these finding represents a breakthrough in POM chemistry not only for the enhanced performance in terms of energy storage, but also considering that the traditional redox behavior of this anion involves four or six electrons as much, depending on the pH.[4–8] **Figure 6.1**A shows the cyclic voltammograms recorded for aqueous solutions of the $Li_6\mathbf{W_{18}}$ salt at different pH values. At neutral pH, $\mathbf{W_{18}}$ experiences four reversible redox processes between the range +0.6 to –0.6 V (*vs* SHE). Each one was associated to a simple one–electron reduction. When decreasing the pH to 4, the two waves below 0 V become two–electron redox processes, in agreement with

previous studies.[4–8] Interestingly, when the POM concentration is increased to 100 mM, both the two–electron waves are shifted ca. 200 mV to more positive potentials, and even more importantly, a new multi–electron wave appears within the same potential window (see **Figure 6.1**B), indicating that high concentration and low pH allows the reduction of POM clusters beyond their previously known limits.

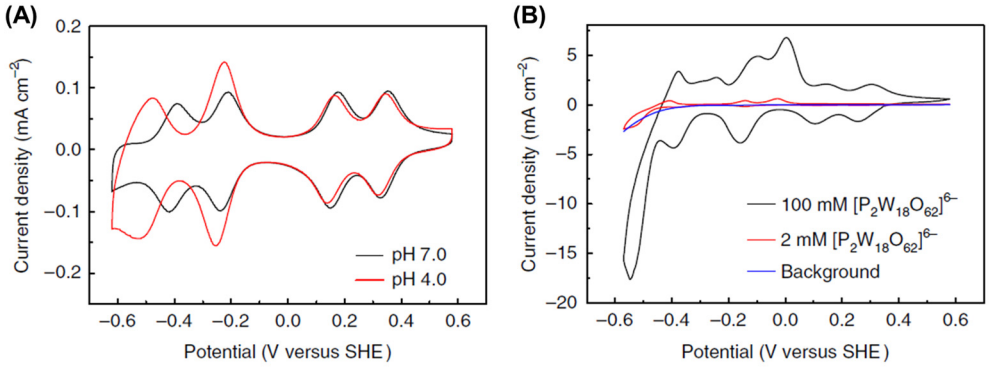

Figure 6.1 | (A) Cyclic voltammograms recorded for a 2 mM solution of $Li_6[P_2W_{18}O_{62}]$ at pH 7 (black line) and in 1 M of H_2SO_4 (pH 4, red line) at a scan rate of 10 mV·s^{-1}. (B) Cyclic voltammograms of a 2 mM (red line) and a 100 mM (black line) solution of $Li_6[P_2W_{18}O_{62}]$, both at pH 4 and recorded at a scan rate of 10 mV·s^{-1}. Blue line corresponds to a cyclic voltammogram of a 1 M H_2SO_4 solution. Taken from ref. 2.

Electrochemical studies revealed that at high POM concentration (100 mM, at the limit of POM solubility) and low pH (close to 1), every cluster can accept up to 18 electrons that can be reversibly extracted by re–oxidation. Passing the same current to a 2 mM solution only allows recovering 4 of the 18 electrons passed through the cluster when re–oxidizing, evincing that super reduction is only possible at high concentration. In addition, the super–reduction process was found strongly dependend on the counter cation used in the POM salt, since the capacity of the POM solution decreases as $Li^+ > Na^+ > K^+$. Furthermore, 14 of the 18 electrons can be spontaneously released as molecular hydrogen when diluting the super–reduced anions in water. Thus, these results are of high interest since they can represent part of the solution to the on–demand energy production.

6.2 Computational Details.

6.2.1 Static DFT calculations.

To determine redox potentials (section 6.3.1), we initially optimized the structures at BP86[9] level of theory with a Slater–type TZP basis set using the ADF2016.01 code.[10] Solvent effects of water were taken into account with the COSMO[11] continuum solvent model (ε = 78.4) and relativistic effects were considered by means of the ZORA approximation.[12] The remaining calculations were performed with Gaussian09 (rev D.01)[13] using the hybrid B3LYP functional[14] and a LANL2DZ basis set[15] for all atoms, with the corresponding pseudopotential for W and P centers. In this case, solvent effects were simulated by means of the IEF–PCM solvent model[16] and frequency calculations were performed at 298 K and 1 atm. To evaluate protonation energies, we used the experimental value of solvation free energy of a proton in solution[17] and the free–energy change in (de)protonation processes was corrected with the standard state correction of 1.9 kcal·mol^{-1} that accounts for the change in free energy in going from gas phase at 1 atm to the standard state of 1 M in solution at 298 K.

6.2.2 Classical MD simulations.

The methodology used for classical simulations is analogous to that explained in previous chapters. In all cases, 50 POM anions were embedded in a cubic solvent box of 94.0^3 Å^3, as well as 300 Li^+ and the number of H_3O^+ required to neutralize the charge of the system. Force field parameters for hydronium cations were taken from the AMBER99[18] force field and the TIP3P water model.[19] Equilibrium distances and angles were taken from the DFT–optimized geometry, obtained at BP86[9] level with a 6–311G(d,p) basis set[20] for all atoms using Gaussian09[13] and the IEF–PCM[16] continuum solvent model (ε = 78.4). Atomic charges were computed from a single–point calculation in gas–phase[21] using the same level of theory, as done for all the simulated POM structures. This procedure was already followed by Wippf and co–workers to model the agglomeration of polyoxotungstates with H_3O^+ cations as linkers.[22] Simulations at lower POM concentration (20 mM) were performed in a simulation box of the same dimensions but decreasing the number of POMs from 50 to 10 and the number of counter cations, accordingly.

6.2.3 *Ab initio* CPMD simulations.

In this chapter, results concerning 3 different simulations are discussed. All them contain one POM cluster embedded in supercells of different size. The first simulation was performed in a cubic supercell of 25^3 Å^3 to avoid possible interactions between POM clusters in neighboring boxes upon rotation of the cluster from its initial position, as Wells–Dawson anions have x = y ≠ z dimensions. Nevertheless, as this rotation was not observed at the simulation time scale, further simulations were performed with orthorhombic cells of 20 × 20 × 25 Å^3 (with $\alpha = \beta = \gamma = 90^0$) to reduce their computational cost. Thus, the simulated systems are:

- **W_{18}–4e** in acid medium: one **W_{18}–4e** anion (q = 10–) embedded in a box of 20 × 20 × 25 Å^3 with; 6 H_3O^+ cations, 4 Li^+ cations and 233 water molecules (935 atoms). The system was simulated for 5.5 ps.
- **$H_{18}W_{18}$–18e** at neutral pH: one **$H_{18}W_{18}$–18e** anion (q = 6–) in a 25^3 Å^3 box with 6 Li^+ cations and 428 water molecules (1390 atoms). The system was simulated for 6.5 ps.
- **$H_{17}W_{18}$–18e(7:10)** at neutral pH: one **$H_{17}W_{18}$–18e(7:10)** anion (q = 7–) in a 20 × 20 × 25 Å^3 box with 4 Li^+ cations and 265 water molecules (898 atoms). This simulation was carried out for 10 ps.

Simulations were performed with the CPMD 4.1 code[23] at the DFT level adopting the generalized gradient–corrected BLYP exchange–correlation functional.[24] The electronic structure was described by expansion of the valence electronic wave functions into a plane–wave basis set, which is limited by an energy cut–off of 70 Ry. The interaction between the valence electrons and the ionic cores was treated using the pseudopotential (PP) approximation. Norm–conserving Troullier–Martins PPs were used for W, P, O and Li centers,[25] which nonlocal part was calculated using the Kleinman–Bylander method.[26] H atoms were described with a Goedecker–type PP.[27] During the MD simulations, the wave functions are propagated in the Car–Parrinello scheme, by integrating the equations of motion derived from the Car–Parrinello Lagrangian.[28] A fictitious electronic mass of 900 au was employed with a time step of 0.144 fs, as H atoms were substituted by D. The Nosé–Hoover thermostat[29] for the nuclear degrees of freedom was used to maintain a temperature at 300 K. All simulations were performed with spin polarization and with PBC starting from geometries that were previously equilibrated with classical MD. In the simulation with **$H_{18}W_{18}$–18e**, a number of cations to neutralize the overall charge was included in the periodic box, while in other simulations, the number of cations

corresponds to the average coordination numbers within 20 Å from the POM center of mass computed from 5 ns classical MD. Previous classical simulations were performed using 6 Li^+ because of the 6:1 stoichiometry of the initial POM salt and when simulating low pH, the number of H_3O^+ ions to reach a pH < 1 was added in the box (*vide infra*). These simulations were performed at MareNostrum4 HPC in Barcelona Super–Computing Center (BSC), where those with the small box size lasted about 43.3 h/ps (wall clock time; 22.5 s/step) using 240 cores (5 nodes of 2 CPUs Intel Xeon Platinum 8160 24C 2.1 GHz with 2GB of RAM per core) intercommunicated with Intel Omni–Path, whereas that with a bigger box size 161.1 h/ps (83.5 s/step) using the same computational architecture.

6.3 Results and Discussion.

6.3.1 Studies of initial reduction states.

The electronic structure of POMs has been extensively studied during the last decades by means of computational chemistry.[9] In fully–oxidized polyoxotungstates in which all the metal ions are in their highest oxidation state, the lowest unoccupied MOs are built up from linear combinations of empty *d orbitals* of tungsten. In a classical structure such as $[P_2W_{18}O_{62}]^{6-}$ (**W_{18}** for short) tungsten atoms are found in a distorted octahedral environment that renders d_{xy} orbitals the most stable ones, followed by the d_{xz} and d_{yz} that are degenerated above in energy (**Figure 6.2**). Hence, injection of electrons in a POM results in a partial occupation of the d(W) orbitals, which causes the appearance of a deep blue coloration in the solution and the corresponding band in the UV–Vis spectrum at about 650 nm associated to transitions of d(W)→d(W) nature.

Cyclic–voltammogram experiments provide valuable information on the redox properties of a given species. As previously mentioned, the initial reduction steps of a fully oxidized **W_{18}** solution at low concentration were analyzed at pH 7 and 4. In the neutral solution, four reversible one–electron reductions were observed in the range of +0.6 and −0.6 V (**Figure 6.1**A).[2] As shown in the molecular orbital (MO) diagram given in **Figure 6.3**, the first and second additional electrons are accommodated in a MO of a_1'' symmetry, whereas the third and fourth are incorporated in two degenerated orbitals of symmetry e''. Reproducing absolute reduction potentials of polyoxometalates in aqueous solutions is still quite inaccessible to computational methods because of their anionic nature and large

size. Nevertheless, relative values are better estimated. Using a GGA functional (BP86) and Slater TZP basis set, we have computed the redox potentials with respect to NHE. Taking an absolute free energy of −4.24 eV for NHE,[30] the redox potential for the first reduction was found to be −0.04 V, which is about 200 mV more negative than the observed potential for the Dawson anion. In terms of molecular orbital energies and neglecting the bielectronic effects, this would mean that the energy of the LUMO should be somewhat more negative than what we get. In line with this relatively small deviation, when we compare experimental and theoretical redox potentials we reproduce rather well the trends for two successive electron reductions, as shown in **Table 6.1**. Hence, the calculated values of 269, 470 and 217 mV show good correspondence with the experimental ones of 180, 390 and 190 mV, although the computed values are slightly shifted towards more negative potentials. Accordingly, the last row in **Table 6.1** shows that the peak–to–peak separations are also well reproduced from the energies of the MO to be populated in the reduction process.

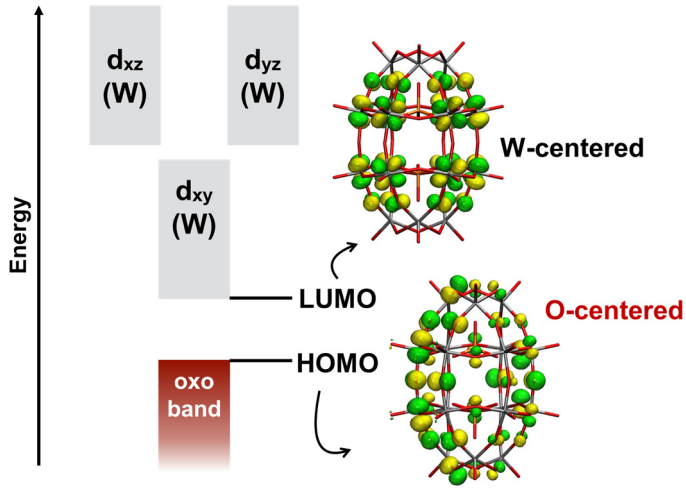

Figure 6.2 | Schematic representation of the frontier MO diagram of the fully oxidized $[P_2W_{18}O_{62}]^{6-}$ (**W_{18}**) anion.

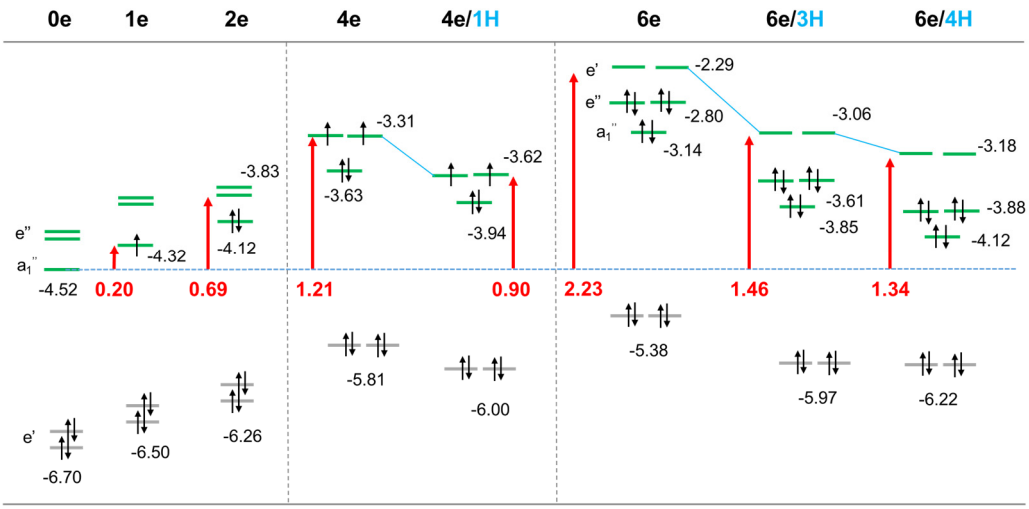

Figure 6.3 | Frontier Molecular Orbital (MO) diagram for different reduction states of the $\{P_2W_{18}O_{62}\}$ cluster. Level energies in grey and green represent, oxo and d(W) orbitals respectively (see text). Energies (eV) were computed with the BP86 functional and a Slater TZP basis set.

Table 6.1 | Comparison of experimental and computed reduction potentials for $[P_2W_{18}O_{62}]^{6-}$ at pH 7.

	W_{18}→W_{18}-1e	W_{18}-1e→W_{18}-2e	W_{18}-2e→W_{18}-3e	W_{18}-3e→W_{18}-4e
$E^{red}(pH=7)^a$	+0.35	+0.17	−0.22	−0.40
ΔE^{red} (exp)^b	–	−180	−390	−180
ΔE^{red} (DFT)^b	–	−217	−470	−269
$\Delta E(MO)^c$	–	200^d	490^e	220^f

^{a} Reduction potentials in V *vs* NHE; ^{b} reduction potential differences for two successive electron reductions in mV. All the reduction potentials were computed with a BP86 functional and a Slater TZP basis set. ^{c} The potential difference (absolute value in mV) between two successive reduction peaks can be estimated from the difference in energies of the MOs that will accept the incoming electron; $^d E_{SOMO,1e}-E_{LUMO,0e}$; $^e E_{LUMO,2e}-E_{SOMO,1e}$; $^f E_{SOMO,3e}-E_{LUMO,2e}$

In acidic conditions (pH 4) the cyclic voltammograms also show four reversible waves, the two first being almost identical to the observed in neutral solution, but the third and fourth correspond to 2e−reduction steps (**Figure 6.1**A). Given that the third wave is centered at −0.24 V, very close to the value of −0.22 V observed for the incorporation of the third electron in the neutral solution, we can assume that the third and the fourth reduction proceed as following: 1) reduction of the **W_{18}−2e** species, 2) chemical protonation of **W_{18}−3e** induced by the increase of the anion basicity, and 3) reduction of

the protonated anion to give **HW_{18}–4e**. Indeed, DFT calculations show that the protonation shifts the redox potential for 3e–reduced species in more than 120 mV toward more positive values. This value was estimated protonating only some of the most basic bridging oxo sites, however the protons might be itinerant among several sites and this could modify the effect in the redox potentials induced by protonation. It is expected that further reductions should occur via successive protonation/electron–reduction steps to give **H_2W_{18}–4e**, **H_2W_{18}–5e**, **H_3W_{18}–5e**, **H_3W_{18}–6e**, etc. As we will describe later, POM agglomeration also plays an important role in the stability and redox properties of the polyoxotungstates.

Figure 6.3 shows the frontier orbitals for different reduction states of the $\{P_2W_{18}O_{62}\}$ cluster. As expected, the molecular orbitals are shifted to higher energies (less negative values) with each electron addition due to the increase of the negative charge supported by the POM cluster. Thus, for example, the energy of the LUMO is shifted from −4.52 eV in the fully oxidized anion to −2.22 eV after reducing it with six electrons. The energy rise is significantly lower if the electron addition is coupled with the protonation of the POM structure. For instance, reduction of the 4e–reduced anion occurs experimentally at ca. −0.50 V (**Figure 6.1**A). As shown in **Figure 6.3** the LUMO of **W_{18}–4e** is 1.21 eV above that of the fully oxidized anion, being unable to explain the experimental difference of ~0.85 V between the reduction potentials of the fully–oxidized and the 4e–reduced anion. However, if we consider the LUMO of the mono–protonated cluster **HW_{18}–4e,** the energy gap from the LUMO of **W_{18}** becomes 0.9 eV and therefore, much closer to the experimental gap between redox waves. When comparing the experimental and computed redox potentials, we cannot unequivocally distinguish the number of protons for each reduction state, but we have estimated that the **W_{18}–6e** species would have at least 3 or 4 protons attached to the POM framework, since otherwise the reduction potentials would be excessively negative. Note that the LUMO of **H_4W_{18}–6e** would be only +1.34 eV above the energy of the LUMO of the fully oxidized **W_{18}** species. This moderate increase in combination with the effect induced by POM agglomeration (*vide infra*) ensures the ability of Dawson anion to be reduced multiple times.

To further prove the proneness of reduced anions to protonate under highly acidic conditions, we carried out a Car–Parrinello Molecular Dynamics (CPMD) simulation for the **W_{18}–4e** species. Previous to this simulation, we performed an initial classical MD run of **W_{18}–4e** (q = 10−) in water at pH ≈ 0.2 (10 H_3O^+ cations in a 30^3 $Å^3$ periodic cubic box) that showed that hydronium cations tend to accumulate close to the highly negatively

charged anion (see **Figure 6.4**). Thus, we started the CPMD simulation from a configuration in which the POM is surrounded by several H_3O^+ cations that are hydrogen–bonded to the terminal oxo groups of the POM. Although the concentration of protons is higher than in the experiments, we only sough to evaluate whether oxygen atoms in **W_{18}–4e** are basic enough to capture protons from the medium or not. **Figure 6.5** shows the evolution of the number of protons associated to the cluster during the 5.5 ps of simulation. At t = 0.5 ps the system has already taken three protons at terminal oxo sites and after more than 2 ps oscillating between geometries with a number of protons ranging from 2 to 5, the system mostly remains tri–protonated until the end of the simulation.

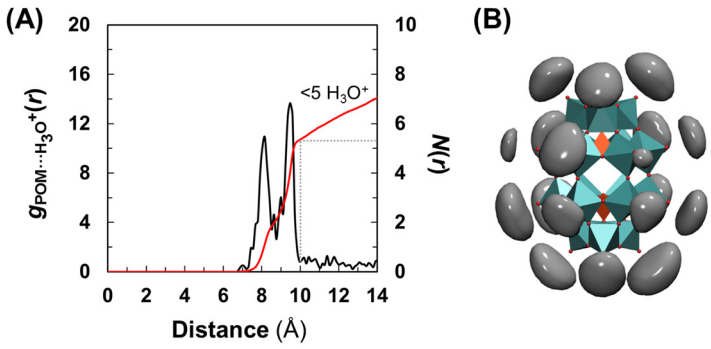

Figure 6.4 | (A) Radial Distribution Function (RDF) between **W_{18}–4e** anion and H_3O^+ cations taking as a reference the center of mass (COM) of both species. Black line represents the RDF while the red one represents the integration of the RDF, $N(r)$, i.e. the average number of H_3O^+ found from the COM of the POM to every distance. First and second peaks are associated to contacts at the belt and the cap regions of the anion, respectively. The distance corresponding to the first minimum after the second peak integrates to 5.3 H_3O^+ cations, indicating that the POM tends to have ca. 5 hydrogen–bonded H_3O^+ ions, in average. (B) Volumetric density of H_3O^+ (depicted in grey) identifies the regions around the terminal oxygen atoms of the POM as those with the highest density of H_3O^+. Data sampled every 2 ps along a 5 ns MD run.

If longer simulation time were computationally affordable for such big systems (< 900 atoms), we should observe the diffusion of these associated protons from the most accessible terminal positions to the bridging ones that are more basic.[9] In fact, static DFT calculations indicate that moving two protons to bridging positions and releasing the third one to give **H_2W_{18}–4e** species would stabilize the cluster by about 28 kcal·mol^{-1} in terms of Gibbs free energy. In **H_2W_{18}–4e**, adding a proton at a terminal position is endothermic by 8.4 kcal·mol^{-1}. Releasing another proton to give **HW_{18}–4e** is also endothermic, although to a lower extent (4.5 kcal·mol^{-1}). Thus, it might be reasonable to think that

W_{18}–4e is di– or mono–protonated at low pH. From this point on and assuming a proton–coupled nature for each subsequent reduction step, it might be sensible to expect a number of protons close to 16 in the structure of the 18 electron–reduced system.

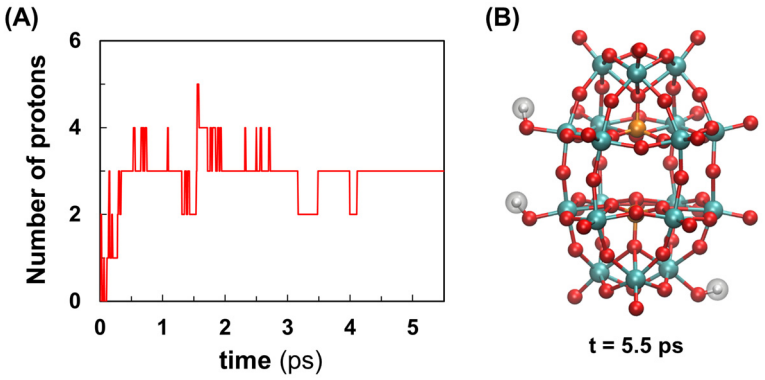

Figure 6.5 | (A) Evolution of the number of protons associated to **W_{18}–4e** during a 5.5 ps CPMD simulation. A distance criterion of ≤1.3 Å was considered for a O—H bond. (B) Snapshot of the protonated cluster (**H_3W_{18}–4e**, q = 7–) at the end of the simulation, highlighting the three protons taken by the bare anion.

6.3.2 Super–reduction process and POM agglomeration as function of the reduction state.

Although protonation plays a key role in stabilizing virtual MOs to facilitate the reduction of the POM cluster, the energy difference between the LUMO of **H_4W_{18}–6e** and that of the fully oxidized anion **W_{18}** (1.34 eV, **Figure 6.3**) is still far from explaining the super reduction process within 0.8 V illustrated in **Figure 6.1**B. This evinces that additional stabilization aside chemical protonation is required to form the metastable **W_{18}–18e** species. As the super–reduction phenomenon only takes place at high concentration of POM salt[2] and depends strongly on the nature of the counter cations, we suspect that the *collective behavior* of the anions in solution might influence the energy levels of their MO and consequently, the reduction potentials and the stabilization of the extra electrons. To assess this point, we initially performed classical MD simulations of 40 ns with 50 $[\mathbf{HW_{18}–4e}]^{9-}$, 50 $[\mathbf{H_2W_{18}–4e}]^{8-}$ or 50 $[\mathbf{H_3W_{18}–6e}]^{9-}$ anions at the experimental conditions (i.e. [POM] = 100 mM, with 300 Li^+ counter cations and counterbalancing the charge with H_3O^+, obtaining a pH close to 1). These simulations were compared to that with 50 fully–oxidized **W_{18}** anions in similar conditions. We also

simulated the 18 electron–reduced cluster, but these results are discussed in the next section.

Visual analysis of the trajectories revealed rather different behavior between the oxidized and reduced POMs (see animations of the trajectories from the Supplementary Material section). While fully–oxidized **W_{18}** anions remain as monomers during the whole simulation, reduced POMs tend to form agglomerate structures. These differences can be appreciated from the comparison of the POM···POM Radial Distribution Functions (RDFs) averaged over the last 10 ns of each simulation, represented in **Figure 6.6**. The **W_{18}···W_{18}** RDF does not show any peak, as a proof for a completely lack of agglomeration. However, those for reduced POMs display an array of peaks between 12.6 and 18.9 Å. These peaks indicate that there is a set of preferred intermolecular distances between reduced anions to interact. Within this range of distances, the POM anions were found to interact mainly via *lithium–mediated* contacts, but also involving hydronium cations acting as linkers and water–mediated interactions. Some direct contacts between anions via direct hydrogen bonds were also observed. The most representative interaction modes between anions are collected in **Figure 6.7**. Both **HW_{18}–4e** and **H_3W_{18}–6e** (with an overall charge of 9–) tend to agglomerate into large *lithium–mediated* oligomers similarly. The agglomerative behavior of **HW_{18}–4e** and **H_3W_{18}–6e** anions was ascribed to their high charge density at the surface, which renders terminal oxygens charged enough to remove the solvation shell from the highly hydrophilic cations to provide long–lived direct contacts. Interestingly, the lower charged **H_2W_{18}–4e** (q = 8–) anions only present incipient hydrogen–bonded adducts. As shown in the RDFs of **Figure 6.6**, **H_2W_{18}–4e** cannot pull the solvation shell out of lithium cations as efficiently as their more charged partners, explaining its lower ability to agglomerate. The same occurs for the fully oxidized **W_{18}** cluster, but as it is not basic enough to have associated protons, there is no possibility for hydrogen bonds. Similar trends were observed for a series of mixed–valence polyoxovanadate cluster with different charge, for which only those bearing the highest negative charges showed ability to agglomerate with alkali metal cations.[31] Although it is not represented, the ion pairing with H_3O^+ cations follows the same trend with the POM charge.

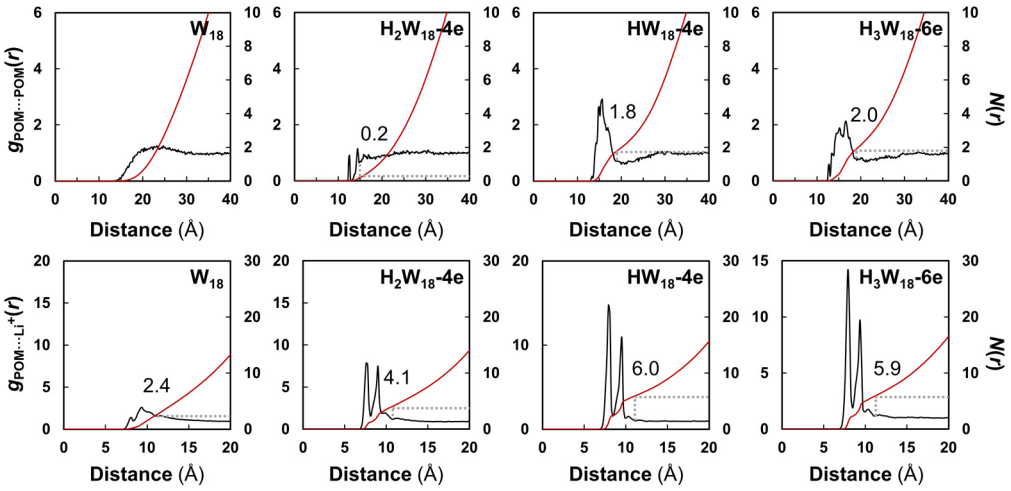

Figure 6.6 | Compilation of the POM···POM and the POM···Li+ RDFs computed taking as a reference the center of mass of both species. Data averaged over the last 10 ns of simulation sampling data every 2 ps. Black lines represent the RDF, $g(r)$, and red lines the coordination number, $N(r)$, obtained from integration of the RDF.

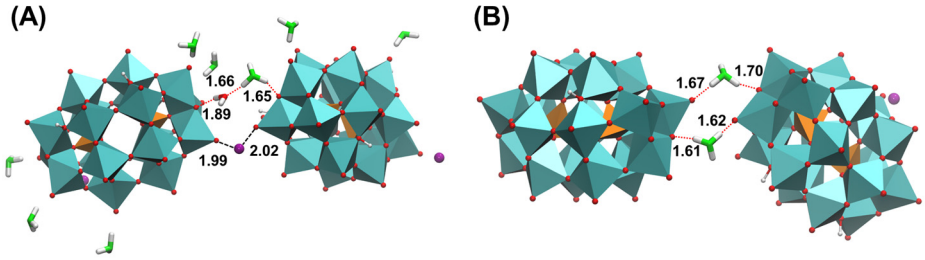

Figure 6.7 | Representative snapshots of the interactions between **H_3W_{18}–6e** anions. Li^+ are represented as purple spheres and H_3O^+ cations are highlighted in green. Snapshot (A) shows a lithium–mediated contact and another one involving a H_3O^+ cation and a water molecule (POM···POM distance from COMs, $r_{POM\cdots POM}$ = 16.0 Å) and (B) exemplifies another interaction mode in which the POMs are linked by two H_3O^+ cations ($r_{POM\cdots POM}$ = 15.8 Å).

Next, taking the case of **HW_{18}–4e** as a representative example, we evaluated the influence of agglomeration on the electronic structure of the POMs. To do so, we took an agglomerate structure from the MD run composed by five anions linked by several Li^+ and H_3O^+ cations, and compared the MO distribution of a given anion in the presence of absence of agglomeration. Interestingly, **Figure 6.8** shows that when **HW_{18}–4e** participates in the supramolecular assembly, its LUMO is significantly stabilized by ~380 mV, and their SOMOs by more than 200 mV. This observation is in line with

electrochemical data that showed a shift of more than 100 mV to more positive values in the reduction potential of the {**W_{18}–4e**} species on going from 2 mM to 100 mM (see **Figure 6.1**B).[2] This effect can be attributed to a notable increase of the ion pairing at high concentration of the POM salt. The IEF–PCM continuous solvent model stabilizes the virtual MOs by ca. 200 mV, whereas the incorporation of the POM into a small agglomerate structure accounts for an additional stabilization of ca. 180 mV (**Figure 6.8**). At low concentration, the ion pairing might not be enough to stabilize the anion as much as in the agglomerate structure, where a single cation interacts with more than one POM simultaneously leading to an increased effective ion pairing. This suggests that the unconventional redox properties of the Li_6**W_{18}** salt arise from its *ability to form agglomerates* that stabilizes the MOs of the POM cluster, allowing reduction processes beyond the limits established so far.

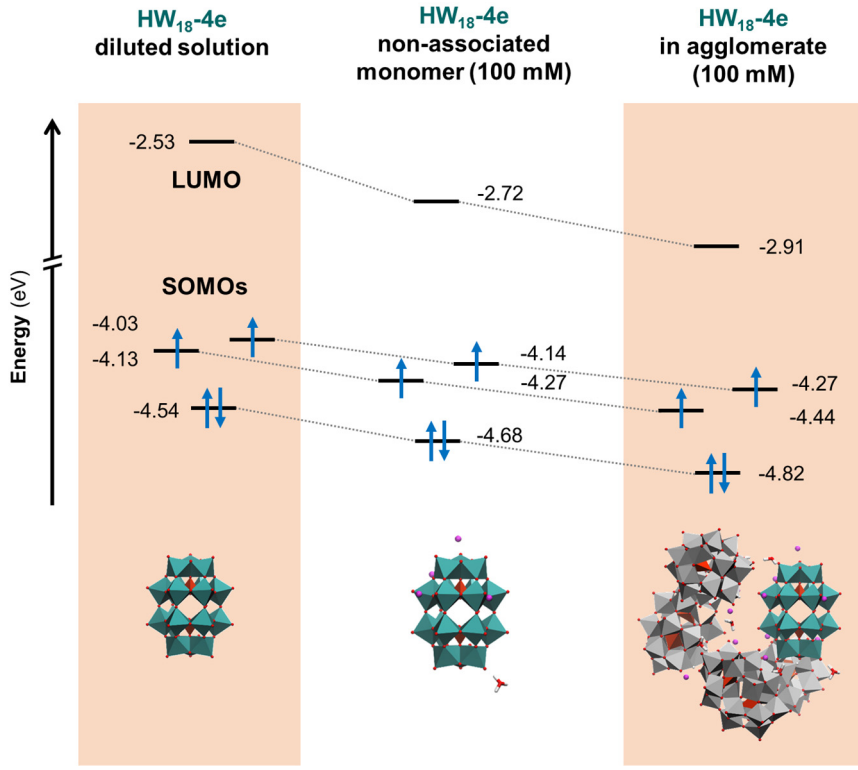

Figure 6.8 | Molecular orbital diagram showing the stabilizing effect of agglomeration on MOs of HW_{18}–4e. Energies (in eV) were computed for the POM highlighted in cyan in the snapshots below using the hybrid–GGA B3LYP functional.

To further validate this hypothesis, we studied the influence of the size of the counter cation by simulating the behavior of 50 **HW_{18}–4e** anions in the presence of K^+ cations instead of Li^+. **Figure 6.9** compares the POM···POM and the POM···cation RDFs for both simulations. In agreement with the lower ability of potassium cations in promoting the super–reduction of **W_{18}** observed experimentally, we found that the POM agglomeration is much less important in the potassium salt than in the lithium one, as illustrated by the difference in the height and the wideness of the peaks. As mentioned above, Li^+ cations can mediate the contacts between **HW_{18}–4e** anions. However, very scarce potassium–mediated contacts were observed in the simulations. Accordingly, the peak in the POM···POM RDF for the simulation with K^+ is centered at 13.5 Å, which corresponds to a configuration in which POMs interact directly to each other through a hydrogen bond, and integrates only to 0.1 neighbors in average (*vs.* 1.8 for Li^+). This also supports that the single effect of acid medium is not enough to achieve super–reduction and therefore, the role of hydronium–mediated contacts between anions in the simulations with Li^+ counter cations is not crucial but auxiliary. An MD study with polyoxovanadate clusters showed that the average interaction energy between a POM and a Li^+ cation is more than twice the interaction energy with bigger K^+ cations, owing the highest charge density of Li^+.[31] Although lithium cations are highly hydrophilic, if POM clusters are charged enough to remove partially the solvation shell, they become involved in stronger and longer–lived POM···cation interactions (see **Figure 6.9**, right) that can mediate more efficient POM···POM pairs, as shown in **Figure 6.6**. For this reason, the lower charge density of large cations is detrimental for POM agglomeration and in turn, provides poorer stabilization of the POM MOs hampering the reduction process.

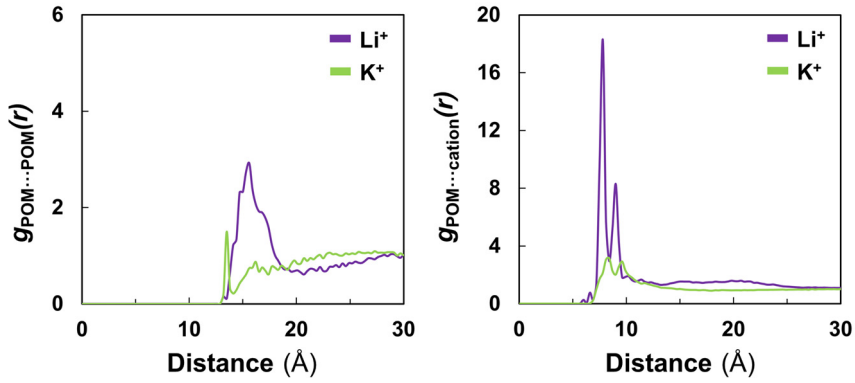

Figure 6.9 | POM···POM (left) and POM···cation RDFs (right) computed during the last 10 ns of simulation with 50 **HW_{18}–4e** anions with 300 Li^+ (purple lines) or K^+ (green lines) counter cations at aqueous solutions 100 mM POM concentration and pH 1. In both cases, the center of mass of the POMs was taken as reference. Data were sampled from trajectories every 2 ps.

6.3.3 The W_{18}–18e species: electronic structure and aggregation ability.

As shown in the previous section, the aggregation ability decreases with the number of associated protons. For this reason, we initially considered for the **W_{18}–18e** anion the upper–limit case of having 18 protons in the structure. An exploratory study revealed that aggregation is enhanced when protons are found in bridging oxygen atoms, as the terminal ones are more accessible to interact with cations. Prompted by these observations, we next evaluated the stability of the super reduced species with 18 protons in bridging oxygens by means of a CPMD run in water. As the system is expected to have a lower number of protons attached, we simulated the system at neutral pH in a cubic simulation box of 25^3 Å, in such a way that the release of the first proton will already lead to a very low pH that reproduces the highly acidic experimental conditions. Analogously to the 4e–reduced POM, this *ab initio* simulation was carried out with spin polarization. As expected, the 18 protons–containing cluster releases a proton at the beginning of the simulation but after 1.2 ps the proton returns to the cluster at a terminal oxo site. The species with 18 protons (17 bridging, 1 terminal) lasts for *ca.* 1 ps and after that, another proton from a bridging position is released to the solution. No additional acid/base processes were observed during the remaining ~2 ps of simulation (see **Figure 6.10**), but at ~4.4 ps, another proton from a bridging position leaves to the bulk yielding the **$H_{15}W_{18}$–18e** species, which remains until the end of the simulation. As initial approach, we performed the simulation with spin polarization constraining the spin multiplicity to 1, and the wave function

evolved to an open–shell singlet configuration in which all the 18 electrons are unpaired and localized over the 18 W atoms.

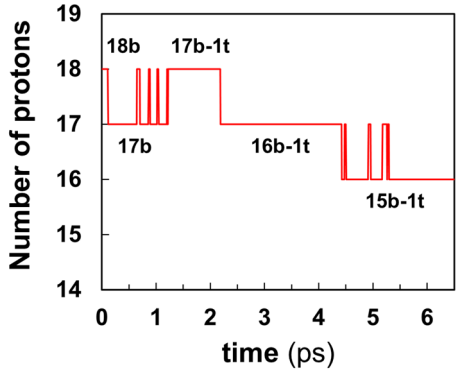

Figure 6.10 | Evolution of the number of protons associated to **W_{18}–18e** during a 6.5 ps CPMD simulation. A distance threshold of ≤1.3 Å was considered for a O—H bond. The labels "b" and "t" stand for protons at bridging and terminal oxygen atoms, respectively. Data were sampled every 7.2 fs.

The most abundant species in the simulation is the 17 proton–containing POM with 16 protons being at bridging positions. For this reason, we took a representative geometry for the **$H_{17}W_{18}$–18e** anion from the trajectory to perform quantum mechanics calculations aiming to determine the electronic structure of the super–reduced species. In addition, DFT calculations discussed below suggested that the final structure is more likely to have 17 associated protons rather than 16 (*vide infra*). Optimization of the structure and the wave function locate one electron on each W center, combining population of d_{xy}–like orbitals with d_{xz} ones in the case of protonation at the terminal oxo group. These metal electrons were predicted to be unpaired but magnetically coupled to some extent, being the most likely configurations an open shell singlet followed by a quintet and a triplet states, which lie only 1.5 and 1.6 kcal·mol^{-1} above in energy. Before reaching this conclusion we had to run dozens of calculations in an iterative process to evaluate the likelihood of several different electronic structures. For this reason, the accuracy of the calculations was limited to a double–ζ basis set. Even so, these calculations were capable of reproducing the qualitative trends required to rationalize the intricate super reduction process.

Figure 6.11A represents the spin density of t for the lowest in energy state, an open shell singlet, and **Figure 6.11**B shows a schematic MO diagram of the most likely configurations. Hence, this system is expected to possess a strong multi–configurational

character although it might not show much intense paramagnetism, as suggested by ongoing EPR studies. Note that the B3LYP energy of the highest SOMO for **$H_{17}W_{18}$–18e** with a bridging:terminal ratio of 16:1 is −3.12 eV, which is only *ca.* 1.40 V above the SOMO of **W_{18}–1e** calculated with the same method. It is also worth to mention that a pure functional was used in the previous section to compare the energy levels of the structure with the experimental electrochemical data, as they give more realistic gaps between occupied and virtual orbitals compared to hybrid functionals, which tend to overstabilize occupied orbitals and in turn, to overestimate HOMO–LUMO gaps. However, a hybrid functional (B3LYP) was used for the comparison among electronic structures and molecular configurations because some percentage of HF exchange is usually required to efficiently localize electron density within a structure. This is of paramount importance when dealing with such large number of unpaired electrons. Otherwise, it is extremely difficult to achieve convergence in the optimization of the wave function during self–consistent field (SCF) iterations.

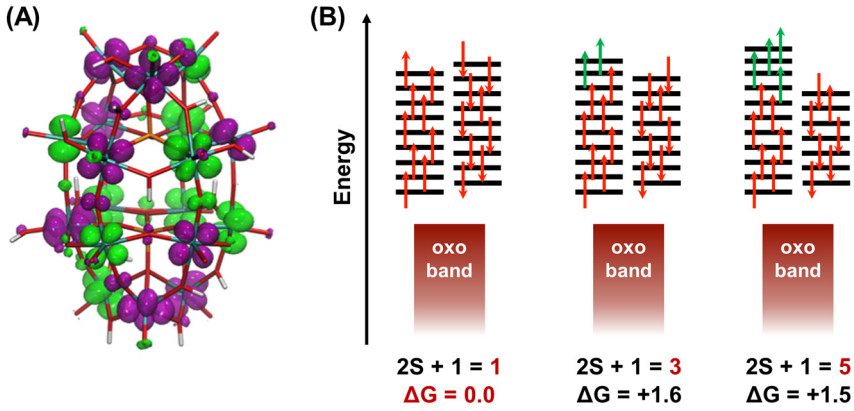

Figure 6.11 | (A) Spin density representation for **$H_{17}W_{18}$–18e** in an open–shell singlet configuration. Purple and green densities correspond to alpha and beta electrons, respectively. (B) Schematic MO diagram of the most likely electron configurations. Relative free energies were computed at B3LYP/LANL2DZ level. Electrons depicted in red and green denote "unpaired but magnetically coupled" and "unpaired and non–coupled" electrons, respectively.

Next, we analyzed the collective behavior in solution of the **$H_{17}W_{18}$–18e** species. **Figure 6.12**A and B represent the POM···POM and the POM···Li^+ RDFs obtained from a classical MD simulation with 50 **$H_{17}W_{18}$–18e**, anions, 300 Li^+ and 50 H_3O^+ cations, in the same conditions than previous simulations reported in this chapter. The POM···POM RDF reveals that the agglomeration in the super reduced anion **$H_{17}W_{18}$–18e** is much

stronger than the reported for the lowly reduced anions. During the last 10 ns of simulation, every **$H_{17}W_{18}$−18e** cluster has an average number of 3.7 neighbors in close contact (*vs.* 2.0 in the case of **H_3W_{18}−6e**, see **Figure 6.6**) that interact via cation−mediated contacts and hydrogen bonds to form large agglomerate structures (see **Figure 6.12**C). In general, as the charge of the POM increases, so does the strength of the POM···Li contacts and in turn, the amount of agglomeration (see **Figure 6.6**). However, although the super reduced anion **$H_{17}W_{18}$−18e** (q = 7−) bears a lower charge than **H_2W_{18}−4e** (q = 8−) or **HW_{18}−4e** (q = 9−) it presents the highest number of interacting Li^+ cations per cluster (6.6). This fact can be ascribed to the ability of the highly protonated anion to interact not only through cation−mediated contacts but also *via* direct hydrogen bonds. **Figure 6.12**D illustrates the formation of a non−negligible H−bonding network between **$H_{17}W_{18}$−18e** anions, which presumably has a synergistic effect with the ion pairing that reinforces the agglomeration by increasing the lifetime of POM···Li^+ contacts. For comparison, we also represented the evolution of hydrogen bonds between **H_2W_{18}−4e** anions, which bear a slightly higher charge but conversely, do not form large agglomerates due to the shortage of hydrogen bonds between clusters. Thus, the cooperative effect of ion pairing and strong POM−H···POM contacts might be responsible for the significant enhancement of the aggregation upon reducing and protonating of the system.

During the CPMD simulation described in **Figure 6.10**, a protonation event involving a terminal position was observed. To evaluate the proneness of the super reduced cluster to get protonated at terminal positions, we performed an additional static DFT study with the **$H_{17}W_{18}$−18e** species moving protons from bridging to terminal oxygen atoms, and comparing their relative energy. **Figure 6.13** exemplifies that moving three protons from bridging to terminal oxygen atoms stabilizes the super−reduced anion by 18.5 kcal·mol^{-1} in terms of free energy. In fully oxidized anions or when the number of electrons in the tungsten d band is small, there is a clear preference for protonating the bridging oxygens over terminal ones. Thus, the counterintuitive protonation at terminal oxygens in super reduced anions might be a consequence of the stabilization of a d_{xz} or a d_{yz} orbital below the highest SOMO upon lengthening the W—O distance with protonation at the terminal oxygen. This stabilization allows an electron to hop from the less stable d_{xy} orbital to a d_{yz}/d_{xz} that now is lower in energy, conferring stability to the reduced POM structure. This concept is graphically illustrated in **Figure 6.14**.

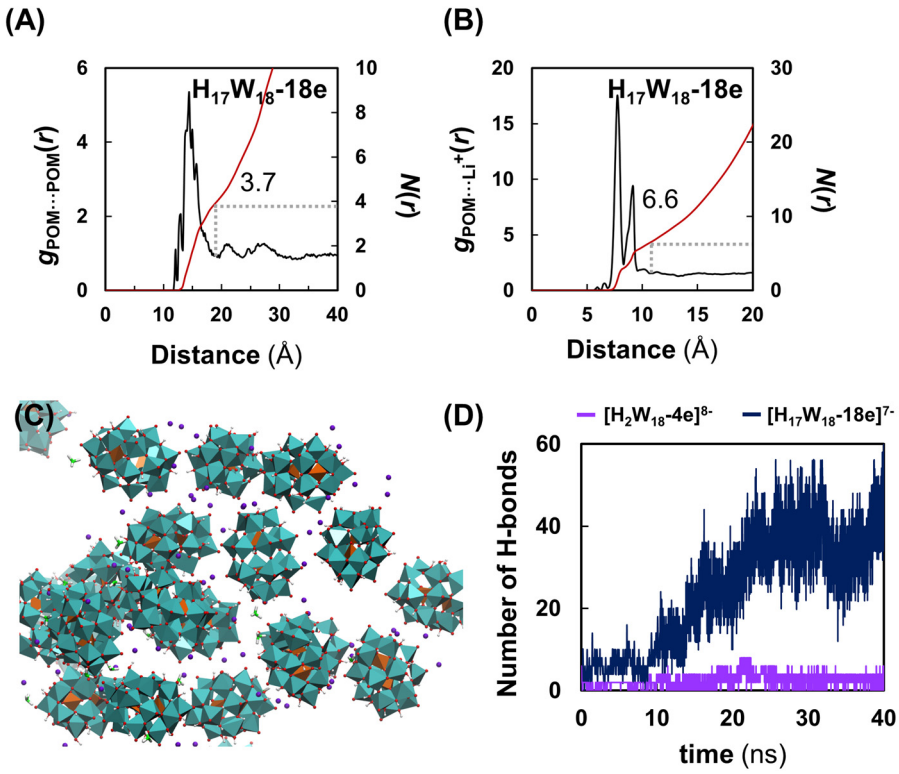

Figure 6.12 | Radial distribution functions between POMs taking as a reference the center of mass of each cluster (A) and between POMs and Li^+ counter cations (B) averaged over the last 10 ns of MD simulation. Both RDFs (black lines) are accompanied by the respective coordination number, N(r) represented in red lines. (C) Snapshot of a **$H_{17}W_{18}$–18e agglomerate** at the last step of the simulation (t = 40 ns). (D) Comparison of the evolution of the number of hydrogen bonds between POMs computed over 40 ns of simulation for **$H_{17}W_{18}$–18e** (blue line) and **H_2W_{18}–4e** (purple line). Criteria for considering hydrogen bond: XH···A distance ≤ 3.5 Å and a X—H···A angle ≥ 130^0.

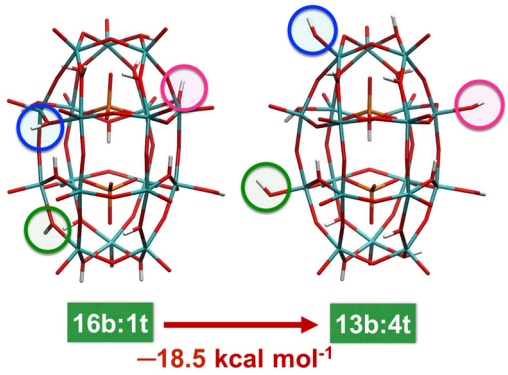

Figure 6.13 | Comparison of the structures of the super reduced $H_{17}W_{18}$**−18e** anion with bridging:terminal ratios of 16:1 and 13:4; highlighting the proton positions in which they differ from each other and the free energy change in going from 16:1 to 13:4.

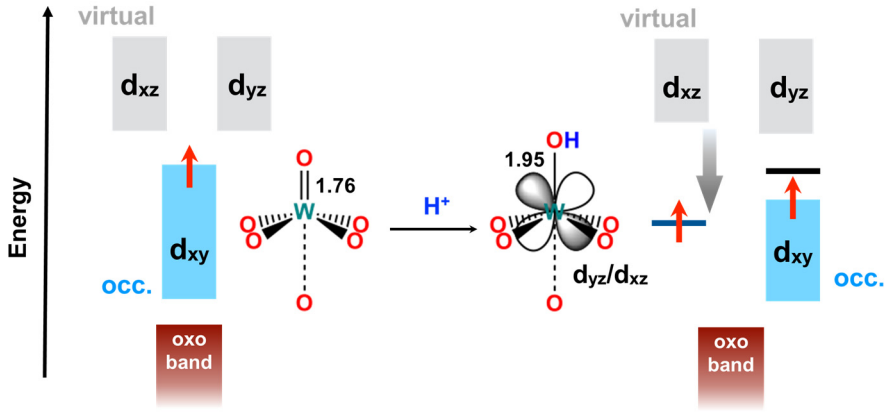

Figure 6.14 | Schematic frontier orbital diagram illustrating the origin of stabilization upon protonating a terminal oxygen in highly reduced POMs.

Moving more protons in this structure might lead to artifacts in the quantification of the free−energy change as all the remaining protons participate in intramolecular hydrogen bonds. For this reason, we performed partial geometry optimizations to keep only one hydrogen bond in the optimized structure, which is the average number of intramolecular hydrogen bonds obtained from the CPMD simulation with explicit solvent. To do so, we constrained all the P···O—H angles but one to 160^0 to mimic the geometry that the hydroxo groups adopt in solution to form hydrogen bonds with solvent water molecules instead than with other oxygen atoms of the POM structure. This approach allowed a systematic analysis of different structures with different *bridging:terminal* ratios, all them with 17 protons (**Table 6.2**). Comparison of the relative free energies strongly suggests

that the super–reduced cluster in aqueous solution might combine protons at bridging and terminal oxygen sites, the species with 7 protons at bridging positions and 10 at terminal ones (7:10) being the most likely proton distribution among the analyzed ones (see second column of **Table 6.2**). Besides, the 4:13 (+3.2 kcal·mol^{-1}), the 10:7 (+10.2 kcal·mol^{-1}) or the 13:4 (+14.2 kcal·mol^{-1}) ones and probably those presenting a proton distribution in between are also rather likely considering that most of the POMs in solution are not as isolated monomers but forming part of a supramolecular agglomerate, in which intermolecular interactions could alter their relative stabilities. Nevertheless, it is important to note that all of them can form agglomerates in a similar manner as shown in **Table 6.2** and **Figure 6.15**A and therefore, none of them is incompatible with the proposed mechanism for the super–reduction process.

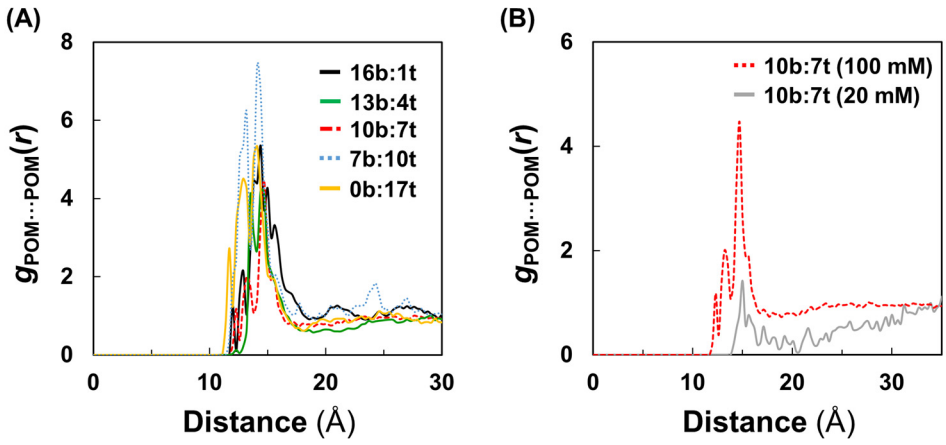

Figure 6.15 | (A) Comparison of the POM···POM RDF for several **$H_{17}W_{18}$–18e** anions with different bridging:terminal ratio of the 17 protonated sites. All the functions were averaged over the last 10 ns of a 40 ns simulations with POM concentration of 100 mM and pH ≈ 1. (B) Comparison of the RDF between **$H_{17}W_{18}$–18e(10:7)** anions at different POM concentrations.

Similarly to what we observed for **HW_{18}–4e** in **Figure 6.8**, the agglomeration of **$H_{17}W_{18}$–18e(7:10)** anions was found to lower the energy of their highest SOMO by 250 mV. Notably, the energy of the highest SOMO of **$H_{17}W_{18}$–18e(7:10)** in the agglomerate represented in **Figure 6.16** (–3.78 eV; B3LYP/LANL2DZ and continuum solvent) is only 0.76 eV higher in energy than the SOMO of the 1e–reduced **W_{18}–1e** (–4.54 eV) computed at the same level of theory, what fully agrees with the observed voltage *window of 0.8 V* for the re–oxidation process (see **Figure 6.1**B). It is also worth mentioning that, as **Figure 6.16** shows, the spin density in the structure of the agglomerate is also localized

mainly on W atoms. Overall, these results clearly show that without the additional stabilization provided by the enhanced ion pairing upon agglomeration, the formation of the super reduced anions would not be possible as the SOMOs in highly reduced species would be too high in energy with respect to those in the initial redox states. Further supporting this conclusion, the **$H_{17}W_{18}$–18e(7:10)** anion showed almost no agglomeration at a concentration of 20 mM (see **Table 6.2** and **Figure 6.15**B). Therefore, agglomeration is not expected neither at a 10–fold lower concentration (2 mM), in agreement with the experimental impossibility of reducing **W_{18}** beyond six electrons at these conditions.

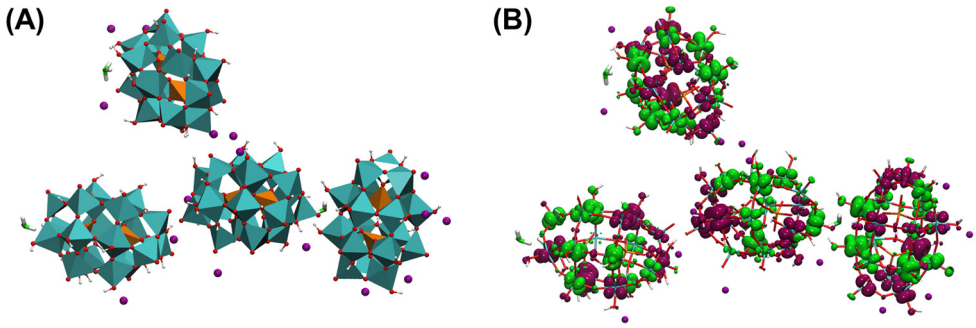

Figure 6.16 | (A) Snapshot of the agglomerate fragment used to evaluate the stabilization in the MOs of the super reduced anion **$H_{17}W_{18}$–18e(7:10)** upon agglomeration. Li^+ are depicted as purple spheres and H_3O^+ cations are highlighted in green. (B) Spin density of the agglomerate structure with 72 unpaired electrons, computed as open–shell singlet.

Table 6.2 | Main Features Concerning the Electronic Structure and Collective Behavior of **$H_{17}W_{18}$–18e** with Different "*bridging:terminal*" Protonation Ratios.[a]

			RDF POM···POM		RDF POM···Li^+		RDF POM···H_3O^+	
bridging:terminal	**ΔG**	**E_{SOMO}**	N_{POM}	$r_{integration}$	N_{Li^+}	$r_{integration}$	$N_{H_3O^+}$	$r_{integration}$
16:1	+32.7	–3.12	2.73	18.6	5.52	9.54	1.30	10.08
13:4	+14.2	–3.28	1.68	17.7	4.69	9.74	1.06	10.26
10:7	+10.2	–3.26	1.34	16.8	4.63	9.58	1.05	10.08
			0.06[b]	16.8[b]	2.13[b]	9.68[b]	0.71[b]	10.08[b]
7:10	0.0	–3.52	2.88	17.1	7.06	9.72	1.19	9.90
4:13	+3.2	–3.33	–[c]	–[c]	–[c]	–[c]	–[c]	–[c]
0:17	+30.5	–3.11	2.60	18.3	5.97	9.54	1.32	10.04

[a] All geometry optimizations were performed constraining the P···O_{bridge}H angles to 160^0 but one, according to the number of intramolecular hydrogen bonds in the CPMD simulation with explicit solvent. The selected phosphorus is that of the POM hemisphere in which the hydroxo group is found. No constrains were used for the 0:17 isomer as it does not contain any proton at a bridging position. Relative Free energies are given in kcal·mol^{-1} and orbital energies in eV. The integration distances for both RDFs are given in Å and refer to the centers of mass of both species. [b] Simulation at a POM concentration of 20 mM. [c] Simulation to be performed.

To evaluate the stability of the **$H_{17}W_{18}$–18e(7:10)** anion, we performed a 10 ps CPMD simulation of this anion in water at pH 7 that showed that the anion keeps the 17 protons during the 99.6 % of the simulated time. Therefore, it is assumable that **$H_{17}W_{18}$–18e(7:10)** represents a realistic molecular model of the super–reduced POM in solution. Furthermore, static DFT calculations indicate that abstracting one proton from this species is endothermic by 5.9 kcal·mol^{-1} (**Table 6.3**) and thus, the **$H_{16}W_{18}$–18e(15:1)** species observed in the CPMD starting from the **$H_{18}W_{18}$–18e** anion might be an intermediate in the formation of a more stable structure, such as the **$H_{17}W_{18}$–18e(7:10)** one, which is more than 30 kcal·mol^{-1} more stable (see **Table 6.2**). Besides, the highest SOMO in **$H_{16}W_{18}$–18e(7:9)** is almost 200 mV above than in **$H_{17}W_{18}$–18e(7:10)**, what is not expected to be compensated with the increase of ion pairing and agglomeration upon increasing the negative charge of the cluster from 7– to 8–. Observing the complete transformation of **$H_{17}W_{18}$–18e(16:1)** into **$H_{17}W_{18}$–18e(7:10)** during the CPMD simulation would require much longer simulation time, as it may involve a vast number of proton transfer steps. On the other hand, **Table**

6.3 shows that protonating a terminal position in **$H_{17}W_{18}$–18e(7:10)** is exothermic by 6.0 kcal·mol^{-1} and goes along with a little stabilization of the highest SOMO. On the basis of these results, it is reasonable to assume that the super reduced anions have a number of protons equal to 17 or 18, as the stabilization or destabilization induced by protonation or deprotonation might be compensated by the change in the agglomeration ability in the presence of alkali cations, which increases with the POM charge.[32]

Table 6.3 | Comparison between several **W_{18}–18e** structures with different protonation states and patterns.[a]

anion	*n* H^+	*q*	*n* unpaired e^-	E_{SOMO}	ΔG
$H_{17}W_{18}$–18e(7:10)	17	7–	18	–3.52	0.0
$H_{16}W_{18}$–18e(7:9)	16	8–	18	–3.35	+5.9
$H_{18}W_{18}$–18e(7:11)	18	6–	18	–3.59	–6.0
$H_{17}W_{18}$–18e(6:7:2*aqua*)	17	7–	16	–3.30	+13.6
$H_{17}W_{18}$–18e(3:2:6*aqua*)	17	7–	6	–3.31	+18.6

[a]All geometry optimizations were performed constraining the P···O_{bridge}H angles to 160^0 but one, according to the number of intramolecular hydrogen bonds in the CPMD simulation with explicit solvent. The selected phosphorus is that of the POM hemisphere in which the hydroxo group is found. The energy of the highest SOMO is given in eV and relative Gibbs free energies in kcal·mol^{-1}.

Previous electrochemical studies suggested that the six–electron–reduced metatungstate $[H_nW_{12}O_{40}]^{(14-n)-}$ exhibits three W—W bonds within a triad that gather all the extra electrons.[33,34] In addition, the formation of the W—W bonds was proposed to be coupled to the transformation of the terminal oxo ligands into more labile aqua ligands.[34] To explore this possibility, we computed two additional structures containing 1 and 6 W—W bonds at the cap regions, labeled as **$H_{17}W_{18}$–18e(6:7:2*aqua*)** and **$H_{17}W_{18}$–18e(3:2:6*aqua*)**, respectively. As depicted in **Figure 6.17**, the optimized structure of **$H_{17}W_{18}$–18e(3:2:6*aqua*)** displays 3 W^{IV} ions in each cap, linked to each other by metallic bonds that range from 2.62 to 2.65 Å. The belt regions are mixed–valent, having W ions with oxidation states of 5+ and 6+. On the other hand, **$H_{17}W_{18}$–18e(6:7:2*aqua*)** is more anisotropic, as only two W^{IV} ions are found in one cap and the remaining 14 electrons are delocalized over the remaining W atoms. In these structures, the overall number of protons was maintained as 17, what allowed us to compare their relative stability to the **$H_{17}W_{18}$–18e(7:10),** which is the most stable species found so far. The last two entries in **Table 6.3** show that the formation of W—W bonds

(along with the electron–electron pairing) does not stabilize the structure of the super–reduced anions, which prefers to keep unpaired all the *d* electrons. In fact, the formation of a single metallic bond is destabilizing by 13.6 kcal·mol^{-1} and it causes the energy of the highest SOMO to be shifted up by ca. 200 mV with respect to the all–W^{V} structure (**Table 6.3**). Thus, unlike other reduced W–based structures, the 18–electron reduced Wells–Dawson does not seem likely to form W—W bonds. Furthermore, this is supported by the fact that the experimental reduction of $\mathbf{W_{18}}$ implicates only 18 electrons, because if the formation of W—W bonds were possible, further reduction of the cluster beyond 18 electrons might be observed owing the presence of fully oxidized W^{VI} ions in the structure.

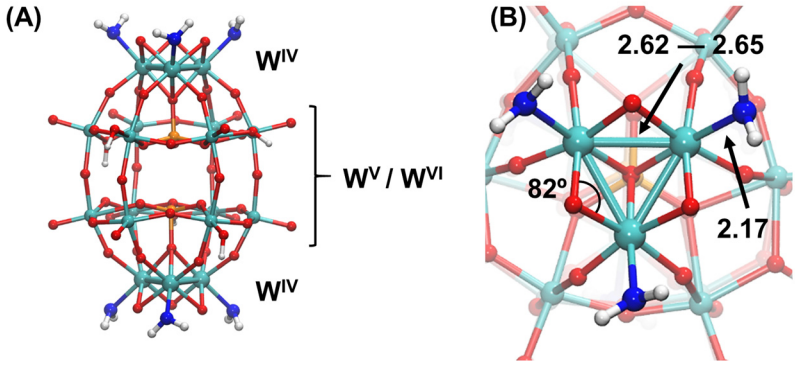

Figure 6.17 | (A) Optimized structure of $\mathbf{H_{17}W_{18}}$**–18e(3:2:6*aqua*)** species presenting 6 W^{IV}—W^{IV} bonds in the cap regions and W^{V}/W^{VI} mixed–valent belts. Aqua ligands are colored in blue. (B) Top view of the same cluster in which main geometrical parameters are given in Å and degrees (^{0}).

Ongoing calculations are devoted to understand the mechanism for the hydrogen evolution reaction (HER) upon diluting an aliquot of the charged solution in water.[2] The working hypothesis is based on the fact that after diluting the super reduced anions will lose stability because: i) the agglomerates will breakdown at a low concentration, which might go along with a decrease of the ion pairing; and ii) the change in the pH from ~1 to ~7 will favor the deprotonation of the POM cluster. The combination of these phenomena will destabilize the MO of the anion enabling the transfer of one electron from the tungsten d band to a proton, either to form a tungsten hydride intermediate or a solvated electron.[35] After that, the basicity of the POM would decrease as a result of a decrease in the number of *d* electrons (from 18 to 16) favoring the release of more protons to the bulk to form molecular hydrogen.

6.4 Concluding Remarks.

A comprehensive study combining static DFT and MD (classical and *ab initio*) simulation techniques allowed us to propose a mechanism for the super–reduction of the $\mathbf{W_{18}}$ cluster with 18 electrons, as well as a plausible molecular and electronic structure. The usual redox behavior of $\mathbf{W_{18}}$ anions involves four or six electrons as much, depending on the pH.[4–8] However, in acidic aqueous solutions in which the concentration of the $Li_6\mathbf{W_{18}}$ salt is close to the solubility limit (100 mM), these anions can experience a series of multi–electron redox processes to yield the super–reduced species $\mathbf{H_nW_{18}–18e}$.[2] Our simulations showed that at the experimental conditions, the lowly reduced anions can agglomerate mostly via lithium–mediated contacts. When forming agglomerates, POMs share their associated cations increasing the effective POM···Li^+ ion pairing. This provides an additional stabilization of almost 400 mV to the unoccupied MOs of the POMs and thus, can qualitatively (if not quantitatively) explain the reduction of $\mathbf{W_{18}}$ beyond the previously reported limits within a relatively narrow potential window of *ca.* 800 mV.[2] Also in agreement with experimental results that indicate that the efficiency of the super–reduction process increases as $K^+ < Na^+ < Li^+$, we observed that lithium cations induce a much stronger agglomeration between POMs than potassium ones, which bear a lower charge density due to their bigger size and therefore, can only provide weaker and shorter–lived POM···cation contacts. Hence, poorer POM stabilization can be expected for big alkali cations that might render more difficult reduction processes.

In addition, we proposed that a plausible structure for the 18 electron–reduced anion might comprise 17 or 18 associated protons located at bridging and terminal positions of the cluster. For the species with 17 protons $\mathbf{H_{17}W_{18}}$, we found that the most likely protonation pattern involves from four to seven protons at terminal oxygen atoms, and the remaining ones being at bridging oxygen centers. It was found that these anions agglomerate much more strongly than other anions formed at lower reduction stages, since in addition to cation–mediated interactions; they can interact with each other also through direct hydrogen bonds. Furthermore, the energy of the MOs in these species accounting for the stabilization upon agglomeration in solution with Li^+ cations is in excellent agreement with the narrow voltage window in which the whole electrochemical process (from 0 to 18 electrons) occurs. Ongoing work is focused on analyzing the molecular mechanism responsible for the HER taking place upon diluting the fully charged solution in water.

6.5 Supplementary Material.

Animations of some representative simulations discussed in this chapter can be accessed by scanning the following QR codes with a smartphone or though the URLs below.

MD simulation 50 $\mathbf{W_{18}}$(100 mM), 300 Li^+	MD simulation 50 $\mathbf{HW_{18}}$**–4e** (100 mM), 300 Li^+, 150 H_3O^+
https://youtu.be/BHgPTfWZP60	https://youtu.be/3XsTsuXfUUs

CPMD simulation
of $\mathbf{W_{18}}$(4e) in acidic medium

https://youtu.be/6KB9lfCGuC8

References

1. a) Katsoulis, D. E. *Chem. Rev.* **1998,** *98,* 359–387; b) Wang, S.–S.; Yang, G.–Y. *Chem. Rev.* **2015**, *115*, 4893–4962; c) Weinstock, I. A.; Schreiber, R. E.; Neumann, R. *Chem.Rev.* **2018**, *118*, 2680–2717; d) Gumerova, N. I.; Rompel, A. *Nat. Rev. Chem.* **2018**, *2*, 0112.
2. Chen, J.–J.; Symes, M. D.; Cronin, L. *Nat. Chem.* **2018**, *10*, 1042–1047.
3. Liu, Y.; Lu, S.; Wang, H.; Yang, C.; Su. X.; Xiang, Y. *Adv. Energy Mater.* **2017**, *7*, 1601224.
4. Pope, M. T.; Papaconstantinou, E. *Inorg. Chem.* **1967,** *6*, 1147–1152.
5. Harmalker, S. P.; Leparulo, M. A.; Pope, M. T. *J. Am. Chem. Soc.* **1983**, *105*, 4286–4292.
6. Keita, B.; Nadjo, L. *J. Electroanal. Chem.* **1987**, *227*, 77–98.
7. Prenzler, P. D.; Boskovic, C.; Bond, A. M.; Wedd, A. G. *Anal. Chem.* **1999**, *71*, 3650–3656.
8. Bernardini, G.; Zhao, C.; Wedd, A. G.; Bond, A. M. *Inorg. Chem.* **2011**, *50*, 5899–5909.
9. a) Perdew, J. P. Phys. Rev. B: Condens. Matter Mater. Phys. **1986**, 33, 8822–8824; b) Perdew, J. P. Phys. Rev. B: Condens. Matter Mater. Phys. **1986**, 34, 7406; c) Becke, A. D. Phys. Rev. A: At., Mol., Opt. Phys. **1988**, 38, 3098–3100.
10. a) Te Velde, G.; Bickelhaupt, F. M.; van Gisbergen, S. J. A.; Fonseca Guerra, C.; Baerends, E. J.; Snijders, J. G.; Ziegler, T. *J. Comput. Chem.* **2001**, *22*, 931–967; b) Fonseca Guerra, C.; Snijders, J. G.; Te Velde, G.; Baerends, E. J. *Theor. Chem. Acc.* **1998**, *99*, 391–403; c) ADF2016, SCM, Theoretical Chemistry; Vrije Universiteit: Amsterdam, The Netherlands, Http://Www.Scm.Com.
11. a) Klamt, A. *J. Phys. Chem.* **1995**, *99*, 2224–2235; b) Klamt, A.; Jonas, V.; Bürger, T.; Lohrenz, J. C. W. *J. Phys. Chem. A* **1998**, *102*, 5074–5085; c) Pye, C. C.; Ziegler, T. *Theor. Chem. Acc.* **1999**, *101*, 396–408.
12. a) van Lenthe, E.; Baerends, E. J.; Snijders, J. G. *J. Chem. Phys.* **1993**, *99*, 4597–4610; b) van Lenthe, E.; Baerends, E. J.; Snijders, J. G. *J. Chem. Phys.* **1994**, *101*, 9783–9792; c) Van Lenthe, E.; Ehlers, A.; Baerends, E. J. *J. Chem. Phys.* **1999**, *110*, 8943–8953; d) Klopper, W.; van Lenthe, J. H.; Hennum, A. C. *J. Chem. Phys.* **2000**, *113*, 9957–9965.
13. Frisch, M. J.; Trucks, G. W.; Schlegel, H. B.; Scuseria, G. E.; Robb, M. A.; Cheeseman, J. R.; Scalmani, G.; Barone, V.; Mennucci, B.; Petersson, G. A.; Nakatsuji, H.; Caricato, M.; Li, X.; Hratchian, H. P.; Izmaylov, A. F.; Bloino, J.; Zheng, G.; Sonnenberg, J. L.; Hada, M.; Ehara, M.; Toyota, K.; Fukuda, R.; Hasegawa, J.; Ishida, M.; Nakajima, T.; Honda, Y.; Kitao, O.; Nakai, H.; Vreven, T.; Montgomery, J. A., Jr.; Peralta, J. E.; Ogliaro, F.; Bearpark, M.; Heyd, J. J.; Brothers, E.; Kudin, K. N.; Staroverov, V. N.; Kobayashi, R.; Normand, J.; Raghavachari, K.; Rendell, A.; Burant, J. C.; Iyengar, S. S.; Tomasi, J.; Cossi, M.; Rega, N.; Millam, J. M.; Klene, M.; Knox, J. E.; Cross, J. B.; Bakken, V.; Adamo, C.; Jaramillo, J.; Gomperts, R.; Stratmann, R. E.; Yazyev, O.; Austin, A. J.; Cammi, R.; Pomelli, C.; Ochterski, J. W.; Martin, R. L.; Morokuma, K.; Zakrzewski, V. G.; Voth, G. A.; Salvador, P.; Dannenberg, J. J.; Dapprich, S.; Daniels, A. D.; Farkas, Ö.; Foresman, J. B.; Ortiz, J. V.; Cioslowski, J.; Fox, D. J. Gaussian 09, revision D.01; Gaussian, Inc.: Wallingford, CT, 2009.
14. a) Lee, C.; Yang, W.; Parr, R. G. *Phys. Rev. B: Condens. Matter Mater. Phys.* **1988**, *37*, 785–789; b) Becke, A. D. *J. Chem. Phys.* **1993**, *98*, 5648–5652; c) Stephens, P. J.; Devlin, F. J.; Chabalowski, C. F.; Frisch, M. J. *J. Phys. Chem.* **1994**, *98*, 11623–11627.
15. Hay, P. J.; Wadt, W. R. *J. Chem. Phys.* **1985**, *82*, 270–283.
16. Cancès, E.; Mennucci, B.; Tomasi, J. *J. Chem. Phys.* **1997**, *107*, 3032–3041.

17. Tissandier, M. D.; Cowen, K. A.; Feng, W. Y.; Gundlach, E.; Cohen, M. H.; Earhart, A. D.; Coe, J. V.; Tuttle, T. R. *J. Phys. Chem. A* **1998**, *102*, 7787–7794.
18. Wang, J.; Cieplak, P.; Kollman, P. *J. Comput. Chem.* **2000**, *21*, 1049–1074.
19. Jorgensen, W. L.; Chandrasekhar, J.; Madura, J. D.; Impey, R.W.; Klein, M. L. *J. Chem. Phys.* **1983**, 79, 926–935.
20. Krishnan, R.; Binkley, J. S.; Seeger, R.; Pople, J. A. *J. Chem. Phys.* **1980**, *72*, 650–654.
21. López, X.; Nieto–Draghi, C.; Bo, C.; Ávalos, J.; Poblet, J. M. *J. Phys. Chem. A* **2005**, *109*, 1216–1222.
22. Chaumont, A.; Wipff G. *Phys. Chem. Chem. Phys.* **2008**, *10*, 6940–6953.
23. IBM Corp.Armonk, N. Y. CPMD; MPI für Festkörperforschung: Stuttgart, Germany, 1990–2006; pp 1997–2001.
24. a) Lee, C.; Yang, C.; Parr, R. G. *Phys. Rev. B: Condens. Matter Mater. Phys.* **1988**, *37*, 785–789; b) Becke, A. D. *Phys. Rev. A: At., Mol., Opt. Phys.* **1988**, *38*, 3098–3100.
25. Troullier, N.; Martins, J. L. *Phys. Rev. B: Condens. Matter Mater. Phys.* **1991**, *43*, 1993–2006.
26. Kleinman L.; Bylander, D. M. *Phys. Rev. Lett.* 1982, 48, 14251428.
27. Hartwigsen, C.; Goedecker, S.; Hutter J. *Phys. Rev. B* **1998**, *58*, 3641.
28. Car, R.; Parrinello, M. *Phys. Rev. Lett.* **1985**, *55*, 2471–2474.
29. a) Nosé, S. *J. Chem. Phys.* **1984**, *81*, 511–519; b) Hoover, W. G. *Phys. Rev. A: At., Mol. Opt. Phys.* **1985**, *31*, 1695–1697.
30. López, X.; Carbó, J. J.; Bo, C.; Poblet, J. M. *Chem. Soc. Rev.* **2012**, *41*, 7537–7571.
31. Kelly, C. P.; Cramer, C. J.; Thrular, D. G. *J. Phys. Chem. B* **2007**, *111*, 408–422.
32. Solé–Daura, A.; Notario–Estévez, A.; Carbó, J. J.; Poblet, J. M.; De Graaf, C.; Monakhov, K. Y.; López, X. *Inorg. Chem.* **2019**, *58*, 3881–3894.
33. Launay, J. P. *J. Inorg. Nucl. Chem.* **1976**, *38*, 807–816.
34. a) Jeannin, Y.; Launay, J. P.; Seid Sedjadi, M. A. *Inorg. Chem.* **1980**, *19*, 2933–2935; b) Piepgrass, K.; Pope, M. T. *J. Am. Chem. Soc.* **1987**, *109*, 1586–1587; c) Boskovic, C.; Sadek, M.; Brownlee, R. T. C.; Bond, A. M.; Wedd, A. G. *J. Chem. Soc., Dalton Trans.* **2001**, *2001*, 187–196.
35. a) Onda, K.; Li, B.; Zhao, J.; Jordan, K. D.; Yang, J.; Petek; H. *Science* **2005**, *308*; 1154–1158; b) Zhao, J.; Li, B.; Onda, K.; Feng, M.; Petek, H. *Chem. Rev.* **2006**, *106*, 4402–4427; c) Fischer, S. A.; Duncan, W. R.; Prezhdo, O. V. *J. Am. Chem. Soc.* **2009**, *131*, 15483–15491; d) Sobolewski, A. L.; Domcke, W. *Phys. Chem. Chem. Phys.* **2002**, *4*, 4–10; e) Abel, B.; Buck, U.; Sobolewskic, A. L.; Domcked, W. *Phys. Chem. Chem. Phys.* **2012**, *14*, 22–34.

UNIVERSITAT ROVIRA I VIRGILI
NEW HORIZONS IN COMPUTATIONAL MODELING OF POLYOXOMETALATES:
BIOLOGICAL ACTIVITY, ENERGY STORAGE AND SUSTAINABLE CATALYSIS.
Albert Solé Daura

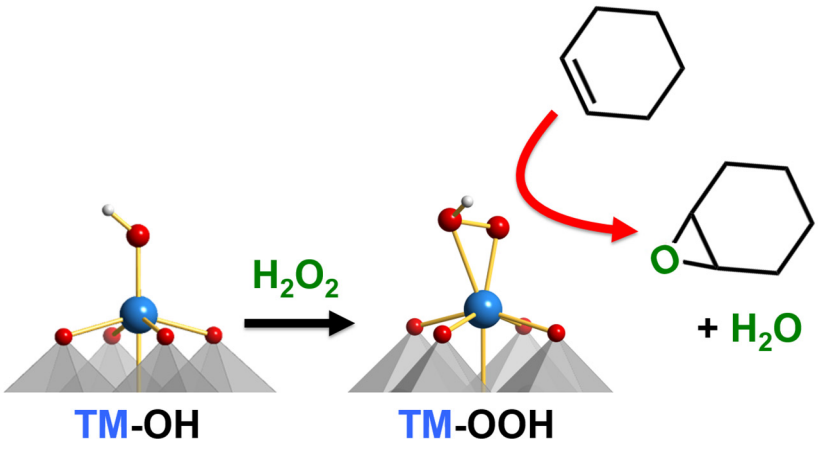

Chapter 7

Computational Studies on Alkene Epoxidation Catalyzed by Early Transition Metal–Substituted Polyoxometalates

UNIVERSITAT ROVIRA I VIRGILI
NEW HORIZONS IN COMPUTATIONAL MODELING OF POLYOXOMETALATES:
BIOLOGICAL ACTIVITY, ENERGY STORAGE AND SUSTAINABLE CATALYSIS.
Albert Solé Daura

CHAPTER 7

Computational Studies on Alkene Epoxidation Catalyzed by Early Transition Metal–Substituted Polyoxometalates

In this chapter we discuss our results in the theoretical analysis of the alkene epoxidation reaction with hydrogen peroxide catalyzed by early TM–substituted POMs. Seeking to support the latest experimental results in the field, we analyzed the mechanism for the alkene epoxidation catalyzed by the Nb^{V}–substituted Lindqvist anion $[Nb(OH)W_5O_{18}]^{2-}$ and with the gained knowledge, we evaluated the role of the nature of the embedded metal ion by comparing the catalytic activity of Nb–POMs with that of Ti^{IV}–substituted analogues. Furthermore, we studied the influence of the ligand environment using the experimentally tested cases of the Nb–substituted Keggin and the Ti–containing hybrid catalyst $[\alpha\text{–}B\text{–}SbW_9O_{33}(^{t}BuSiO)_3Ti(O^{i}Pr)]^{3-}$, which promotes the selective epoxidation of allylic alcohols with hydrogen peroxide. Finally, we characterized the mechanism responsible for the main side reaction, that is the non–productive decomposition of the hydrogen peroxide, which explains the trends in selectivity for catalysts with different metal ions.

The results subject to this chapter collect collaboration projects with several experimental groups, including those of Prof. O. A. Kholdeeva based in Boreskov Institute of Catalysis (Russia), Prof. R. J. Errington from Newcastle University (UK) and Dr. G. Guillemot and Prof. A. Proust from Sorbonne Université (France).

7.1 Experimental Background.

During the two last decades, TM–substituted POMs have been successfully used as treatable molecular models of single–site silica supported catalysts.[1–12] In particular, studies with Ti–substituted POMs were devoted to understand the reactivity of Ti–containing silicalites as selective catalysts for the epoxidation of alkenes. Some years ago, it was found that Nb–containing silicalites exhibit higher product selectivity and faster reactivity than their Ti–containing analogues,[13,14] although the reasons for that are still not fully understood. To shed some light onto the alkene epoxidation by Nb–containing catalysts, Kholdeeva and co–workers synthesized a series of Nb^{V}–substituted Lindqvist anions, i.e. the Nb–methoxy $(Bu_4N)_2[(CH_3O)NbW_5O_{18}]$

(**1a**^{Nb}),[15] which was prepared in collaboration with the Errington group, the μ–oxo dimer $(Bu_4N)_4[(NbW_5O_{18})_2O]$ (**1D**^{Nb}) and the Nb–monosubstituted monomer $(Bu_4N)_3[Nb(O)W_5O_{18}]$ (**1b**^{Nb}),[16] all them represented in **Figure 7.1**. These species were treated with aqueous solution of H_2O_2 and applied to the epoxidation cyclohexene (CyH) as a representative example of alkene substrate, for which the dimeric **2D**^{Nb} and the Nb–methoxy **1a**^{Nb} resulted more reactive than **1b**^{Nb} (see **Table 7.1**). In the presence of water, **2D**^{Nb} and **1a**^{Nb} can be hydrolyzed to yield the protonated Nb–substituted Lindqvist monomer $[Nb(OH)W_5O_{18}]^{2-}$ (**2**^{Nb}), also represented in **Figure 7.1**. Accordingly, entries 2 and 3 in **Table 7.1** show that the catalytic activity of **1b**^{Nb} significantly increases after the addition of acid because protons tend to associate to the anionic POM framework, giving access to species **2**^{Nb}, which is the same species generated in the hydrolysis of the other precursors.

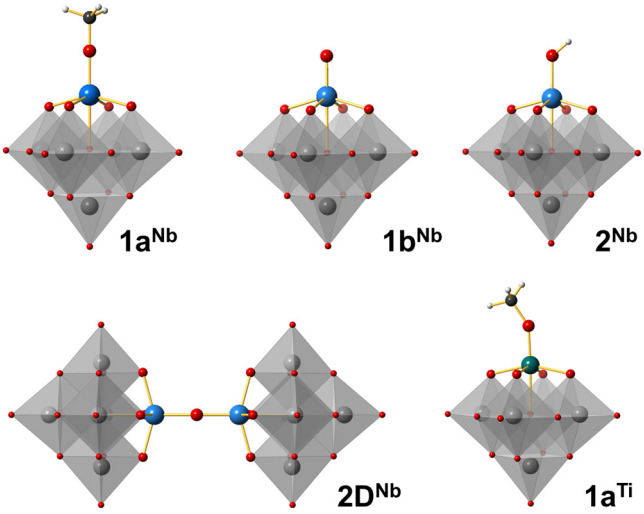

Figure 7.1 | 3D representation for several metal–substituted polyoxotungstates of the Lindqvist structure.

Table 7.1 | CyH oxidation with H_2O_2 in the presence of Nb and Ti catalysts.[a]

				Product selectivity, %[d]	
Entry	**POM**	**Time, h**	**CyH conver, %**	**heterolytic**	**homolytic**
1	**1b**^{Nb}	5	55	92	8
2	**1b**^{Nb} + 1 equiv H^+	2	74	83	12
3	**1b**^{Nb} + 0.1 equiv H^+	3	74	87	9
4	**2D**^{Nb} [c]	1.5	76	87	7
5	**1a**^{Nb}	0.2	31	86	12
6	**1a**^{Nb}	2	67	90	10
7	Nb,Si[e]	0.3	34	71	21
8	**1a**^{Ti}	3	30	59	36
9	Ti,Si[e]	2.5	35	65	27

[a] Reaction conditions: 0.2 M CyH, 0.2 M H_2O_2 (30%), 0.004 M POM, 50 °C, 1 mL CH_3CN. [b] Hydrogen peroxide utilization efficiency = total yield of products based on the oxidant consumed. [c] Concentration of Nb–dimer was 0.002 M. [d] Based on the substrate consumed. [e] Reaction conditions: 0.1 mmol CyH, 0.1 mmol H_2O_2, catalyst 0.003 mmol Ti or Nb, 50 °C, 1 mL CH_3CN. Data taken from ref. 17. The remaining data were adapted from refs 15 and 16.

A wide range of experimental techniques, including elemental analysis, UV–vis, FT–IR, Raman, ^{93}Nb, ^{17}O and ^{183}W NMR spectroscopy, cyclic voltammetry, and potentiometric titration supported the formation of a protonated Nb–peroxo complex $[HNb(O_2)W_5O_{18}]^{2-}$ (**3**^{Nb}) bearing a Nb–(η^2–OO) moiety upon treating the Nb–hydroxo complex **2**^{Nb} with H_2O_2. **Scheme 7.1** summarizes all the possible equilibria that can be established between the aforementioned species. Importantly, **3**^{Nb} can readily promote the epoxidation of double bonds, whereas its non–protonated counterpart $[HNb(O_2)W_5O_{18}]^{3-}$ (**4**^{Nb}) resulted inert towards alkenes. On the other hand, the Nb–substituted Keggin anion $[PW_{11}O_{39}Nb(O_2)]^{4-}$ (**4K**^{Nb}) also displayed poor reactivity towards alkenes, even in the presence of acid.[16]

Scheme 7.1 | Possible Nb–POM species and interconversion in the presence of aqueous H_2O_2. The employed precursors are highlighted in blue.

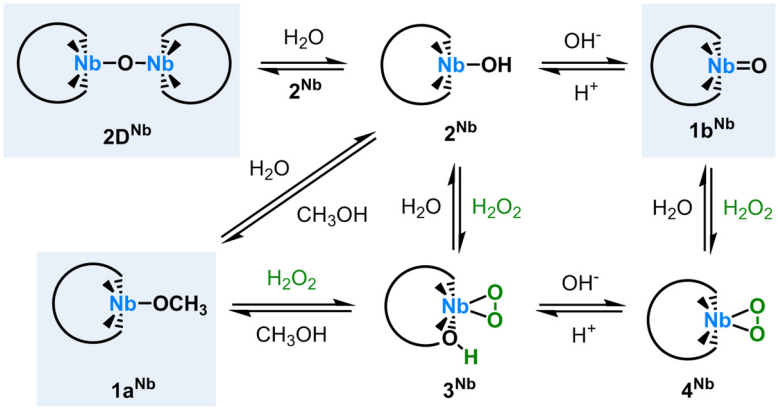

To better understand the differences between Nb^{V}– and Ti^{IV}–based systems as epoxidation catalysts, a Ti^{IV}–subsituted Lindqvist anion $(Bu_4N)_3[(CH_3O)TiW_5O_{18}]$ (**1a^{Ti}** in **Figure 7.1**) was synthesized to compare its catalytic performance with that of the structurally analogous **1a^{Nb}**.[15] It is worth comparing the results displayed in entries 5 and 8 of **Table 7.1** with those in entries 7 and 9, respectively, since they evince that indeed, the performance of TM–substituted POMs is rather similar than the reported for their heterogeneous counterparts. Moreover, as in the heterogeneous catalysts, the Ti complex was less reactive and less selective towards heterolytic products than the Nb–containing ones. In fact, **Figure 7.2** shows graphically how the apparent activation energy (E_a) for Cyclooctene (CyOct) epoxidation is lower for Nb, while Ti exhibits a lower E_a for the H_2O_2 decomposition reaction. The latter is supposed to proceed via formation of radical species on the basis of mechanistic studies on other systems[18–25] and therefore, it has been related to the formation of homolytic products in the presence of alkenes.

As a different approach to model single–site silica–supported catalysts, the group of Guillemot and Proust developed a silanol–decorated polyoxotungstate, $[\alpha\text{–B–}SbW_9O_{33}(^{t}BuSiOH)_3]^{3-}$, that can coordinate a Ti center in a tetrahedral environment leading to the $[\alpha\text{–B–}SbW_9O_{33}(^{t}BuSiO)_3Ti(O^{i}Pr)]^{3-}$ (**1^{TiW9}**) complex represented in **Figure 7.3**,[4] fairly mimicking the coordination environment that is present in the heterogeneous TS–1 epoxidation catalyst.[5,6] Specifically, **1^{TiW9}** showed the ability to selectively epoxidize allylic alcohols at room temperature, achieving high conversions, while conversions for non–functionalized alkenes under the same conditions were reported to remain insignificant.[4]

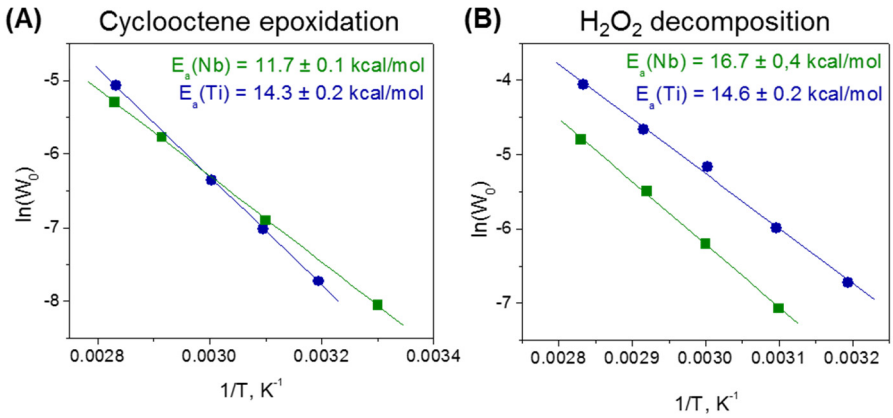

Figure 7.2 | Arrhenius plots for **1a**^{Ti} and **1a**^{Nb}–catalyzed CyOct epoxidation (A) and H_2O_2 decomposition (B). Reaction conditions: 0.1 *M* CyOct, 0.1 *M* H_2O_2, 0.004 *M* POM, 1 mL CH_3CN (for epoxidation); 0.2 *M* H_2O_2, 0.008 *M* POM, 2 mL CH_3CN (for H_2O_2 decomposition). Adapted from ref. 15.

To shed some light onto the reasons governing the experimental observations presented above, we initially characterized the molecular mechanism for the alkene epoxidation by Nb–substituted POMs and compared it with their Ti–containing analogues aiming to explain their different catalytic performance. Also, we evaluated the influence of the nature of the metal ligands and coordination environment seeking to disclose the origin of selectivity towards allylic alcohols observed for the hybrid catalyst **TiSbW$_9$,** in which Ti is fixed to the structure by silanol groups. Moreover, we characterized the mechanism responsible for the main side reaction competing with the alkene epoxidation, that is the non–productive decomposition of hydrogen peroxide.

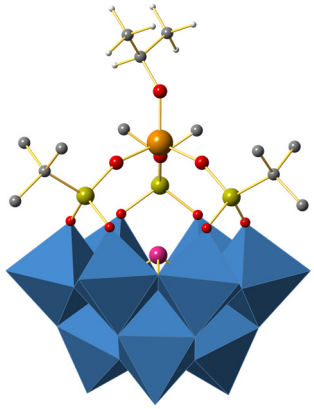

Figure 7.3 | Combined balls–and–sticks and polyhedral representation of the Ti–isopropoxide catalyst precursor ($\mathbf{1}^{\mathbf{TiW9}}$). H atoms in ^{t}BuSiO groups are omitted for clarity. Color code: Ti (orange), Si (yellow), W (blue), Sb (magenta), O (red), C (grey), H (white). Note that colors were adapted for the sake of consistency with our collaborators.

7.2 Computational Details.

The DFT analysis of the reaction pathways was carried out with Gaussian09 rev. C01 software.[26] Geometry optimization of reagents, intermediates, transition states and products was made using B3LYP density functional.[27] LANL2DZ pseudopotential[28] was used for W, Ti and Nb atoms and 6–31g(d,p) basis set[29] was used for other atoms. The geometry optimization was full and without any symmetry constrains, and solvent effects of acetonitrile were included using the IEF–PCM implicit solvation model[30] as implemented in Gaussian09.[26] This level of theory has been proved to be accurate and reliable enough to study the reactivity concerning POMs and their transition metal–substituted analogues, always showing a high degree of consistency with experimental outcomes and kinetic studies.[11,12,31] Time–dependent DFT (TD–DFT) calculations were performed with the long–range corrected CAM–B3LYP functional[32] as implemented in Gaussian 09 using the same basis set. In order to compute protonation energies (ΔG_{H+}), we took the experimental standard free energy of a proton in aqueous solution 272.2 kcal·mol^{-1}.[33] The standard state correction of +1.9 kcal·mol^{-1} (from ideal gas at 1 atm to 1 mol L^{-1} at 298.15 K) was applied to the free energy of all the species. MECP structures were obtained using Gaussian09[26] and the MECP code by Harvey et al.[34] by means of the easyMECP wrapper.[35]

7.3 Results and Discussion.

7.3.1 Mechanistic study of alkene epoxidation with H_2O_2 catalyzed by Nb–Lindqvist catalysts.

To understand the reaction mechanism at atomistic level and identify the active species of the oxygen transfer process, we have performed DFT calculations on Nb–substituted Lindqvist anions using CyH as substrate. In this section, the "Nb" tag in the labels of the species has been omitted since only the reactivity of Nb compounds is discussed. **Figures 7.4** and **7.5** depict the calculated free energy profiles for the hydrolysis of the methoxy precursor **1a** and for the epoxidation of CyH with H_2O_2 catalyzed by $[Nb(OH)W_5O_{18}]^{2-}$ (**2**) anion. Initially, the hydrolysis of **1a** to generate the active catalytic species **2** shows an accessible, computed free–energy barrier of 12.2 kcal·mol^{-1} (**TS1'$_w$**). The hydroxo complex **2** can be also regenerated after the final oxygen transfer step (**Figure 7.5**), and although the corresponding methoxy complex is slightly lower in energy (3.6 kcal·mol^{-1}), the reverse transformation (**2** → **1a**) is unlikely because of the low concentration of CH_3OH compared to other reagents. The Nb–monosubstituted dimer **2D** was not included in the profiles since its formation from two monomers (**2**) was found to be endothermic by 2.7 kcal·mol^{-1}. Therefore, it is not expected to affect the overall kinetics of the reaction. The absence of the dimer and the methoxy derivative during the course of the reaction agrees with the fact that the E_a for epoxidation of CyOct was determined to be the same (11.4 kcal·mol^{-1}) regardless the employed catalytic precursor.[15,16]

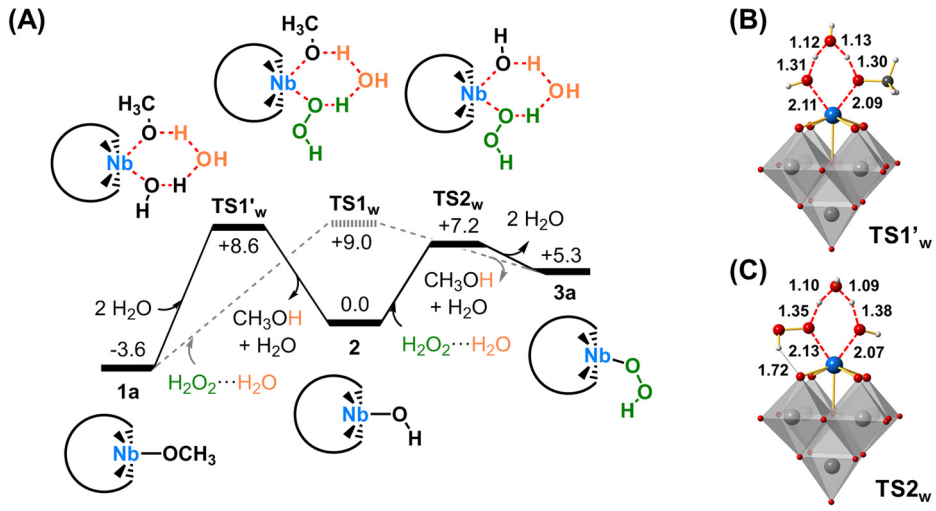

Figure 7.4 | (A) Gibbs free energy profile (kcal·mol^{-1}) for the hydrolysis of the methoxy precursor **1a** and the heterolytic activation of H_2O_2. Black, solid lines depict the most favorable reaction pathway, while less favorable one is shown in dashed lines. (B) and (C) represent the DFT–optimized structures for the **TS1'**$_w$ and **TS2**$_w$ transition states, in which main distances are shown in Å.

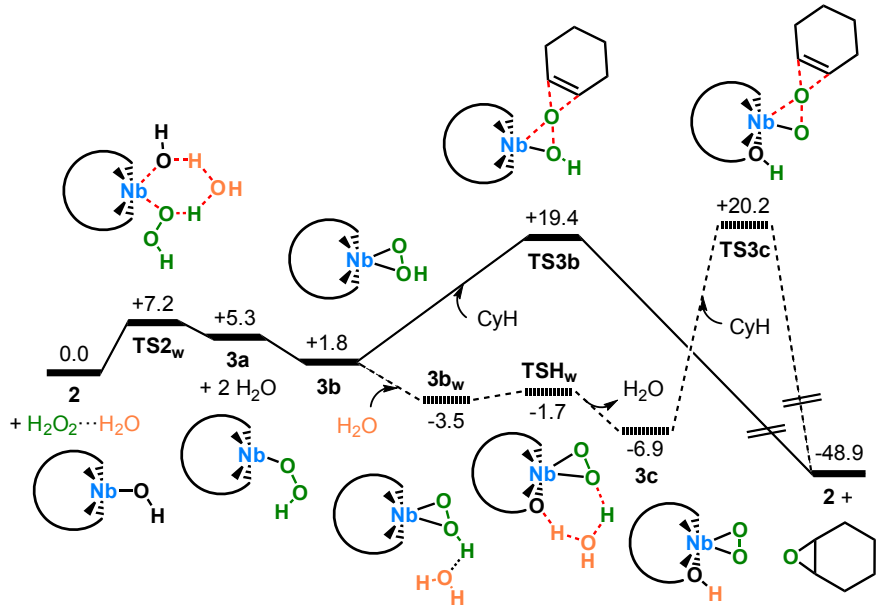

Figure 7.5 | Gibbs free energy profile (kcal·mol^{-1}) for the epoxidation of CyH catalyzed by **NbW$_5$**. Black lines depict the most favorable reaction pathway, while less favorable ones are shown in dashed lines.

The metal–hydroxo complex **2** can then interact with H_2O_2 through a substitution mechanism assisted by a solvent water molecule acting as proton shuttle (see **TS2$_w$** in **Figure 7.4**) to give the $[(\eta^1\text{–HOO})NbW_5O_{18}]^{2-}$ hydroperoxo species **3a** and one water molecule. The computed free–energy barrier for the H_2O_2 activation is rather small, 7.2 kcal·mol^{-1}, in line with the fast formation of the peroxo complex observed experimentally.[15,16] It is worth mentioning that in anhydrous conditions, or in low water concentration, the formation of hydroperoxo species **3a** could also occur *via* a 4–membered ring transition state (**TS2**) without the water–assisted H–transfer showing a smooth free–energy barrier of 15.3 kcal·mol^{-1} (see **Figure 7.6**). The free energy barriers for *trimolecular processes* were calculated considering the possible formation of a H_2O_2···H_2O or a H_2O···H_2O adduct as reactants of the overall process. The formation of a peroxide···water adduct was computed to be exothermic by 0.5 kcal·mol^{-1} from the individual molecules and thus, barriers involving these species were determined as $[\Delta G_{TS} - (\Delta G_{reactant} + \Delta G_{H_2O_2\cdots H_2O})]$. Conversely, the formation of a water dimer was estimated to be slightly endothermic (+0.7 kcal·mol^{-1}), in such a way that barriers involving water dimers were calculated as the difference in energy from the three separated reactants to the trimolecular TS.

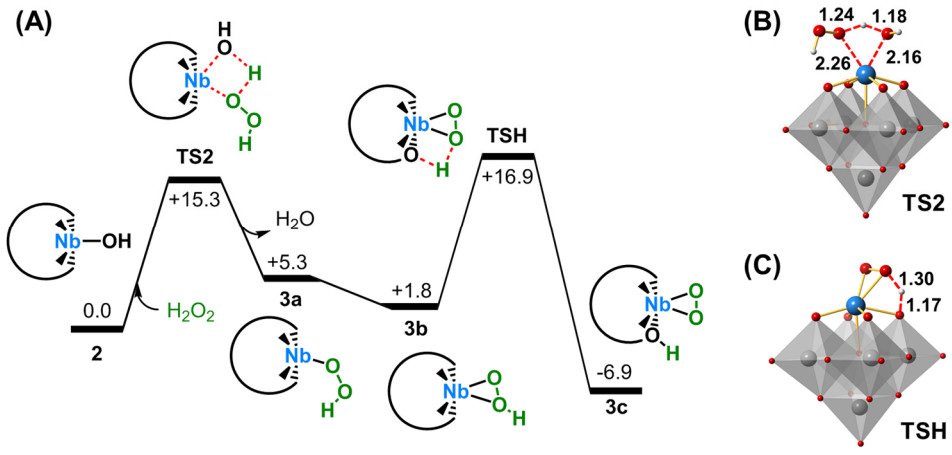

Figure 7.6 | (A) Gibbs free–energy profile (kcal·mol^{-1}) for an alternative water–free path to form the catalyst resting state **3c** from the active catalytic species **2**. (B) and (C) represent the DFT–optimized structures for the TSs involved in this process, in which main distances are shown in Å

The generated η^1–OOH species (**3a**) can evolve to the more stable η^2–OOH species **3b** because the size of the second–row Nb^V ion allows to accommodate 7–fold coordination. The η^2–hydroperoxo species **3b** is lower in energy (–3.5 kcal·mol^{-1}) than

the corresponding η^1–hydroperoxo **3a**, but higher in energy (+8.7 kcal·mol^{-1}) than the corresponding η^2–peroxo complex **3c** in agreement with experimental data (*vide supra*). Nb–peroxo complex **3c** can be formed from **3b** via water–assisted hydrogen transfer from the hydroperoxo moiety to a bridging W–O–Nb oxygen, overcoming a very smooth free–energy barrier (1.8 kcal·mol^{-1}, see **Figure 7.5**). The computed **TSH$_w$** (**Figure 7.7**) resulted lower in energy than the **3b** intermediate due to artificial overstabilization of the structure when adding the water molecule. Therefore, we computed the barrier from the **3b$_w$** adduct in which the interaction between **3b** and the water molecule is already established. As in the H_2O_2 activation step, this proton transfer could also occur without the assistance of water, although it would need to overcome a significantly higher free–energy barrier of 15.3 kcal·mol^{-1} (**3b** → **TSH** in **Figure 7.6**).

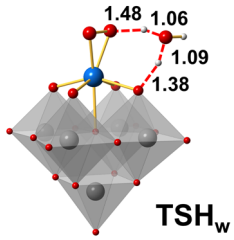

Figure 7.7 | DFT–optimized structures for **TSH$_w$** involved in the formation of the Nb–peroxo species **3c** from the hydroperoxo **3b**. Main distances are shown in Å.

The position of the proton at Nb–O–W in the structure of **3c** is thermodynamically favored relative to protonation at the W–O–W bridging oxygen and at the peroxo moiety by 3.0 and 8.7 kcal·mol^{-1}, respectively, as supported by spectroscopic techniques.[16] Specifically, the UV spectrum of H_2O_2–treated **1b** displayed a substantial red shift in the presence of 1 equivalent of acid (**Figure 7.8**A). The TD–DFT simulated spectrum for Nb–peroxo species $[Nb(O_2)W_5O_{18}]^{3-}$ (**4**) shows one peak centered around 305 nm, as shown in **Figure 7.8**B. The absorption arises from the HOMO to LUMO excitation, which has a π^*_{O-O}→d(M) nature. The protonation of **4** at the bridging Nb–O–W oxygen to give **3c** shifts the peak for π^*_{O-O}→d(M) excitation to 315 nm, reproducing nicely the experimental red shift and further supporting the experimental protonation of the catalyst. The molecular orbital analysis revealed that upon protonation at the POM framework the d–type orbitals of W suffer a larger stabilization than the π^*_{O-O}–type orbital of peroxo moiety reducing the energy gap (see **Figure 7.9**).

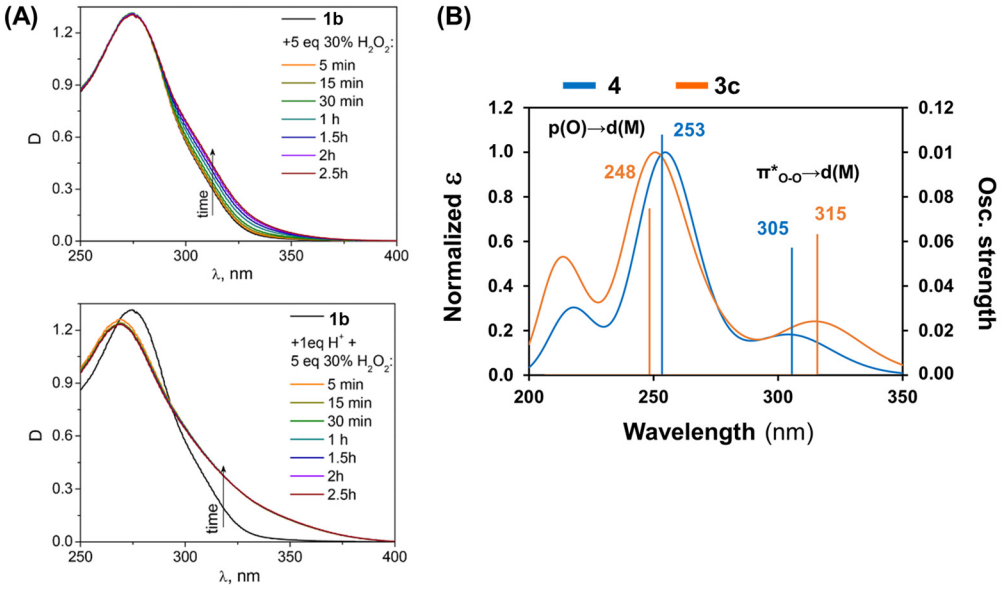

Figure 7.8 | (A) UV–vis spectra of $[Nb(O)W_5O_{18}]^{3-}$ (**1b**) after addition of 5 equiv. of H_2O_2. (top) or 1 equiv. of $HClO_4$ and 5 equiv. of H_2O_2 (down). Conditions: 0.0005 M **1b**, CH_3CN, 20°C.[16] (B) TD–DFT–simulated UV spectra for Nb–peroxo species $[Nb(O_2)W_5O_{18}]^{3-}$ (**4**, blue line) and its protonated partner $[HNb(O_2)W_5O_{18}]^{2-}$ (**3c**, orange line).

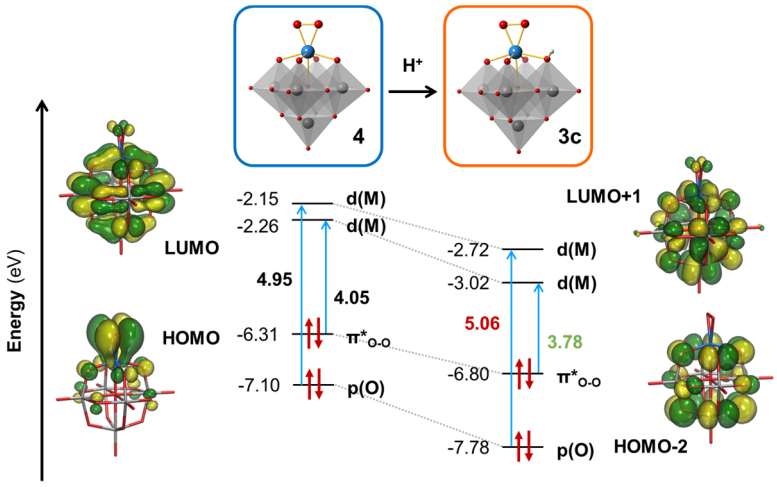

Figure 7.9 | Schematic MO diagram showing the main orbital interactions involved in the transitions that are highlighted in the spectra of **Figure 7.8**. Green and red colors for ΔE are used to show that the transition became less or more energetic, respectively, upon protonation. The trend in the energy differences can be directly related to the shearing of the bands in the spectrum in the presence of acid.

We have analyzed the heterolytic oxygen transfer to CyH from both side–on Nb–hydroperoxo (**3b**) and –peroxo (**3**) species. **Figure 7.10** collects the geometries of the reactants and the transition states, as well as the corresponding free energy barriers. The less stable hydroperoxo anion **3b** shows a lower free energy barrier than the peroxo anion **3c** (17.6 *vs* 27.1 kcal·mol^{-1}). In Nb–hydroperoxo species **3b**, the alkene attack occurs preferably at the proximal, non–protonated α–oxygen because the σ^*_{O-O} orbital is polarized toward O_α, favoring the donation from the nucleophilic double bond.[7] In this case, the transition state for β–oxygen transfer is 2.3 kcal·mol^{-1} higher than the corresponding transition state for α–oxygen transfer **TS3b**. Nevertheless, the β–oxygen transfer could be favored in complexes with metal ions in sterically hindered or strongly embedded in non–flexible environment that make the O_β more accessible to the substrate.[10]

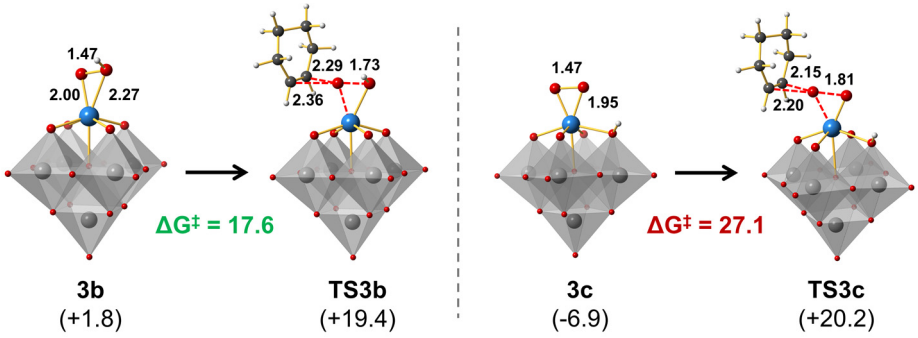

Figure 7.10 | Combined balls–and–sticks and polyhedral representation of some of the most relevant intermediates (**3b** and **3c**) and transition states (**TS3b** and **TS3c**) in reaction mechanism. Main distances are shown in Å. Free energy barriers for the electrophilic O–transfer step occurring from **3b** and **3c** are shown in kcal·mol^{-1}.

Another important feature of the potential free–energy profile (**Figure 7.5**) is the relative rates between the hydrogen and the oxygen transfer from **3b** to form the peroxo species **4** (**TSH$_w$**) and the epoxide (**TS3b**), respectively. The hydrogen transfer is computed to be much faster, and thus, it is reasonable to assume that most of the reacting species, reaching the Nb–hydroperoxo **3b** intermediate, evolve to the Nb–peroxo complex **3c**, which becomes the resting–state of the catalytic process. From Nb–peroxo species **3c**, the reaction can proceed directly to oxygen transfer to the alkene through **TS3c** structure, overcoming a computed free–energy barrier of 27.1 kcal·mol^{-1}, or it can go back to the less stable but more reactive Nb–hydroperoxo species **3b**, overcoming an overall free–energy barrier (**3c** → **TS3b**) of 26.3 kcal·mol^{-1}. In summary, our calculations

indicate that most of the reaction proceeds via heterolytic oxygen transfer from Nb–η^2–hydroperoxo species **3b**, involving a previous formation of protonated Nb–peroxo species **3c**, which acts as the resting–state of the process. However, other two energetically accessible paths might contribute to the formation of epoxides: (i) the direct oxygen transfer from **3b** without the formation of peroxo species **3c**, and (ii) the heterolytic oxygen transfer from the Nb–peroxo species **3c**. Besides the limitations of the methodology described in Computational Details section, the computed relative rates of reaction paths could be influenced by a counteraction (TBA^+, tetrabutylammonium) effect. Recently, atomistic molecular dynamics simulations on TBA–POM salt in a water–acetonitrile mixture showed that the hydrophobic TBA counter cations are tightly attached to anionic POMs repelling the water molecules around the TBA–POM ion pairs.[36] This effect could slow down the water–assisted H–transfer in hydroperoxo **3b** to form peroxo complex **3c**, favoring the direct oxygen transfer to alkene from **3b**.

To further validate our proposed mechanism, we analyzed the zero–point corrected energy profile (**Figure 7.11**) for CyOct epoxidation by **2** and compared it with the experimental E_a (11.7 ± 0.8 kcal·mol^{-1}) in **Figure 7.2**. In the absence of entropic effects, the computed overall energy barrier for direct oxygen transfer from hydroperoxo species **3b** is 5.8 kcal·mol^{-1} (too low) while those involving the formation of peroxo species **3c** are about 16 kcal·mol^{-1} (too high). However, assuming that several paths contribute to the reaction, the weighted average of the computed energy barriers should be close to experimental E_a value. It is worth mentioning that during the preparation of this thesis, we revisited the ZPE–corrected energy barrier from **3c** to **TS3b** with a more extended basis set, 6–311+(d,p) for main group atoms and LANL2TZ(f) for Nb, and found a value of 10.9 kcal·mol^{-1}, which is in better agreement with the experimental E_a of 11.7. This suggests that besides the contribution of multiple paths, the use of larger basis sets might improve the accuracy of the results.

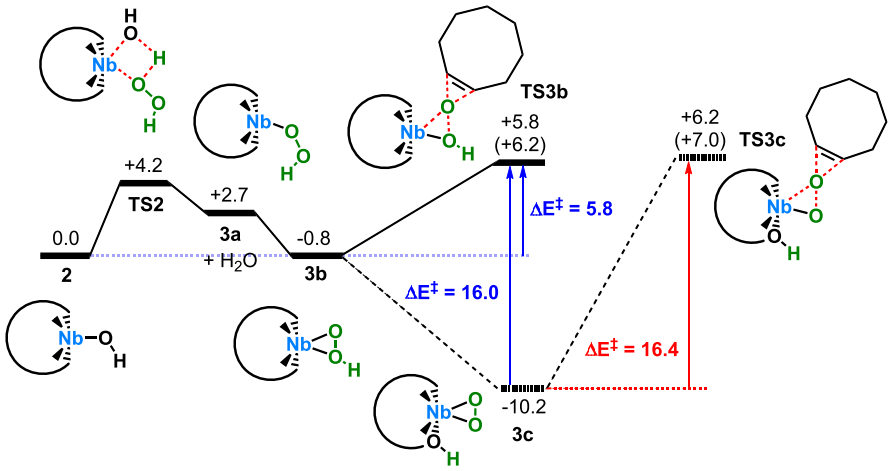

Figure 7.11 | Calculated zero–point corrected energy profile (kcal·mol^{-1}) for the epoxidation of cyclooctene (CyOct) and cyclohexene (CyH) in parenthesis with H_2O_2 catalyzed by **2**.

Next, to understand the role of protons on the reactivity, we evaluated feasibility of the epoxidation process using the non–protonated peroxo species $[Nb(O_2)W_5O_{18}]^{3-}$ **4**. The free–energy barrier for the oxygen transfer from **4** to CyH was computed to be 31.6 kcal·mol^{-1}, which is larger than that for the epoxidation by protonated peroxo species **3c**, 26.3 kcal·mol^{-1} (from **3c** to **TS3b**). This is consistent with lack of reactivity observed over species **4**. Moreover, the free–energy barrier for H_2O_2 activation by the non–protonated species **2** is ~4 kcal·mol^{-1} higher than that from the protonated species **3**. Thus, protonation has two important consequences in the catalytic performance of Nb–substituted anions: (i) it allows forming the more reactive Nb–hydroperoxo species, and (ii) it reduces the overall negative charge of the POM favoring the electrophilic oxygen transfer to the alkene as observed also for Ti–substituted POMs.[9]

7.3.2 Influence of the metal ion in the reaction mechanism.

A previous study on the effect of the metal nature on the oxygen transfer mechanism showed that when we move from Ti down and across to Nb in the periodic table, both peroxo and hydroperoxo energy barriers decrease, but the latter does it more appreciably.[7] However, in order to obtain a complete picture of the reaction, one should also evaluate the effect of the larger radius of Nb^V ion on the stabilization of 7–coordinated species such as η^2–peroxo and η^2–hydroperoxo ones. Here, we performed a detailed comparison of the free–energy landscape for Nb– and Ti–based catalysts on the heterolytic epoxidation of

alkenes, using $[(CH_3O)NbW_5O_{18}]^{2-}$ (**1a^{Nb}**) and $[(CH_3O)TiW_5O_{18}]^{3-}$ (**1a^{Ti}**) complexes (see **Figure 7.3**), and CyH substrate. As in the previous section, we have considered three different reaction paths for the electrophilic oxygen transfer to the CyH substrate, namely, the oxygen transfer from the peroxo ligand, and the α– and β–oxygen transfer from the hydroperoxo moiety (see **Scheme 7.2**).

Scheme 7.2 | Possible pathways for oxygen transfer to CyH from peroxo and hydroperoxo species in transition metal–substituted polyoxometalates. Overall free energy barriers for all paths are shown in kcal·mol^{-1}, highlighted in green the most likely mechanism for each metal.

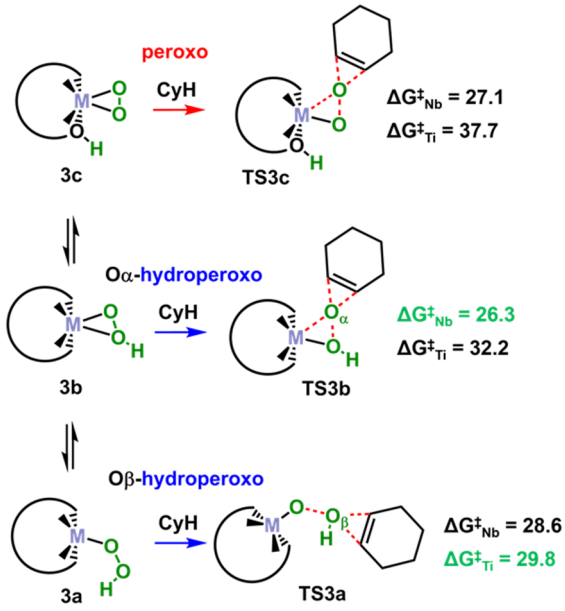

Figure 7.12 compares the computed free–energy profiles for the most favorable heterolytic pathways in which the transition metal–hydroxo species $[(HO)MW_5O_{18}]^{n-}$ (M = Nb and Ti), **2^{Nb}** and **2^{Ti}**, act as catalysts. As for Nb, the methoxy precursor **1a^{Ti}** is slightly more stable than **2^{Ti}** (by 2.1 kcal·mol^{-1}) and can generate the catalytically active species **2^{Ti}** overcoming a moderate free energy barrier of 23.0 kcal·mol^{-1} (*vs* 12.2 for Nb). After that, the interaction of **2^{Ti}** with H_2O_2 gives access to the $[(\eta^1\text{–HOO})TiW_5O_{18}]^{3-}$ hydroperoxo species **3a^{Ti}** releasing a water molecule. In agreement with kinetic experiments,[15] this process was computed to be faster for Nb than for Ti species, $\Delta G^{\ddagger}$(**2** → **TS2$_w$**) = 7.2 and 15.5 kcal·mol^{-1}, respectively (see **Figure 7.12**). This fact was ascribed to the larger radius of Nb that affords a 7–fold coordination in the transition state geometry

more readily than Ti. The same effect might explain the faster hydrolysis of the methoxy precursor (**1a** → **2**) observed for Nb as compared to Ti.

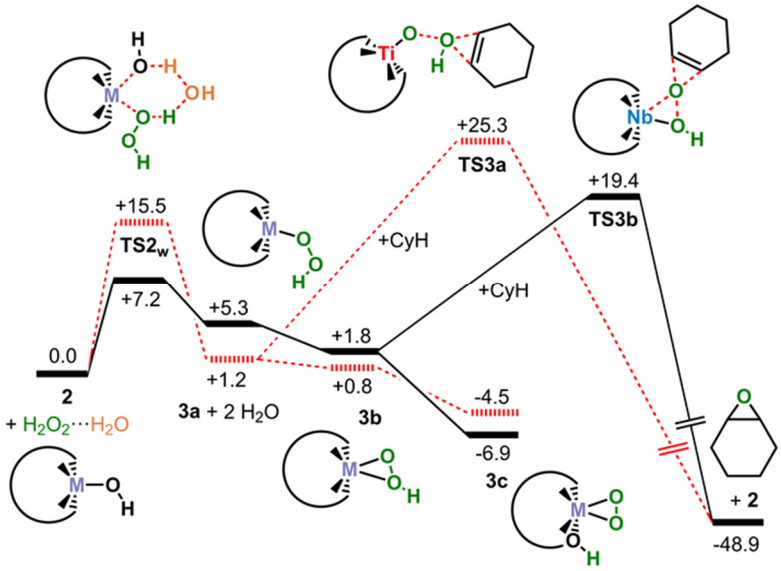

Figure 7.12 | Calculated potential free–energy profile (kcal·mol^{-1}) for CyH epoxidation with H_2O_2 by $[(CH_3O)NbW_5O_{18}]^{2-}$ (**1a^{Nb}**) anion (solid black lines) and $[(CH_3O)TiW_5O_{18}]^{3-}$ (**1a^{Ti}**) anion (dashed red lines).

The generation of hydroperoxo species **3a** is somewhat endergonic (+5.3 and +1.2 kcal·mol^{-1} for Nb and Ti, respectively). However, **3a** can evolve to the corresponding η^2–hydroperoxo species $[(\eta^2\text{–HOO})MW_5O_{18}]^{n-}$ (**3b**), and then to the protonated peroxo complex $[(\eta^2\text{–}O_2)MW_5O_{18}H]^{n-}$ (**3c**). This sequential process is downhill in energy for both metals, resulting in an overall exergonic process where the peroxo complex **3c** lies below the reactants by 6.9 and 4.5 kcal·mol^{-1} for Nb and Ti, respectively. This is consistent with the successful isolation of peroxo complexes by treatment of hydroxo and methoxo species with H_2O_2.[15] For Nb we had found that the most favorable pathway proceeds via α–oxygen transfer to CyH from Nb–η^2–hydroperoxo species **3b^{Nb}** involving prior formation of Nb–peroxo species **3c^{Nb}** and resulting in an overall free–energy barrier (**3c^{Nb}** → **TS3b^{Nb}**) of 26.3 kcal·mol^{-1}.[16] As anticipated in **Scheme 7.2**, in the case of Ti–substituted Lindqvist anion, the β–oxygen transfer pathway (**3c^{Ti}** → **TS3a^{Ti}**) becomes energetically favored over the α–oxygen hydroperoxo (**3c^{Ti}** → **TS3b^{Ti}**) and the peroxo (**3c^{Ti}** → **TS3c^{Ti}**) paths by 2.2 and 7.7 kcal·mol^{-1}, respectively. Although the O_α is more electrophilic than the O_β, it has been demonstrated that when the metal ion is sterically

hindered or found in a highly rigid environment (i.e., reluctant to increase its coordination number), the β–oxygen transfer can prevail over the α–oxygen pathway.[10] More interestingly, on going from Nb– to Ti–substituted catalyst the overall free–energy barrier for heterolytic oxygen transfer increases by 3.5 kcal·mol^{-1} in agreement with the conversion values reported in **Table 7.1**. **Figure 7.13** compares the key transition–state structures and the free–energy barriers for the epoxidation process by Nb– and Ti–substituted catalysts. Decreasing the formal oxidation state of the metal from Nb^{V} to Ti^{IV}, we expect a lower electrophilicity of the M–η^2–OOH moiety towards the attack of the nucleophilic alkene.[9] The metal charge effect is manifested in a higher energy of the σ^*_{O-O} orbitals in Ti–η^2–hydroperoxo complex (+0.64 and +1.73 eV for Nb and Ti, respectively), and in a larger free–energy barrier for the α–oxygen transfer ($\mathbf{\Delta G^{\ddagger}(3b \rightarrow TS3b)}$ = 17.6 *vs.* 26.9 kcal·mol^{-1} for Nb and Ti, respectively). Thus, we can explain the higher activity of Nb catalyst and the preference for the β–oxygen transfer path of Ti catalyst. Furthermore, the differences in oxygen transfer mechanisms can be related to the different regioselectivities observed in H_2O_2–based epoxidation of some alkenes such limonene over Ti– and Nb–silicates.[13a,14a,15] Thus, the β–oxygen transfer from Ti(η^1–OOH) would favor the epoxidation of the more nucleophilic, internal C=C bond in limonene whereas the α–oxygen transfer from Nb(η^2–OOH) would result in epoxidation of the less sterically hindered, external C=C–bond.

Again, to validate the mechanistic proposal, we compared the Arrhenius activation energies for CyOct epoxidation over the $\mathbf{1a^{Nb}}$ catalyst (11.7 kcal·mol^{-1}) and $\mathbf{1a^{Ti}}$ (14.3 kcal·mol^{-1}) with computed zero–point corrected energies.[16] For Nb, we observed that the α–oxygen transfer from hydroperoxo species $\mathbf{3b^{Nb}}$ entails an overall barrier of 16 kcal·mol^{-1} from peroxo species $\mathbf{3c^{Nb}}$, whereas in the case of the Ti catalyst the barrier for the most likely process ($\mathbf{3c^{Ti} \rightarrow TS3a^{Ti}}$) accounts for 20 kcal·mol^{-1}. The values obtained for these processes with a larger basis set (6–311G+(d,p) for main group atoms and LANL2TZ(f) for active metal ions) are 10.9 and 13.3, respectively, which are much closer to the experimental E_a. Thus, despite the methodological limitations, calculations are able to reproduce the increase of experimental E_a upon replacement of the metal.

As shown below and as anticipated by experimental results, the nature of the metal ion has also an important influence on the product selectivity.

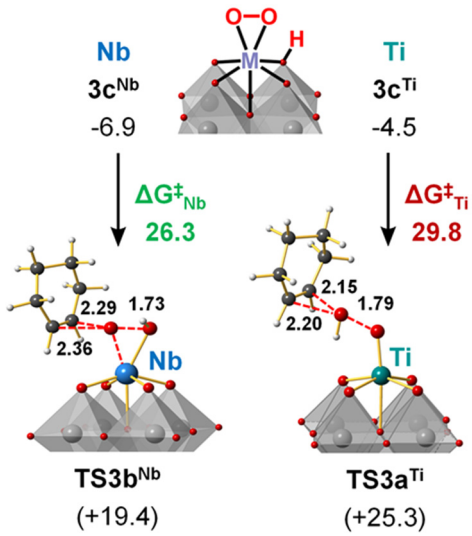

Figure 7.13 | Computed structures of the most favorable transition states for heterolytic oxygen transfer to CyH (α–oxygen for Nb, **TS3b^{Nb}** and β–oxygen for Ti, **TS3a^{Ti}**) Relative free–energies and free–energy barriers in kcal·mol^{-1}, and distances in Å.

7.3.3 Influence of the ligand environment in reactivity.

7.3.3.1 Effect of polyoxometalate framework in Nb–POMs catalysts: electrophilicity vs. basicity.

As commented above, aside from several Nb–substituted anions of Lindqvist structure, the catalytic activity of the Nb–substituted Keggin anion was also explored experimentally. Unlike its Lindqvist counterpart, the Keggin–based catalyst displayed a poor performance in alkene epoxidation regardless the presence or absence of acid.[16] Aiming to rationalize these experimental results, we analyzed computationally the features and catalytic activity of $[PW_{11}O_{39}Nb(O_2)]^{4-}$ (**4K^{Nb}**) and $[HPW_{11}O_{39}Nb(O_2)]^{3-}$ (**3cK^{Nb}**). Two main trends are observed in **Table 7.2**, which collects the computed protonation energies (ΔG_{H+}) and the free–energy barriers for oxygen transfer ($\Delta G^{\ddagger}_{Otrans}$) through peroxo (**4^{Nb}**/**4K^{Nb}** → **TS4^{Nb}**/**TS4K^{Nb}**) and hydroperoxo (**3c^{Nb}**/**3cK^{Nb}** → **TS3b^{Nb}**/**TS3bK^{Nb}**) paths. First, ongoing from Lindqvist to Keggin anion the charge density decreases as reflected in the total charge per metal ratio (q/M).[31,37] Consequently, the POM becomes better electrophile favoring the oxygen transfer to the nucleophilic alkene by ~2 kcal·mol^{-1}.[9] Second, the less basic Keggin anion is more difficult to protonate resulting in an endergonic process according to our calculations (+2.7 kcal·mol^{-1} for **4K^{Nb}**

+ $1H^+ \rightarrow$ **3cK^{Nb}**). Thus, although Keggin structures are more reactive as oxygen transfer agents than Lindqvist ones, they are more difficult to be activated via protonation. Overall, these opposite trends might result in a loose of reactivity for Keggin structures. In summary, for the alkene epoxidation by Nb–substituted POMs the art consists of tuning the charge density of the anion. The POM should have low electron density in order to favor the electrophilic oxygen transfer to alkenes, but be basic enough to be protonated and enable the hydroperoxo path.

Table 7.2 | Calculated protonation energies (ΔG_{H+}) and energy barriers for oxygen transfer (ΔG_{Otrans}) from Lindqvist (**4^{Nb}** and **3c^{Nb}**) and Keggin (**4K^{Nb}** and **4cK^{Nb}**) anions in kcal·mol^{-1}.

catalyst	ΔG_{H+}	Active species	*q/M*	$\Delta G^{\ddagger}_{Otrans}$
4^{Nb}	–	**4^{Nb}**	0.50	31.6
4K^{Nb}	–	**4K^{Nb}**	0.33	29.6
4^{Nb} + $1H^+$	−3.7	**3c^{Nb}**	0.33	26.3[a]
4K^{Nb} + $1H^+$	+2.7	**3cK^{Nb}**	0.25	23.8[a]

[a] Free–energy barriers through hydroperoxo path.

7.3.3.2 Hybrid organic–inorganic Ti–containing catalysts.

7.3.3.2.1 Inner– vs. outer–sphere electrophilic oxygen transfer.

Unlike the fully inorganic metal–substituted POMs discussed in previous sections, the Ti center in **1^{TiW9}** is coordinated by more labile organic silanol groups in a tetrahedral fashion (see **Figure 7.3**), allowing the selective epoxidation of electron–rich allylic alcohols with H_2O_2 at room temperature.[4] To investigate the role of the ligand nature and the reasons for the observed selectivity, we analyzed computationally the mechanism responsible for the epoxidation of allylic alcohols with H_2O_2 catalyzed by **1^{TiW9}**. As a representative substrate, we selected the experimentally tested 3–methyl–2–buten–1–ol, which showed significant conversions and selectivity towards the epoxide product. In addition to previously characterized mechanisms (*i* and *ii* in **Scheme 7.3**), we explored two novel reaction pathways (*iii* and *iv*) specific for allylic alcohols that are highlighted in green in **Scheme 7.3**.

Scheme 7.3 | Possible mechanisms for alkene epoxidation with H_2O_2 catalyzed by Ti–containing silanol–decorated polyoxotungstates.

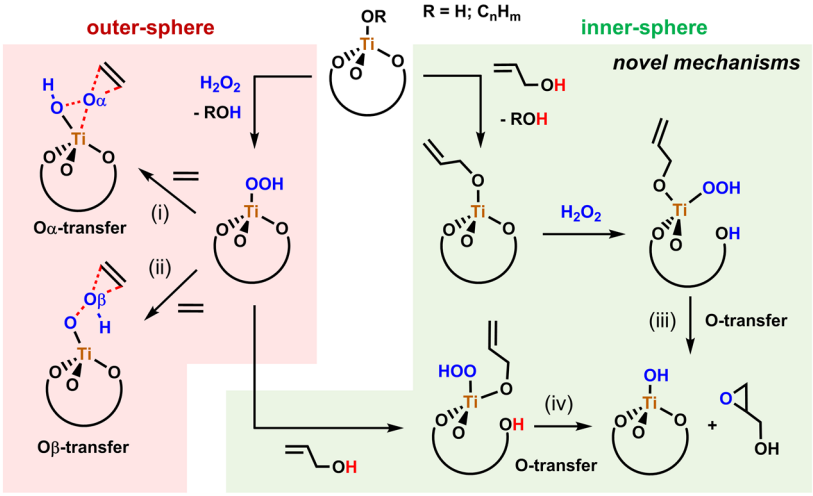

Figure 7.14 shows the free–energy profile for the epoxidation of 3–methyl–2–buten–1–ol with H_2O_2 by the active catalytically species $\mathbf{2}^{\mathbf{TiW9}}$. After the formation of $\mathbf{2}^{\mathbf{TiW9}}$, this can interconvert to the more stable species $\mathbf{2b}^{\mathbf{TiW9}}$ through a smooth free–energy barrier of 11.0 kcal·mol^{-1}. In agreement with the NMR monitoring of the reaction,[4] which suggests that a Ti–alcoholate complex is the catalyst resting–state, we found that complex $\mathbf{2b}^{\mathbf{TiW9}}$ is the most stable species in the reaction medium *prior* to epoxidation (see **Figure 7.14**). From $\mathbf{2b}^{\mathbf{TiW9}}$, we can envisage two paths to incorporate the hydroperoxide moiety in the catalyst structure. A first one involves going back to the Ti–hydroxo species $\mathbf{2}^{\mathbf{TiW9}}$, which can react with H_2O_2 via water–mediated substitution mechanism to give species $\mathbf{3b}^{\mathbf{TiW9}}$ through a free energy barrier of 15.3 kcal·mol^{-1} (from $\mathbf{2b}^{\mathbf{TiW9}}$ to $\mathbf{TS}_{\mathbf{2b-3b}}{}^{\mathbf{TiW9}}$). Note that the direct conversion of $\mathbf{2b}^{\mathbf{TiW9}}$ into $\mathbf{3b}^{\mathbf{TiW9}}$ could also occur overcoming a higher but still accessible barrier of 17.9 kcal·mol^{-1}. Alternatively, H_2O_2 can coordinate the Ti center through a dissociative addition to one of the Ti—OSi bonds that connect the active metal ion with the silanol functions anchored to the POT framework. In this process, the coordination of the OOH group to the Ti center is concomitant with the proton transfer to the silanol oxygen yielding complex $\mathbf{3d}^{\mathbf{TiW9}}$ (see **Figure 7.15**). The hydroperoxide ligand in $\mathbf{3b}^{\mathbf{TiW9}}$ and $\mathbf{3d}^{\mathbf{TiW9}}$ coordinates in a η^2 fashion resulting in five–coordinated complexes similar to those reported recently in a computational study of TS–1 zeolite catalyst.[38]

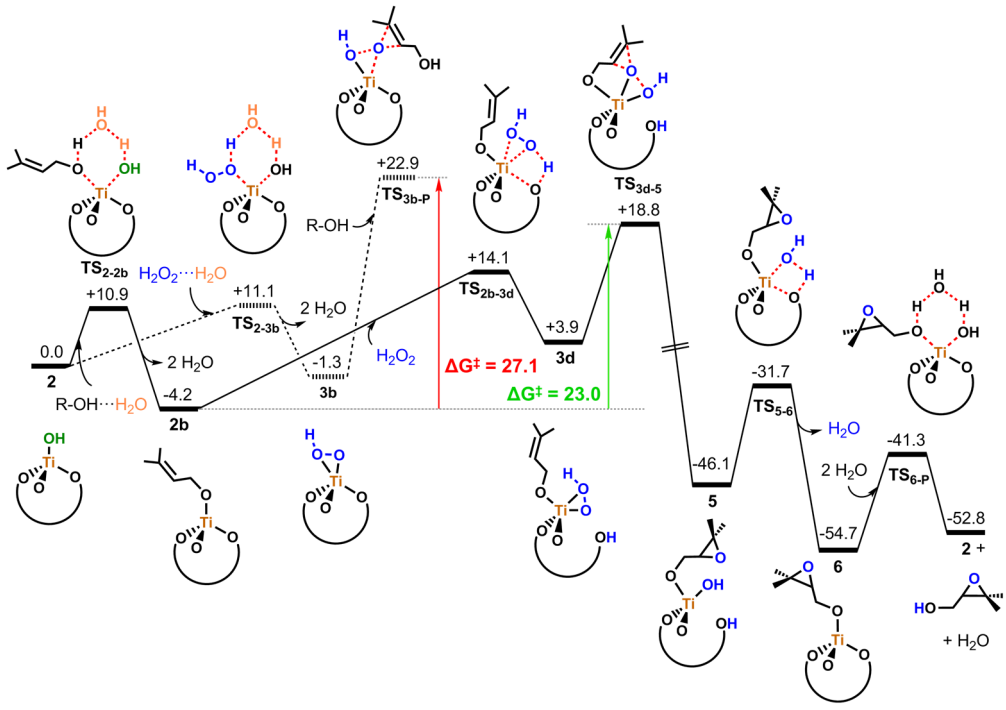

Figure 7.14 | Calculated Gibbs free–energy profile (kcal·mol^{-1}) for the epoxidation of 3–methyl–2–buten–1–ol by H_2O_2 over the $[\alpha$–B–$SbW_9O_{33}(^tBuSiO)_3Ti(OH)]^{3-}$ catalyst (**2**^{TiW9}). R–OH stands for 1–methyl–2–buten–1–ol. Dashed lines represent the more energy demanding outer–sphere path. The "TiW9" superscript in the labels of the species has been omitted for clarity.

Both species **3b**^{TiW9} and **3d**^{TiW9} contain a Ti–hydroperoxo moiety which can transfer an electrophilic oxygen to the double bond following respectively an *outer–sphere* or an *inner–sphere* mechanism (**Scheme 7.3**). Importantly, in the latter the alcohol group of the substrate plays an explicit role allowing its coordination to the Ti center. The activation of H_2O_2 by **2b**^{TiW9} via scission of one of the Ti—OSi junctions (**TS$_{2b-3d}$**^{TiW9} in **Figure 7.15**) causes a partial detachment of the Ti from the support, lengthening the Sb···Ti distance from 3.90 Å in **2b**^{TiW9} to 4.15 Å in **TS$_{2b-3d}$**^{TiW9} and up to 4.42 Å in the structure of the resulting in alkoxy–hydroxo intermediate **3d**^{TiW9}. Then, the electrophilic oxygen of the hydroperoxo ligand transfers intramolecularly to the electron–rich double bond of the substrate through **TS$_{3d-5}$**^{TiW9} (**Figure 7.15**) overcoming a moderate energy barrier of 14.9 kcal·mol^{-1}. This kind of TS structure was also proposed for the bimetallic titanium–based catalyst used in the Sharpless epoxidation.[39–42] For the sake of comparison, we analyzed the energy cost of transferring the less electrophilic O_β. In this case, transferring O_α is

favored by 9.0 kcal·mol^{-1}, indicating that in dichelate complex **3d**^{TiW9} the Ti is found in a non–rigid coordination environment.

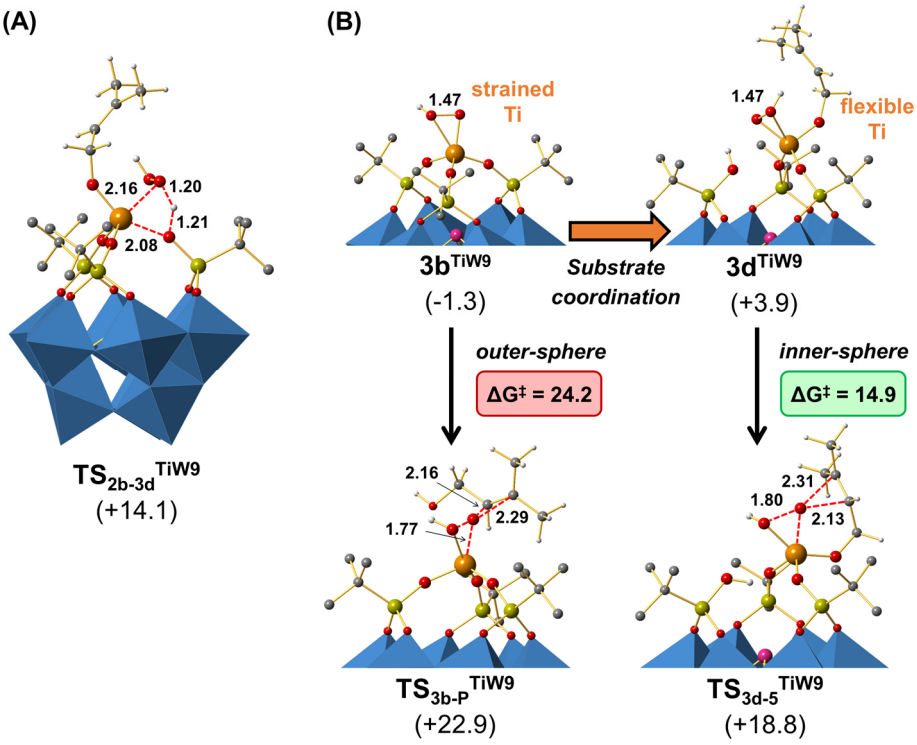

Figure 7.15 | DFT–optimized structures for **TS**$_{2b-3d}^{TiW9}$ (A), intermediates **3b**^{TiW9} and **3d**^{TiW9} and the TSs associated to the outer– and the inner–sphere electrophilic O–transfer to the alkene (**TS**$_{3b-P}^{TiW9}$ and **TS**$_{3d-5}^{TiW9}$, respectively) (B). Relative free energies and free–energy barriers are shown in kcal·mol^{-1}. Red dashed lines represent those bonds being formed or broken in the TS structure. Main distances are shown in Å. Hydrogen atoms of ^{t}Bu groups have been omitted for clarity.

We also examined the *outer–sphere* O–transfer mechanism, which is directly compared to the *inner–sphere* one in **Figure 7.15**. Akin to the inner–sphere paths, the Ti–hydroperoxo complex **3b**^{TiW9} is more prone to transfer the α–oxygen to an approaching alkene rather than the β one, although the difference in energy between paths is small ($\Delta\Delta G^{\ddagger} < 1$ kcal·mol^{-1}). The corresponding TS (**TS**$_{3b-P}^{TiW9}$ in **Figure 7.15**) was found to be 4.1 kcal·mol^{-1} higher in energy than the TS associated to the inner–sphere O–transfer (**TS**$_{3d-5}^{TiW9}$), indicating that the O–transfer step is more likely to proceed via inner–sphere mechanism. Moreover, we analyzed the outer–sphere O–transfer occurring from the Ti–hydroxo–hydroperoxo intermediate in which one of the Ti—OSi bonds is

cleft by the addition of H_2O_2 to $\mathbf{2}^{TiW9}$. The TS for this alternative path is even more unstable than $\mathbf{TS_{3b-P}}^{TiW9}$ (29.4 vs. 23.0 kcal·mol^{-1}) and therefore, this possibility was ruled out.

After the O–transfer to the alkene, the formation of intermediate $\mathbf{5}^{TiW9}$ confers the reaction a strongly irreversible character, the reverse barrier being higher than 60 kcal·mol^{-1}. Next, the initial tris–silanol coordination environment around Ti is regenerated through a condensation of the Ti–OH group and the silanol function in $\mathbf{5}^{TiW9}$ to release a water molecule and complex $\mathbf{6}^{TiW9}$. Finally, protonation of the alkoxy ligand by a water molecule via $\mathbf{TS_{6-P}}^{TiW9}$ releases the epoxide product and regenerates the active Ti–hydroxo species $\mathbf{2}^{TiW9}$ closing the catalytic cycle. The free–energy barriers for these steps are 14.4 and 13.4 kcal·mol^{-1}, respectively (see **Figure 7.14**), and TS and intermediate structures are shown in **Figure 7.16**. Note that albeit intermediate $\mathbf{6}^{TiW9}$ is slightly more stable than $\mathbf{2}^{TiW9}$, the latter can evolve to species $\mathbf{2b}^{TiW9}$ after coordinating a substrate molecule, which is about 2 kcal·mol^{-1} more stable than $\mathbf{6}^{TiW9}$. We also analyzed if intermediate $\mathbf{6}^{TiW9}$ could interact with the allylic alcohol or H_2O_2 rather than with H_2O, to give directly intermediate $\mathbf{2b}^{TiW9}$ or $\mathbf{3b}^{TiW9}$. The corresponding TSs were found to be higher in energy than $\mathbf{TS_{6-P}}^{TiW9}$ by 4.5 and 5.9 kcal·mol^{-1}, respectively.

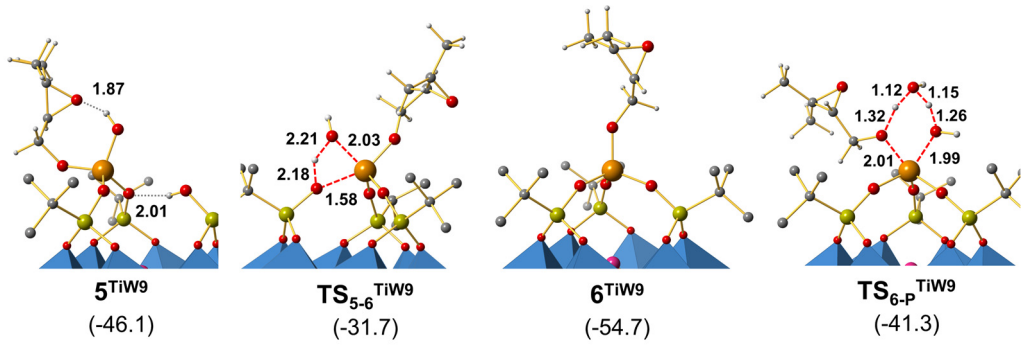

Figure 7.16 | Transition state and intermediate structures for releasing the epoxide product to regenerate the Ti–OH species. Hydrogen atoms in ^{t}Bu substituents of the silanol functions are omitted for clarity. Main distances are shown in Å and relative free energies are given in kcal·mol^{-1}.

The combination of the *H_2O_2 activation* and the *O–transfer steps* from the Ti–alcoholate $\mathbf{2b}^{TiW9}$ was identified to be the rate–limiting process of the whole catalytic cycle. Thus, the computed overall free energy barrier for the epoxidation of 3–methyl–2–buten–1–ol, $\Delta G^{\ddagger}(\mathbf{2b}^{TiW9} \rightarrow \mathbf{TS_{3d-5}}^{TiW9})$, is 23.0 kcal·mol^{-1} (highlighted with a green arrow in **Figure 7.14**). This value is in excellent agreement with the experimental value of 22.3 extracted

from the experimental rate constant.[4] Furthermore, the nature of the rate determining steps is also consistent with kinetic experiments that indicated a first order on H_2O_2 concentration and a pseudo–zero order dependence on alkene concentration, further validating our mechanistic proposal.

Moreover, the clear preference for the inner–sphere path might explain the higher conversions reported for allylic alcohols compared to non–functionalized alkenes,[4] for which only the more energetic outer–sphere path is accessible as they lack the alcohol functionality in the substrate. For the allylic alkene, the overall free–energy barrier of the outer–sphere mechanism without formation of intermediate **3d^{TiW9}** would become 24.2 kcal·mol^{-1}, still 1.2 kcal·mol^{-1} higher than the inner–sphere mechanism ($\Delta G^{\ddagger}_{overall}$ = 23.0 kcal·mol^{-1}). For the non–functionalized 2–methyl–2–pentene substrate, the computed free energy barrier is rather high (28.7 kcal·mol^{-1}) in agreement with the experimentally reported low yields. However, note that the higher barrier must not only be attributed to the outer–sphere mechanism, but also to the intrinsic features (electronic and steric) of the alkene.

7.3.3.2.2 Factors influencing reactivity.

Previous computational studies on Ti–epoxidation[7,11,43] suggest that the smoother barriers in the inner–sphere path can be ascribed to the higher flexibility of the Ti center after releasing the strain imposed by one of the Ti—OSi bonds, as illustrated in **Figure 7.15**. Thus, in the transition state for O–transfer **TS$_{3d-5}^{TiW9}$**, the flexibility of Ti center accommodates easily the 5–fold trigonal bipyramidal coordination that stabilizes the structure, while in **TS$_{3b-P}^{TiW9}$** the Ti coordination is closer to distorted square–based pyramid (see **Figure 7.15**). We have also examined other possible factors explaining the differences between the inner– and the outer–sphere mechanisms, and in turn, the origin of the catalytic activity for these hybrid POTs. **Table 7.3** summarizes the results of the analysis of the electronic and steric features of **3b^{TiW9}** and **3d^{TiW9}** as epoxidizing species for the outer– and the inner–sphere mechanisms, respectively. The analysis of electronic effects via natural population analysis (NPA) does not show dramatic differences between the two paths, even if there is a tendency to favor the outer sphere mechanism. Upon substrate coordination to Ti via allylic oxygen the $\pi_{C=C}$ orbital of the substrate becomes slightly deeper in energy (less nucleophile) and the σ^*_{O-O} of the hydroperoxide group, which receives alkene attack, becomes slightly higher in energy (less electrophile) as shown in **Table 7.3**. To evaluate the impact of steric effects on reactivity, we computed

the overall free–energy barriers for both paths ($\mathbf{3b^{TiW9}} \rightarrow \mathbf{TS_{3b-P}^{TiW9}}$ and $\mathbf{3b^{TiW9}} \rightarrow \mathbf{TS_{3d-5}^{TiW9}}$) substituting the ^{t}Bu groups in the silanol functions by less bulky methyl groups. We observed that both barriers are decreased to almost the same extent in going from ^{t}Bu to Me ($\Delta\Delta G^{\ddagger}$ of 6.6 and 6.5 kcal·mol^{-1}, respectively) as shown in **Figure 7.17**. Thus, steric effects have a similar overall influence in both mechanisms although they act at different stages of the overall process (**Figure 7.17**): the oxygen transfer step for outer–sphere mechanism ($\mathbf{3b^{TiW9}} \rightarrow \mathbf{TS_{3b-P}^{TiW9}}$) and the formation of hydroperoxo species for the inner–sphere ($\mathbf{2b^{TiW9}} \rightarrow \mathbf{3d^{TiW9}}$). More importantly, reducing steric bulkiness around the Ti has a significant effect on the overall free–energy barrier, which might lead to the design of more active catalysts (see **Table 7.3**). In this regard, a combined experimental and theoretical work aimed to the rational design of catalytic species with tailored steric properties is under way.

Table 7.3 | Main parameters that control electronic and steric factors in the O–transfer step from epoxidizing species $\mathbf{3b^{TiW9}}$ and $\mathbf{3d^{TiW9}}$.[a]

Species (*path*)	$E(\pi_{C=C})$	$E(\sigma^*_{O-O})$	$\Delta G^{\ddagger}$**(overall)**		$\Delta\Delta G^{\ddagger}_{Otrans}$
			^{t}BuSi	**MeSi**	
$\mathbf{3b^{TiW9}}$ (*outer*)	−6.83	+0.33	24.2	19.2	5.0
$\mathbf{3d^{TiW9}}$ (*inner*)	−6.97	+0.54	13.4	12.1	1.3

[a]Orbital energies (in eV) obtained from Natural Bond Orbital (NBO) analysis; free energies in kcal·mol^{-1}.

Overall, we found that in the inner–sphere mechanism the energy penalty associated with breaking a Ti—OSi is largely compensated by the release in the geometrical strain around the Ti center which lowers the energy of the transition state for oxygen transfer. Furthermore, this effect might explain the higher catalytic activity reported for the heterogeneous TS–1 catalyst in the presence of protic alcohol solvents. The role of the solvent in the alkene epoxidation over TS–1 has been a matter of debate during years. Some authors proposed that the nature of the solvent only affects the adsorption/desorption equilibrium of the substrates.[44–47] Some other authors claimed that alcohol solvent molecules play an active role in the catalytic cycle,[48,49] loosely coordinating the tetrahedral Ti center and stabilizing the Ti(η^1–OOH) intermediate by forming a 5–membered ring that involves a hydrogen bond between the alcohol proton and the O_β

of the hydroperoxide. This, together with an increase of the ligand electrophilicity by induction effects, was hypothesized to accelerate the epoxidation reaction.[49] Now, our calculations strongly suggest that instead of that, the enhanced reactivity when using alcoholic solvents might come from their ability to cleave Ti—OSi junctions *to release strain* around the Ti center.

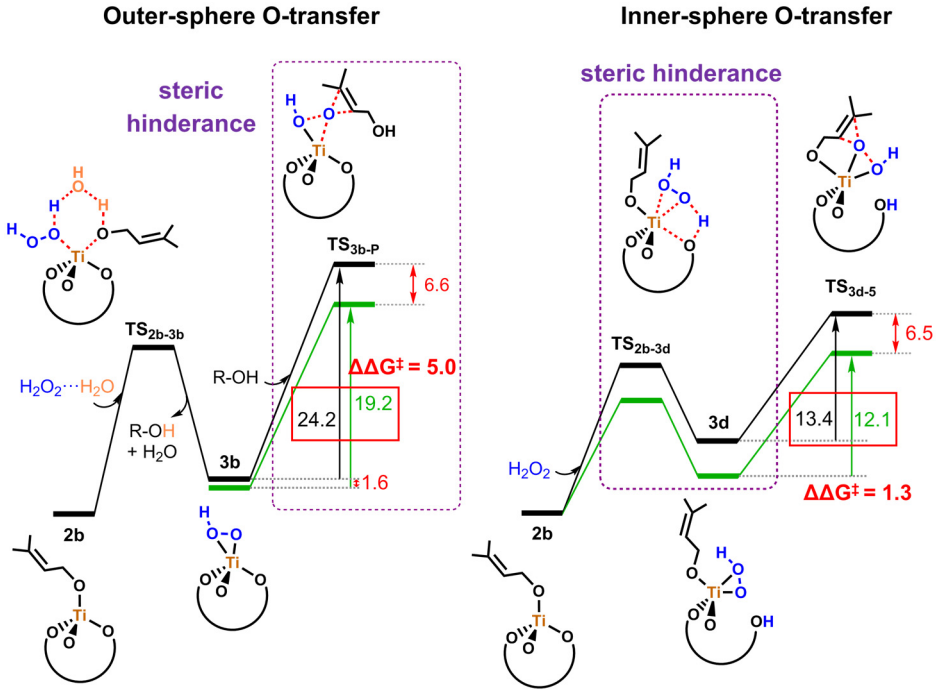

Figure 7.17 | Pictorial free–energy profiles for the outer– and inner–sphere O–transfer showing the influence of the steric bulkiness of the substituents in the silanol functions on the reaction mechanism. The step being more strongly affected by steric effects is highlighted and key energy differences are shown in kcal·mol^{-1}. Solid black lines represent the reaction profile on the sterically hindered catalyst with ^{t}Bu groups, while green ones describe the reaction profile resulting from replacing the ^{t}Bu by smaller methyl groups. The "TiW9" superscript in the labels of the species has been omitted for clarity.

Further supporting the ability of the $\{\alpha$–B–$SbW_9O_{33}(^{t}BuSiOH)_3\}$ to mimic the metal environment of single–site silica–supported catalysts, the same scaffold was successfully used to isolate a low–valent V^{III} species.[6] This species corresponds to the oxygen vacancy intermediate formed in Mars–van Krevelen–type oxidations occurring on silica–supported catalysts. In addition, as in the heterogeneous system, the V^{V}=O complex is formed upon reacting the V^{III} derivative with molecular oxygen. In fact, we participated in a combined experimental and theoretical work[6] devoted to analyze the electronic

structure and electrochemical stability of the V^{III} complex as well as the electrophotochemical properties of its V^{V}–oxo partner.

7.3.4 Mechanistic study on the H_2O_2 decomposition side reaction.

The selective oxidation of alkenes using green oxidants such as H_2O_2 is one of the main goals in oxidation catalysis.[50–52] Therefore is both of academic and industrial interest to understand the processes governing oxidation reactions but also those that are detrimental for selectivity. The H_2O_2 disproportionation is the main side reaction competing with alkene epoxidation and consists in the formation of two water molecules and oxygen from two molecules of oxidant. Besides being detrimental for the efficiency of the process by itself, the non–productive decomposition of H_2O_2 has been extensively related to the formation of undesired, so–called *homolytic products* that include organic hydroperoxides, enols or enones.

Ongoing studies in collaboration with Kholdeeva's group focuses on the alkene epoxidation reaction catalyzed by Zr^{IV}–substituted Lindqvist anions, and although the results concerning the epoxidation reaction are still being analyzed, we have studied the reaction mechanism responsible for the H_2O_2 decomposition within the framework of this project. In contrast with the homolytic pathways that have been proposed for other systems,[18–25] we found for TM–POMs a novel, plausible *heterolytic mechanism* for H_2O_2 decomposition that agrees with the fact that conventional radical scavengers (2,6–di–*tert*–butyl–4–methylphenol) produced no effect on the oxidation rate and product distribution in the epoxidation reaction catalyzed by Nb^{V}– and Ti^{IV}–substituted Lindqvist anions.[15] **Figure 7.18** shows the free–energy profile calculated for this new mechanistic proposal. Initially, the activation of a first molecule of H_2O_2 occurs as previously described fot $\mathbf{2^{Nb}}$ and $\mathbf{2^{Ti}}$ catalysts (*vide supra*) to form the Zr– peroxo species $\mathbf{3c^{Zr}}$. The Zr–OO moiety in $\mathbf{3c^{Zr}}$ can then perform an outer–sphere attack on an oxygen atom of a second H_2O_2 molecule to promote the heterolytic O—O bond cleavage in it, which can occur concomitantly with a proton transfer from the POM framework to the leaving hydroxyl group ($\mathbf{TS_{3c–7}^{Zr}}$, represented in **Figure 7.19**). In the computed transition state, the hydrogen transfer from the POM framework activates electrophilically the H_2O_2 molecule which facilitates the nucleophilic attack from the peroxo moiety. Here we cannot discard that during the Zr–peroxo attack, explicit solvent molecules participate in the polarization of the O–O bond instead of the mobile POM proton, or in addition to it. The computed process occurs through an affordable free–energy barrier of 20.2 kcal·mol^{-1}

from **3c**^{Zr} and generates a the Zr–trioxidane species **7**^{Zr}, Zr[η^2–OO(OH)] (**Figure 7.19**) and a water molecule, in an overall exothermic process (by more than 10 kcal·mol^{-1}, see **Figure 7.18**). To our knowledge, this is the first time that such complex is proposed to participate in metal–catalyzed oxidation reactions.

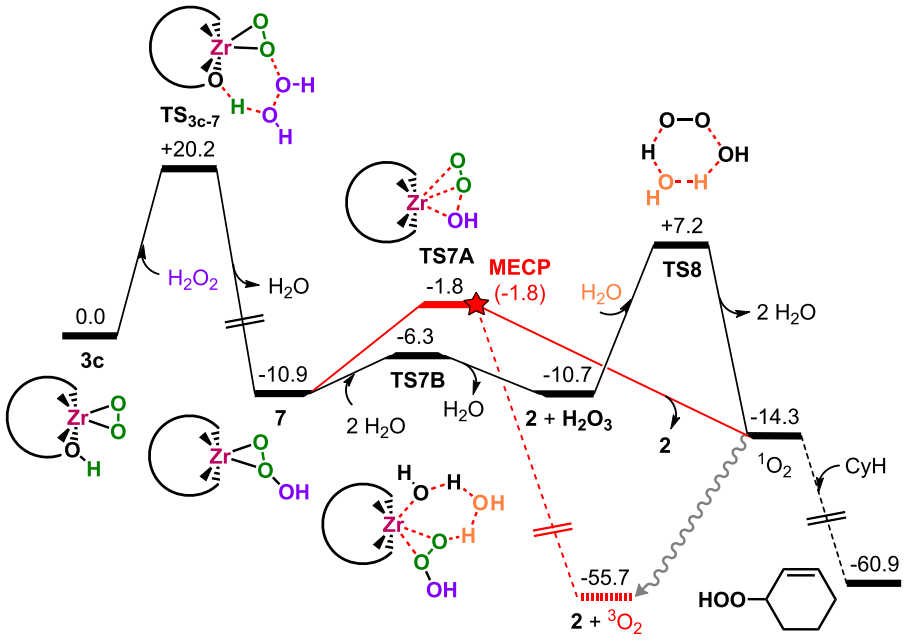

Figure 7.18 | Gibbs free–energy profile (kcal·mol^{-1}) for the decomposition of H_2O_2 catalyzed by a Zr^{IV}–substituted Lindqvist anion, which produces a singlet oxygen molecule that in turn, is capable of activating allylic C—H bonds of CyH to form the main by–products. The most likely pathway is represented in black solid lines. Dashed lines denote triplet state, and the red star stands for a minimum energy crossing point (MECP) between the singlet and the triplet potential energy surfaces.

Intermediate **7**^{Zr} can rapidly evolve through **TS7A**^{Zr} (**Figure 7.18**) to release singlet molecular oxygen and regenerate the Zr–hydroxo species **2**^{Zr} with a small free–energy barrier of 9.1 kcal·mol^{-1}. Along the pathway the reaction could hop from the singlet to the triplet potential energy surfaces yielding **2**^{Zr} and the more stable triplet molecular oxygen, $^3O_2$. We found a minimum energy crossing point (MECP) very close to **TS7A**^{Zr} in the free–energy landscape since their energies and geometries are almost identical. Due to the influence of heavy metal atoms in the structure of **MECP**, the spin–orbit coupling (SOC) is expected to be large, favoring the transition from the singlet to the triplet surface. The TS in the triplet state surface could not be located and geometry optimization algorithms brought the structure to products.

Alternatively, in the presence of water, $\mathbf{7^{Zr}}$ can release trioxidane (H_2O_3) to the medium overcoming a smoother free–energy barrier of 4.6 kcal·mol^{-1} (**TS7B^{Zr}**, **Figure 7.18**) also regenerating $\mathbf{2^{Zr}}$, which can be reincorporated to the main catalytic cycle. Trioxidane is known to decompose in the presence of water into a water molecule and singlet molecular oxygen $^1O_2$.[53] At the employed level of theory, the free–energy barrier for the H_2O_3 decomposition is 17.9 kcal·mol^{-1} (**Figure 7.18**). This value is close to the enthalpy barriers found before,[53b] suggesting that the entropic contribution for this process is small, in line with the lightness of the molecules involved and their proneness for being close in the medium due to their highly polar nature. Note that the high concentration of water compared to that of $\mathbf{2^{Zr}}$ is expected to favor going forward through **TS8^{Zr}** over the reverse reaction to proceed through **TS7A^{Zr}**. Then, the radiative decay to the ground state triplet oxygen ($^3O_2$) could occur in the microseconds time–scale.[54] Nonetheless, $^1O_2$ has shown the ability to activate allylic C—H bonds in organic molecules,[55] and therefore, if $^1O_2$ reaches a CyH substrate molecule in solution, they can react through an ene–like the mechanism that involves two adjacent transition states with no intervening intermediate, as found by Singleton et al.[56] The first TS corresponds to the symmetric attack of the $^1O_2$ to the double bond that yields a kind of perepoxide complex, which is actually the second TS connecting two minima that represent the allylic proton abstraction at both sides of the double bond. Thus, this mechanism would explain the formation of the α, β–unsaturated organic hydroperoxide (HP), which is computed to be strongly exothermic (by more than 40 kcal·mol^{-1}). Notably, this is to our knowledge the first atomistic description of non–productive decomposition of H_2O_2 over TM–substituted POM catalysts that in addition, demonstrates that the formation of the main by–products is indeed related to the H_2O_2 disproportionation reaction, as previously postulated from an experimental perspective. Aiming to support the herein proposed reaction mechanism, our experimental collaborators are currently working on the detection of singlet oxygen after treating Zr–Lindqvist catalysts with H_2O_2.

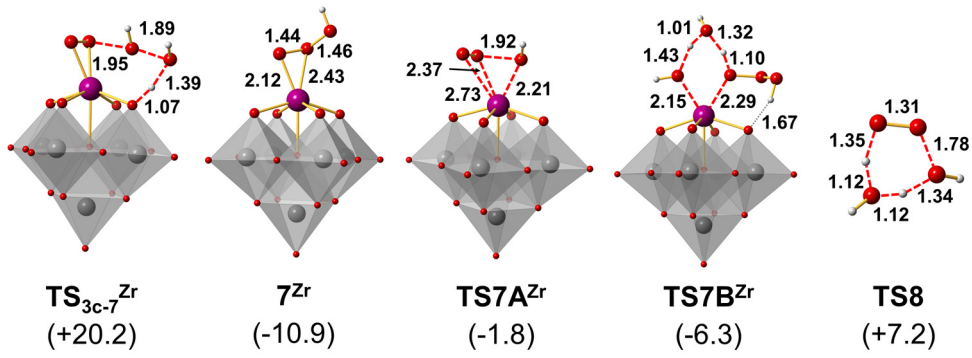

Figure 7.19 | DFT–optimized geometries for the most relevant species in the reaction profile depicted in **Figure 7.18**.

Next, we analyzed whether this mechanistic proposal can explain the higher selectivity of Nb^{V}– compared to Ti^{IV}–containing catalysts. **Table 7.4** compares the calculated free–energy barriers for the epoxidation of CyOct and H_2O_2 decomposition by **1a^{Nb}** and **1a^{Ti}** catalysts. Most importantly, the difference between the height of free–energy barriers for epoxidation and H_2O_2 decomposition is larger in the Nb^{V} (4.6 kcal·mol^{-1}) than in Ti^{IV} catalyst (2.2 kcal·mol^{-1}). This indicates that the H_2O_2 decomposition side reaction is less capable to compete with the alkene epoxidation path in Nb, in excellent agreement with the higher selectivity reported experimentally. This trend was ascribed, again, to the higher oxidation state of Nb, that makes the peroxo group more electrophilic, favoring the O–transfer to the alkene while the effect in the H_2O_2 decomposition process is less clear. According to our computed transition state, the lower overall negative charge featured by the Nb catalyst hampers the nucleophilic attack to the second H_2O_2 molecule but conversely it facilitates the proton transfer to H_2O_2. As mentioned above, the explicit solvent could play the role of acidic hydrogen at the POM, and in that case we would expect that the reduced nucleophilicity of the Nb–peroxo group dominates the reactivity towards H_2O_2 slowing down the decomposition rate in agreement with experimental findings.

It is also important mentioning that although some of the obtained barriers are somewhat too high (>30 kcal·mol^{-1}) for reproducing experimental conversions of **Table 7.1**, refinement of the geometries and energies at 6–311G+(d,p)/LANL2TZ(f) level led to more moderate free–energy barriers that range from 22 to 27 kcal·mol^{-1}, as shown in parenthesis in **Table 7.4**. Moreover, the computed ZPE–corrected electronic energy barriers for H_2O_2 decomposition mechanism using the large basis set (13.6 kcal·mol^{-1} for

Nb and 14.5 kcal·mol^{-1} for Ti) do not reproduce the trend in experimental E_a (16.7 and 14.6 kcal·mol^{-1}, respectively). Currently, additional computational simulations and experimental work by our collaborators are in progress to assess quantitatively the rate of H_2O_2 decomposition on going from Ti^{IV}– to Nb^{V}–substituted POM catalysts.

Table 7.4 | Comparison of catalytic activity and selectivity between **1a^{Nb}** and **1a^{Ti}** catalysts in the epoxidation of CyOct with H_2O_2.[a]

Transition Metal	Product selectivity[b] (heterolytic : homolytic)	$\Delta G^{\ddagger}$(overall)		$\Delta\Delta G^{\ddagger}$
		epox.	H_2O_2 decomp.	
Nb^{V}	86:12	25.8 (22.2)	30.4 (25.6)	4.6 (3.4)
Ti^{IV}	59:36	29.6 (24.5)	31.8 (26.6)	2.2 (2.1)

[a] Values in parenthesis correspond to the more extended basis set: 6–311G+(d,p) for main group atoms and LANL2TZ(f) for Nb and Ti. Free energies in kcal·mol^{-1}. [b] Based on CyH conversion of ~30% (see **Table 7.1**, entries 5 and 8).

7.4 Concluding Remarks.

In this chapter we have enlarged the current knowledge on alkene epoxidation reactions with H_2O_2 catalyzed by TM–substituted POM systems. Remarkably, computational results showed in all cases a high degree of consistency with experimental outcomes from our collaborators.

Initially, we studied the mechanism responsible for the alkene epoxidation catalyzed by Nb–substituted Lindqvist POMs using CyH as alkene substrate. The Nb–hydroxo complex **2^{Nb}** can be readily formed from all the analyzed precursors either via hydrolysis of the Nb—OR bond or via protonation upon the addition of acid. The Nb—OH group permits the heterolytic activation of H_2O_2 to yield the Nb–hydroperoxo species that evolves to the more stable protonated peroxo complex **3c^{Nb}**, which was identified as the resting state of the catalytic cycle. In the presence of CyH, the less stable but more reactive η^2–hydroperoxo species **3b^{Nb}** was found to be the main epoxidizing species since it can drive the electrophilic O–transfer to the alkene through a less energy–demanding pathway than the peroxo complex **3c^{Nb}**. The direct O–transfer from the non–protonated peroxo anion **4^{Nb}** complex is more energy–demanding, explaining the lack of reactivity observed

experimentally for this complex. Thus, the presence of protons in the catalyst structure was found to be crucial since it allows the O–transfer through the more favorable hydroperoxo path and reduces the overall charge of the catalyst, increasing its electrophilicity and consequently, accelerating the electrophilic O–transfer step. Similarly, on going from Ti^{IV}– to Nb^{V}–substituted Lindqvist catalysts, the increase of the oxidation state makes the metal center more electrophilic, lowering significantly the energy barrier for the O–transfer to the alkene from the hydroperoxo intermediate. In addition, depending on the nature of metal and its coordination environment, the hydroperoxo species transfers preferentially the nondistorted β–oxygen (for the Ti, which is more reluctant to increase its coordination number) or the more electrophilic α–oxygen (for the Nb with a nonrigid coordination environment, less reluctant to increase its coordination number).

Next, we evaluated the influence of the ligand environment of the metal using two experimentally tested cases. The Nb–substituted Keggin anion bears a lower charge density than its Lindqvist partner and therefore, it can transfer an electrophilic oxygen to the alkene through a smoother free–energy barrier. However, the lower charge density also renders the catalyst more difficult to protonate, explaining the poorer activity observed experimentally. Thus, optimal TM–POM catalysts might need to balance their charge density to be basic enough for accepting protons but not too much in order to be electrophilic enough to transfer an oxygen atom to the double bond of the alkene. On the other hand, the lability of the metal ligand bonds in the hybrid organic–inorganic $\mathbf{1}^{\mathbf{TiW9}}$ allows their epoxidation through an *inner–sphere* mechanism unprecedented in POM chemistry. The resting state of the catalyst corresponds to the Ti–alcoholate complex, which can coordinate a H_2O_2 molecule cleaving one of the Ti—OSi junctions and increasing the flexibility around the Ti center. The resulting Ti–hydroperoxo complex enables the intramolecular oxygen transfer to occur through a smooth free energy barrier due to the enhanced flexibility of the Ti^{IV} ion. The outer–sphere O–transfer involves a more strained TS geometry that manifests in a higher free energy barrier (by ~4 $kcal{\cdot}mol^{-1}$), which is fully consistent with the lower reactivity observed for non–functionalized alkenes, for which the inner–mechanism is not possible.

Finally, as a part of an ongoing study with Zr^{IV}–substituted Lindqvist catalysts, we studied the mechanism responsible for the H_2O_2 disproportionation side reaction. After the activation of a first molecule of oxidant, the protonated peroxo complex **3c** can promote the *heterolytic* O—O cleavage in a second molecule of H_2O_2 via an outer–sphere

nucleophilic attack of the Zr(OO) moiety. This generates H_2O_3 releasing a molecule off water in a step–wise process. In the presence of water, H_2O_3 decomposes into water and a singlet oxygen. The latter is highly reactive against allylic protons, explaining the formation of the so–called "homolytic products". More importantly, since the rate–determining step of this process is the nucleophilic attack of the peroxo ligand to an external H_2O_2 molecule, the proposed mechanism can explain the higher selectivity of more electrophilic Nb^V catalysts compared to Ti^{IV} ones. We had observed that increasing the charge of the metal ion from Ti^{IV} to Nb^V makes the peroxo group more electrophilic, reducing the energy barrier for the alkene epoxidation reaction. Interestingly, we found that increasing the electrophilicity of the catalyst has a second positive effect in the catalytic activity slowing down the kinetics for the H_2O_2 decomposition side–reaction. In conclusion, Nb^V single–site catalysts combine a *flexible* coordination environment with a *high* oxidation state, which results in an improved catalytic performance.

References

1. a) Kholdeeva, O. A.; Trubitsina, T. A.; Timofeeva, M. N.; Maksimov, G. M.; Maksimovskaya, R. I.; Rogov, V. A. *J. Mol. Catal. A: Chem.* **2005**, *232*, 173–178; b) Maksimchuk, N. V.; Melgunov, M. S.; Mrowiec–Białoń, J.; Jarzębski, A. B.; Kholdeeva, O. A. *J. Catal.* **2005**, *235*, 175–183; c) Kholdeeva, O. A.; Maksimovskaya, R. I. *J. Mol. Catal. A: Chem.* **2007**, *262*, 7–24; d) Hussain, F.; Bassil, B. S.; Kortz, U.; Kholdeeva, O. A.; Timofeeva, M. N. De Oliveira, P.; Keita, B.; Nadjo, L. *Chem. Eur. J.* **2007**, *13*, 4733–4742; e) Kholdeeva, O. A.; Donoeva, B. G.; Trubitsina, T. A.; Al–Kadamany, G.; Kortz, U. *Eur. J. Inorg. Chem.* **2009**, *2009*, 5134–5141; f) Donoeva, B. G.; Trubitsyna, T. A.; Al–Kadamany, G.; Kortz, U.; Kholdeeva, O. A. *Kinet. Catal.* **2010**, *51*, 816–822; g) Kholdeeva, O. A.; Maksimov, G. M.; Maksimovskaya, R. I.; 1283 Kovaleva, L. A.; Fedotov, M. A.; Grigoriev, V. A.; Hill, C. L. *Inorg. Chem.* **2000**, *39*, 3828–3837; h) Kholdeeva, O. A.; Kovaleva, L. A.; Maksimovskaya, R. I.; Maksimov, G. M. *J. Mol. Catal. A: Chem.* **2000**, *158*, 223–229; i) Kholdeeva, O. A.; Trubitsina, T. A.; Maksimov, G. M.; Golovin, A. V.; Maksimovskaya, R. I. *Inorg. Chem.* **2005**, *44*, 1635–1642.
2. Kholdeeva, O. A.; Trubitsina, T. A.; Maksimovskaya, R. I.; Golovin, A. V.; Neiwert, W. A.; Kolesov, B. A.; López, X.; Poblet, J. M. *Inorg. Chem.* **2004**, *43*, 2284–2292.
3. a) Kholdeeva, O. A. *Top. Catal.* **2006**, *40*, 229–243; b) Kholdeeva, O. A. *Eur. J. Inorg. Chem.* **2013**, *2013*, 1595–1605.
4. Zhang, T.; Mazaud, L.; Chamoreau, L–M.; Paris, C.; Proust, A.; Guillemot, G. *ACS Catal.* **2018**, *8*, 2330–2342.
5. Guillemot, G.; Matricardi, E.; Chamoreau, L–M.; Thouvenot, R.; Proust, A. *ACS Catal.* **2015**, *5*, 7415–7423.
6. Zhang, T.; Solé–Daura, A.; Hostachy, S.; Blanchard, S.; Paris, C.; Li, Y.; Carbó, J. J.; Poblet, J. M.; Proust, A.; Guillemot, G. *J. Am. Chem. Soc.* **2018**, *140*, 14903–14914.
7. Antonova, N.; Carbó, J. J.; Kortz, U.; Kholdeeva, O.A.; Poblet, J. M. *J. Am. Chem. Soc.* 2010, *132*, 7488–7497.
8. Donoeva, B. G.; Trubitsina, T. A.; Antonova, N. A.; Carbó, J. J.; Poblet, J. M.; Al–Kadamany, G.; Kortz, U.; Kholdeeva, O. A. *Eur. J. Inorg. Chem.* 2010, *2010*, 5312–5317.
9. Jiménez–Lozano, P.; Ivanchikova, I. D.; Kholdeeva, O. A.; Poblet, J. M.; Carbó, J. J. *Chem. Commun.* 2012, *48*, 9266–9268.
10. Jiménez–Lozano, P.; Skobelev, I. Y.; Kholdeeva, O. A.; Poblet, J. M.; Carbó, J. J. *Inorg. Chem.* 2016, *55*, 6080–6084.
11. Skobelev, I. Y.; Zalomaeva, O. V.; Kholdeeva, O. A.; Poblet, J. M.; Carbó, J. J. *Chem. Eur. J.* 2015, *21*, 14496–14506.
12. Skobelev, I. Y.; Evtushok, V. Y.; Kholdeeva, O. A.; Maksimchuk, N. V.; Maksimovskaya, R. I.; Ricart, J. M.; Poblet, J. M.; Carbó, J. J. *ACS Catal.* **2017**, *7*, 8514–8523.
13. a) Gallo, A.; Tiozzo, C.; Psaro, R.; Carniato, F.; Guidotti, M. *J. Catal.* **2013**, *298*, 77–83; b) Tiozzo, C.; Bisio, C.; Carniato, F.; Guidotti, M. *Catal. Today* **2014**, *235*, 49–57; c) Thornburg, N. E.; Thompson, A. B.; Notestein, J. M. *ACS Catal.* **2015**, *5*, 5077–5088.
14. a) Ivanchikova, I. D.; Maksimchuk, N. V.; Skobelev, I. Y.; Kaichev, V. V.; Kholdeeva, O. A. *J. Catal.* **2015**, *332*, 138–148.

15. Maksimchuk, N. V.; Ivanchikova, I. D.; Maksimov, G. M.; Eltsov, I. V.; Evtushok, V. Y.; Kholdeeva, O. A.; Lebbie, D.; Errington, J.; Solé–Daura, A.; Poblet, J. M.; Carbó, J. J. *ACS Catal.* **2019**, *9*, 6262–6275.
16. Maksimchuk, N. V.; Maksimov, G. M.; Evtushok, V. Yu.; Ivanchikova, I. D.; Chesalov, Yu. A.; Maksimovskaya, R. I.; Kholdeeva, O. A.; Solé–Daura, A.; Poblet, J. M.; Carbó, J. J. *ACS Catal.* **2018**, *8*, 9722–9737.
17. Kholdeeva, O. A.; Ivanchikova, I. D.; Maksimchuk, N. V.; Skobelev, I. Y. *Catal. Today* **2019**, *333*, 63–70.
18. Shul'pin, G. B.; Kozlov, Y. N.; Nizova, G. V.; Süss–Fink, G.; Stanislas, S.; Kitaygorodskiyc, A.; Kulikova, V. S. *J. Chem. Soc., Perkin Trans.* **2001**, *2*, 1351–1371.
19. Kirillova, M. V.; Kuznetsov, M. L.; Romakh, V. B.; Shul'pina, L. S.; Fraústo da Silva, J. J. R.; Pombeiro, A. J. L.; Shul'pin, G. B. *J. Catal.* **2009**, *267*, 140–157.
20. Yoon, C. W.; Hirsekorn, K. F.; Neidig, M. L.; Yang, X.; Tilley, T. D. *ACS Catal.* **2011**, *1*, 1665–1678.
21. Szécsényi, Á.; Li, G.; Gascon, J.; Pidko, E. *ACS Catal.* **2018**, *8*, 7961–7972.
22. a) Lousada, C. M.; Johansson, A. J.; Brinck, T.; Jonsson, M. *J. Phys. Chem. C* **2012**, *116*, 9533–9543; b) Lousada, C. M.; Johansson, A. J.; Brinck, T.; Jonsson, M. *Phys. Chem. Chem. Phys.* **2013**, *15*, 5539–5552.
23. Ryan, P.; Konstantinov, I.; Snurr, R. Q.; Broadbelt, L. J. *J. Catal.* **2012**, *286*, 95–102.
24. Plauck, A.; Stangland, E. E.; Dumesic, J. A.; Mavrikakis, M. *PNAS* **2016**, *2016*, E1973–E1982.
25. Wang, Y.; Balbuena, P. B. *J. Chem. Theory Comput.* **2005,** *1,* 935–943.
26. Frisch, M. J.; Trucks, G. W.; Schlegel, H. B.; Scuseria, G. E.; Robb, M. A.; Cheeseman, J. R.; Scalmani, G.; Barone, V.; Mennucci, B.; Petersson, G. A.; Nakatsuji, H.; Caricato, M.; Li, X.; Hratchian, H. P.; Izmaylov, A. F.; Bloino, J.; Zheng, G.; Sonnenberg, J. L.; Hada, M.; Ehara, M.; Toyota, K.; Fukuda, R.; Hasegawa, J.; Ishida, M.; Nakajima, T.; Honda, Y.; Kitao, O.; Nakai, H.; Vreven, T.; Montgomery, J. A., Jr.; Peralta, J. E.; Ogliaro, F.; Bearpark, M.; Heyd, J. J.; Brothers, E.; Kudin, K. N.; Staroverov, V. N.; Kobayashi, R.; Normand, J.; Raghavachari, K.; Rendell, A.; Burant, J. C.; Iyengar, S. S.; Tomasi, J.; Cossi, M.; Rega, N.; Millam, J. M.; Klene, M.; Knox, J. E.; Cross, J. B.; Bakken, V.; Adamo, C.; Jaramillo, J.; Gomperts, R.; Stratmann, R. E.; Yazyev, O.; Austin, A. J.; Cammi, R.; Pomelli, C.; Ochterski, J. W.; Martin, R. L.; Morokuma, K.; Zakrzewski, V. G.; Voth, G. A.; Salvador, P.; Dannenberg, J. J.; Dapprich, S.; Daniels, A. D.; Farkas, Ö.; Foresman, J. B.; Ortiz, J. V.; Cioslowski, J.; Fox, D. J. Gaussian 09, revision C.01; Gaussian, Inc.: Wallingford, CT, 2009.
27. a) Lee, C.; Yang, W.; Parr, R. G. *Phys. Rev. B: Condens. Matter Mater. Phys.* **1988**, *37*, 785–789; b) Becke, A. D. *J. Chem. Phys.* **1993**, *98*, 5648–5652; c) Stephens, P. J.; Devlin, F. J.; Chabalowski, C. F.; Frisch, M. J. *J. Phys. Chem.* **1994**, *98*, 11623–11627.
28. Hay, P. J.; Wadt, W. R. *J. Chem. Phys.* **1985**, *82*, 270–283.
29. a) Francl, M. M.; Pietro, W. J.; Hehre, W. J.; Binkley, J. S.; Gordon, M. S.; DeFrees, D. J.; Pople, *J. J. Chem. Phys.* **1982**, *77*, 3654–3665; b) Hehre, W. J.; Ditchfield, R.; Pople, J. A. *J. Chem. Phys.* **1972**, *56*, 2257–2261; c) Hariharan, P. C.; Pople, J. A. *Theoret. Chim. Acta* **1973**, *28*, 213–222.
30. Cancès, E.; Mennucci, B.; Tomasi, J. *J. Chem. Phys.* **1997**, *107*, 3032–3041.
31. López, X.; Carbó, J. J.; Bo, C.; Poblet, J. M. *Chem. Soc. Rev.* **2012**, *41*, 7537–7571.
32. Yanai, T.; Tew, D. P.; Handy, N. C. *Chem. Phys. Lett.* **2004**, *393*, 51–57.
33. Tissandier, M. D.; Cowen, K. A.; Feng, W. Y.; Gundlach, E.; Cohen, M. H.; Earhart, A. D.; Coe, J. V.; Tuttle, T. R. *J. Phys. Chem. A* **1998**, *102*, 7787–7794.

34. Harvey, J. N.; Aschi, M.; Schwarz, H.; Koch, W. *Theor. Chem. Acc.* **1998**, *99*, 95–99.
35. Rodríguez–Guerra Pedregal, J.; Funes–Ardoiz, I.; Maseras, F. "EasyMECP: Quick setup of MECPcalculations with Gaussian," 2018. https://github.com/jaimergp/easymecp.
36. Nikoloudakis, E.; Karikis, K.; Laurans, M.; Kokotidou, C.; Solé–Daura, A.; Carbó, J. J.; Charisiadis, A.; Charalambidis, G.; Izzet, G.; Mitraki, A.; Douvas, A. M.; Poblet, J. M.; Proust, A.; Coutsolelos, A. G. *Dalton Trans.* **2018**, *47*, 6304–6313.
37. a) López, X.; Miró, P.; Carbó, J. J.; Rodríguez–Fortea, A.; Bo C.; Poblet, J. M. *Theor. Chem. Acc.* **2011**, 128, 393–404; b) López, X.; Fernández, J. A.; Poblet, J. M. *Dalton Trans.* **2006**, 1162–1167; c) Solé–Daura, A.; Goovaerts, V.; Stroobants, K.; Absillis, G.; Jiménez–Lozano, P.; Poblet, J. M.; Hirst, J. D.; Parac–Vogt, T. N.; Carbó, J. J. *Chem. Eur. J.* **2016**, *22*, 15280–15289.
38. Li, M.; Yan, X.; Zhu, M.; Wang, M.; Zhou, D. *Catal. Sci. Technol.* **2018**, *8*, 4975–4985.
39. Finn, M. G.; Sharpless, K. B. *J. Am. Chem. Soc.* **1991**, *113*, 113–126.
40. Cui, M.; Adam, W.; Shen, J. H.; Luo, X. Min.; Tan, X. J.; Chen, K. X.; Ji, R. Y.; Jian, H. L. *J. Org. Chem.* **2002**, *67*, 1427–1435.
41. Pérez, Y.; Morante–Zarcero, S.; Del Hierro, I.; Sierra, I.; Fajardo, M.; Otero, M. *Chirality*, **2006**, *18*, 44–48.
42. Wu, Y.–D.; Lai, D. K. W. *J. Am. Chem. Soc.* **1995**, *117*, 11327–11336.
43. a) Wells, D. H.; Delgass, W. N.; Thomson, K. T. *J. Am. Chem. Soc.* **2004**, *126*, 2956–2962; b) Wells, D. H.; Joshi, A. M.; Delgass, W. N.; Thomson, K. T. A *J. Phys. Chem. B*, **2006**, *110*, 14627–14639.
44. Sever, R. R.; Root, T. W. *J. Phys. Chem. B* **2003**, *107*, 4090–4099.
45. Derouane, E. G. Zeolites as solid solvents. *J. Mol. Catal. A* **1998**, *134*, 29–45.
46. Langhendries, G.; De Vos, D. E.; Baron, G. V.; Jacobs, P. A. *J. Catal.* **1999**, *187*, 453–463.
47. Wu, L.; Liu, Q.; Su, X.; Mi, Z. *Front. Chem. China* **2008**, *3*, 112–117.
48. Clerici, M. G. *Appl. Catal.* **1991**, *68*, 249–261.
49. Clerici, M. G. *Topics in Catalysis* **2001**, *15*, 257–263.
50. *Modern Heterogeneous Oxidation Catalysis: Design, Reactions and Characterization*; Mizuno, N., Ed.; Wiley–VCH: Weinheim, 2009.
51. *Liquid Phase Oxidation via Heterogeneous Catalysis: Organic Synthesis and Industrial Applications;* Clerici, M.G., Kholdeeva, O.A., Eds.; Wiley: Hoboken, 2013.
52. Cavani, F.; Teles, J. H. *ChemSusChem* **2009**, *2*, 508–534.
53. a) Cerkovnik, J.; Plesničar, B. *J. Am. Chem. Soc.* **1993**, *115*, 12169–12170; b) Plesničar, B.; Tuttle, T.; Cerkovnik, J.; Cremer, D. *J. Am. Chem. Soc.* **2003**, *125*, 11553–11564; c) Wu, A.; Cremer, D.; Gauss, J. *J. Phys. Chem. A* **2003**, *107*, 8737–8745; d) Plesničar, B.; Cerkovnik, J.; Tekavec, T.; Koller, J. *J. Am. Chem. Soc.* **1998**, *120*, 8005–8006; e) Plesničar, B.; Cerkovnik, J.; Tekavec, T.; Koller, J. *Chem.–Eur. J.* **2000**, *6*, 809–819.
54. Bregnhøj, M.; Westberg, M.; Jensen, F.; Ogilby, P. R. *Phys. Chem. Chem. Phys.* **2016**, *18*, 22946–22961.
55. a) Stephenson L. M.; Grdina M. J.; Orfanopoulos, M. *Acc. Chem. Res.* **1980**, *13*, 419–425; b) Alsters, P. L.; Jary W.; Nardello–Rataj, V.; Jean–Marie, A. *Org. Process Res. Dev.* **2009**, *14*, 259–262.
56. Singleton, D. A.; Hang, C.; Szymanski, M. J.; Meyer, M. P.; Leach, A. G.; Kuwata, K. T.; Chen, J. S.; Greer, A.; Foote, C. S.; Houk, K. N. *J. Am. Chem. Soc.* **2003**, *125*, 1319–1328.

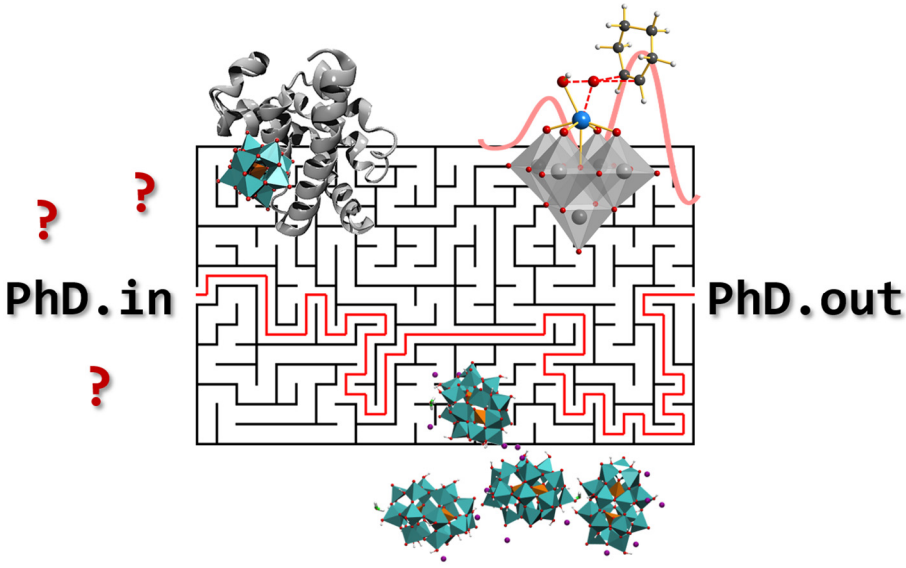

Chapter 8

General Conclusions

UNIVERSITAT ROVIRA I VIRGILI
NEW HORIZONS IN COMPUTATIONAL MODELING OF POLYOXOMETALATES:
BIOLOGICAL ACTIVITY, ENERGY STORAGE AND SUSTAINABLE CATALYSIS.
Albert Solé Daura

CHAPTER 8

General Conclusions

This last chapter summarizes the main achievements and conclusions that have emerged from the studies comprised in Chapters 3 to 7 of this doctoral thesis.

Chapter 3: Probing the Interaction between Polyoxometalates and Proteins using Molecular Dynamics Simulations.

- The interaction between POMs and biological systems mainly involves charge attraction and hydrogen bonds with positively charged and polar amino acids, although water–mediated interactions with polar amino acids were also observed.
- Hydrolytically active Ce– and Zr–containing POMs can establish persistent interactions at two positively charged patches of lysozyme surface that could be related with the experimentally observed hydrolysis.
- The charge density of the POM, as well as their size and shape were identified as important molecular parameters influencing the affinity of POMs towards biological systems.

Chapter 4: Structure–Activity Relationships for the Affinity of Chaotropic Polyoxometalates towards Proteins.

- The affinity of POMs to biological systems depends quadratically on their charge density due to the shift from chaotropic (water–structure–breaking) to kosmotropic (water–structure–forming) behavior of POMs in solution as their charge increase. This causes a parabolic growth of the interaction energy between the POM and the solvent, whereas that with the protein increases linearly. POMs with moderate charges (q/M = 0.33) show more affinity towards proteins because they can balance their interaction with the solvent and the protein.
- Positively charged pockets of lysozyme are size–specific for Keggin–type anions. Smaller POMs show sub–optimal interactions because they cannot interact with several amino acids; and too bulky anions leave a too large part of their surface

exposed to the solvent during their interactions with the protein, being more easily pulled to the solvent bulk.

- A multivariate model with predictive ability for POM affinity towards proteins was built using the *q/M* ratio and the novel shape–weighted volume (V_S) parameters as descriptors of the charge density of the POM and its size and shape, respectively. The model used the *% time binding* as a time–derived response variable obtained from MD simulations with 13 different POMs. This allowed identifying the charge density as the main parameter governing their affinity to biological systems, whereas their size and shape play minor role.

Chapter 5: Modeling the Reactivity of Polyoxometalates towards Biological Systems.

- The hydrolysis mechanism involves four main steps: i) the initial coordination of the Zr^{IV} center to the amide oxygen; ii) the nucleophilic attack to the amide carbon of either the Zr–hydroxo ligand or an external water molecule assisted by the Zr–OH moiety as a general base; the protonation of the amide nitrogen; and iv) the C—N bond cleavage.
- The reaction rate is governed by the energy difference between the reactants and the TS for the C—N cleavage, which is very sensitive to the protein conformation.
- The overall free–energy barriers averaged over protein conformation showed no significant difference between reactive and non–reactive peptide bonds of the protein, being unable to explain the observed selectivity and indicating that the origin of selectivity lies on the biochemical environment of the cleavage site.
- Constrained MD simulations indicate that unlike non–reactive sites, the Asn44—Arg45 peptide bond of HEWL (site II) is surrounded by an array of positively charged and polar amino acids that can trap the POM protease during its coordination to the cleavage site, which might be able to reduce the associated energy penalty and in turn, accelerate the rate of the hydrolysis reaction.

- The reductive cleavage of the disulfide bond in DTNB can be achieved by single electron transfer process from a previously reduced phosphotungstate Keggin anion, $[PW_{12}O_{40}]^{4-}$. After the S—S bond scissile, a second reduction of the generated radical fragment must involve a second POM molecule.

- The reduction of more kinetically stable dicysteine–based polypeptides requires the use of stronger POM reductants, due to larger reorganization energy required to accept an electron from the POM and the less stable character of the formed radical anion.
- The reduction of the disulfide bond in AGT_{ox} protein might be feasible using the one electron–reduced metatungstate ion, $[H_2W_{12}O_{40}]^{7-}$.

Chapter 6: Modeling Super–Reduced Polyoxometalates for Energy Storage.

- Upon reducing the Wells–Dawson anion (**W_{18}**) with Li^+ counter cations at the experimental conditions, POMs become protonated and form cation–mediated agglomerate structures that stabilize the unoccupied *d*(W) orbitals allowing the super–reduction beyond six electrons observed experimentally.
- Simulations with K^+ cations revealed less persistent ion–pairing that hampers the POM agglomeration, explaining the less efficient redox processes in the presence of cations bigger than Li^+.
- The most favorable electronic structure for the super–reduced anion (**W_{18}–18e**) corresponds to an open–shell singlet in which the 18 electrons are unpaired but magnetically coupled. In addition, our calculations suggested that the structure of **W_{18}–18e** might incorporate a number of protons close to 17, which are distributed over the bridging and terminal oxygen positions.
- Super–reduced anions were found to form agglomerates in solution (via cation–mediated contacts and direct hydrogen bonds) that confer them metastable character.
- The energy levels of the super–reduced anion within an agglomerate structure are in fairly good agreement with the narrow experimental window of potential in which the whole super–reduction process occurs. This supports the plausibility of the proposed structures and further validates the proposed super–reduction mechanism for the process.

Chapter 7: Computational Studies on Alkene Epoxidation Catalyzed by Early Transition Metal–Substituted Polyoxometalates.

- The epoxidation of alkenes with H_2O_2 catalyzed by the Nb^V–substituted Lindqvist anion involves the initial heterolytic activation of H_2O_2 to yield a protonated Nb–peroxo complex, which is in equilibrium with the less stable Nb–hydroperoxo.

The Nb–hydroperoxo can transfer the electrophilic alpha–oxygen to the alkene through a lower free–energy barrier than the peroxo complex. Therefore, the presence of protons in the catalyst structure is essential to allow the hydroperoxo path and to increase the electrophilicity of the peroxo moiety.

- The replacement of Ti^{IV} by Nb^{V} increases the electrophilicity of the metal–hydroperoxo moiety favoring the electrophilic oxygen transfer to the alkene, in agreement with the higher conversion achieved experimentally for Nb. Also, since Ti is more reluctant to increase its coordination sphere, it is more likely to transfer the beta–O through a non–distorted TS.
- Optimal epoxidation catalysts should balance their charge density to be basic enough to have associated protons, but not too much in order to be able to transfer an electrophilic oxygen atom to the alkene.
- Hybrid catalysts with labile Ti—OSi bonds allowed the selective epoxidation of allylic alcohols through an *inner–sphere* O–transfer mechanism after the coordination of the substrate to the metal center through the alcoholate group, which involves lower free–energy barriers than the *outer–sphere* mechanism due to an increased flexibility of the metal center.
- Preliminary results suggest that the H_2O_2 decomposition side reaction requires the metal–peroxo group to switch its role from electrophile to nucleophile to promote the heterolytic cleavage of an external molecule of H_2O_2. Interestingly, this would explain the higher selectivity towards the epoxide product reported for Nb, which coordinates a more electrophilic peroxo group.

Overall, we have made a step forward in the computational modeling of polyoxometalates, further probing the capability of computational methods to provide accurate answers to complex questions that arise from the latest scientific progresses. Moreover, some of the achievements reported in this thesis result from the cooperation between several rerearch groups with background in different areas of expertise, highlighting the importance of developing multidisciplinary projects that combine experimental and computational chemistry to reach high standards of quality in chemical research.

UNIVERSITAT ROVIRA I VIRGILI
NEW HORIZONS IN COMPUTATIONAL MODELING OF POLYOXOMETALATES:
BIOLOGICAL ACTIVITY, ENERGY STORAGE AND SUSTAINABLE CATALYSIS.
Albert Solé Daura

UNIVERSITAT ROVIRA I VIRGILI
NEW HORIZONS IN COMPUTATIONAL MODELING OF POLYOXOMETALATES:
BIOLOGICAL ACTIVITY, ENERGY STORAGE AND SUSTAINABLE CATALYSIS.
Albert Solé Daura

Appendix

An appendix section with supplementary information can be accessed on-line through the following QR code or URL:

http://www.quimica.urv.cat/w3qf/tesis/ASoleDaura-appendix.pdf

UNIVERSITAT ROVIRA I VIRGILI
NEW HORIZONS IN COMPUTATIONAL MODELING OF POLYOXOMETALATES:
BIOLOGICAL ACTIVITY, ENERGY STORAGE AND SUSTAINABLE CATALYSIS.
Albert Solé Daura

External collaborations

Some of the projects included in this thesis have been carried out in collaboration with other research groups. Hereunder, they are all listed grouped by institutions and in order of appearance:

- **The University of Nottingham (UK)**
  - Prof. Jonathan D. Hirst
  - Dr. Graham N. Newton
  - Dr. Nicholas J. Mitchell

- **KU Leuven (Belgium)**
  - Prof. Tatjana N. Parac-Vogt

- **Nottingham Trent University (UK)**
  - Dr. David Robinson

- **University of Glasgow (UK)**
  - Prof. Leroy Cronin

- **Boreskov Institute of Catalysis (Russia)**
  - Prof. Oxana A. Kholdeeva

- **Newcastle University (UK)**
  - Dr. R. John Errington

- **Sorbonne Université (France)**
  - Prof. Anna Proust
  - Dr. Geoffroy Guillemot

UNIVERSITAT ROVIRA I VIRGILI
NEW HORIZONS IN COMPUTATIONAL MODELING OF POLYOXOMETALATES:
BIOLOGICAL ACTIVITY, ENERGY STORAGE AND SUSTAINABLE CATALYSIS.
Albert Solé Daura

Acknowledgements / Agraïments

A títol personal, el desenvolupament de la tesi doctoral ha representat una etapa de creixement professional i personal molt gran, probablement com per tants altres. Estic convençut que gran part d'aquest creixement ha estat degut a la qualitat humana de les persones de les que m'he envoltat durant aquests anys i que per tant, mereixen una menció en aquest manuscrit.

Per començar vull agrair als meus directors de tesi, Jordi i Josep Maria, el seu esforç constant per fer que aquesta tesi arribés a bon port, amés de la plena llibertat que m'han donat en tot moment per invertir el meu temps en les coses que em semblessin necessàries o interessants. També us estic profundament agraït per haver tingut sempre en consideració la meva opinió, hipòtesis i propostes sobre els diferents projectes en els que hem treballat plegats.

Jordi, tot i que segurament no en siguis conscient, de tu és probablement de qui més coses hagi après durant aquests anys. Apart de portar-me a tenir un esperit bastant més crític amb la ciència i la societat del que tenia fa quatre anys, m'has ensenyat a reduir la dimensió dels problemes per resoldre'ls de forma efectiva. Aquestes ensenyances m'acompanyaran sempre. Gràcies.

Josep Maria, tu has estat un referent i l'encarnació de la veu de l'experiència, així com un punt de suport al què acudir en situacions complicades. Per la teva part, en tots el casos has sabut respondre donant-me el consell que feia falta (amb un característic punt d'humor àcid) perquè aquesta tesi s'hagi pogut dur a terme de forma satisfactòria. Moltes gràcies per tot el que m'has ensenyat durant aquests anys i per la teva confiança, espero poder deixar el llistó a l'alçada que es mereix.

Seguidament, m'agradaria agrair a la resta de companyes i companys del grup de Química Quàntica de la URV la seva calidesa fent que cada dia el *coffee break* realment representés un *break* i que creuar-se'ls pel passadís fos una raó per somriure. Per començar, m'agradaria agrair-vos a vosaltres, Xavi i Toni, el fet d'haver dipositat en mi la vostra confiança per desenvolupar projectes paral·lels a aquesta tesi. Xavi, també t'estic agraït per haver tingut sempre temps per discutir amb mi qualsevol aspecte de la química dels POMs. A tu Toni, et vull agrair tota l'ajuda i coneixement que m'has transmès en el camp de les metadinàmiques, que estic segur que em serà de gran utilitat en el futur. També m'agradaria fer-te una menció especial a tu, Anna. De no haver estat per tu, segurament ara

mateix no estaria escrivint aquesta tesi. Gràcies per haver-me despertat passió per la química teòrica. A la resta de membres, Coen, Rosa, Mar i Maria, moltes gràcies per haver format part d'aquesta aventura d'una manera o d'una altra i per ajudar-me a interpretar resultats relacionats amb la vostra àrea d'experiència. Ha estat un plaer compartir tot aquest temps amb vosaltres. Rosa, tu també et mereixes una menció especial ja que la teva assistència en qualsevol tipus de tràmit administratiu ha estat impecablement eficaç i de ben segur m'ha estalviat molt de temps i maldecaps. No em vull oblidar dels engranatges indispensables d'aquest grup: Elisenda, Jose i Moisés, moltes gràcies per ajudar-me a solucionar tots els entrebancs tècnics que se m'han posat per davant.

També us vull agrair a la resta de companyes i companys amb els que he compartit el rang de doctorand el fet d'haver estat sempre disposats a fer una riallada. Roser, tu probablement siguis amb qui més records he acumulat. Aquests últims mesos han estat una mica durs, però estic segur que amb perspectiva res serà per tant! No oblidis el "Pangea Lifestyle". Almu, ha estat un plaer poder treballar amb tu en l'estudi del V_{18} i discutir tota mena de resultats. Viatjar amb tu també va ser una experiència molt divertida. Antonio, tú al final has conseguido que no pueda mirarte a los ojos durante la hora de la comida. Gracias por aportar siempre ese toque de humor tan necesario. Aitor, aunque acabes de llegar, creo que puedo hacerte extensiva la dedicatoria de Antonio. Marc, et podria dir alguna cosa similar a l'Antonio, però vull destacar que qualsevol discussió científica que hem tingut sempre ha estat altament interessant i inspiradora. Sort amb tot el que et proposis, que estic segur que ho aconseguiràs. Toni, tu has entrat trepitjant fort. Compartir rutina, viatges i temps amb tu és una cosa que només puc qualificar de divertida. Gràcies per tanta primavera i trinaranjus. I switch to English to acknowledge the asian sector of our group. Jianfang, it has been a great pleasure to meet you. I wish all the best for your future, hopefully in Europe. Fei (aka Julia), Zhongling and Yeamin, our time together in the group it has been somewhat shorter, but it has been really nice to share funny time with you. Gantulga, during the short time we worked together you showed a huge capability for learning. I am convinced you will be able to overcome any kind of bump on the road.

Gràcies també als antics companys i amics, especialment Magda, Ximo, Diego, Laura i Sergi. Hem viscut grans moments plegats i espero que en quedin molts més per davant. Us desitjo molta sort i molts èxits en tots els projectes que emprengueu. Tant debò en algun moment els nostres camins es tornin a creuar.

Now it is time for people in Nottingham. First of all, I would like to thank you Jonathan for your kind hospitality that went far beyond your duty. I would like to extend my thanks to Pilar and Katelina; all the time I spent with you and Jonathan in *Baresca* o *Revolución de Cuba* was amazing and I keep nice memories from that. Thank you very much for your warmth and hospitality. David, I am very grateful for all the help you gave me with QM/MM calculations. Without your assistance I would be still struggling with error messages. Steve, Pritesh, Greg and Adam. You made my time in Nottingham much more pleasant. I am also thankful for the vast number of idioms and slang words you thought me, I swear I will try to use them properly.

Irene, tú me has acompañado desde el día uno de esta aventura. Bajo cualquier circunstancia, yo también tendré siempre tiempo para un vermut (o dos…). Adrià i Maria, moltes gràcies a vosaltres també per les bones estones.

A les amigues i amics del cercle més estret que hi heu estat a les dures i a les madures, Beki, Ester, Cris i Marta, Marc i Anna moltes gràcies a tots. També m'agradaria fer extensiu aquest agraïment a la Vero i la Laia, que encara que sigui difícil quadrar dates, sempre acabin trobant un cap de setmana per agafar vols i passar-lo junts.

Per acabar, m'agradaria agrair als meus pares i a la meva família tots els ànims i el suport incondicional que he rebut per part seva. Em falten paraules per agrair-vos tota la vostra paciència i les paraules amables que m'heu fet arribar.

UNIVERSITAT ROVIRA I VIRGILI
NEW HORIZONS IN COMPUTATIONAL MODELING OF POLYOXOMETALATES:
BIOLOGICAL ACTIVITY, ENERGY STORAGE AND SUSTAINABLE CATALYSIS.
Albert Solé Daura

UNIVERSITAT ROVIRA I VIRGILI
NEW HORIZONS IN COMPUTATIONAL MODELING OF POLYOXOMETALATES:
BIOLOGICAL ACTIVITY, ENERGY STORAGE AND SUSTAINABLE CATALYSIS.
Albert Solé Daura

UNIVERSITAT
ROVIRA i VIRGILI

NEW HORIZONS IN COMPUTATIONAL MODELING OF POLYOXOMETALATES: BIOLOGICAL ACTIVITY, ENERGY STORAGE AND SUSTAINABLE CATALYSIS

Albert Solé Daura